Insights into assembly of the type IVa pilus machine in *Myxococcus xanthus*

Dissertation

zur Erlangung des Grades eines

Doktor der Naturwissenschaften

(Dr. rer.nat.)

des Fachbereichs Biologie der Philipps-Universität Marburg

Vorgelegt von

Marco André Herfurth

Aus Wiesbaden

Marburg, 2023

Die vorliegende Dissertation wurde von Juli 2019 bis August 2023 am Max Planck Institut für Terrestrische Mikrobiologie unter Leitung von Prof. Dr. Lotte Søgaard-Andersen angefertigt.

Vom Fachbereich Biologie der Philipps-Universität Marburg (Hochschulkennziffer 1180) als Dissertation angenommen am 14.08.2023

Erstgutachter(in): Prof. Dr. Lotte Søgaard-Andersen
Zweitgutachter(in): Prof. Dr. Martin Thanbichler

Weitere Mitglieder der Prüfungskomission:
Prof. Dr. Gert Bange
Prof. Dr. Lennart Randau
Prof. Dr Johann Heider

Tag der Disputation: 24.11.2023

Parts of this thesis have been published, are submitted or in preparation for publication:

Herfurth, M., Treuner-Lange, A., Glatter, T., Wittmaack, N., Hoiczyk, E., Pierik, A. J., & Søgaard-Andersen, L. (2022). A noncanonical cytochrome c stimulates calcium binding by PilY1 for type IVa pili formation. *Proceedings of the National Academy of Sciences*, *119*(6), e2115061119.

Herfurth, M., Pérez-Burgos, M., & Søgaard-Andersen, L. (2023) Mechanism of polar localization of the type IVa pilus machine. *mBio (in press).* bioRxiv: 10.1101/2023.06.22.546063

Herfurth, M., Müller, F., Søgaard-Andersen, L. & Glatter, T. (2023) A miniTurboID-based proximity labeling protocol to identify conditional protein interactomes *in vivo* in *Myxococcus xanthus*. *Manuscript submitted for publication.*

Pérez-Burgos, M., Herfurth, M., Kaczmarczyk A., Huber, K., Glatter, T., Jenal, U., Seifert, R., & Søgaard-Andersen, L. A burst of c-di-GMP during cytokinesis ensures the generation of phenotypically identical and symmetrical daughter cells. *Manuscript in preparation*.

Publications that are not discussed in this thesis:

Treuner-Lange, A., Chang, Y. W., Glatter, T., Herfurth, M., Lindow, S., Chreifi, G., Jensen, G. J., & Søgaard-Andersen, L. (2020). PilY1 and minor pilins form a complex priming the type IVa pilus in *Myxococcus xanthus*. *Nature communications*, 11(1), 5054.

Schwabe, J., Pérez-Burgos, M., Herfurth, M., Glatter, T., & Søgaard-Andersen, L. (2022). Evidence for a widespread third system for bacterial polysaccharide export across the outer membrane comprising a composite OPX/β-Barrel translocon. *mBio*, *13*(5), e0203222.

Treuner-Lange, A., Zheng, W., Viljoen, A., Lindow, S., Herfurth, M., Dufrêne, Y. F., Søgaard-Andersen, L., & Egelman, E. H. (2023). Large pilin subunits provide distinct structural and mechanical properties for the *Myxococcus xanthus* type IV pilus. *Manuscript submitted for publication.* bioRxiv*:* 10.1101/2023.07.22.550172

1. Abbreviations 7

2. Erklärung 8

3. Abstract 9

4. Zusammenfassung 10

5. Introduction 12

5.1 Introduction to type IV pili 12

5.1.1 Prokaryotic secretion systems 12

5.1.2 The type IV filament family 13

5.1.3 The T4aP machine 14

5.1.4 Other secretion systems of the type IV filament family 24

5.1.5 Assembly of secretion systems 28

5.2 The interplay between type IV pili and c-di-GMP 30

5.2.1 Introduction to c-di-GMP 30

5.2.2 Role of T4aP in concert with c-di-GMP in surface colonialization 31

5.2.3 Regulation of T4aP by c-di-GMP in phototaxis 34

5.3 Introduction to *Myxococcus xanthus* 36

5.3.1 The life style of *M. xanthus* 36

5.3.2 T4aP-dependent motility 36

5.3.3 Gliding motility 38

5.3.4 Regulation of polarity 39

5.3.5 Function of c-di-GMP in *M. xanthus* 41

6. Scope of the study 46

7. References 48

8. Results 58

8.1 A noncanonical cytochrome *c* stimulates calcium binding by PilY1 for type IVa pili formation 58

8.1.1 Supplementary material 71

8.2 Mechanism of polar localization of the type Iva pilus machine 102

8.2.1 Supplementary material 140

8.3 A burst of c-di-GMP during cytokinesis ensures the generation of phenotypically identical and symmetrical daughter cells 150

8.3.1 Supplementary material.....194

8.4 A miniTurboID-based proximity labeling protocol to identify conditional protein interactomes in vivo in *Myxococcus xanthus* 211

9. Discussion and outlook of the study 232

1. Abbreviations

Active-site	A-site
Amphipathic helical loop	AHL
Cryo-electron tomography	Cryo-ET
Diguanylate cyclase	DGC
Exopolysaccharide	EPS
GTPase-activating protein	GAP
Guanine nucleotide exchange factor	GEF
Inhibitory-site	I-site
Inner membrane	IM
Outer membrane	OM
Peptidoglycan	PG
Phosphodiesterase	PDE
T4aP machine	T4aPM
Tetratricopeptide repeat	TPR
Type II secretion system	T2SS
Type III secretion system	T3SS
Type IV filament family	T4FF
Type IV pili	T4P
Type IVa pili	T4aP
Type IVb pili	T4bP
Type IVc pili	T4cP

2. Erklärung

Ich versichere, dass ich meine Dissertation mit dem Titel „Insights into assembly of the type IVa pilus machine in *Myxococcus xanthus*“ selbstständig ohne unerlaubte Hilfe angefertigt und mich dabei keiner anderen als der von mir ausdrücklich bezeichneten Quellen und Hilfsmittel bedient habe.

Diese Dissertation wurde in der jetzigen oder einer ähnlichen Form noch bei keiner anderen Hochschule eingereicht und hat noch keinen sonstigen Prüfungszwecken gedient.

Marburg, den 14.08.2023

Marco Herfurth

3. Abstract

Type IVa pili (T4aP) are widely distributed and highly versatile bacterial cell surface structures that function in motility, adhesion, biofilm formation and virulence. Key to their function is their ability to undergo extension/adhesion/retraction cycles powered by the cell envelope-spanning T4aP machine. Assembly of the T4aP machine in *Myxococcus xanthus* follows an outside-in parthway, starting with the incorporation of the PilQ secretin in the OM, which then recruits the periplasmic, inner membrane and cytoplasmic components. Additionally, a complex composed of four minor pilins and PilY1 primes T4aP extension and is also present at the pilus tip mediating adhesion. Here we focuse on the assembly of the bipolarly localized T4aP machine in the rod-shaped bacterium *M. xanthus*.

The genome of *M. xanthus* encodes for three sets of minor pilins and PilY1. Here, we find that one of these minor pilin and PilY1 gene clusters includes a noncanonical cytochrome *c,* which we named TfcP. While TfcP has an unusually low redox potential that makes a function in respiration unlikely, it is conditionally essential for T4aP dependent motility by promoting the accumulation of PilY1.1 in the presence of low calcium concentrations. We suggest that TfcP extends the range of calcium concentration at which PilY1.1 can function, making its function more robust against environmental fluctuations.

Next, we focused on the assembly of new T4aP machines in the new poles of cells after cell division. We demonstrate that PilQ starts to be recruited to the nascent poles during cytokinesis, but mostly is recruited to the new poles after completion of cytokinesis. This recruitment depends on the peptidoglycan-binding AMIN domains of PilQ and we propose that this mechanism is general for AMIN domain containing secretins. Additionally, PilQ transiently recruits the pilotin Tgl to the nascent and new poles, which then induces the multimerization of PilQ in the outer membrane. We suggest that the transient interaction between PilQ and Tgl is mediated by the unfolded β-lip of PilQ, the domain that is integrated into the outer membrane.

In addition, we uncover that the diguanylate cyclase DmxA is important for the symmetric assembly of the T4aP machine at the new cell poles after cytokinesis. In the absence of DmxA, cells exhibit a misregulated cell polarity and a very heterogeneous polar localization of the T4aP machine, which leads to an increased reversal frequency. DmxA is recruited to the division site by components of the divisiome shortly before the completion of cytokinesis and rapidly elevates the cellular c-di-GMP level. We suggest that this burst of c-di-GMP regulates the symmetric incorporation of polar landmarks at the new cell poles in both daughter cells.

Lastly, we establish a detailed protocol for the application of miniTurboID-based proximity labeling in *M. xanthus.* We apply this protocol to the polarity regulator MglA, and utilize proximity labeling to compare the conditional interactome of MglA.

4. Zusammenfassung

Typ IVa pili (T4aP) sind weiteverbreitete und vielseitige, bakterielle Zelloberflächen Strukturen, die zu Motilität, Adhesion, Biofilm Bildung und Virulenz beitragen. Ihrer Funktionsweise basiert auf der Eigenschaft Zyklen von Verlängerung/Adhäsion/Rückzug zu durchlaufen, die von einer Zellhülle umspannenden T4aP Maschine angetrieben werden. Der Aufbau der T4aP Maschine in *Myxococcus xanthus* erfolgt von außen nach innen und beginnt mit dem Einbau des secretins PilQ in die äußere Membran, welches dann periplasmatische Protein und Komponenten aus der inneren Membran und dem Zytoplasma rekrutiert. Zusätzlich initiiert ein Komplex aus Minor Pilinen und PilY1 die Verlängerung von T4aP und befindet sich ebenfalls an der Spitze des Pilus, wo der Komplex Adhäsion ermöglicht.

Hier fokussieren wir uns auf den Aufbau der bipolaren T4aP Maschine in dem stäbchenförmigen Bakterium *M. xanthus.* Das Genom von *M. xanthus* codiert für drei Sätze von Minor Pilinen und PilY1. Hierbei haben wir festgestellt, dass eines dieser Gen Cluster ein nicht-kanonisches Cytochrom c enthält, welches wir TfcP genannt haben. Während TfcP ein unüblich niedriges Redox-Potential besitzt, welches eine Funktion im Stoffwechsel unwahrscheinlich macht, ist TfcP bedingt essenziell für T4aP abhängige Motilität, weil es die Akkumulation von PilY1.1 in Gegenwart von niedrigen Calcium Konzentrationen erlaubt. Wir schlagen vor, dass TfcP die Spanne an Calcium Konzentrationen, in denen PilY1.1 funktional ist, erweitert und dadurch dessen Funktion robuster gegeben über Änderungen in der Umwelt macht.

Als nächstes untersuchen wir den Aufbau neuer T4aP Maschinen an den neuen Zellpolen nach der Zellteilung. Wir zeigen, dass PilQ während der Zytokinese an den entstehenden Polen rekrutiert wird, aber hauptsächlich nach Abschluss der Zytokinese an den neuen Polen rekrutiert wird. Diese Rekrutierung hängt von den peptidoglykanbindenden AMIN-Domänen von PilQ ab, und wir schlagen vor, dass dieser Mechanismus für Secretins mit AMIN-Domänen im Allgemeinen gilt. Darüber hinaus rekrutiert PilQ vorübergehend das Pilotin Tgl an den entstehenden und neuen Polen, was dann die Multimerisierung von PilQ in der äußeren Membran induziert. Wir vermuten, dass die vorübergehende Interaktion zwischen PilQ und Tgl durch die ungefaltete β-Lippe von PilQ vermittelt wird, die in die äußere Membran integriert ist.

Zusätzlich haben wir herausgefunden, dass die Diguanyletcyclase DmxA für den symmetrischen Aufbau des T4aP-Mechanismus an den neuen Zellpolen nach der Zytokinese wichtig ist. In Abwesenheit von DmxA zeigen die Zellen eine fehlerhafte Zellpolarität und eine sehr heterogene polare Lokalisierung des T4aP-Machine. DmxA wird kurz vor Abschluss der Zytokinese von Komponenten des Divisoms an der Teilungsstelle rekrutiert und erhöht rasch den zellulären c-di-GMP-Spiegel. Wir vermuten, dass dieser Anstieg von c-di-GMP die symmetrische Bildung/Verteilung von polaren Landmarken an den neuen Zellpolen reguliert.

Schließlich haben wir ein detailliertes Protokoll für die Anwendung des auf MiniTurboID basierenden Proximity Labelings in M. xanthus erstellt. Wir wenden dieses Protokoll auf den Regulator MglA an und nutzen das Proximity Labeling, um das bedingte Interaktom von MglA zu vergleichen.

5. Introduction

5.1 Introduction to type IV pili

5.1.1 Prokaryotic secretion systems

Bacteria are exposed to dynamic and rapidly changing environments, presenting a constant challenge for their survival. To overcome these challenges, cells have adapted the ability to sense and respond to environmental cues on multiple levels. At the single cell level, these outputs can generate changes in e.g. gene expression, metabolism, and motility behavior or in some cases, cells undergo differentiation with the formation of highly resistant spores. Alternatively, cells can coordinate to form a biofilm by secreting proteins and sugars (Lopez *et al.*, 2010), enabling bacteria to thrive in diverse ecological niches.

Bacterial protein secretion systems comprise a group of protein complexes involved in numerous cellular functions and fundamental for cells to interact with their environment (Silhavy *et al.*, 2010). These systems enable the translocation of folded or unfolded proteins from the cytoplasm to other cellular compartments or the extracellular space, enabling cells to interact with and manipulate their surroundings in diverse ways (Green & Mecsas, 2016, Christie, 2019). Due to their broad and crucial role for individual cells as well as for the formation of bacterial communities and host-pathogen interactions, understanding how secretion systems function has been a central research goal. Furthermore, secretion systems have been implicated in the virulence of pathogenic bacteria, making them key targets for therapeutic interventions (Blasey *et al.*, 2022, Dumenil, 2019).

Despite sharing the common goal of facilitating protein translocation, secretion systems use very different mechanisms to overcome the obstacles that they encounter to fulfill their function (Christie, 2019, Green & Mecsas, 2016). Generally, these systems are divided into one- and two-step secretion systems, depending on across how many membranes the secretion system translocates its substrate. CTwo-step systems are only found in Gram-negative bacteria, and their substrate is first translocated to the periplasm *via* the general secretory pathway and subsequently secreted across the outer membrane (OM) (Christie, 2019, Green & Mecsas, 2016).Two-step systems either only span the OM, e.g. the substrate of the type V secretion system forms a β-barrel pore through which it crosses the OM, and therefore the system is also referred to as autotransporter (Bernstein, 2019), or span the entire cell envelope, but only transport their substrate across the OM (Christie, 2019, Green & Mecsas, 2016). For instance, while the substrates of the type II secretion system (T2SS) is transported to the periplasm via the general secretory pathway, the T2SS utilizes ATP hydrolysis in the cytoplasm to power the transport of its substrate over a dedicated OM channel (Naskar *et al.*, 2021).

Secretion systems with one-step mechanism are found in Gram-positive and Gram-negative bacteria and translocate their substrate directly from the cytoplasm to the extracellular space (Christie, 2019, Green & Mecsas, 2016). One-step systems, such as the type III (T3SS) and type VI secretion system, translocate effectors into other cells by either forming a needle-like structure and pore in the OM of host cells , or repurposing a contractile phage tail-like structure to deliver effectors by piercing the cell wall of host cells (Christie, 2019, Green & Mecsas, 2016, Galán & Waksman, 2018). Additionally, the one-step type VII secretion system (also called ESX pathway in mycobacteria (Vaziri & Brosch, 2019)), only occurs in Gram-positive bacteria and transports its substrate across the IM to the cell surface (Christie, 2019, Green & Mecsas, 2016). In addition to their unique adaptations, there are common parts and mechanisms shared between different classes of secretion systems. For instance, the T2SS and T3SS employ a similar OM pore to translocate their substrate across the OM, termed secretin (Christie, 2019, Green & Mecsas, 2016). Understanding the commonalities and differences in these secretion systems can shed light on the evolution, function, and regulation of these fascinating cellular machineries.

5.1.2 The type IV filament family

The type IV filament family (T4FF), one of the most versatile families of secretion systems, encompasses the T2SS, type IVa pili (T4aP), type IVb pili (T4bP), type IVc pili (T4cP) (also referred to as Tad pili), mannose-sensitive hemagglutination (MSH) pili, competence pili of Gram-positive bacteria as well as the archaeal archaellum (Figure 1) (Denise *et al.*, 2019, Beeby, 2019). The members of this family are cell envelope spanning secretions systems with a common architecture that synthesize a protein filament termed a pilus. T4P and the archaellum can extend several micrometer beyond the cell surface (Pelicic, 2008). In contrast, the short pseudopilus of the T2SS likely under normal conditions does not cross the OM (Korotkov *et al.*, 2012).

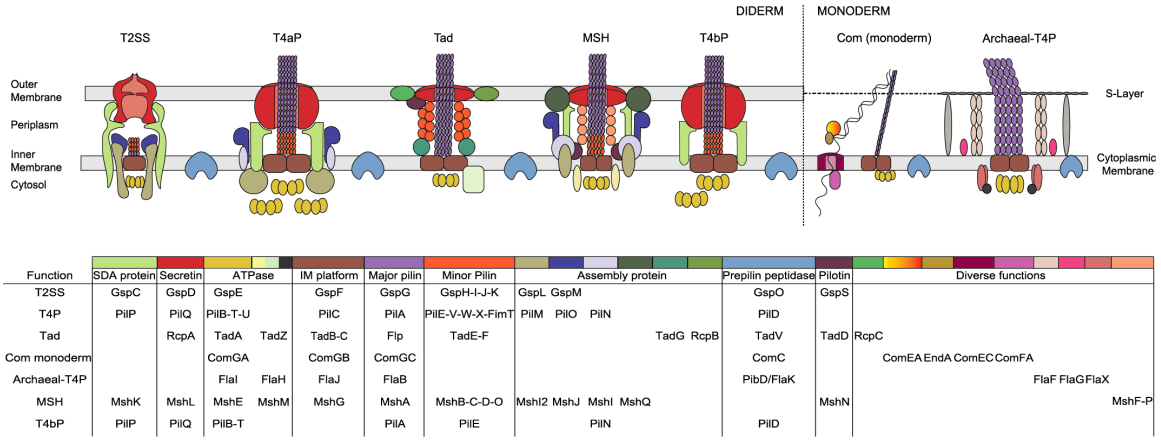

Figure 1 Architecture and nomenclature of the different secretions systems of the T4FF. Reused from (Denise *et al.*, 2019) under the CC BY 4.0 license.

Among the different types of pili assembled by T4FF, T4aP are the most prominent group, found in both Gram-positive and Gram-negative bacteria (Denise *et al.*, 2019). T4aP play various roles in processes such as motility, adhesion, biofilm formation, surface sensing, host cell recognition, virulence and DNA uptake (Pelicic, 2008, Berry & Pelicic, 2015, Craig *et al.*, 2019). T4aP are six-seven nanometer in diameter and can extend several micrometer beyond the cell surface. The pilus is predominantly composed of a helical assembly of pilin subunits, termed major pilin. These protein filaments undergo cycles of extension, adhesion and retraction, employing a simple mechanism that, with the addition of specialized proteins, allows for the diverse functions mentioned above (Merz *et al.*, 2000, Skerker & Berg, 2001).

5.1.3 The T4aP machine

T4aP are assembled from a cell envelope spanning multi-protein complex termed the T4aP machine (T4aPM). In Gram-negative bacteria, the T4aPM is composed of an OM pore, an alignment complex, a motor complex, which power pilus extension and retraction, the major pilins that make up most of the pilus filament, and minor pilins that form the pilus tip together with the PilY1 protein filament (McCallum *et al.*, 2019b, Treuner-Lange *et al.*, 2020). The structure, function and assembly of the T4aPM has been best studied in Gram-negative bacteria, such as *Myxococcus xanthus, Pseudomonas aeruginosa* and *Neisseria* sp. Gram-positive bacteria can also have a T4aPM with a similar composition, but lack the OM components (Piepenbrink & Sundberg, 2016).

Secretin

Assembly of the T4aPM is best understood in *M. xanthus* and *P. aeruginosa* and starts with the assembly of the integral OM pore, the secretin (Friedrich *et al.*, 2014, Chang *et al.*, 2016, Carter *et al.*, 2017). The secretin is a >1 MDa homooligomeric protein complex that forms a pore through which the pilus passes the OM (Chang *et al.*, 2016, Gold *et al.*, 2015). Secretins belong to the OM β-barrel proteins in which the barrel consists of multiple subunits. Moreover, secretins have been reported to be incorporated into the OM independent of the Bam-complex (Dunstan *et al.*, 2015, Huysmans *et al.*, 2015). The exact number of subunits in the T4aP secretin has not been unambiguously determined, or, alternatively, the oligomeric structure of T4aPM varies between species, and structures with symmetries between 12 and 15 subunits have been reported (Chang *et al.*, 2016, McCallum *et al.*, 2021, Weaver *et al.*, 2020). Furthermore, secretins are not exclusive to the T4aPM but also are an essential component of other T4P systems, the T2SS and the T3SS (Majewski *et al.*, 2018).

While secretins share an overall common domain architecture, some variations exist among the different secretion systems (Barbat *et al.*, 2022). The N-terminal part of the secretins shows the highest variability. While it contains at least an N0-domain and an N3-domain (Figure 2), it can contain additional N-domains (Silva *et al.*, 2020, D'Imprima *et al.*, 2017). The N0-domain

shares homology with the signaling domain of TonB-dependent receptors and, in the case of the T4aPM, interacts with the IM lipoprotein PilP of the alignment complex (see below) (Balasingham *et al.*, 2007, Koo *et al.*, 2012, Tammam *et al.*, 2013). The N3-domain harbors a ring-building motif and, in the T2SS system, this domain initiates secretin oligomerization independently of the remaining secretin domains prior to the insertion into the OM (Guilvout *et al.*, 2014). Additionally, the N-terminus of T4aP secretins can contain a variable number of peptidoglycan (PG) binding amidase N-terminal (AMIN) domains (Weaver *et al.*, 2020, Chang *et al.*, 2016). Due to their flexible connection and variable orientation, AMIN domains could neither be imaged in cryo-electron tomography (cryo-ET) nor in cryo-electron microcopy (cryo-EM) structures of secretins (Weaver *et al.*, 2020, McCallum *et al.*, 2021, Chang *et al.*, 2016). However, they have been implicated in targeting and in guiding the localization of the T4aPM (Carter *et al.*, 2017). The C-terminal secretin forming region represent the most conserved part of the secretin family (Majewski *et al.*, 2018). It contains the β-lip region and the secretin domain, which together adopt a fold comprising four antiparallel β-sheets that oligomerize into a larger, double-walled barrel structure, with a gate and a amphipathic helical loop (AHL) (Figure 2) (Weaver *et al.*, 2020, McCallum *et al.*, 2021). The secretin and N-domains form a vestibule, which represents the majority of the secretin structure and extends deeply into the periplasm (Chang *et al.*, 2016). The gate, formed by two strands of the inner β-barrel, closes the vestibule of the non-piliated T4aPM to the extracellular space (Chang *et al.*, 2016, Weaver *et al.*, 2020). The secretin of thermophilic bacteria such as *Thermus thermophilus* possess an additional gate with unknown function that is formed by one of the N-domains (D'Imprima *et al.*, 2017). The amphipathic β-lip forms the part of the secretin that integrates into the OM (Figure 2) (Worrall *et al.*, 2016, Weaver *et al.*, 2020) and can extend out of the OM forming structures termed crowns (D'Imprima *et al.*, 2017). Adjacent to the β-lip, the AHL associates with the inner leaflet of the OM and represents the most conserved region of secretins (Figure 2) (Weaver *et al.*, 2020).

Pilotin

The mechanism by which secretins assemble and integrate into the OM has not been fully resolved, but generally, relies on a cognate pilotin protein. Pilotins are OM-lipoproteins that are important to transport secretin monomers to the OM (Koo *et al.*, 2008, Collin *et al.*, 2011), insert secretins in the OM (Worrall *et al.*, 2016, Hardie *et al.*, 1996a), assist in secretin oligomerization (Koo *et al.*, 2008, Carbonnelle *et al.*, 2005, Friedrich *et al.*, 2014) and/or stabilize secretin monomers (Koo *et al.*, 2012, Daefler *et al.*, 1997, Hardie *et al.*, 1996b, Silva *et al.*, 2020). While pilotins of different secretion systems generally have similar functions, they are structurally highly diverse (Silva *et al.*, 2020).

In the context of the T4aP, *P. aeruginosa, Neisseria gonorrhoeae* and *M. xanthus* utilize the pilotins PilF, PilW and Tgl, respectively (Rodriguez-Soto & Kaiser, 1997, Carbonnelle *et al.*, 2005, Kim *et al.*, 2006). These T4aP pilotins share high structural or predicted structural similarity, consisting of 13 antiparallel α-helices that form six tetratricopeptide repeat (TPR) domains (Rodriguez-Soto & Kaiser, 1997, Kim *et al.*, 2006, Trindade *et al.*, 2008). Generally, TPR-domains are involved in mediating protein-protein interactions (D'Andrea & Regan, 2003). In line with this, the pilotin of *P. aeruginosa* has been shown to directly interact with an unidentified interface within the secretin forming region of PilQ (Koo *et al.*, 2013). In the absence of their cognate pilotins, T4aP secretins do not form heat- and SDS-resistant multimers (Koo *et al.*, 2008, Nudleman *et al.*, 2006). The reported role of T4aP pilotins in the OM localization of their cognate secretins suggest that they may have different modes of action. While in *P. aeruginosa*, it was shown that in the absence of the pilotin, the PilQ monomers accumulate at the inner membrane (IM) (Koo *et al.*, 2008), the secretin of *Neisseria meningitidis* was reported to arrive at the OM independently of the pilotin (Carbonnelle *et al.*, 2005). Additionally, lack of Tgl in *M. xanthus* can be extracellularly complemented by OM-exchange with a Tgl^+ donor (Nudleman *et al.*, 2005, Nudleman *et al.*, 2006, Wall *et al.*, 1998, Wei *et al.*, 2011), suggesting that Tgl can fulfill its function after being inserted into the OM.

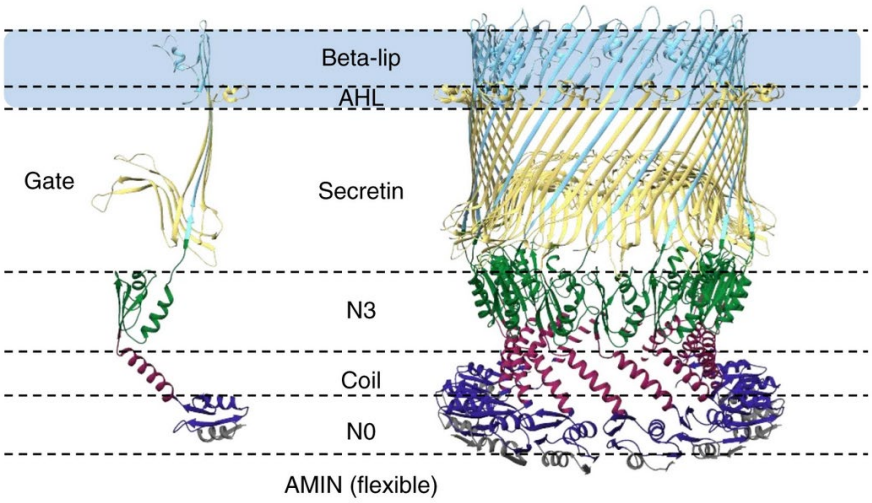

Figure 2 Structure and domain architecture of the secretin of the *Vibrio cholerae* competence pilus. Different domains are color coded, β-lip: teal, AHL: AHL and secretin: yellow, N3: green, Coil: purple, N0: blue. Reused from (Weaver *et al.*, 2020) under the CC BY 4.0 license.

TsaP

In addition to the pilotin, the PG-binding protein TsaP is important for the correct conformation of the secretin. TsaP stabilizes the correct conformation of PilQ through direct and stable interactions (Figure 3), and was visualized as a ring of spike densities around the T4aPM (McCallum *et al.*, 2021, Siewering *et al.*, 2014, Chang *et al.*, 2016). TsaP contains several domains that are connected by flexible linkers. The N-terminus consists of a PG-binding LysM-

domain, which is a domain widely distributed in pro- and eukaryotic proteins (Buist *et al.*, 2008), and has been shown to bind PG (Siewering *et al.*, 2014), while the C-terminus of TsaP forms two β-roll domains (McCallum *et al.*, 2021). TsaP forms a ring with C7 symmetry around the secretin in *P. aeruginosa*, corresponding to a total of 14 β-roll domains each of which interacts with one PilQ monomer (McCallum *et al.*, 2021). Consequently, TsaP and PilQ form a complex with a 1:2 ratio (McCallum *et al.*, 2021). Lack of TsaP leads to the formation of periplasmic pili in *N. gonorrhoeae* (Siewering *et al.*, 2014). In *M. xanthus,* deletion of *tsaP* resulted in reduced T4aP formation and altered the conformation of the T4aPM by increasing the distance between PilQ and the periplasmic alignment complex (Siewering *et al.*, 2014, Chang *et al.*, 2016).

Alignment complex

The alignment complex bridges and aligns the OM components of the T4aPM with the IM and IM-anchored components and is composed of the transmembrane IM proteins PilN and PilO, the IM lipoprotein PilP and the cytoplasmic protein PilM (Figure 3) (Chang *et al.*, 2016, Li *et al.*, 2013). The genes encoding these proteins are usually found in one locus together with the gene encoding the secretin (Balasingham *et al.*, 2007). Additionally, the four proteins of the alignment complex stabilize each other (Sampaleanu *et al.*, 2009, Bischof *et al.*, 2016, Friedrich *et al.*, 2014) and therefore are sensitive to their stoichiometry (Ayers *et al.*, 2009).

The C-terminus of PilP folds into a β-fold and interacts with the N0-domain of PilQ, connecting PilQ to the IM (Figure 3) (Balasingham *et al.*, 2007, Li *et al.*, 2013, Tammam *et al.*, 2013). The N-terminus of PilP is disordered and has been shown to interact with PilN and PilO (Tammam *et al.*, 2011). Deletion of *pilP* results in reduced PilQ accumulation in *N. gonorrhoeae* and to loss of accumulation of the remaining alignment complex in *M. xanthus* (Friedrich *et al.*, 2014, Drake *et al.*, 1997).

PilN and PilO are IM transmembrane proteins that have a similar domain architecture with a short cytoplasmic N-terminus and a large periplasmic domain that contains a coiled-coil and ferredoxin-like core domain (Leighton *et al.*, 2016, Sampaleanu *et al.*, 2009). PilN and PilO can form homodimers as well as heterodimers through interactions between their coiled-coil and core domains (Sampaleanu *et al.*, 2009, Leighton *et al.*, 2016, Leighton *et al.*, 2015). The conformation of the heterocomplex has been proposed to be involved in the regulation of extension and retraction of T4aP as well as T4aP function (Leighton *et al.*, 2015). Consistently, significant conformational changes have been observed for this complex, when comparing cryo-ET images of the piliated and unpiliated T4aPM (Chang *et al.*, 2016). In addition to regulation of extension and retraction, a complex formed by the N-terminus of PilQ, PilN, PilO and PilP interacts with the major pilin PilA, suggesting that the alignment complex is involved in recruiting major pilin subunits into the T4aPM (Tammam *et al.*, 2013). This recruitment is

hypothesized to be necessary to exclude pilins from homologous systems, such as the T2SS from entering the T4aPM (Tammam *et al.*, 2013).

PilM is a cytoplasmic, actin-like protein, which acts as an adaptor between the extension or retraction ATPases and the platform protein (Chang *et al.*, 2016, Bischof *et al.*, 2016). Binding of PilM to the T4aPM is mediated by the N-terminal cytoplasmic region of PilN (Figure 3) and the interaction with PilN is important for the stability of PilM (Bischof *et al.*, 2016, Karuppiah & Derrick, 2011, McCallum *et al.*, 2016). Furthermore, PilM can bind ATP, with the ATP-bound state exhibiting higher affinity for PilN than the ADP bound state (McCallum *et al.*, 2016). For *M. xanthus* and *P. aeruginosa* it has been shown that PilB binds to PilM (Bischof *et al.*, 2016, McCallum *et al.*, 2016), and furthermore, that *P. aeruginosa* PilM preferentially binds the extension ATPase PilB when bound to PilN, whereas free PilM prefers interacting with the retraction ATPase, suggesting that the PilM-PilN interaction regulates pilus extension/retraction dynamics (McCallum *et al.*, 2016).

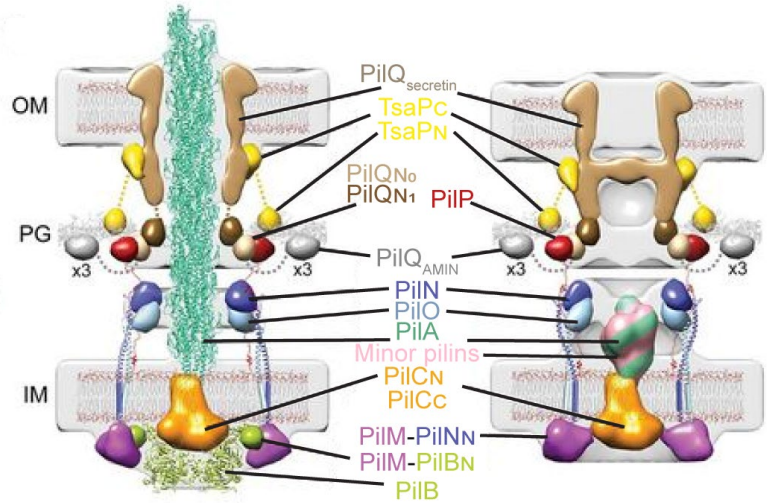

Figure 3 Model of the T4aPM. Pseudoatomic model of the piliated (left) and unpiliated (right) T4aPM of *M. xanthus*. Names of proteins or their domains are indicated and color coded according to the colors used in the model (N: N-terminal; C: C-terminal). Modified from (Chang *et al.*, 2016) under license of the AAAS.

Motor complex

Pilus extension/retraction dynamics are powered by a motor complex consisting of the IM platform protein PilC and either the extension ATPase PilB or the retraction ATPases PilT and PilU (Figure 3). PilC is proposed to be a dimeric, integral IM protein that consists of α-helices and contains at least three transmembrane helices (Bischof *et al.*, 2016, Georgiadou *et al.*, 2012). The platform protein is necessary for the addition of new pilus subunits at the base of the growing pilus fiber (Takhar *et al.*, 2013). PilC, interacts with the hexameric secretion ATPase (PilB, PilT or PilU), and is thought to transduce the force generated by ATP hydrolysis

to help add or remove major pilin subunits during extension and retractions of a pilus. It not only interacts directly with the T4P extension and retraction ATPase, but also with the major pilin and alignment complex (Bischof *et al.*, 2016, Georgiadou *et al.*, 2012, Takhar *et al.*, 2013). The localization of *M. xanthus* PilC depends on the assembly of the upstream components of the T4P machine but in contrast to most other T4aPM components, the protein accumulates without remaining the T4aPM components (Friedrich *et al.*, 2014).

The T4aPM relies on at least two ATPases for its function: PilB for T4aP extension and PilT for T4aP retraction (Bulyha *et al.*, 2009, Chiang *et al.*, 2008). Aside from the two major ATPases, organisms like *P. aeruginosa* or *Neisseria* sp. encode additional PilT paralogs that either are important for twitching motility or modulate the speed of T4aP retractions (Kurre *et al.*, 2012, Chiang *et al.*, 2005). Secretion ATPases belong to the family of AAA+ ATPases (Craig *et al.*, 2019) and form a C2 symmetric hexameric ring structure (McCallum *et al.*, 2017, Satyshur *et al.*, 2007, McCallum *et al.*, 2019a). ATP hydrolysis by individual subunits of the hexamer is thought to follow a clockwise direction, driven by conformational changes in different subunits that enhance the affinity for ATP binding in the adjacent subunit in the clockwise direction (McCallum *et al.*, 2017, Satyshur *et al.*, 2007). The binding of PilT to PilC induces significant conformational changes in PilT and modulates its ATPase activity (McCallum *et al.*, 2019a).

The PilB and PilT ATPases can localize dynamically and represent a mechanism to generate directionality in T4aP-dependent motility. In the rod-shaped *M. xanthus* cells PilT localizes bipolarly and PilB exclusively to the leading pole (Jakovljevic *et al.*, 2008, Bulyha *et al.*, 2009). PilB and PilT of *P. aeruginosa* localize to both poles, while the PilT paralog PilU only localizes at the leading pole (Chiang *et al.*, 2005). Importantly, while proteins can localize to the same pole, PilB and PilT bind to the T4aPM machine in a mutually exclusive manner (Chang *et al.*, 2016). However, it is not clear how the switch between T4aP extension and retraction is mediated. It has been proposed that surface contact induces conformational changes in the pilus which are either sensed by a sensory system (Talà *et al.*, 2019), or are transmitted to the alignment complex of the T4aPM and lead to the switch between extension and retraction ATPase (Chang *et al.*, 2016). Alternatively, it was suggested that the exchange of PilB and PilT is based on stochastic binding and unbinding events (Koch *et al.*, 2021).

Several models have been proposed to explain how PilB and PilT and PilC facilitate T4aP extension and retraction (Craig *et al.*, 2019). In all these models, the sequential conformational changes of the hexameric ATPase drive rotation of the suggested PilC dimer, leading to the polymerization of T4aP (Craig *et al.*, 2019). One proposed mechanism suggests that PilC forms a binding site for the IM-located PilA and uses the force generated by the extension ATPase to extract the PilA subunits from the IM, adding it to the pilus base. Subsequently, PilC

rotates and adds a new PilA subunit to assemble the helical pilus filament (Chang *et al.*, 2016). Another model, referred to as the "compression model," proposes that a ring formed by PilC acts as a gate, allowing PilA subunits to passively bind to the pilus base. Subsequently, the platform protein is compressed, pushing the pilus outwards (Craig *et al.*, 2019). Following compression, the gate of the platform protein reopens at a new position (Craig *et al.*, 2019). When the pilus is retracted this process is reversed by switching the direction of PilC rotation (Craig *et al.*, 2019). Contrary to extension, retraction can also happen spontaneously. In this process, the pilus “collapses” into the IM only utilizing the energy stored in the pilus filament (Chlebek *et al.*, 2021).

Major pilin

The individual pilin subunits of the pilus filaments are termed major and minor pilins according to their abundance within the pilus. All pilins share a generic domain architecture and have a type 3 signal peptide (Mattick, 2002). The processed protein contains a hydrophobic N-terminal α-helix and a C-terminal globular domain (Mattick, 2002). The N-terminal hydrophobic α-helix contains three conserved residues, Glu5, which is important for pilus assembly, as well as Pro22 and Gly/Pro42, which break the helix and lead to a kinked helix structure (Parge *et al.*, 1995, Craig *et al.*, 2003). The C-terminal globular domain of major pilins of T4aP possesses two conserved regions, the α-β-loop and the D-region, as well as a variable region (Craig *et al.*, 2003, Kolappan *et al.*, 2016). The α-β-loop follows the N-terminal α-helix and represents a short loop, which is surface exposed, suggested to be involved in subunit interactions, and can undergo posttranslational modification (Craig *et al.*, 2006). The D-region forms a β-hairpin, which is enclosed by a disulfide bridge in the C-terminus of the globular domain (Craig *et al.*, 2003).

Pilins are inserted into the IM by the Sec-system and subsequently processed by a prepilin peptidase (Nunn & Lory, 1991), which recognizes the type 3 signal peptide in the cytoplasm and cleaves the prepilin leader peptide (between six and seven residues in T4aP) between a conserved Gly and Phe residue (Strom & Lory, 1987, Giltner *et al.*, 2012). The Gly residue is essential for the recognition of the leader peptide (Strom & Lory, 1987). Subsequently, the prepilin peptidase methylates the N-terminal Phe residue (Strom *et al.*, 1993a). The function of the N-terminal methylation is not clear, but it is hypothesized to either promote the extraction of pilin subunits from the IM or stabilize pilin subunits in the pilus filament (Giltner *et al.*, 2012). In addition to methylation, the pilin subunits can undergo further posttranslational modifications and are often glycosylated. Glycosylation in *P. aeruginosa* leads to an advantage in pathogenesis and represents a mechanism for host cell adherence and phase variation in *N. gonorrhoeae* (Aas *et al.*, 2007, Horzempa *et al.*, 2006, Jennings *et al.*, 2011, Smedley *et al.*, 2005).

Prior to pilus assembly, the major pilins form a pool in the IM, where they are anchored by the N-terminal α-helix (Strom & Lory, 1987). When the pilus is extended, the subunits are extracted from the IM pool and added to the base of the growing filament. Subsequently, the N-terminal hydrophobic α-helix forms the core of the pilus filament via hydrophobic interactions (Pelicic, 2008). Additionally, the pilus filament is stabilized by a salt bridge between Glu5 and N-terminal amine of the mature pilin, giving rise to an extremely stable structure that can withstand forces of up to 150 pN (Clausen *et al.*, 2009) and possesses spring-like flexible properties (Biais *et al.*, 2010, Beaussart *et al.*, 2014). As mentioned, the globular domains of the major pilin form the surface of the assembled pilus filament (Craig *et al.*, 2006). When the pilus is retracted, the major pilins are recycled back into the IM and can be used for a new round of extension and retraction (Pelicic, 2008).

Prepilin peptidase

As described above, the prepilin peptidase is necessary for the maturation of the prepilin by processing the prepilin leader peptide (Nunn & Lory, 1991, Strom & Lory, 1987). Prepilin peptidases are integral IM bifunctional enzymes, possessing proteolytic as well as methylation activity (Strom *et al.*, 1993b). They form a subclass of the Asp proteases and contain an active site consisting of two conserved Asp residues (LaPointe & Taylor, 2000). In addition to the two conserved Asp residues in the active site, prepilin peptidases also can contain four conserved Cys residues (Strom *et al.*, 1993a), which are essential for the methylation activity by coordinating a zinc ion (Aly *et al.*, 2013). Both active sites are located on the cytoplasmic side of the protein, and therefore S-adenosylmethionine is suspected to be the methyl donor for methylation (Strom & Lory, 1987). Since the prepilin peptidase is active in cell-free systems only containing peptidase and substrate, it was concluded that no additional proteins are necessary for its activity (Aly *et al.*, 2013).

Priming complex

The pilus is not only composed of major pilins, but additionally contains minor pilins. Together with PilY1 (see below) they form the priming complex, which occupies the unpiliated T4aPM and plays a crucial role in the assembly of T4aP (Figure 3) (Giltner *et al.*, 2010, Nguyen *et al.*, 2015b, Treuner-Lange *et al.*, 2020). Minor pilins have the same overall domain architecture as the major pilin and also contain an N-terminal hydrophobic α-helix with a prepilin leader peptide, but they have globular domains of variable sizes (Jacobsen *et al.*, 2020, Burrows, 2012). The role of the minor pilins in the formation of a priming complex was proposed based on their close homology to minor pseudopilins, which form a complex that primes the formation of the pseudopilus (Cisneros *et al.*, 2012), and the ability of *P. aeruginosa* pseudopilins to cross-complement the deletion of minor pilins in a retraction-deficient background (Δ*pilT*) (Nguyen *et al.*, 2015b). Consistent with this function, most of the minor pilins are essential for

T4aP formation (Giltner *et al.*, 2010, Treuner-Lange *et al.*, 2020). The number of minor pilins, their paralogs and their role in T4aP formation can vary in different species. *P. aeruginosa* encodes five minor pilins (*pilE, pilV, pilW, pilX and fimU*), while the *M. xanthus* genome encodes three paralogous gene clusters for the four minor pilins (*pilV, pilW, pilX and fimU*) (Giltner *et al.*, 2010, Treuner-Lange *et al.*, 2020). Among these, PilV, PilW and PilX are essential for T4aP formation, while FimU and PilE only play a minor role in T4aP formation (Treuner-Lange *et al.*, 2020, Nguyen *et al.*, 2015a). PilX, which shares homology with the minor pseudopilin GspK and lacks the conserved Glu5 residue, is suggested to form the top of the minor pilin complex where it interacts with the PilY1 protein (Treuner-Lange *et al.*, 2020).

PilY1 proteins are large adhesins with a highly conserved C-terminal PilY1-domain. The PilY1-domain adopts a β-propeller fold and represents the binding interface between PilY1 and the minor pilin complex (Orans *et al.*, 2010, Treuner-Lange *et al.*, 2020). The N-terminal domain of PilY1 proteins is less conserved, but can contain a von Willebrand A domain, which is involved in adhesion in eukaryotic cells (Siryaporn *et al.*, 2014). PilY1 represents the tip adhesin of the priming complex and is indispensable for the assembly of T4aP (Treuner-Lange *et al.*, 2020, Nguyen *et al.*, 2015b) and the presence of PilC1 (PilY1 of *Neisseria sp.*) and PilY1.3 of *M. xanthus* at the pilus tip has been demonstrated using immunogold-labeling (Rudel *et al.*, 1995, Xue *et al.*, 2022). In addition to T4aP formation, the PilY1 proteins have been implicated in adhesion, host cell recognition and surface sensing (Webster *et al.*, 2021b, Nassif *et al.*, 1994, Hoppe *et al.*, 2017). A conserved calcium-binding motif in the PilY1-domain is important for the function of PilY1 proteins (Parker *et al.*, 2015). While calcium binding regulates host cell adhesion, but not pilus formation in *N. meningitidis* (Cheng *et al.*, 2013), calcium-binding by PilY1 of *P. aeruginosa* has been suggested to regulate extension and retraction of T4aP through conformational changes in PilY1 (Orans *et al.*, 2010). The PilY1 protein of *P. aeruginosa* contains a second calcium-binding motif which additionally mediates the binding of eukaryotic integrin to promote the adhesion to epithelial cells (Johnson *et al.*, 2011). Similar to the minor pilins, the PilY1 proteins in some species occur as multiple paralogs, that either are encoded in distinct loci in the genome like PilC1 and PilC2 of *Neisseria sp.,* or together with an individual minor pilin gene cluster like in *M. xanthus* (Treuner-Lange *et al.*, 2020).

The priming complex is proposed to be anchored to the pilus tip when the pilus is extended allowing adhesion of the pilus through PilY1 (Rudel *et al.*, 1995, Treuner-Lange *et al.*, 2020, Giltner *et al.*, 2010, Xue *et al.*, 2022). Supporting this, cryo-ET images of pili revealed a kinked structure at the pilus tip (Treuner-Lange *et al.*, 2020). Furthermore, surface sensing of *P. aeruginosa* is mediated by the N-terminal von Willebrand A domain which contains a conserved disulfide bridge that undergoes conformational changes upon surface contact

(Webster *et al.*, 2021b). Lastly, it is hypothesized that the priming complex is pulled back, when the pilus is retracted and stops the retraction process when the complex reaches the IM platform protein (Figure 4) (Treuner-Lange *et al.*, 2020).

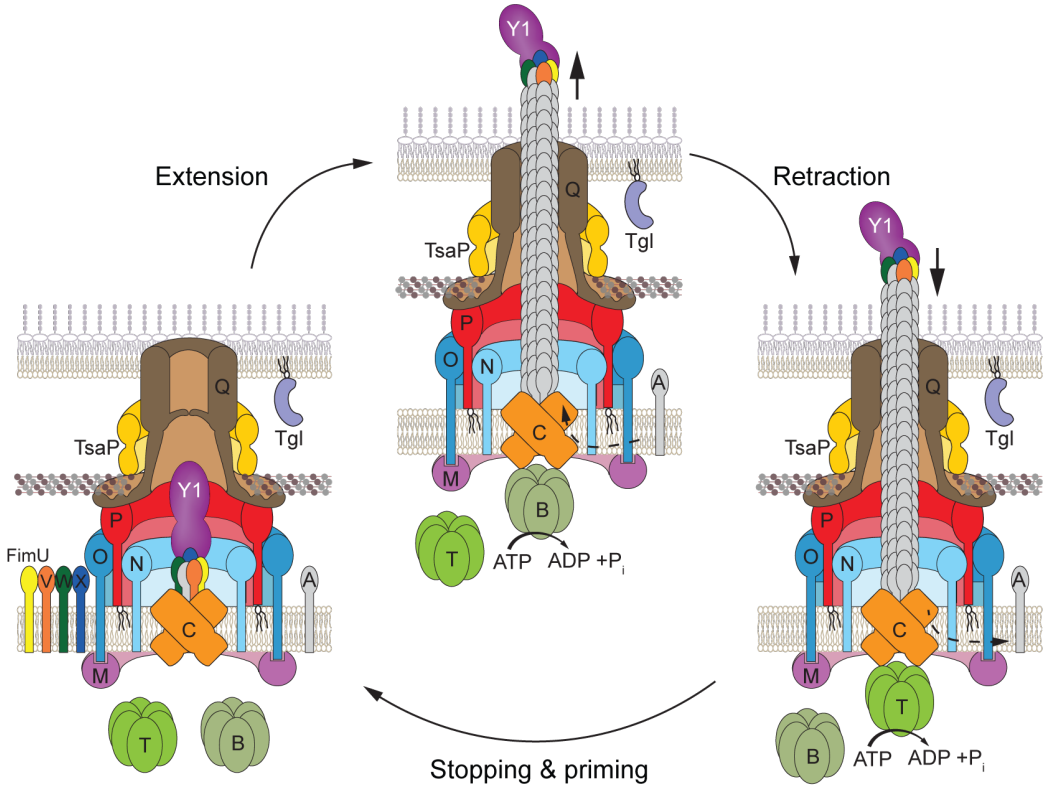

Figure 4 Extension and retraction cycles of the T4aPM. The T4aPM undergoes cycles of priming, extension, retraction and stopping. Prior to T4aP extension, the T4aPM is in an unpiliated state. No ATPase is bound to the machine, the secretin gate is closed and the priming complex is ready to support pilus extension. For pilus extension, PilB binds to the base of the T4aPM, the pilus extends and the priming complex remains at the pilus tip. T4aP then adhere to the substrate which has been suggested to cause a conformational change that induces T4aP retraction. Subsequently, PilT replaces PilB at the base of the T4aPM, and PilA subunits are recycled back into the IM. This process continues until the priming complex reaches the base of the T4aPM and can promote a next extension-retraction cycle. Proteins depicted with one letter follow the Pil nomenclature. P_i represents inorganic phosphate.

Non-core minor pilins

To further expand the functional range of T4aP, cells can incorporate non-core minor pilins into pilus filaments, adding specialized functions. *N. gonorrhoeae* and *N. meningitidis* cells exhibit a particularly large variety of non-core minor pilins, which all are non-essential for T4aP formation. The minor pilin PilV has been suggested to be incorporated along the length of the pilus and is important for the adhesion to host cells (Winther-Larsen *et al.*, 2001, Barnier *et al.*, 2021). Interestingly, PilV has a small globular domain with a partially exposed conserved epitope on the pilus surface, which is essential for the recognition of host cells (Barnier *et al.*, 2021). This domain is hypothesized to maintain high specificity to host-cells, while the major

pilin PilE undergoes high sequence variation to evade the immune response (Barnier *et al.*, 2021).

Second, the non-core minor pilin ComP is essential for natural competence of *N. gonorrhoeae* (Wolfgang *et al.*, 1999). The globular domain of ComP binds DNA with a specific recognition motif with high affinity (Berry *et al.*, 2013, Berry *et al.*, 2016). ComP is proposed to be occasionally incorporated along the pilus filament, exposing its DNA binding regions to the pilus surface, which allows cells to efficiently pull DNA to the cell surface (Berry *et al.*, 2016).

Third, PilX has also been suggested to be incorporated along the pilus and is crucial for the aggregation of *N. meningitidis* cells (Helaine *et al.*, 2005, Helaine *et al.*, 2007). The D-region of PilX forms the α-pigtail, which is modeled to extend out of the pilus surface as a hook-like structure with which opposing pili attach upon retraction, pulling cells toward each other (Helaine *et al.*, 2007).

5.1.4 Other secretion systems of the type IV filament family

T4bP and T4cP

The T4bP and T4cP are the closest homolog of the T4aP. T4bP are mostly found in enterobacteria, with notable examples being the toxin-coregulated pilus (Tcp) of *V. cholerae,* or the bundle-forming pilus (Bfp) of *Escherichia coli.* On the other hand, T4cP are widely distributed in all bacterial species and include the Flp pilus of *Aggregatibacter actinomycetemcomitans* and the Cpa pilus of *Caulobacter crescentus* (Roux *et al.*, 2012, Tomich *et al.*, 2007). The genes required for T4bP and T4cP assembly are usually encoded in one operon, suggesting that these gene clusters are distributed via horizontal gene transfer (Tomich *et al.*, 2007, Roux *et al.*, 2012).

Generally, T4bP and T4cP are involved in adhesion and aggregation, but not in motility (Ellison *et al.*, 2022b). Many components of the T4P subclasses exhibit high similarity and they are mainly differentiated based on the sequence of the major pilin (Figure 1). The major pilin of T4bP and T4cP have a longer leader sequence with a length of 15 to 30 amino acids, and mature major pilins of T4bP usually have longer sequences with a total of 180 to 200 amino acids, whereas mature major pilins of T4cP are shorter than T4aP (Giltner *et al.*, 2012). Additionally, while the T4aP major pilin contains a methylated Phe residue at the first position of the mature protein, T4bP and T4cP can contain different residues at position one and are not always methylated (Roux *et al.*, 2012). Furthermore, unlike T4aP, T4bP and T4cP systems usually lack a retraction ATPase (Ellison *et al.*, 2022b). Retraction of T4bP is suggested to be passive or, in the case of the Tcp of *V. cholerae*, induced through the incorporation of the minor pilin TcpB, which blocks pilus extension (Ng *et al.*, 2016). In contrast, T4cP proteins possess a bifunctional ATPase that powers extension and retraction (Ellison *et al.*, 2019). Additionally,

components of the T4bP alignment complex may differ from the PilM, PilN, PilO, and PilP homologs found in T4aPM. For example, the alignment complex of the Tcp system in *V. cholerae* is comprised of three proteins (i.e TcpS, TcpD, and TcpR), rather than the PilM, PilN, PilO, and PilP homologs (Chang *et al.*, 2017). As opposed to the other T4P systems, the secretins of the T4bP can be lipoproteins, also referred to as liposecretins, and are transported to the OM via the Lol-pathway (Bose & Taylor, 2005, Lieberman *et al.*, 2012).

Competence pili

The competence pili (Com-pili) are specialized structures derived from T4P that facilitate the uptake of extracellular DNA in Gram-positive bacteria. The morphology of Com-pili can vary significantly among different species. In *Bacillus subtilis* Com-pili traverse the cell wall, but do not extend far beyond the cell surface, while in *Streptococcus pneumonia,* Com-pili have been observed to extend in the micrometer range, similar to other T4P structures (Laurenceau *et al.*, 2013). The Com-pilus machine has similarity to the canonical T4aPM (Figure 1). It includes a prepilin peptidase, IM platform protein and extension ATPase. However, due to lack of the OM in Gram-positive bacteria, the Com-pilus machinery lacks the corresponding OM and periplasmic components (i.e. PilQ, TsaP, PilP) (Burton & Dubnau, 2010). In addition, the Com-pilus machine is associated with a DNA translocation complex, which facilitates the processing and import of single-stranded DNA molecules (Burton & Dubnau, 2010). Although the Com-pilus machine does not possess a known retraction ATPase, retraction forces of up to 40 pN have been measured for the *B. subtilis* Com-pili (Maier *et al.*, 2004).

T2SS

The T2SS has repurposed the mechanism of pilus extension and retraction to secrete folded proteins from the periplasm to the extracellular space (Korotkov *et al.*, 2012). To fulfill this function, the pilus only reaches the OM but does not cross it and is therefore termed pseudopilus (Campos *et al.*, 2010). While the overall architecture of T4P and T2SS systems is similar, some components are not shared between the systems and have structural differences (Figure 1) (Ayers *et al.*, 2010).

In contrast to T4aP secretins, T2SS secretin oligomers have been unambiguously characterized as C15 symmetric (Barbat *et al.*, 2022). The canonical T2SS secretin contains four N-domains, the N0-, N1-, N2- and N3-domain, which form pentadecameric rings and extend deeply into the periplasm (Chernyatina & Low, 2019). T2SS possess an additional C-terminal S-domain, with which they interact with their pilotin (Howard *et al.*, 2019). Importantly, the interaction between the cognate pilotin and secretin pairs in the T2SS is suggested to be stable and can be observed by cryo-ET (Yin *et al.*, 2018). In addition to these general features, T2SS secretins are classified as *Vibrio* and *Klebsiella* type secretins, which are distinguished by the presence of an additional top gate at the outer leaflet of the OM and based on the fold

of their cognate pilotin (Howard *et al.*, 2019, Naskar *et al.*, 2021). The N0-domain of the secretin connects the OM-complex to the IM assembly consisting of three proteins: the PilP homolog GspC, which interacts with the secretin and extends through the IM into the cytoplasm, the PilO homolog GspM, and GspL (Figure 5). GspL functionally represents a fusion of PilN with a truncated variant of PilM (Chernyatina & Low, 2019, McCallum *et al.*, 2016, Korotkov *et al.*, 2012).

Substrates of the T2SS are extruded through the secretin by the pseudopilus. The pseudopilus is composed of one major pseudopilin (GspG) and four minor pseudopilins (GspH, GspI, GspJ and GspK), which prime pseudopilus extension via the formation of a priming complex (Figure 5) (Campos *et al.*, 2010, Cisneros *et al.*, 2012). A trimeric tip-complex consisting of GspJ, GspI and GspK is connected to the major pseudopilus via one or two subunits of GspH (Korotkov & Hol, 2008). In contrast to T4aP, the T2SS does not contain a homolog of the PilY1 protein, and instead, the priming complex may interact with the substrate of the secretion system (Treuner-Lange *et al.*, 2020). The pseudopilus, similar to the T4aP, forms a helical assembly of the major pseudopilin GspG (Kohler *et al.*, 2004). Both GspG and GspK are calcium-binding proteins, and stability of the pseudopilus depends on calcium ions (Korotkov & Hol, 2008, Korotkov *et al.*, 2009, Lopez-Castilla *et al.*, 2017).

The assembly of the pseudopilus is powered by a motor complex consisting of a hexameric extension ATPase and a likely dimeric platform protein with high homology to the corresponding components of the T4aPM (Korotkov *et al.*, 2012). Unlike the T4aPM, the T2SS does not include a retraction ATPase, and retraction may occur through passive disassembly of the pseudopilus (Naskar *et al.*, 2021). The length of the pseudopilus is regulated by the minor pseudopilin GspK, located at the top of the pseudopilus, which is proposed to sterically hinder pseudopilus extension at the secretin pore (Durand *et al.*, 2005).

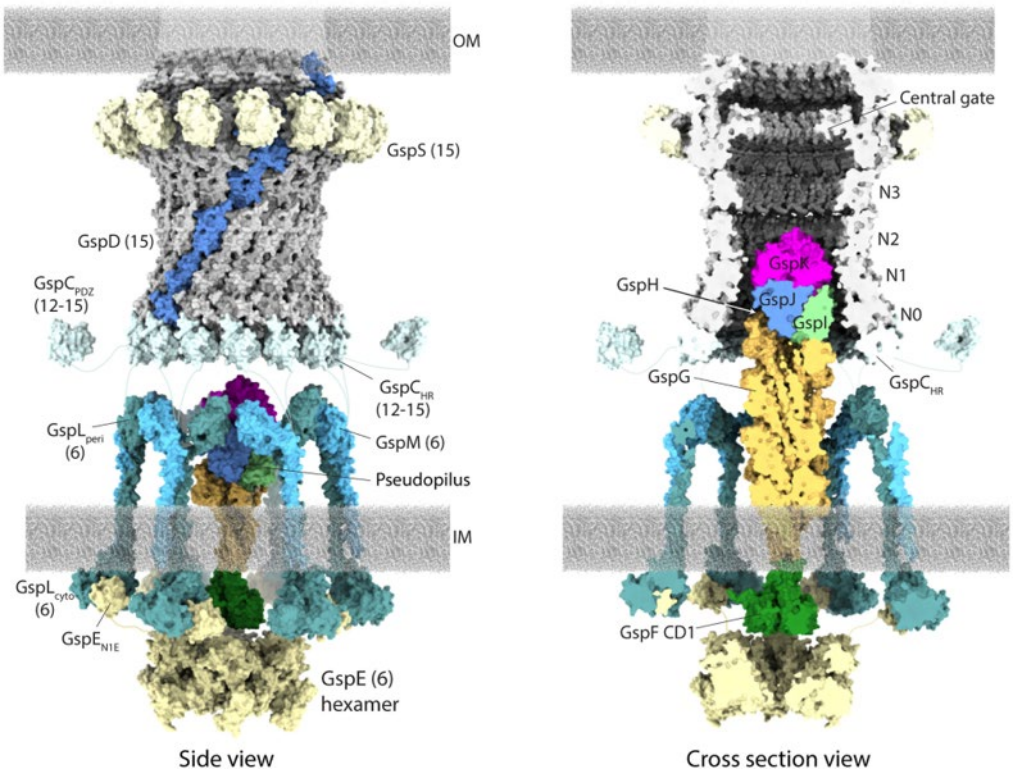

Figure 5 Molecular architecture of the T2SS. In the left panel, the side view of the T2SS machine is shown. Names of proteins are indicated. Numbers next to names indicate the number of proteins in one complex. In the right panel, a cross section view of the T2SS machine is shown. N-domains of GspD and the gate are indicated. Minor pseudopilins are labeled. Reused from (Naskar *et al.*, 2021) under the CC BY 4.0 license.

Archaellum

As another member of the T4FF, the archaellum, while being structurally similar to the T4aP, represents a functional homolog to the bacterial flagellum and promotes swimming motility in archaea through the rotation of a cell surface filament (Figure 1) (Kinosita *et al.*, 2016). The filament is composed of archaellins, which, similar to pilins, are processed by a type 3 signal peptidase (Albers *et al.*, 2003). The archaellum itself can be composed of two alternating subunits (Gambelli *et al.*, 2022). Since the outer barrier of archeal cells usually is constituted by a surface-layer (S-layer) composed of protein (Albers & Meyer, 2011), the archaellum machine does not contain a secretin. Instead, the assembly of the archaellum is thought to be initiated by the localization of the platform protein FlaJ, which is suggested to recruit the assembly ATPase FlaI as well as the ATPase accessory factor FlaH (Reindl *et al.*, 2013, Chaudhury *et al.*, 2016). FlaI activity is responsible for archaellum extension and rotation, and FlaH, a RecA homolog, has been suggested to coordinate the switch between extension and rotation (Chaudhury *et al.*, 2016). The alignment complex consists of three proteins, FlaX/FlaCDE, which anchors FlaH and FlaI to the platform protein, and FlaF and FlaG, which

anchor the machine to the S-layer and additionally act as stator (Banerjee *et al.*, 2012, Tsai *et al.*, 2020).

5.1.5 Assembly of secretion systems

Assembly of large, cell envelope-spanning secretion systems in Gram-negative bacteria typically follows a specific order, with the outside-in assembly pathway being the most commonly reported for the T4FF (Lybarger *et al.*, 2009, Friedrich *et al.*, 2014, Chang *et al.*, 2017, Chang *et al.*, 2016). In this pathway, assembly starts with the incorporation of the secretin at the OM, which accumulates independently of other components and recruits downstream components of the corresponding machine either before or after oligomerization (Lybarger *et al.*, 2009, Friedrich *et al.*, 2014, Chang *et al.*, 2017, Chang *et al.*, 2016, Carter *et al.*, 2017).

In the T4aPM of *M. xanthus,* proper assembly of the PilQ secretin in the OM is crucial for the assembly of all T4aPM components. In the absence of the secretin, downstream components either do not accumulate or fail to localize (Friedrich *et al.*, 2014). This assembly dependency follows a sequential chain from the secretin to the alignment complex components (Friedrich *et al.*, 2014, Chang *et al.*, 2016). However, the platform protein accumulates independently of the remaining T4aPM and the extension and retraction ATPase have been reported to localize independently of the T4aPM (Friedrich *et al.*, 2014). In the T4aPM system of *P. aeruginosa*, the secretin recruits components of the alignment complex prior to its localization in the OM, unlike in *M. xanthus* (Carter *et al.*, 2017). Similar localization dependencies are observed in the T2SS and T4bP systems of *V. cholera*, where secretin localization precedes assembly complex localization (Lybarger *et al.*, 2009, Chang *et al.*, 2017). However, in the case of the T4aPM of *Neisseria sp.* the alignment complex is suggested to assemble and function even in the absence of the secretin (Carbonnelle *et al.*, 2006, Goosens *et al.*, 2017, Siewering *et al.*, 2014). It is worth noting that the ability to assemble without the secretin may be species-specific, as the T4aPM in Gram-positive bacteria can generally assemble without a secretin (Piepenbrink & Sundberg, 2016).

The mechanism underlying the assembly and OM integration of secretins is not fully understood. Unlike canonical β-barrel proteins, secretins are thought to integrate into the OM independently of the Bam system (Dunstan *et al.*, 2015). Based on findings from T4aP, T2SS and T3SS, secretins can arrive to the OM either with or without the assistance of a cognate pilotin (Carter *et al.*, 2017, Carbonnelle *et al.*, 2005, Majewski *et al.*, 2021). In the case of the T2SS, the pilotin is suggested to co-transport the secretin via the Lol pathway while, in case of the T4aPM, pilotin-dependent transport was only suggested for *P. aeruginosa,* where the pilotin at the OM was suggested to "pull" the secretin across the periplasm to the OM (Carter *et al.*, 2017). However, other secretins were reported to ‘arrive’ at the OM independently of the

pilotin, such as the T4aP secretin of *N. meningitidis* or liposecretins of the T2SS (Carbonnelle *et al.*, 2005, Viarre *et al.*, 2009). Once at the OM, secretin monomers were suggested to strongly associate with the membrane via the AHL (Worrall *et al.*, 2016). Additionally, in the case of the T4aPM, the secretin may bind to a polar landmark, such as pole-specific PG (Carter *et al.*, 2017). The secretin monomers then oligomerize into a prepore structure and this is mediated by the N3-domains (Guilvout *et al.*, 2014). Although the mechanism for OM integration of secretins has not been resolved, the prepore and pilotin are hypothesized to generate OM-perturbations which allow the β-lip of the secretin to integrate into the OM (Worrall *et al.*, 2016). Following secretin assembly, the alignment complex and motor complex are recruited to the secretin, emphasizing the importance of the secretin in initiating and guiding the assembly of secretion systems (Lybarger *et al.*, 2009, Friedrich *et al.*, 2014, Chang *et al.*, 2017, Chang *et al.*, 2016, Carter *et al.*, 2017).

Following the outside-in assembly pathway, the localization of the secretin defines where the corresponding secretion system is assembled. For different secretion systems, different localization patterns have been observed. Secretion systems that are involved in the transport of proteins out of the cell, such as the T2SS and T3SS, have been reported to localize dispersed around the cell, while the T4aPM, which promotes motility, in many cases adopts a defined localization pattern (Lybarger *et al.*, 2009, Friedrich *et al.*, 2014, Chang *et al.*, 2016, Carter *et al.*, 2017, Diepold *et al.*, 2010). Of note, the T4aPM has not been directly localized in many organisms, but piliation patterns have been reported based on fluorescence and electron microscopy. On one hand, many rod-shaped cells exhibit polar piliation pattern, with *M. xanthus* and *P.aeruginosa* assembling pili only at one pole at a time (Friedrich *et al.*, 2014, Sun *et al.*, 2000, Chiang *et al.*, 2005), the rod-shaped cyanobacterium *Thermosynechococcus vulcanus* assembling pili at both poles (Nakane *et al.*, 2022). On the other hand, coccoid cells such as *N. meningitidis, Moraxella catarrhallis* or *Synechocystis* sp. exhibit a peritrichous piliation pattern (Stephens *et al.*, 1985, Ahmed *et al.*, 1990, Bhaya *et al.*, 1999). Additionally, there are more specialized localization patterns, like *Acinetobacter baylyi* in which pili localize along the cell length (Ellison *et al.*, 2022a), or the filament forming cyanobacterium *Nostoc punctiforme,* which localizes the T4aPM to the junctions between cells in the filament (Khayatan *et al.*, 2015). These different patterns may allow cells to move efficiently by means of T4aP-dependent motility (Potapova *et al.*, 2020, Ellison *et al.*, 2022a).

5.2 The interplay between type IV pili and c-di-GMP

5.2.1 Introduction to c-di-GMP

Cyclic-di-GMP is a widespread bacterial second messenger involved in a variety of cellular functions. Generally, c-di-GMP is associated with lifestyle switches, such as the transition between a motile and a sessile lifestyle, or the transition from virulence to persistence. However, it also regulates processes such as cell cycle progression, temperature sensing and development (Jenal *et al.*, 2017, Römling *et al.*, 2013, Randall *et al.*, 2022, Hengge, 2009).

C-di-GMP metabolism depends on two classes of enzymes (Figure 6). First, diguanylate cyclases (DGCs) synthesize c-di-GMP from two molecules of GTP (Römling *et al.*, 2013). To catalyze this reaction, DGCs contain a GGDEF/GGEEF signature sequence motif, the active-site (A-site), to which the GTP molecule binds prior to catalysis(Römling *et al.*, 2013). Additionally, DGCs often contain an inhibitory-site (I-site), which binds c-di-GMP and leads to allosteric product-inhibition of the A-site (Römling *et al.*, 2013). The second class of enzymes, the phosphodiesterases (PDEs), break down c-di-GMP and can be categorized into two subgroups based on their catalytic site. PDEs feature either an HD-GYP or EAL motif in their active site and can degrade c-di-GMP to pGpG or directly to GMP (Jenal *et al.*, 2017).

C-di-GMP regulates cellular processes on multiple levels. It can interact with RNA-riboswitches to influence gene expression (Bordeleau *et al.*, 2015, Jenal *et al.*, 2017), or induce conformational changes in various effector proteins including degenerate DGC or PDE domains thathave lost their catalytic activity but retain affinity for c-di-GMP, transcription factors, PilZ domain proteins and MshEN proteins (Jenal *et al.*, 2017, Wang *et al.*, 2016, Cheang *et al.*, 2019, Qi *et al.*, 2011).

While c-di-GMP generally is a diffusible signaling molecule, different signaling architectures allow the formation of highly complex and specific c-di-GMP signaling networks (Hengge, 2009, Hengge, 2021, Jenal *et al.*, 2017, Junkermeier & Hengge, 2023). With the discovery that different c-di-GMP signaling enzymes can be expressed in parallel but generate highly specific outputs, the concept of local and global signaling pools was developed (Hengge, 2021, Junkermeier & Hengge, 2023). Global pools are based on the rapid diffusion of c-di-GMP within the cell where it can bind to different effectors leading to a global cellular response (Jenal *et al.*, 2017, Junkermeier & Hengge, 2023). Contrary to this, in local pool signaling, the c-di-GMP produced by a DGC is directly captured by a specific PDE or effector in close proximity, thus generating a spatially confined signaling module (Figure 6B) (Hengge, 2021, Junkermeier & Hengge, 2023). PDEs, which keep global c-di-GMP levels low, or specific PDEs as part of the local signaling module, can minimize crosstalk between local signaling pools (Jenal *et al.*, 2017). In addition to spatially regulated signaling, temporal specificity can also occur in c-di-

GMP signaling networks. Specifically, this can be achieved either by the temporal regulation of the synthesis of DGCs, PDEs and/or effectors or through the combination of matching c-di-GMP binding affinities of DGCs, PDEs and effectors. In the latter scheme for a temporal signaling architecture, signaling partners are activated sequentially, with a DGC producing c-di-GMP based on its inhibitory constant (K_i), subsequently allowing the activation of an effector with appropriate dissociation constant (K_d), or alternatively, activation of a PDE with appropriate activation constant (K_m) (Figure 6C) (Jenal *et al.*, 2017).

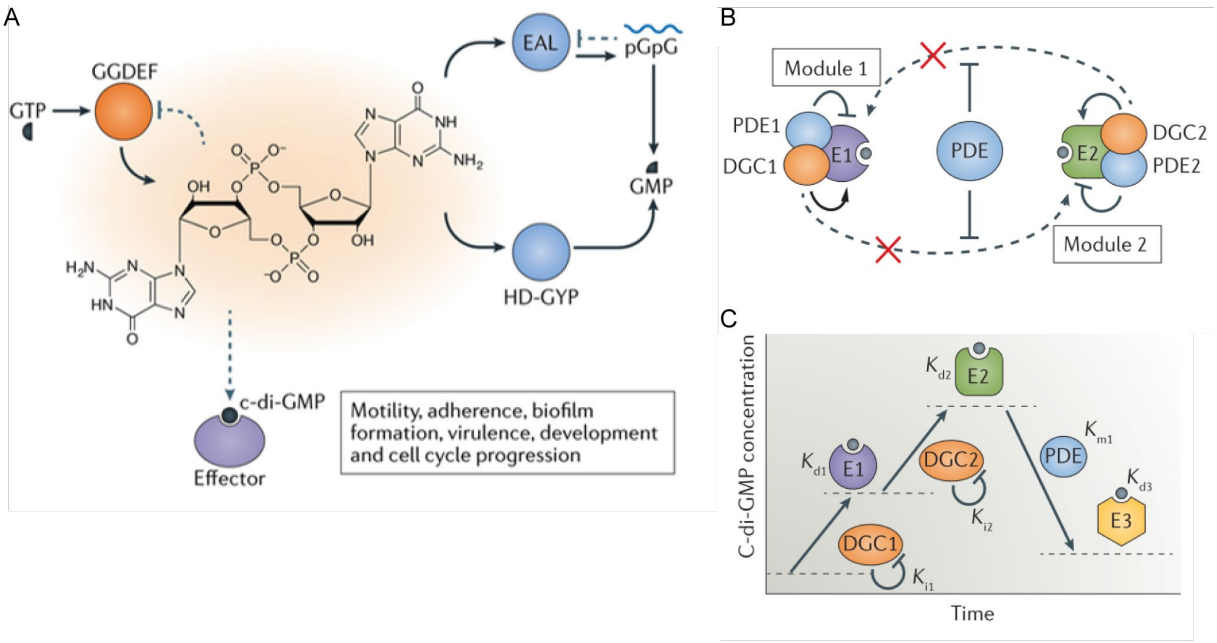

Figure 6 Schematics of different c-di-GMP signaling architectures. A) Schematic of the c-di-GMP signaling network. C-di-GMP is synthesized from two GTP molecules by GGDEF domain-containing DGCs (orange) and degraded by PDEs (blue). DGCs and PDEs are allosterically inhibited by c-di-GMP and pGpG, respectively (stippled lines). Effectors bind c-di-GMP (stippled arrow) and regulate the depicted processes. B) Spatially resolved signaling networks in which DGCs, PDEs and effectors (E) are in close proximity to each other. Crosstalk between two signaling modules is inhibited by PDEs. C) Temporally resolved c-di-GMP signaling network. Defined by their biochemical properties DGCs, effectors (E) and PDEs are sequentially activated over time. Reproduced with permission from Springer Nature (Jenal *et al.*, 2017).

5.2.2 Role of T4aP in concert with c-di-GMP in surface colonialization

Regulated by c-di-GMP, bacteria can undergo a life style switch from planktonic, often involving flagella-based motility, to sessile, where cells attach to a surface and form a biofilm (Laventie & Jenal, 2020). T4P play a crucial role in this transition by facilitating surface attachment and surface-associated motility, and c-di-GMP can modulate the dynamics of T4P to promote either initial or sustained surface attachment (O'Toole & Wong, 2016, Laventie & Jenal, 2020). Different regulatory mechanism can modulate T4aP in response to changing c-di-GMP levels to promote surface colonialization.

While the role of T4aP and c-di-GMP in surface colonialization has been studied extensively in different organisms, it is best understood in *P. aeruginosa*, in which an intricate signaling cascade rapidly elevates the c-di-GMP level upon surface contact to promote adhesion and biofilm formation (Figure 7) (Laventie & Jenal, 2020). In this process, initial surface contact is sensed by the Pil-Chp chemosensory system and components of the flagellar motor, resulting in an increase in the cellular level of the second messengers cAMP and c-di-GMP (Laventie *et al.*, 2019, Luo *et al.*, 2015). This first increase in c-di-GMP activates T4aP formation to promote surface attachment through the PilZ domain containing effector FimW (Laventie *et al.*, 2019). After this initial attachment stage, cells undergo further surface adaptation. The transcriptional regulator Vfr binds cAMP to activate transcription of the FimS/AlgR two-component system, which subsequently upregulates expression of the minor pilins and PilY1 (Belete *et al.*, 2008), as well as production of the secreted polysaccharide alginate (Luo *et al.*, 2015, Lizewski *et al.*, 2002, Whitchurch *et al.*, 1996). PilY1 has beensuggested to activate the DGC SadC, by sensing surface contact through a conformational change in a disulfide bridge in the N-terminal von Willebrand A domain (Kuchma *et al.*, 2010, Webster *et al.*, 2021b). While SadC in planktonic cells is inhibited by the alignment complex protein PilO, signaling between PilY1 and PilO leads to the activation of SadC (Webster *et al.*, 2021a, Luo *et al.*, 2015). Consequently, SadC further increases the c-di-GMP level to inhibit swarming motility and promote biofilm formation (Webster *et al.*, 2021a, Luo *et al.*, 2015). After the initial attachment, the c-di-GMP effector FimX (see below) promotes T4aP formation to facilitate the motility of *P. aeruginosa* cells on a surface (Laventie *et al.*, 2019).

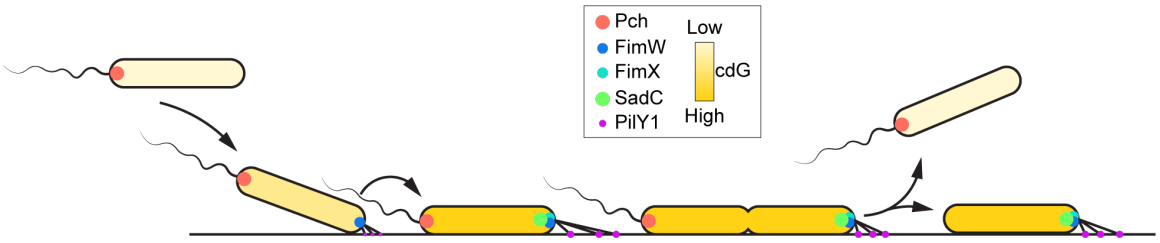

Figure 7 Surface induced c-di-GMP response of *P. aeruginosa*. Planktonic *P. aeruginosa* cells encounter a surface. Initial surface attachment is regulated by T4aP, promoted through FimW, and c-di-GMP levels increase. Further increased c-di-GMP levels activate FimX and promote pili formation. Cells divide asymmetrically, generating a piliated, attached cell, and a flagellated cell, where Pch keeps c-di-GMP level low to promote swimming (Laventie *et al.*, 2019, Webster *et al.*, 2021b).

During surface adaptation, FimW and the PDE Pch jointly facilitate dispersal of cells and surface adhesion. These two proteins are asymmetrically distributed at the two poles in surface-associated cells. Upon cell division, Pch localizes to the flagellated pole and maintains low c-di-GMP levels in the cell inheriting that pole, while FimW localizes to the piliated pole and promotes pilus formation and adhesion. This generates two different types of offspring:

First, a piliated offspring, which can sustain the biofilm and second an unpiliated offspring with flagella, which can explore new habitats (Laventie *et al.*, 2019).

While FimW regulates the assembly of the *P. aeruginosa* T4aP to promote attachment, FimX regulates T4aP formation to promote motility (Huang *et al.*, 2003, Laventie *et al.*, 2019). FimX is a multidomain protein that includes a receiver domain, lacking the Asp residue critical for phosphorylation, a PAS-domain, and degenerate GGDEF and EAL domains (Huang *et al.*, 2003). Deletion of *fimX* leads to a reduction of twitching motility in *P. aeruginosa* (Huang *et al.*, 2003, Kazmierczak *et al.*, 2006). FimX localizes to the leading cell pole of moving cells or bipolarly in non-moving cells (Jain *et al.*, 2017, Huang *et al.*, 2003). At the leading pole, FimX interacts with the extension ATPase to promote T4aP formation (Jain *et al.*, 2017). Consistently, FimX exhibits a diffused localization in the absence of PilB or the T4aPM (Jain *et al.*, 2017). The interaction between FimX and PilB directly depends on the receiver domain and the GGDEF and EAL domains of FimX (Kazmierczak *et al.*, 2006). The GGDEF and EAL domains are both enzymatically inactive, the EAL domain has a high affinity for c-di-GMP (Navarro *et al.*, 2009), which upon binding induces a conformational change in the receiver domain, crucial for the unipolar localization of FimX (Qi *et al.*, 2011, Huang *et al.*, 2003). Consistently, a FimX variant with a non-binding EAL domain localizes at both poles, while the deletion of the EAL domain leads to loss of FimX localization (Jain *et al.*, 2017).

Xanthomonas sp. employs a c-di-GMP effector homologous to FimX together with the PilZ domain-containing protein PilZ to promote T4aP formation *via* PilB (Guzzo *et al.*, 2009). Contrary, to *P. aeruginosa,* where FimX binds directly to PilB, in *Xanthomonas,* PilZ binds to PilB with high affinity and acts as an adaptor between FimX and PilB (Llontop *et al.*, 2021). In the ternary complex, PilZ interacts with the EAL domain of FimX and the N-terminus of PilB (Llontop *et al.*, 2021, Guzzo *et al.*, 2013). FimX then enhances the ATPase activity of PilB, promoting T4aP extension (Jain *et al.*, 2017). In the presence of high levels of c-di-GMP, the interaction between FimX and PilZ is inhibited, leading to a reduction of PilB activity and consequently of T4aP formation (Wei *et al.*, 2021).

While c-di-GMP in *P. aeruginosa* and *Xanthomonas* regulates T4aP formation via the effector FimX, *V. cholerae* MshA pili are regulated by c-di-GMP directly binding to the N-terminal domain of the extension ATPase MshE (Jones *et al.*, 2015, Wang *et al.*, 2016). An elevated level of c-di-GMP is suggested to promote pilus extension by enhancing the binding affinity of MshE to the T4PM, thereby facilitating efficient surface attachment (Floyd *et al.*, 2020). Notably, the MshE c-di-GMP binding domain is not only found in extension ATPases but can also be coupled to other output domains to regulate various processes such as exopolysaccharide synthesis (Junkermeier & Hengge, 2021, Sellner *et al.*, 2021).

A different mechanism to control T4P to promote aggregation and biofilm formation is used by *Clostridium difficile*, which controls the transcription of T4aP genes via c-di-GMP binding riboswitches (Bordeleau *et al.*, 2015). The genome of *C. difficile* contains 16 c-di-GMP binding riboswitches, out of which four are classified as type 2 riboswitch and twelve as type 1 (Lee *et al.*, 2010). The type 2 riboswitches are activated at elevated c-di-GMP levels and promote the expression of T4P components, while type 1 riboswitches regulate flagellum formation and are repressed by c-di-GMP (Lee *et al.*, 2010, Bordeleau *et al.*, 2015).

5.2.3 Regulation of T4aP by c-di-GMP in phototaxis

Cyanobacteria are phototrophic bacteria that utilize light for oxygenic photosynthesis. Therefore, sensing and responding to light is a central aspect of their lifestyle. Cyanobacteria often utilize T4aP to move towards favorable light and this behavior is regulated through light-sensing enzymes that generate c-di-GMP as their output signal (Enomoto *et al.*, 2023). The cell wall of coccoid *Synechocystis* sp. can focus light, resulting in the illumination of a small spot on the distal side of the cell with very high intensity (Schuergers *et al.*, 2016). This allows cells to perceive from which direction they are illuminated (Schuergers *et al.*, 2016). *Synechocystis* cells use cyanobacteriochromes, which possess an N-terminal GAF domain that binds a chromophore, to perceive light with a specific wavelength (Ikeuchi & Ishizuka, 2008). When illuminated with blue light, the DGC Chp2 (cyanobacterial phytochrome 2) is activated and increases the cellular level of c-di-GMP, which then inhibits T4aP-dependent motility (Savakis *et al.*, 2012). A second DGC, Cip1, represses motility towards red light (Angerer *et al.*, 2017). Interestingly, the cellular c-di-GMP level does not increase significantly when Cip1 is active, suggesting that the protein represses motility by generating a local c-di-GMP pool (Angerer *et al.*, 2017). Furthermore, *Synechocystis sp.* encodes two minor pilin gene clusters: *pilA5-6* which is involved in natural competence and DNA uptake, and *pilA9-12* (Oeser *et al.*, 2021). Elevated c-di-GMP levels repress the transcription of *pilA5-6* (Song *et al.*, 2018, Wallner *et al.*, 2020).

The rod-shaped *T. vulcanus* exhibits a bipolar piliation pattern, and assemble pili at both subpolar regions to move perpendicular to its long axis toward green light (Nakane *et al.*, 2022). While the exact mechanism regulating the direction in which cells move and how c-di-GMP functions in this process is still under investigation, phototaxis of *T. vulcanus* and *Syneccocystis* has been suggested to be regulated by the localization of the extension ATPase (Nakane *et al.*, 2022, Schuergers *et al.*, 2015). To perceive and respond to light, *T. vulcanus* possess three c-di-GMP metabolizing enzymes. The DGC SesA synthesizes c-di-GMP when it is illuminated with blue light, while the PDE SesB is degrades c-di-GMP in the presence of teal light and SesC can either synthesizes c-di-GMP under blue or degrade c-di-GMP under green light conditions (Enomoto *et al.*, 2014, Enomoto *et al.*, 2015). Together the three

enzymes can integrate the light composition. This leads to a high c-di-GMP level upon illumination with red or blue light, resulting in either to aggregation and random motion of cells, or conversely phototaxis upon illumination with green or teal light (Nakane *et al.*, 2022).

5.3 Introduction to *Myxococcus xanthus*

5.3.1 The life style of *M. xanthus*

M. xanthus is a rod-shaped, Gram-negative member of the Myxococcota that can be found in terrestrial habitats (Reichenbach, 1999, Waite *et al.*, 2020). With a genome size of 9.1 Mb the *M. xanthus* genome is one of the largest found in the bacterial kingdom (Goldman *et al.*, 2006). Enabled by its approx. 7500 genes, *M. xanthus* exhibits social behavior and undergoes intricate lifestyle switches (Goldman *et al.*, 2006). In the presence of nutrients, *M. xanthus* cells grow and divide and use two distinct motility systems, T4aP-dependent and gliding motility (Shi & Zusman, 1993) to move over different surfaces in a coordinated manner, occasionally reversing their direction of movement upon a signal from the Frz-chemosensory system (Muñoz-Dorado *et al.*, 2016, Carreira *et al.*, 2022). *M. xanthus* cells use various secretion systems to lyse other bacteria and utilize these as a nutrient source (Muñoz-Dorado *et al.*, 2016, Seef *et al.*, 2021, Thiery *et al.*, 2022). Upon nutrient limitation, cells coordinate to form macroscopic structures, termed fruiting bodies, inside which the cells differentiate to spores that can resist multiple stresses, and then germinate upon encountering nutrients (Konovalova *et al.*, 2010).

5.3.2 T4aP-dependent motility

One of the two motility systems of *M. xanthus* depends on the formation of T4aP and is predominantly used by groups of cells (therefore also termed social motility) moving over soft surfaces (Shi & Zusman, 1993). T4aP-dependent motility of *M. xanthus* is functionally linked to the synthesis of secreted polysaccharides, such as a polysaccharide called EPS, a biosurfactant-polysaccharide (BPS) as well as the O-antigen of the lipopolysaccharides (Pérez-Burgos & Søgaard-Andersen, 2020a).

The T4aP of *M. xanthus* are synthesized from a canonical T4aPM, which consists of at least 15 proteins encoded in multiple genetic loci, of which the *pil*-locus encodes most of the machine components (Friedrich *et al.*, 2014, Treuner-Lange *et al.*, 2020, Siewering *et al.*, 2014, Kaiser, 1979). The T4aPM of *M. xanthus* is incorporated at both poles, while only one of the poles at a time assemble pili (Jakovljevic *et al.*, 2008, Friedrich *et al.*, 2014, Bulyha *et al.*, 2009). The assembly pathway as well as the structure of the *M. xanthus* T4aPM have been extensively studied by fluorescence microscopy and cryo-ET.

Assembly of the *M. xanthus* T4aPM follows the outside-in assembly pathway, starting with oligomerization of the PilQ secretin in the OM (Friedrich *et al.*, 2014). PilQ oligomerization depends on the pilotin Tgl and is essential for the accumulation and stability of all components of the alignment complex (Nudleman *et al.*, 2006, Chang *et al.*, 2016, Friedrich *et al.*, 2014).

The PG-binding protein TsaP forms a ring around the assembled secretin, which stabilizes its conformation and is necessary for efficient T4aP formation (Siewering *et al.*, 2014, Chang *et al.*, 2016). PilP, PilO, PilN and PilM assemble the alignment complex of the *M. xanthus* T4aPM and follow a cascade of accumulation and localization dependencies (Friedrich *et al.*, 2014, Chang *et al.*, 2016). The proteins of the motor complex (PilC, PilB and PilT) do not depend on the remaining components of the T4aPM for accumulation, but PilC does not localize to the poles without the secretin and/or alignment complex (Friedrich *et al.*, 2014). Conversely, the two T4aPM ATPases of *M. xanthus,* PilB and PilT for extension and retraction, respectively, localize independently of the T4aPM (Bulyha *et al.*, 2009, Jakovljevic *et al.*, 2008, Friedrich *et al.*, 2014). PilB localizes to the leading cell pole, while PilT localizes in a bipolar asymmetric fashion, with the stronger cluster at the lagging cell pole (Potapova *et al.*, 2020, Bulyha *et al.*, 2009). While T4aP formation is abolished in the absence of PilB, Δ*pilT* cells are hyper-piliated (Yang *et al.*, 2010). In addition to PilT, the genome of *M. xanthus* encodes four additional PilT paralogs outside of the *pil*-locus, for which the function is not known (Clausen *et al.*, 2009).

The genome of *M. xanthus* encodes three minor pilin and *pilY1* gene clusters, referred to as cluster_1, cluster_2 and cluster_3 (Chang *et al.*, 2016, Treuner-Lange *et al.*, 2020). Combinations of deletions of whole clusters and cluster components revealed that either cluster_1 or cluster_3 alone can promote T4aP formation, while no function for cluster_2 has been identified (Treuner-Lange *et al.*, 2020). Additionally, interactions between the minor pilins, PilY1 and the major pilin were shown, a putative priming complex was imaged as a kinked pilus tip, and PilY1.3 imaged at the pilus tip using immunogold labeling (Treuner-Lange *et al.*, 2020, Xue *et al.*, 2022).

This observation raised the question of why *M. xanthus* encodes three of these clusters. Different studies suggest that the different clusters may be regulated in different ways to promote motility on different surfaces (Treuner-Lange *et al.*, 2020, Xue *et al.*, 2022). Supporting this, the transcription of *pilY1.1* and *pilY1.3* is differentially regulated by the HsfA-HsfB phosphorelay, although the environmental signal regulating HsfA-HsfB is unknown (Xue *et al.*, 2022). Additionally, PilY1.1 contains an N-terminal domain that putatively binds sugars, and PilY1.1 was suggested to promote T4aP-dependent motility by binding to EPS (Xue *et al.*, 2022). In contrast, PilY1.3 contains an N-terminal von Willebrand A domain and was suggested to bind to proteins (Treuner-Lange *et al.*, 2020, Xue *et al.*, 2022). Currently, it is not known under which conditions cluster_2 promotes motility (Treuner-Lange *et al.*, 2020).

5.3.3 Gliding motility

Gliding motility, also known as adventurous motility, is preferentially employed by single cells moving on solid surfaces (Shi & Zusman, 1993). Gliding motility relies on the formation of cell envelope-spanning Agl/Glt complexes (Figure 8) (Islam & Mignot, 2015). The Agl/Glt complexes assemble at the leading cell pole, move along the long cell axis (Shi & Zusman, 1993, Mignot *et al.*, 2005), adhere to the substratum and remain fixed relative to it, while moving towards the lagging pole where they disintegrate (Mignot *et al.*, 2007, Mauriello *et al.*, 2010, Faure *et al.*, 2016, Treuner-Lange *et al.*, 2015). The motility machinery driving gliding motility consists of three large sub-complexes (Figure 8): the Agl-complex, which is an integral IM complex; the Glt-complex, which spans the whole cell envelope, and a cytoplasmic complex of AglZ, MreB and MglA (see below) (Jakobczak *et al.*, 2015, Treuner-Lange *et al.*, 2015, Sun *et al.*, 2011, Mauriello *et al.*, 2010, Luciano *et al.*, 2011).

The Agl-complex forms a TolQR/MotAB-like proton channel formed by AglQ, AglR, and AglS. The AglQRS-motor complex utilizes proton motive force to power the movement of Agl/Glt complexes (Sun *et al.*, 2011, Nan *et al.*, 2011). In line with this, the Agl/Glt complexes are immobilized in the absence of the Agl-complex, or when this is inhibited by disrupting the proton motive force (Sun *et al.*, 2011).

The Glt-complex, consisting of cytoplasmic, IM, periplasmic and OM proteins, spans the entire cell envelope (Nan *et al.*, 2010, Luciano *et al.*, 2011, Jakobczak *et al.*, 2015, Islam *et al.*, 2023). The cytoplasmic TPR-domain protein GltI is the only cytoplasmic protein of the Glt-complex and proposed to form a scaffold for the Glt-complex and AglZ, MreB as well as MglA (Treuner-Lange *et al.*, 2015, Mauriello *et al.*, 2010). The transmembrane proteins GltG and GltJ represent the IM components of the Glt-complex (Luciano *et al.*, 2011). GltG directly interacts with AglR, and conformational changes in AglR, induced by proton motive force, are thought to be transmitted to the Glt-complex to drive its movement (Luciano *et al.*, 2011). GltJ contains a cytoplasmic ZnR domain, which represents an interaction interface, suggested to interact with cytoplasmic proteins that are important for gliding motility (Islam & Mignot, 2015). The periplasmic subcomplex of the Glt-complex contains three periplasmic proteins GltD, GltE and GltF (Luciano *et al.*, 2011). GltD and the IM lipoprotein GltE contain TPR-domains and have been suggested to facilitate the interaction between IM and OM proteins of the Glt-complex (Luciano *et al.*, 2011). The function of GltF is not well understood, but was suggested to interact with GltG or GltJ (Faure *et al.*, 2016). The OM-complex consists of the three β-barrel proteins GltA, GltB and GltH. Assembly of GltA and GltB depends on the OM-lipoprotein GltK, as well as the TPR-domain protein GltC (Jakobczak *et al.*, 2015). GltC is further stabilized through its interaction with GltA and GltB (Jakobczak *et al.*, 2015). Finally, the OM-complex attaches to the substrate via the OM-lipoprotein CglB, which is exposed on the cell surface (Islam *et al.*,

2023). Adhesion by CglB was suggested to be facilitated by its von Willebrand A domain (Islam *et al.*, 2023).

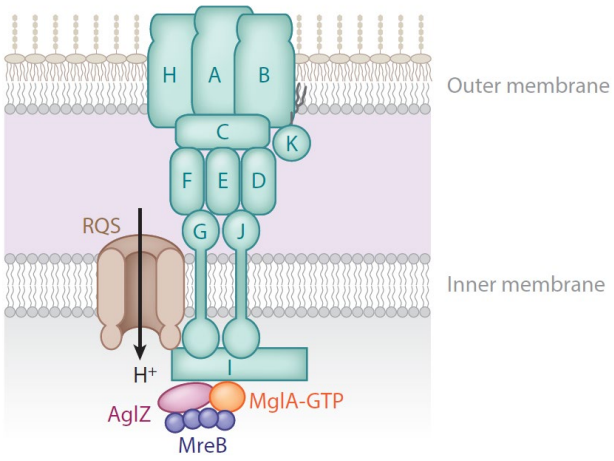

Figure 8 Model of the Agl/Glt gliding machine of *M. xanthus*. Proteins labeled with single letters in aqua and brown have the Glt and Agl prefixes, respectively. GltK is an OM lipoprotein. Reproduced with permission of the publisher (Schumacher & Søgaard-Andersen, 2017).

5.3.4 Regulation of polarity

M. xanthus cells are highly polarized and they translocate across a surface surface in the direction of their long cell axis with well-defined leading and lagging cell poles (Carreira *et al.*, 2022, Schumacher & Søgaard-Andersen, 2017, Zhang *et al.*, 2012a). Occasionally, polarity is inversed by signaling of the Frz-chemosensory system, resulting in an inversion of polarity (Keilberg *et al.*, 2012a, Leonardy *et al.*, 2010, Zhang *et al.*, 2010).

The main regulator of polarity is the small, Ras-like GTPase MglA that together with a set of proteins forms the so-called polarity module (Figure 9) (Carreira *et al.*, 2022, Szadkowski *et al.*, 2022). MglA is a nucleotide-dependent molecular switch, in which polar localization is defined by the nucleotide-bound state: MglA-GTP represents the active form of MglA and binds to the leading cell pole, while MglA-GDP represents the inactive form and is diffused within the cell (Leonardy *et al.*, 2010, Zhang *et al.*, 2010). The activity of MglA, is regulated by its cognate GTPase-activating protein (GAP) complex, consisting of MglB and RomY, as well as its guanine nucleotide exchange factor (GEF), a complex of RomR and RomX (Szadkowski *et al.*, 2022, Leonardy *et al.*, 2007, Szadkowski *et al.*, 2019, Zhang *et al.*, 2010). The interaction between these proteins ultimately results in asymmetric localization at the two poles (Carreira *et al.*, 2020). The base of the interaction network relies on the ability of RomR to localize to the poles independently of the other polarity proteins (Carreira *et al.*, 2020). RomR and MglB promote their polar localization through a positive feedback, which is generated by the

formation of a heteromeric complex of MglB, RomR and the roadblock domain protein MglC (Carreira *et al.*, 2023). MglA-GTP inhibits the positive feedback by inhibiting the interaction between MglC and MglB (Carreira *et al.*, 2020, Carreira *et al.*, 2023). Consequently, most of RomR and MglB localize to the cell pole with less MglA-GTP, which is the lagging cell pole (Figure 9) (Carreira *et al.*, 2020). Additionally, at the lagging pole, the GAP activity of MglB is stronger than at the leading pole due to the presence of the co-GAP RomY (Szadkowski *et al.*, 2022). In contrast, the GEF activity of the RomR-RomX complex is stronger at the leading pole (Szadkowski *et al.*, 2019). Consequently, most of MglA-GTP localizes to the pole opposing the pole with the stronger accumulation of RomR and MglB (Figure 9) (Carreira *et al.*, 2020). Due to its stimulation of both motility systems, the pole containing most MglA-GTP constitutes the leading pole (Carreira *et al.*, 2020, Szadkowski *et al.*, 2022).

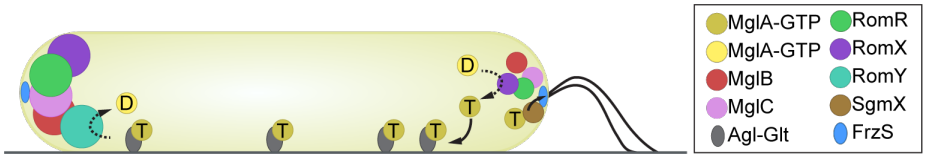

Figure 9 Organization of polarity proteins in *M. xanthus*. Proteins are colored according to the legend. Yellow D and brown T represent MglA-GDP and MglA-GTP, respectively. Stippled arrows indicate the transition from MglA-GTP to MglA-GDP or *vice versa.* Sold arrows indicate stimulation of T4aP-dependent motility and the formation of Agl/Glt complexes. Adapted from (Szadkowski *et al.*, 2022, Bautista *et al.*, 2023).

The GTP-bound form of MglA stimulates of T4aP formation through the effector SgmX and the assembly of the gliding motility complexes through the effectors AglZ and MreB (Figure 9) (Potapova *et al.*, 2020, Mauriello *et al.*, 2010, Treuner-Lange *et al.*, 2015, Mercier *et al.*, 2020). SgmX is a large, cytoplasmic TPR domain protein that regulates T4aP formation by recruiting the extension ATPase PilB to the leading pole (Potapova *et al.*, 2020). SgmX itself is recruited to the poles by MglA and the polar scaffold FrzS (Bautista *et al.*, 2023, Mercier *et al.*, 2020, Potapova *et al.*, 2020). The FrzS binding site of SgmX is located in TPR domains 9-11 and it is covered by TPR domains 12-14 (Mercier *et al.*, 2020). The binding of MglA-GTP to a region in TPR domains 12-14 uncovers the FrzS binding site and thereby selectively recruits SgmX to FrzS at the leading pole activating T4aP formation at the leading pole (Bautista *et al.*, 2023). MglA promotes the assembly of Agl/Glt complexes at the leading cell pole by forming a complex with AglZ and MreB (Mauriello *et al.*, 2010, Treuner-Lange *et al.*, 2015). AglZ is recruited to the leading cell pole by MglA (Mauriello *et al.*, 2010), where it forms a scaffold that facilitates the formation of the Glt-complex at the leading cell pole via GltI (Treuner-Lange *et al.*, 2015). GltI then recruits the IM and periplasmic Glt and Agl-complex, which start to move along the cell length together with MreB (Faure *et al.*, 2016, Treuner-Lange *et al.*, 2015, Mauriello *et al.*, 2010).

The Frz chemosensory system induces the inversion of the polarity module (Keilberg *et al.*, 2012b, Zhang *et al.*, 2012b). It consists of the chemoreceptor FrzCD, FrzA and the histidine kinase FrzE (Bustamante *et al.*, 2004). FrzE induces the inversion of polarity by first autophosphorylating its own response regulator domain and then transferring this phosphory-group to the two response regulators of the Frz system FrzZ and FrzX (Inclan *et al.*, 2008). FrzZ contains two response regulator domains, which are boh phosphorylated by FrzE, resulting in the MglA dependent localization of FrzZ to the leading cell pole (Inclan *et al.*, 2007, Kaimer & Zusman, 2013). The single domain response regulator FrzX is also phosphorylated by FrzE and localizes to the lagging cell pole upon phosphorylation (Guzzo *et al.*, 2018). Two models have been proposed how the Frz system promotes the inversion of the polar localization of the proteins of the polarity module. In the first mode, phosphorylated FrzX excludes MglB from the lagging cell pole, while phosphorylated FrzZ excludes MglA-GTP from the leading pole (Guzzo *et al.*, 2018). In the second model, phosphorylated FrzX is suggested to inhibit MglB GAP activity at the lagging cell pole, while phosphorylated FrzZ at the leading cell pole could break the negative feedback between RomR and MglB or promote MglB binding (Carreira *et al.*, 2020).

5.3.5 Function of c-di-GMP in *M. xanthus*

The second messenger c-di-GMP is involved in the regulation of different aspects of the *M. xanthus* life cycle, including T4aP-dependent motility, synthesis of the extracellular matrix,development and chromosome organization (Overgaard *et al.*, 2006, Petters *et al.*, 2012, Skotnicka *et al.*, 2016a, Skotnicka *et al.*, 2016b, Pérez-Burgos & Søgaard-Andersen, 2020b, Skotnicka *et al.*, 2020, Kuzmich *et al.*, 2021b, Seidel *et al.*, 2023). The genome of *M. xanthus* encodes c-di-GMP metabolizing enzymes and effectors, such as PilZ or MshEN domain proteins, but does not contain any riboswitches (Pérez-Burgos & Søgaard-Andersen, 2020b).

During growth, the c-di-GMP level of *M. xanthus* was reported to be constant (Skotnicka *et al.*, 2016a). However, when *M. xanthus* cells undergo development, the c-di-GMP level increases ~20 fold (Skotnicka *et al.*, 2016b). Manipulating the c-di-GMP level in growing cells by expression of a heterologous PDE or DGC, leads to a defect in T4aP-dependent motility (Skotnicka *et al.*, 2016a). While increasing the c-di-GMP level represses the transcription of the major pilin *pilA*, it is not known how the decreased c-di-GMP level regulates T4aP-dependet motility (Skotnicka *et al.*, 2016a). Conversely, during development, increasing the c-di-GMP level by expression of a heterologous DGC did not show any adverse effects, while expression of a heterologous PDE inhibited fruiting body formation and sporulation (Skotnicka *et al.*, 2016b).

Of the 26 *M. xanthus* genes encoding potential c-di-GMP metabolizing enzymes, 18 encode a GGDEF domain-containing proteins, among which 11 are predicted to be active based on the amino acid sequence of the active site, and two encode EAL and five HD-GYP domain-containing proteins (Skotnicka *et al.*, 2016a, Pérez-Burgos & Søgaard-Andersen, 2020b). Systematic inactivation of these proteins revealed that DmxA, SgmT and TmoK are involved in T4aP-dependent motility, while PmxA and DmxB are important for development (Skotnicka *et al.*, 2016a, Skotnicka *et al.*, 2016b, Petters *et al.*, 2012).

The DGC DmxA is an integral IM protein, in which the N-terminus is anchored in the IM, while the C-terminus is exposed to the cytoplasm (Skotnicka *et al.*, 2016a). The C-terminus contains tandem GAF domains and an active GGDEF domain, which contains a c-di-GMP binding I-site (Skotnicka *et al.*, 2016a). While no deletion mutant for *dmxA* could be obtained, an insertional mutant exhibited a defect in T4aP-dependent motility (Skotnicka *et al.*, 2016a). This defect was suggested to originate from an increased EPS synthesis (Skotnicka *et al.*, 2016a). Conversely, while DmxA is an active DGC, c-di-GMP levels were only slightly elevated in the *dmxA* insertional mutant (Skotnicka *et al.*, 2016a). Additionally, DmxA is dispensable during development and is downregulated at the transcriptional level during this stage (Skotnicka *et al.*, 2016b, Kuzmich *et al.*, 2021a).

Two degenerate GGDEF domain-containing proteins, TmoK and SgmT, were implicated inmotility. TmoK contains an inactive GGDEF domain, which does not bind c-di-GMP, a GAF domain, a receiver domain and a histidine kinase domain (Skotnicka *et al.*, 2016a). Deletion of TmoK caused a mild defect in T4aP-dependent motility and an increase in EPS synthesis and cell agglutination (Skotnicka *et al.*, 2016a). Since TmoK neither synthesizes nor binds c-di-GMP it was suggested that it functions independently of c-di-GMP (Skotnicka *et al.*, 2016a). SgmT, contains GAF, histidine kinase, receiver and GGDEF domains. The GGDEF-domain contains a c-di-GMP binding I-site and inactive A-site, and deletion of SgmT leads to a slight increase of cellular c-di-GMP (Skotnicka *et al.*, 2016a, Petters *et al.*, 2012). While binding of c-di-GMP regulates the localization of SgmT in cytoplasmic foci, the role of this regulation in the function of SgmT is not clear (Petters *et al.*, 2012). SgmT was suggested to phosphorylate the DNA-binding response regulator DigR after activation through ligand binding of its GAF domains. Together SgmT and DigR regulate the synthesis of proteins of the extracellular matrix, motility and development (Overgaard *et al.*, 2006, Petters *et al.*, 2012, Skotnicka *et al.*, 2016b).

DmxB is a DGC with an N-terminal receiver domain and C-terminal GGDEF domain that synthesizes and binds c-di-GMP (Skotnicka *et al.*, 2016b). While DmxB is dispensable during growth, it plays a pivotal role in significantly increasing the c-di-GMP level during the first 48 hours of development (Skotnicka *et al.*, 2016b, Skotnicka *et al.*, 2016a). Because releasing

DmxB from allosteric inhibition *via* its I-site leads to an increase in c-di-GMP levels, but no effect on fruiting body formation or sporulation, and the deletion of DmxB can be largely complemented by the heterologous expression of DgcA from *C. crescentus,* it was concluded that an elevated cellular c-di-GMP level is necessary for development of *M. xanthus* (Skotnicka *et al.*, 2016b). Transcription of DmxB is repressed by the regulator MrpC during growth, but its transcription increases throughout the developmental process (Skotnicka *et al.*, 2016b, Kuzmich *et al.*, 2021a). Since genes of the *eps*-locus were downregulated in absence of DmxB, it was suggested that the elevated c-di-GMP level during development activates the NtrC-like transcriptional regulator EpsI/Nla24, which binds c-di-GMP, to promote EPS synthesis (Skotnicka *et al.*, 2016b).

PmxA is the only active PDE of *M. xanthus* that has been extensively characterized. In absence of PmxA, *M. xanthus* cells form irregular fruiting bodies and are defective in development in submerged culture (Skotnicka *et al.*, 2016b). PmxA is an integral IM protein with a periplasmic Cache domain at its N-terminus and cytoplasmic HAMP and HD-GYP domains. PmxA functions as a bifunctional PDE, degrading both c-di-GMP and 3',3'-cGAMP, with cGAMP degradation likely being its main function (Kuzmich *et al.*, 2021a, Wright *et al.*, 2020). Transcription of PmxA increases during development by direct binding of MrpC to the promoter (Kuzmich *et al.*, 2021a).

The genome of *M. xanthus* encodes 26 PilZ domain-containing proteins, which typically serve as c-di-GMP effectors (Pérez-Burgos & Søgaard-Andersen, 2020b). Upon individually deleting 24 of these genes, six could be identified to have a function in motility,development and/or chromosome organization (Kuzmich *et al.*, 2021b, Seidel *et al.*, 2023). Lack of PixA, which contains a PilZ domain and a response regulator domain, leads to a hyper-reversing phenotype due to a more symmetric polar localization of MglA (Kuzmich *et al.*, 2021b). Interestingly, while PixA binds c-di-GMP through its PilZ domain *in vitro*, c-di-GMP binding *in vivo* appears to be dispensable for the function of PixA (Kuzmich *et al.*, 2021b). Similarly, PlpA regulates the reversal frequency by affecting the localization of MglA and this function was reported to be independent of c-di-GMP binding (Pogue *et al.*, 2018). PixB is also important for the regulation of the reversal frequency during motility. Additionally, PixB is important for fruiting body formation and sporulation by an unknown mechanism (Kuzmich *et al.*, 2021b). While c-di-GMP binding by PixB is dispensable for the regulation of the reversal frequency, it is important for its function during development (Kuzmich *et al.*, 2021b). In addition to PixB, the PilZ domain-containing Ser/Thr-Kinase Pkn1 is important for sporulation and transcription of *pkn1* is upregulated during development through MrpC (Muñoz-Dorado *et al.*, 1991, Kuzmich *et al.*, 2021b). Although c-di-GMP binding was not tested for Pkn1, the PilZ domain is not predicted to bind c-di-GMP (Kuzmich *et al.*, 2021b).

The nucleotide-associated protein CdbA adopts a ribbon-helix-helix fold through which it mutually exclusively binds DNA and c-di-GMP (Skotnicka *et al.*, 2020). Accordingly, the affinity for DNA *in vitro* is decreased in the presence of c-di-GMP (Skotnicka *et al.*, 2020). CdbA is essential for the viability of the cells, and the depletion of CdbA leads to defects in chromosome segregation and organization (Skotnicka *et al.*, 2020). Although CdbA binds DNA in a sequence-specific manner, DNA binding does not seem to regulate transcription of downstream genes (Skotnicka *et al.*, 2020). Instead, due to its structural properties and high abundance, it was suggested that CdbA is a nucleoid-associated protein (NAP) that binds and bends chromosomal DNA and, therefore, is important for chromosome organization (Skotnicka *et al.*, 2020). During a suppressor screen of cells depleted for CdbA, the PilZ domain protein CdbS was identified to restore viability of cells that lack CdbA (Seidel *et al.*, 2023). CdbS accumulation was suggested to depend on the two PilZ-DnaK chaperones CsdK1 and CsdK2, which are transcriptionally repressed through CdbA (Seidel *et al.*, 2023).

Table 1 Overview of proteins, which were characterized and reported to bind c-di-GMP or contain domains that can bind c-di-GMP.

	Name	**Binding**	**Activity**	**Function in regulation of:**	**Reference**
DGC	DmxA	+	+	EPS synthesis & T4aP-dependent motility	(Skotnicka *et al.*, 2016a)
	SgmT	+	-	Extracellular matrix proteins & T4aP-dependent motility	(Skotnicka *et al.*, 2016a, Petters *et al.*, 2012)
	TmoK	-	-	T4aP-dependent motility	(Skotnicka *et al.*, 2016a)
	DmxB	+	+	Development	(Skotnicka *et al.*, 2016b)
PDE	PmxA*	n/a	+/cGA	Development	(Skotnicka *et al.*, 2016b, Wright *et al.*, 2020)
	Name	**Binding**	**Binding site important for function**	**Function in regulation of:**	**Reference**
PilZ	PixA	+	-	Reversal frequency	(Kuzmich *et al.*, 2021b)
	PixB	+	+ (only during development)	Reversal frequency & development	(Kuzmich *et al.*, 2021b)
	Pkn1	not tested	not tested	Development	(Kuzmich *et al.*, 2021b)
	PlpA	-	-	Reversal frequency	(Pogue *et al.*, 2018)
	2902	not tested	not tested	Development	(Kuzmich *et al.*, 2021b)
	CdbS	+	-	Suppressor of Δ*cdbA*	(Seidel *et al.*, 2023)
	CsdK1	not tested	not tested	Accumulation of CdbS	(Seidel *et al.*, 2023)
	CsdK2**	not tested	-	Accumulation of CdbS	(Seidel *et al.*, 2023)

Other	CdbA	+	+	Essential for viability	(Skotnicka *et al.*, 2020)
	EpsI/ Nla24	+	not tested	EPS synthesis	(Skotnicka *et al.*, 2016b)

*For PmxA, not only c-di-GMP but also cyclic-GAMP (cGA) hydrolysis was reported.

**For CsdK2, a point mutation in the potentially c-di-GMP binding residues in the PilZ domain did not affect the interaction with CdbS in a bacterial two-hybrid assay.

6. Scope of the study

T4aP are widespread and multifunctional cell appendages in many different and highly relevant bacterial species. *M. xanthus* is a valuable model organism for studying the function and regulation of T4aP in bacteria. In this study we focused on elucidating different aspects of T4aP biology.

First, we addressed the function of the three minor pilin and PilY1 gene clusters of *M. xanthus*. While the function of proteins of cluster_3 of *M. xanthus* has been studied previously (Treuner-Lange *et al.*, 2020), we focused on the investigation of the proteins encoded in cluster_1. Specifically, we studied the function of a new T4aP accessory protein, which we termed TfcP. We showed that TfcP is an unusual cytochrome *c* with a very low redox-potential. Furthermore, we unraveled that TfcP promotes the accumulation of PilY1.1 in the presence of low calcium concentrations, and suggest that this broadens the range of environmental conditions under which T4aP of *M. xanthus* can function.

Second, we analyzed the assembly of the T4aPM of *M. xanthus.* It has been reported, that polar assembly of the T4aPM initiates during cell division and that the pilotin TgI has an essential function in this process (Friedrich *et al.*, 2014, Nudleman *et al.*, 2006). Here we focused on elucidating the mechanism underlying PilQ secretin assembly and the function of the pilotin TgI in this process. We found that PilQ incorporation to nascent and new poles initiates during cytokinesis and that this process depends on the PG-binding AMIN domains of PilQ. Furthermore, we propose that the presence/absence of AMIN domains in T4aPM secretins explains different T4aPM localization patterns in different bacteria. Additionally, we found that TgI induces PilQ oligomerization in the OM, and is therefore transiently recruited to the nascent and new poles by PilQ. Based on structural predictions, we suggest that TgI and PilQ interact through a conserved region in the β-lip of PilQ, and that this mechanism could be conserved for other cognate secretin-pilotin pairs.

Third, we sought to deepen our understanding of the function of the DGC DmxA in motility. Here, using biochemistry and cell biology, we verify that DmxA is an active DGC and show that Δ*dmxA* cells are show a defect in motility because they hyper-reverse. Additionally, we show that DmxA is recruited to the constriction at the late stage of cytokinesis by the divisome. When localized, DmxA rapidly increases the c-di-GMP level and this is important for the symmetric distribution and incorporation of polar proteins in both daughter cells after cytokinesis. In the absence of DmxA, this symmetry is not set up correctly, leading to an abnormal cell polarity and an increase in the reversal frequency.

Last, we established a method to identify conditional interactomes in *M. xanthus.* Specifically, we developed a protocol to perform mini-TurboID-based proximity labeling in bacteria. We

present a detailed method protocol and provide a proof of concept experiment. Using the well-studied GTPase MglA, the key regulator of the polarity module of *M. xanthus*, we verified known direct and indirect interaction partners of MglA. Furthermore, by comparing the interactome of MglA from cells grown in suspension culture with surface grown cells, we identified new candidates that could be conditional interactors of MglA.

7. References

Aas, F.E., Vik, A., Vedde, J., Koomey, M., and Egge-Jacobsen, W. (2007) *Neisseria gonorrhoeae* O-linked pilin glycosylation: functional analyses define both the biosynthetic pathway and glycan structure. *Mol Microbiol* **65**: 607-24.

Ahmed, K., Rikitomi, N., Nagatake, T., and Matsumoto, K. (1990) Electron microscopic observation of *Branhamella catarrhalis*. *Microbiol Immunol* **34**: 967-75.

Albers, S.V., and Meyer, B.H. (2011) The archaeal cell envelope. *Nat Rev Microbiol* **9**: 414-26.

Albers, S.V., Szabo, Z., and Driessen, A.J. (2003) Archaeal homolog of bacterial type IV prepilin signal peptidases with broad substrate specificity. *J Bacteriol* **185**: 3918-25.

Aly, K.A., Beebe, E.T., Chan, C.H., Goren, M.A., Sepulveda, C., Makino, S., Fox, B.G., and Forest, K.T. (2013) Cell-free production of integral membrane aspartic acid proteases reveals zinc-dependent methyltransferase activity of the *Pseudomonas aeruginosa* prepilin peptidase PilD. *Microbiologyopen* **2**: 94-104.

Angerer, V., Schwenk, P., Wallner, T., Kaever, V., Hiltbrunner, A., and Wilde, A. (2017) The protein Slr1143 is an active diguanylate cyclase in *Synechocystis sp.* PCC 6803 and interacts with the photoreceptor Cph2. *Microbiology (Reading)* **163**: 920-30.

Ayers, M., Howell, P.L., and Burrows, L.L. (2010) Architecture of the type II secretion and type IV pilus machineries. *Future Microbiol* **5**: 1203-18.

Ayers, M., Sampaleanu, L.M., Tammam, S., Koo, J., Harvey, H., Howell, P.L., and Burrows, L.L. (2009) PilM/N/O/P proteins form an inner membrane complex that affects the stability of the *Pseudomonas aeruginosa* type IV pilus secretin. *J Mol Biol* **394**: 128-42.

Balasingham, S.V., Collins, R.F., Assalkhou, R., Homberset, H., Frye, S.A., Derrick, J.P., and Tonjum, T. (2007) Interactions between the lipoprotein PilP and the secretin PilQ in *Neisseria meningitidis*. *J Bacteriol* **189**: 5716-27.

Banerjee, A., Ghosh, A., Mills, D.J., Kahnt, J., Vonck, J., and Albers, S.V. (2012) FlaX, a unique component of the crenarchaeal archaellum, forms oligomeric ring-shaped structures and interacts with the motor ATPase FlaI. *J Biol Chem* **287**: 43322-30.

Barbat, B., Douzi, B., and Voulhoux, R. (2022) Structural lessons on bacterial secretins. *Biochimie*.

Barnier, J.P., Meyer, J., Kolappan, S., Bouzinba-Segard, H., Gesbert, G., Jamet, A., Frapy, E., Schonherr-Hellec, S., Capel, E., Virion, Z., Dupuis, M., Bille, E., Morand, P., Schmitt, T., Bourdoulous, S., Nassif, X., Craig, L., and Coureuil, M. (2021) The minor pilin PilV provides a conserved adhesion site throughout the antigenically variable meningococcal type IV pilus. *Proc Natl Acad Sci U S A* **118**: e2109364118.

Bautista, S., Schmidt, V., Guiseppi, A., Mauriello, E.M.F., Attia, B., Elantak, L., Mignot, T., and Mercier, R. (2023) FrzS acts as a polar beacon to recruit SgmX, a central activator of type IV pili during *Myxococcus xanthus* motility. *EMBO J* **42**: e111661.

Beaussart, A., Baker, A.E., Kuchma, S.L., El-Kirat-Chatel, S., O'Toole, G.A., and Dufrene, Y.F. (2014) Nanoscale adhesion forces of *Pseudomonas aeruginosa* type IV pili. *ACS Nano* **8**: 10723-33.

Beeby, M. (2019) Evolution of a family of molecular Rube Goldberg contraptions. *PLoS Biol* **17**: e3000405.

Belete, B., Lu, H., and Wozniak, D.J. (2008) *Pseudomonas aeruginosa* AlgR regulates type IV pilus biosynthesis by activating transcription of the *fimU-pilVWXY1Y2E* operon. *J Bacteriol* **190**: 2023-30.

Bernstein, H.D. (2019) Type V secretion in Gram-negative bacteria. *EcoSal Plus* **8**: 10.1128/ecosalplus.ESP-0031-2018.

Berry, J.L., Cehovin, A., McDowell, M.A., Lea, S.M., and Pelicic, V. (2013) Functional analysis of the interdependence between DNA uptake sequence and its cognate ComP receptor during natural transformation in *Neisseria* species. *PLoS Genet* **9**: e1004014.

Berry, J.L., and Pelicic, V. (2015) Exceptionally widespread nanomachines composed of type IV pilins: the prokaryotic Swiss Army knives. *FEMS Microbiol Rev* **39**: 134-54.

Berry, J.L., Xu, Y., Ward, P.N., Lea, S.M., Matthews, S.J., and Pelicic, V. (2016) A comparative structure/function analysis of two type IV pilin DNA receptors defines a novel mode of DNA binding. *Structure* **24**: 926-34.

Bhaya, D., Watanabe, N., Ogawa, T., and Grossman, A.R. (1999) The role of an alternative sigma factor in motility and pilus formation in the cyanobacterium *Synechocystis* sp. strain PCC6803. *Proc Natl Acad Sci U S A* **96**: 3188-93.

Biais, N., Higashi, D.L., Brujic, J., So, M., and Sheetz, M.P. (2010) Force-dependent polymorphism in type IV pili reveals hidden epitopes. *Proc Natl Acad Sci U S A* **107**: 11358-63.

Bischof, L.F., Friedrich, C., Harms, A., Søgaard-Andersen, L., and van der Does, C. (2016) The type IV pilus assembly ATPase PilB of *Myxococcus xanthus* interacts with the inner membrane platform protein PilC and the nucleotide-binding protein PilM. *J Biol Chem* **291**: 6946-57.

Blasey, N., Rehrmann, D., Riebisch, A.K., and Muhlen, S. (2022) Targeting bacterial pathogenesis by inhibiting virulence-associated type III and type IV secretion systems. *Front Cell Infect Microbiol* **12**: 1065561.

Bordeleau, E., Purcell, E.B., Lafontaine, D.A., Fortier, L.C., Tamayo, R., and Burrus, V. (2015) Cyclic di-GMP riboswitch-regulated type IV pili contribute to aggregation of *Clostridium difficile*. *J Bacteriol* **197**: 819-32.

Bose, N., and Taylor, R.K. (2005) Identification of a TcpC-TcpQ outer membrane complex involved in the biogenesis of the toxin-coregulated pilus of Vibrio cholerae. *J Bacteriol* **187**: 2225-32.

Buist, G., Steen, A., Kok, J., and Kuipers, O.P. (2008) LysM, a widely distributed protein motif for binding to (peptido)glycans. *Mol Microbiol* **68**: 838-47.

Bulyha, I., Schmidt, C., Lenz, P., Jakovljevic, V., Hone, A., Maier, B., Hoppert, M., and Søgaard-Andersen, L. (2009) Regulation of the type IV pili molecular machine by dynamic localization of two motor proteins. *Mol Microbiol* **74**: 691-706.

Burrows, L.L. (2012) Prime time for minor subunits of the type II secretion and type IV pilus systems. *Mol Microbiol* **86**: 765-9.

Burton, B., and Dubnau, D. (2010) Membrane-associated DNA transport machines. *Cold Spring Harb Perspect Biol* **2**: a000406.

Bustamante, V.H., Martinez-Flores, I., Vlamakis, H.C., and Zusman, D.R. (2004) Analysis of the Frz signal transduction system of *Myxococcus xanthus* shows the importance of the conserved C-terminal region of the cytoplasmic chemoreceptor FrzCD in sensing signals. *Mol Microbiol* **53**: 1501-13.

Campos, M., Nilges, M., Cisneros, D.A., and Francetic, O. (2010) Detailed structural and assembly model of the type II secretion pilus from sparse data. *Proc Natl Acad Sci U S A* **107**: 13081-6.

Carbonnelle, E., Helaine, S., Nassif, X., and Pelicic, V. (2006) A systematic genetic analysis in *Neisseria meningitidis* defines the Pil proteins required for assembly, functionality, stabilization and export of type IV pili. *Mol Microbiol* **61**: 1510-22.

Carbonnelle, E., Helaine, S., Prouvensier, L., Nassif, X., and Pelicic, V. (2005) Type IV pilus biogenesis in *Neisseria meningitidis*: PilW is involved in a step occurring after pilus assembly, essential for fibre stability and function. *Mol Microbiol* **55**: 54-64.

Carreira, L.A.M., Szadkowski, D., Lometto, S., Hochberg, G.K.A., and Søgaard-Andersen, L. (2023) Molecular basis and design principles of switchable front-rear polarity and directional migration in Myxococcus xanthus. *Nat Commun* **14**: 4056.

Carreira, L.A.M., Szadkowski, D., Müller, F., and Søgaard-Andersen, L. (2022) Spatiotemporal regulation of switching front-rear cell polarity. *Curr Opin Cell Biol* **76**: 102076.

Carreira, L.A.M., Tostevin, F., Gerland, U., and Søgaard-Andersen, L. (2020) Protein-protein interaction network controlling establishment and maintenance of switchable cell polarity. *PLoS Genet* **16**: e1008877.

Carter, T., Buensuceso, R.N., Tammam, S., Lamers, R.P., Harvey, H., Howell, P.L., and Burrows, L.L. (2017) The type IVa pilus machinery is recruited to sites of future cell division. *mBio* **8**: e02103-16.

Chang, Y.W., Kjaer, A., Ortega, D.R., Kovacikova, G., Sutherland, J.A., Rettberg, L.A., Taylor, R.K., and Jensen, G.J. (2017) Architecture of the *Vibrio cholerae* toxin-coregulated pilus machine revealed by electron cryotomography. *Nat Microbiol* **2**: 16269.

Chang, Y.W., Rettberg, L.A., Treuner-Lange, A., Iwasa, J., Søgaard-Andersen, L., and Jensen, G.J. (2016) Architecture of the type IVa pilus machine. *Science* **351**: aad2001.

Chaudhury, P., Neiner, T., D'Imprima, E., Banerjee, A., Reindl, S., Ghosh, A., Arvai, A.S., Mills, D.J., van der Does, C., Tainer, J.A., Vonck, J., and Albers, S.V. (2016) The nucleotide-dependent interaction of FlaH and FlaI is essential for assembly and function of the archaellum motor. *Mol Microbiol* **99**: 674-85.

Cheang, Q.W., Xin, L., Chea, R.Y.F., and Liang, Z.X. (2019) Emerging paradigms for PilZ domain-mediated C-di-GMP signaling. *Biochem Soc Trans* **47**: 381-8.

Cheng, Y., Johnson, M.D., Burillo-Kirch, C., Mocny, J.C., Anderson, J.E., Garrett, C.K., Redinbo, M.R., and Thomas, C.E. (2013) Mutation of the conserved calcium-binding motif in *Neisseria gonorrhoeae* PilC1 impacts adhesion but not piliation. *Infect Immun* **81**: 4280-9.

Chernyatina, A.A., and Low, H.H. (2019) Core architecture of a bacterial type II secretion system. *Nat Commun* **10**: 5437.

Chiang, P., Habash, M., and Burrows, L.L. (2005) Disparate subcellular localization patterns of *Pseudomonas aeruginosa* type IV pilus ATPases involved in twitching motility. *J Bacteriol* **187**: 829-39.

Chiang, P., Sampaleanu, L.M., Ayers, M., Pahuta, M., Howell, P.L., and Burrows, L.L. (2008) Functional role of conserved residues in the characteristic secretion NTPase motifs of the *Pseudomonas aeruginosa* type IV pilus motor proteins PilB, PilT and PilU. *Microbiology (Reading)* **154**: 114-26.

Chlebek, J.L., Denise, R., Craig, L., and Dalia, A.B. (2021) Motor-independent retraction of type IV pili is governed by an inherent property of the pilus filament. *Proc Natl Acad Sci U S A* **118**: e2102780118.

Christie, P.J. (2019) The Rich Tapestry of Bacterial Protein Translocation Systems. *Protein J* **38**: 389-408.

Cisneros, D.A., Bond, P.J., Pugsley, A.P., Campos, M., and Francetic, O. (2012) Minor pseudopilin self-assembly primes type II secretion pseudopilus elongation. *EMBO J* **31**: 1041-53.

Clausen, M., Jakovljevic, V., Søgaard-Andersen, L., and Maier, B. (2009) High-force generation is a conserved property of type IV pilus systems. *J Bacteriol* **191**: 4633-8.

Collin, S., Guilvout, I., Nickerson, N.N., and Pugsley, A.P. (2011) Sorting of an integral outer membrane protein via the lipoprotein-specific Lol pathway and a dedicated lipoprotein pilotin. *Mol Microbiol* **80**: 655-65.

Craig, L., Forest, K.T., and Maier, B. (2019) Type IV pili: dynamics, biophysics and functional consequences. *Nat Rev Microbiol* **17**: 429-40.

Craig, L., Taylor, R.K., Pique, M.E., Adair, B.D., Arvai, A.S., Singh, M., Lloyd, S.J., Shin, D.S., Getzoff, E.D., Yeager, M., Forest, K.T., and Tainer, J.A. (2003) Type IV pilin structure and assembly: X-ray and EM analyses of *Vibrio cholerae* toxin-coregulated pilus and *Pseudomonas aeruginosa* PAK pilin. *Mol Cell* **11**: 1139-50.

Craig, L., Volkmann, N., Arvai, A.S., Pique, M.E., Yeager, M., Egelman, E.H., and Tainer, J.A. (2006) Type IV pilus structure by cryo-electron microscopy and crystallography: implications for pilus assembly and functions. *Mol Cell* **23**: 651-62.

D'Andrea, L.D., and Regan, L. (2003) TPR proteins: the versatile helix. *Trends Biochem Sci* **28**: 655-62.

D'Imprima, E., Salzer, R., Bhaskara, R.M., Sanchez, R., Rose, I., Kirchner, L., Hummer, G., Kuhlbrandt, W., Vonck, J., and Averhoff, B. (2017) Cryo-EM structure of the bifunctional secretin complex of *Thermus thermophilus*. *Elife* **6**: e30483.

Daefler, S., Guilvout, I., Hardie, K.R., Pugsley, A.P., and Russel, M. (1997) The C-terminal domain of the secretin PulD contains the binding site for its cognate chaperone, PulS, and confers PulS dependence on pIVf1 function. *Mol Microbiol* **24**: 465-75.

Denise, R., Abby, S.S., and Rocha, E.P.C. (2019) Diversification of the type IV filament superfamily into machines for adhesion, protein secretion, DNA uptake, and motility. *PLoS Biol* **17**: e3000390.

Diepold, A., Amstutz, M., Abel, S., Sorg, I., Jenal, U., and Cornelis, G.R. (2010) Deciphering the assembly of the *Yersinia* type III secretion injectisome. *EMBO J* **29**: 1928-40.

Drake, S.L., Sandstedt, S.A., and Koomey, M. (1997) PilP, a pilus biogenesis lipoprotein in *Neisseria gonorrhoeae*, affects expression of PilQ as a high-molecular-mass multimer. *Mol Microbiol* **23**: 657-68.

Dumenil, G. (2019) Type IV pili as a therapeutic target. *Trends Microbiol* **27**: 658-61.

Dunstan, R.A., Hay, I.D., Wilksch, J.J., Schittenhelm, R.B., Purcell, A.W., Clark, J., Costin, A., Ramm, G., Strugnell, R.A., and Lithgow, T. (2015) Assembly of the secretion pores GspD, Wza and CsgG into bacterial outer membranes does not require the Omp85 proteins BamA or TamA. *Mol Microbiol* **97**: 616-29.

Durand, E., Michel, G., Voulhoux, R., Kurner, J., Bernadac, A., and Filloux, A. (2005) XcpX controls biogenesis of the *Pseudomonas aeruginosa* XcpT-containing pseudopilus. *J Biol Chem* **280**: 31378-89.

Ellison, C.K., Fei, C., Dalia, T.N., Wingreen, N.S., Dalia, A.B., Shaevitz, J.W., and Gitai, Z. (2022a) Subcellular localization of type IV pili regulates bacterial multicellular development. *Nat Commun* **13**: 6334.

Ellison, C.K., Kan, J., Chlebek, J.L., Hummels, K.R., Panis, G., Viollier, P.H., Biais, N., Dalia, A.B., and Brun, Y.V. (2019) A bifunctional ATPase drives tad pilus extension and retraction. *Sci Adv* **5**: eaay2591.

Ellison, C.K., Whitfield, G.B., and Brun, Y.V. (2022b) Type IV Pili: dynamic bacterial nanomachines. *FEMS Microbiol Rev* **46**.

Enomoto, G., Ni Ni, W., Narikawa, R., and Ikeuchi, M. (2015) Three cyanobacteriochromes work together to form a light color-sensitive input system for c-di-GMP signaling of cell aggregation. *Proc Natl Acad Sci U S A* **112**: 8082-7.

Enomoto, G., Nomura, R., Shimada, T., Ni Ni, W., Narikawa, R., and Ikeuchi, M. (2014) Cyanobacteriochrome SesA is a diguanylate cyclase that induces cell aggregation in *Thermosynechococcus*. *J Biol Chem* **289**: 24801-9.

Enomoto, G., Wallner, T., and Wilde, A. (2023) Control of light-dependent behaviour in cyanobacteria by the second messenger cyclic di-GMP. *microLife* **4**: uqad019.

Faure, L.M., Fiche, J.B., Espinosa, L., Ducret, A., Anantharaman, V., Luciano, J., Lhospice, S., Islam, S.T., Treguier, J., Sotes, M., Kuru, E., Van Nieuwenhze, M.S., Brun, Y.V., Theodoly, O., Aravind, L., Nollmann, M., and Mignot, T. (2016) The mechanism of force transmission at bacterial focal adhesion complexes. *Nature* **539**: 530-5.

Floyd, K.A., Lee, C.K., Xian, W., Nametalla, M., Valentine, A., Crair, B., Zhu, S., Hughes, H.Q., Chlebek, J.L., Wu, D.C., Hwan Park, J., Farhat, A.M., Lomba, C.J., Ellison, C.K., Brun, Y.V., Campos-Gomez, J., Dalia, A.B., Liu, J., Biais, N., Wong, G.C.L., and Yildiz, F.H. (2020) c-di-GMP modulates type IV MSHA pilus retraction and surface attachment in *Vibrio cholerae*. *Nat Commun* **11**: 1549.

Friedrich, C., Bulyha, I., and Søgaard-Andersen, L. (2014) Outside-in assembly pathway of the type IV pilus system in *Myxococcus xanthus*. *J Bacteriol* **196**: 378-90.

Galán, J.E., and Waksman, G. (2018) Protein-injection machines in bacteria. *Cell* **172**: 1306-18.

Gambelli, L., Isupov, M.N., Conners, R., McLaren, M., Bellack, A., Gold, V., Rachel, R., and Daum, B. (2022) An archaellum filament composed of two alternating subunits. *Nat Commun* **13**: 710.

Georgiadou, M., Castagnini, M., Karimova, G., Ladant, D., and Pelicic, V. (2012) Large-scale study of the interactions between proteins involved in type IV pilus biology in *Neisseria meningitidis*: characterization of a subcomplex involved in pilus assembly. *Mol Microbiol* **84**: 857-73.

Giltner, C.L., Habash, M., and Burrows, L.L. (2010) *Pseudomonas aeruginosa* minor pilins are incorporated into type IV pili. *J Mol Biol* **398**: 444-61.

Giltner, C.L., Nguyen, Y., and Burrows, L.L. (2012) Type IV pilin proteins: versatile molecular modules. *Microbiol Mol Biol Rev* **76**: 740-72.

Gold, V.A., Salzer, R., Averhoff, B., and Kuhlbrandt, W. (2015) Structure of a type IV pilus machinery in the open and closed state. *Elife* **4**: e07380.

Goldman, B.S., Nierman, W.C., Kaiser, D., Slater, S.C., Durkin, A.S., Eisen, J.A., Ronning, C.M., Barbazuk, W.B., Blanchard, M., Field, C., Halling, C., Hinkle, G., Iartchuk, O., Kim, H.S., Mackenzie, C., Madupu, R., Miller, N., Shvartsbeyn, A., Sullivan, S.A., Vaudin, M., Wiegand, R., and Kaplan, H.B. (2006) Evolution of sensory complexity recorded in a myxobacterial genome. *Proc Natl Acad Sci U S A* **103**: 15200-5.

Goosens, V.J., Busch, A., Georgiadou, M., Castagnini, M., Forest, K.T., Waksman, G., and Pelicic, V. (2017) Reconstitution of a minimal machinery capable of assembling periplasmic type IV pili. *Proc Natl Acad Sci U S A* **114**: E4978-E4986.

Green, E.R., and Mecsas, J. (2016) Bacterial Secretion Systems: An Overview. *Microbiol Spectr* **4**: 4.1.13.

Guilvout, I., Chami, M., Disconzi, E., Bayan, N., Pugsley, A.P., and Huysmans, G.H. (2014) Independent domain assembly in a trapped folding intermediate of multimeric outer membrane secretins. *Structure* **22**: 582-9.

Guzzo, C.R., Dunger, G., Salinas, R.K., and Farah, C.S. (2013) Structure of the PilZ-FimXEAL-c-di-GMP complex responsible for the regulation of bacterial type IV pilus biogenesis. *J Mol Biol* **425**: 2174-97.

Guzzo, C.R., Salinas, R.K., Andrade, M.O., and Farah, C.S. (2009) PILZ protein structure and interactions with PILB and the FIMX EAL domain: implications for control of type IV pilus biogenesis. *J Mol Biol* **393**: 848-66.

Guzzo, M., Murray, S.M., Martineau, E., Lhospice, S., Baronian, G., My, L., Zhang, Y., Espinosa, L., Vincentelli, R., Bratton, B.P., Shaevitz, J.W., Molle, V., Howard, M., and Mignot, T. (2018) A gated relaxation oscillator mediated by FrzX controls morphogenetic movements in *Myxococcus xanthus*. *Nat Microbiol* **3**: 948-59.
Hardie, K.R., Lory, S., and Pugsley, A.P. (1996a) Insertion of an outer membrane protein in *Escherichia coli* requires a chaperone-like protein. *EMBO J* **15**: 978-88.
Hardie, K.R., Seydel, A., Guilvout, I., and Pugsley, A.P. (1996b) The secretin-specific, chaperone-like protein of the general secretory pathway: separation of proteolytic protection and piloting functions. *Mol Microbiol* **22**: 967-76.
Helaine, S., Carbonnelle, E., Prouvensier, L., Beretti, J.L., Nassif, X., and Pelicic, V. (2005) PilX, a pilus-associated protein essential for bacterial aggregation, is a key to pilus-facilitated attachment of *Neisseria meningitidis* to human cells. *Mol Microbiol* **55**: 65-77.
Helaine, S., Dyer, D.H., Nassif, X., Pelicic, V., and Forest, K.T. (2007) 3D structure/function analysis of PilX reveals how minor pilins can modulate the virulence properties of type IV pili. *Proc Natl Acad Sci U S A* **104**: 15888-93.
Hengge, R. (2009) Principles of c-di-GMP signalling in bacteria. *Nature Reviews Microbiology* **7**: 263-273.
Hengge, R. (2021) High-specificity local and global c-di-GMP signaling. *Trends Microbiol* **29**: 993-1003.
Herfurth, M., Treuner-Lange, A., Glatter, T., Wittmaack, N., Hoiczyk, E., Pierik, A.J., and Søgaard-Andersen, L. (2022) A noncanonical cytochrome c stimulates calcium binding by PilY1 for type IVa pili formation. *Proc Natl Acad Sci U S A* **119**.
Hoppe, J., Unal, C.M., Thiem, S., Grimpe, L., Goldmann, T., Gassler, N., Richter, M., Shevchuk, O., and Steinert, M. (2017) PilY1 promotes *Legionella pneumophila* infection of human lung tissue explants and contributes to bacterial adhesion, host cell invasion, and twitching motility. *Front Cell Infect Microbiol* **7**: 63.
Horzempa, J., Comer, J.E., Davis, S.A., and Castric, P. (2006) Glycosylation substrate specificity of *Pseudomonas aeruginosa* 1244 pilin. *J Biol Chem* **281**: 1128-36.
Howard, S.P., Estrozi, L.F., Bertrand, Q., Contreras-Martel, C., Strozen, T., Job, V., Martins, A., Fenel, D., Schoehn, G., and Dessen, A. (2019) Structure and assembly of pilotin-dependent and -independent secretins of the type II secretion system. *PLoS Pathog* **15**: e1007731.
Huang, B., Whitchurch, C.B., and Mattick, J.S. (2003) FimX, a multidomain protein connecting environmental signals to twitching motility in *Pseudomonas aeruginosa*. *J Bacteriol* **185**: 7068-76.
Huysmans, G.H., Guilvout, I., Chami, M., Nickerson, N.N., and Pugsley, A.P. (2015) Lipids assist the membrane insertion of a BAM-independent outer membrane protein. *Sci Rep* **5**: 15068.
Ikeuchi, M., and Ishizuka, T. (2008) Cyanobacteriochromes: a new superfamily of tetrapyrrole-binding photoreceptors in cyanobacteria. *Photochem Photobiol Sci* **7**: 1159-67.
Inclan, Y.F., Laurent, S., and Zusman, D.R. (2008) The receiver domain of FrzE, a CheA-CheY fusion protein, regulates the CheA histidine kinase activity and downstream signalling to the A- and S-motility systems of *Myxococcus xanthus*. *Mol Microbiol* **68**: 1328-39.
Inclan, Y.F., Vlamakis, H.C., and Zusman, D.R. (2007) FrzZ, a dual CheY-like response regulator, functions as an output for the Frz chemosensory pathway of *Myxococcus xanthus*. *Mol Microbiol* **65**: 90-102.
Islam, S.T., Jolivet, N.Y., Cuzin, C., Belgrave, A.M., My, L., Fleuchot, B., Faure, L.M., Mahanta, U., Kezzo, A.A., Saidi, F., Sharma, G., Fiche, J.B., Bratton, B.P., Herrou, J., Nollmann, M., Shaevitz, J.W., Durand, E., and Mignot, T. (2023) Unmasking of the von Willebrand A-domain surface adhesin CglB at bacterial focal adhesions mediates myxobacterial gliding motility. *Sci Adv* **9**: eabq0619.
Islam, S.T., and Mignot, T. (2015) The mysterious nature of bacterial surface (gliding) motility: A focal adhesion-based mechanism in Myxococcus xanthus. *Semin Cell Dev Biol* **46**: 143-54.
Jacobsen, T., Bardiaux, B., Francetic, O., Izadi-Pruneyre, N., and Nilges, M. (2020) Structure and function of minor pilins of type IV pili. *Med Microbiol Immunol* **209**: 301-8.
Jain, R., Sliusarenko, O., and Kazmierczak, B.I. (2017) Interaction of the cyclic-di-GMP binding protein FimX and the Type 4 pilus assembly ATPase promotes pilus assembly. *PLoS Pathog* **13**: e1006594.
Jakobczak, B., Keilberg, D., Wuichet, K., and Søgaard-Andersen, L. (2015) Contact- and protein transfer-dependent stimulation of assembly of the gliding motility machinery in *Myxococcus xanthus*. *PLoS Genet* **11**: e1005341.
Jakovljevic, V., Leonardy, S., Hoppert, M., and Søgaard-Andersen, L. (2008) PilB and PilT are ATPases acting antagonistically in type IV pilus function in *Myxococcus xanthus*. *J Bacteriol* **190**: 2411-21.
Jenal, U., Reinders, A., and Lori, C. (2017) Cyclic di-GMP: second messenger extraordinaire. *Nat Rev Microbiol* **15**: 271-84.
Jennings, M.P., Jen, F.E., Roddam, L.F., Apicella, M.A., and Edwards, J.L. (2011) *Neisseria gonorrhoeae* pilin glycan contributes to CR3 activation during challenge of primary cervical epithelial cells. *Cell Microbiol* **13**: 885-96.
Johnson, M.D., Garrett, C.K., Bond, J.E., Coggan, K.A., Wolfgang, M.C., and Redinbo, M.R. (2011) *Pseudomonas aeruginosa* PilY1 binds integrin in an RGD- and calcium-dependent manner. *PLoS One* **6**: e29629.
Jones, C.J., Utada, A., Davis, K.R., Thongsomboon, W., Zamorano Sanchez, D., Banakar, V., Cegelski, L., Wong, G.C., and Yildiz, F.H. (2015) C-di-GMP Regulates Motile to Sessile Transition by Modulating MshA Pili Biogenesis and Near-Surface Motility Behavior in Vibrio cholerae. *PLoS Pathog* **11**: e1005068.
Junkermeier, E.H., and Hengge, R. (2021) A novel locally c-di-GMP-controlled exopolysaccharide synthase required for bacteriophage N4 infection of *Escherichia coli*. *mBio* **12**: e0324921.
Junkermeier, E.H., and Hengge, R. (2023) Local signaling enhances output specificity of bacterial c-di-GMP signaling networks. *Microlife* **4**: uqad026.

Kaimer, C., and Zusman, D.R. (2013) Phosphorylation-dependent localization of the response regulator FrzZ signals cell reversals in *Myxococcus xanthus*. *Mol Microbiol* **88**: 740-53.
Kaiser, D. (1979) Social gliding is correlated with the presence of pili in *Myxococcus xanthus*. *Proc Natl Acad Sci U S A* **76**: 5952-6.
Karuppiah, V., and Derrick, J.P. (2011) Structure of the PilM-PilN inner membrane type IV pilus biogenesis complex from Thermus thermophilus. *J Biol Chem* **286**: 24434-42.
Kazmierczak, B.I., Lebron, M.B., and Murray, T.S. (2006) Analysis of FimX, a phosphodiesterase that governs twitching motility in *Pseudomonas aeruginosa*. *Mol Microbiol* **60**: 1026-43.
Keilberg, D., Wuichet, K., Drescher, F., and Søgaard-Andersen, L. (2012a) A response regulator interfaces between the Frz chemosensory system and the MglA/MglB GTPase/GAP module to regulate polarity in *Myxococcus xanthus*. *PLoS Genet* **8**: e1002951.
Keilberg, D., Wuichet, K., Drescher, F., and Søgaard-Andersen, L. (2012b) A response regulator interfaces between the Frz chemosensory system and the MglA/MglB GTPase/GAP module to regulate polarity in *Myxococcus xanthus*. *Plos Genetics* **8**.
Khayatan, B., Meeks, J.C., and Risser, D.D. (2015) Evidence that a modified type IV pilus-like system powers gliding motility and polysaccharide secretion in filamentous cyanobacteria. *Mol Microbiol* **98**: 1021-36.
Kim, K., Oh, J., Han, D., Kim, E.E., Lee, B., and Kim, Y. (2006) Crystal structure of PilF: functional implication in the type 4 pilus biogenesis in *Pseudomonas aeruginosa*. *Biochem Biophys Res Commun* **340**: 1028-38.
Kinosita, Y., Uchida, N., Nakane, D., and Nishizaka, T. (2016) Direct observation of rotation and steps of the archaellum in the swimming halophilic archaeon *Halobacterium salinarum*. *Nature Microbiology* **1**: 16148.
Koch, M.D., Fei, C., Wingreen, N.S., Shaevitz, J.W., and Gitai, Z. (2021) Competitive binding of independent extension and retraction motors explains the quantitative dynamics of type IV pili. *Proc Natl Acad Sci U S A* **118**: e2014926118.
Kohler, R., Schafer, K., Muller, S., Vignon, G., Diederichs, K., Philippsen, A., Ringler, P., Pugsley, A.P., Engel, A., and Welte, W. (2004) Structure and assembly of the pseudopilin PulG. *Mol Microbiol* **54**: 647-64.
Kolappan, S., Coureuil, M., Yu, X., Nassif, X., Egelman, E.H., and Craig, L. (2016) Structure of the *Neisseria meningitidis* type IV pilus. *Nat Commun* **7**: 13015.
Konovalova, A., Petters, T., and Søgaard-Andersen, L. (2010) Extracellular biology of *Myxococcus xanthus*. *FEMS Microbiol Rev* **34**: 89-106.
Koo, J., Burrows, L.L., and Howell, P.L. (2012) Decoding the roles of pilotins and accessory proteins in secretin escort services. *FEMS Microbiol Lett* **328**: 1-12.
Koo, J., Tammam, S., Ku, S.Y., Sampaleanu, L.M., Burrows, L.L., and Howell, P.L. (2008) PilF is an outer membrane lipoprotein required for multimerization and localization of the *Pseudomonas aeruginosa* type IV pilus secretin. *J Bacteriol* **190**: 6961-9.
Koo, J., Tang, T., Harvey, H., Tammam, S., Sampaleanu, L., Burrows, L.L., and Howell, P.L. (2013) Functional mapping of PilF and PilQ in the *Pseudomonas aeruginosa* type IV pilus system. *Biochemistry* **52**: 2914-23.
Korotkov, K.V., Gray, M.D., Kreger, A., Turley, S., Sandkvist, M., and Hol, W.G. (2009) Calcium is essential for the major pseudopilin in the type 2 secretion system. *J Biol Chem* **284**: 25466-70.
Korotkov, K.V., and Hol, W.G. (2008) Structure of the GspK-GspI-GspJ complex from the enterotoxigenic *Escherichia coli* type 2 secretion system. *Nat Struct Mol Biol* **15**: 462-8.
Korotkov, K.V., Sandkvist, M., and Hol, W.G. (2012) The type II secretion system: biogenesis, molecular architecture and mechanism. *Nat Rev Microbiol* **10**: 336-51.
Kuchma, S., Ballok, A., Merritt, J., Hammond, J., Lu, W., Rabinowitz, J.D., and O'Toole, G.A., (2010) Cyclic-di-GMP-mediated repression of swarming motility by *Pseudomonas aeruginosa*: the pilY1 gene and its impact on surface-associated behaviors. In.: Am Soc Microbiol, pp.
Kurre, R., Hone, A., Clausen, M., Meel, C., and Maier, B. (2012) PilT2 enhances the speed of gonococcal type IV pilus retraction and of twitching motility. *Mol Microbiol* **86**: 857-65.
Kuzmich, S., Blumenkamp, P., Meier, D., Szadkowski, D., Goesmann, A., Becker, A., and Søgaard-Andersen, L. (2021a) CRP-Like transcriptional regulator MrpC curbs c-di-GMP and 3',3'-cGAMP nucleotide levels during development in *Myxococcus xanthus*. *mBio* **13**: e0004422.
Kuzmich, S., Skotnicka, D., Szadkowski, D., Klos, P., Pérez-Burgos, M., Schander, E., Schumacher, D., and Søgaard-Andersen, L. (2021b) Three PilZ domain proteins, PlpA, PixA, and PixB, have distinct functions in regulation of motility and development in *Myxococcus xanthus*. *J Bacteriol* **203**: e0012621.
LaPointe, C.F., and Taylor, R.K. (2000) The type 4 prepilin peptidases comprise a novel family of aspartic acid proteases. *J Biol Chem* **275**: 1502-10.
Laurenceau, R., Pehau-Arnaudet, G., Baconnais, S., Gault, J., Malosse, C., Dujeancourt, A., Campo, N., Chamot-Rooke, J., Le Cam, E., Claverys, J.P., and Fronzes, R. (2013) A type IV pilus mediates DNA binding during natural transformation in *Streptococcus pneumoniae*. *PLoS Pathog* **9**: e1003473.
Laventie, B.J., and Jenal, U. (2020) Surface Sensing and Adaptation in Bacteria. *Annu Rev Microbiol* **74**: 735-60.
Laventie, B.J., Sangermani, M., Estermann, F., Manfredi, P., Planes, R., Hug, I., Jaeger, T., Meunier, E., Broz, P., and Jenal, U. (2019) A surface-induced asymmetric program promotes tissue colonization by *Pseudomonas aeruginosa*. *Cell Host Microbe* **25**: 140-152 e6.
Lee, E.R., Baker, J.L., Weinberg, Z., Sudarsan, N., and Breaker, R.R. (2010) An allosteric self-splicing ribozyme triggered by a bacterial second messenger. *Science* **329**: 845-8.
Leighton, T.L., Dayalani, N., Sampaleanu, L.M., Howell, P.L., and Burrows, L.L. (2015) Novel role for PilNO in type IV pilus retraction revealed by alignment subcomplex mutations. *J Bacteriol* **197**: 2229-38.

Leighton, T.L., Yong, D.H., Howell, P.L., and Burrows, L.L. (2016) Type IV pilus alignment subcomplex proteins PilN and PilO form homo- and heterodimers in vivo. *J Biol Chem* **291**: 19923-38.
Leonardy, S., Freymark, G., Hebener, S., Ellehauge, E., and Søgaard-Andersen, L. (2007) Coupling of protein localization and cell movements by a dynamically localized response regulator in *Myxococcus xanthus*. *EMBO J* **26**: 4433-44.
Leonardy, S., Miertzschke, M., Bulyha, I., Sperling, E., Wittinghofer, A., and Søgaard-Andersen, L. (2010) Regulation of dynamic polarity switching in bacteria by a Ras-like G-protein and its cognate GAP. *EMBO J* **29**: 2276-89.
Li, C., Wallace, R.A., Black, W.P., Li, Y.Z., and Yang, Z. (2013) Type IV pilus proteins form an integrated structure extending from the cytoplasm to the outer membrane. *PLoS One* **8**: e70144.
Lieberman, J.A., Frost, N.A., Hoppert, M., Fernandes, P.J., Vogt, S.L., Raivio, T.L., Blanpied, T.A., and Donnenberg, M.S. (2012) Outer membrane targeting, ultrastructure, and single molecule localization of the enteropathogenic Escherichia coli type IV pilus secretin BfpB. *J Bacteriol* **194**: 1646-58.
Lizewski, S.E., Lundberg, D.S., and Schurr, M.J. (2002) The transcriptional regulator AlgR is essential for *Pseudomonas aeruginosa* pathogenesis. *Infect Immun* **70**: 6083-93.
Llontop, E.E., Cenens, W., Favaro, D.C., Sgro, G.G., Salinas, R.K., Guzzo, C.R., and Farah, C.S. (2021) The PilB-PilZ-FimX regulatory complex of the type IV pilus from *Xanthomonas citri*. *PLoS Pathog* **17**: e1009808.
Lopez-Castilla, A., Thomassin, J.L., Bardiaux, B., Zheng, W., Nivaskumar, M., Yu, X., Nilges, M., Egelman, E.H., Izadi-Pruneyre, N., and Francetic, O. (2017) Structure of the calcium-dependent type 2 secretion pseudopilus. *Nat Microbiol* **2**: 1686-95.
Lopez, D., Vlamakis, H., and Kolter, R. (2010) Biofilms. *Cold Spring Harb Perspect Biol* **2**: a000398.
Luciano, J., Agrebi, R., Le Gall, A.V., Wartel, M., Fiegna, F., Ducret, A., Brochier-Armanet, C., and Mignot, T. (2011) Emergence and modular evolution of a novel motility machinery in bacteria. *PLoS Genet* **7**: e1002268.
Luo, Y., Zhao, K., Baker, A.E., Kuchma, S.L., Coggan, K.A., Wolfgang, M.C., Wong, G.C., and O'Toole, G.A. (2015) A hierarchical cascade of second messengers regulates *Pseudomonas aeruginosa* surface behaviors. *mBio* **6**: e02456-14.
Lybarger, S.R., Johnson, T.L., Gray, M.D., Sikora, A.E., and Sandkvist, M. (2009) Docking and assembly of the type II secretion complex of *Vibrio cholerae*. *J Bacteriol* **191**: 3149-61.
Maier, B., Chen, I., Dubnau, D., and Sheetz, M.P. (2004) DNA transport into *Bacillus subtilis* requires proton motive force to generate large molecular forces. *Nat Struct Mol Biol* **11**: 643-9.
Majewski, D.D., Okon, M., Heinkel, F., Robb, C.S., Vuckovic, M., McIntosh, L.P., and Strynadka, N.C.J. (2021) Characterization of the pilotin-secretin complex from the *Salmonella enterica* type III secretion system using hybrid structural methods. *Structure* **29**: 125-138 e5.
Majewski, D.D., Worrall, L.J., and Strynadka, N.C. (2018) Secretins revealed: structural insights into the giant gated outer membrane portals of bacteria. *Curr Opin Struct Biol* **51**: 61-72.
Mattick, J.S. (2002) Type IV pili and twitching motility. *Annu Rev Microbiol* **56**: 289-314.
Mauriello, E.M., Mouhamar, F., Nan, B., Ducret, A., Dai, D., Zusman, D.R., and Mignot, T. (2010) Bacterial motility complexes require the actin-like protein, MreB and the Ras homologue, MglA. *EMBO J* **29**: 315-26.
McCallum, M., Benlekbir, S., Nguyen, S., Tammam, S., Rubinstein, J.L., Burrows, L.L., and Howell, P.L. (2019a) Multiple conformations facilitate PilT function in the type IV pilus. *Nat Commun* **10**: 5198.
McCallum, M., Burrows, L.L., and Howell, P.L. (2019b) The dynamic structures of the type IV pilus. *Microbiol Spectr* **7**: 7.2.02.
McCallum, M., Tammam, S., Khan, A., Burrows, L.L., and Howell, P.L. (2017) The molecular mechanism of the type IVa pilus motors. *Nat Commun* **8**: 15091.
McCallum, M., Tammam, S., Little, D.J., Robinson, H., Koo, J., Shah, M., Calmettes, C., Moraes, T.F., Burrows, L.L., and Howell, P.L. (2016) PilN binding modulates the structure and binding partners of the *Pseudomonas aeruginosa* type IVa pilus protein PilM. *J Biol Chem* **291**: 11003-15.
McCallum, M., Tammam, S., Rubinstein, J.L., Burrows, L.L., and Howell, P.L. (2021) CryoEM map of *Pseudomonas aeruginosa* PilQ enables structural characterization of TsaP. *Structure* **29**: 457-466 e4.
Mercier, R., Bautista, S., Delannoy, M., Gibert, M., Guiseppi, A., Herrou, J., Mauriello, E.M.F., and Mignot, T. (2020) The polar Ras-like GTPase MglA activates type IV pilus via SgmX to enable twitching motility in *Myxococcus xanthus*. *Proc Natl Acad Sci U S A* **117**: 28366-73.
Merz, A.J., So, M., and Sheetz, M.P. (2000) Pilus retraction powers bacterial twitching motility. *Nature* **407**: 98-102.
Mignot, T., Merlie, J.P., Jr., and Zusman, D.R. (2005) Regulated pole-to-pole oscillations of a bacterial gliding motility protein. *Science* **310**: 855-7.
Mignot, T., Shaevitz, J.W., Hartzell, P.L., and Zusman, D.R. (2007) Evidence that focal adhesion complexes power bacterial gliding motility. *Science* **315**: 853-6.
Muñoz-Dorado, J., Inouye, S., and Inouye, M. (1991) A gene encoding a protein serine/threonine kinase is required for normal development of *M. xanthus*, a gram-negative bacterium. *Cell* **67**: 995-1006.
Muñoz-Dorado, J., Marcos-Torres, F.J., Garcia-Bravo, E., Moraleda-Munoz, A., and Perez, J. (2016) Myxobacteria: moving, killing, feeding, and surviving together. *Front Microbiol* **7**: 781.
Nakane, D., Enomoto, G., Bahre, H., Hirose, Y., Wilde, A., and Nishizaka, T. (2022) *Thermosynechococcus* switches the direction of phototaxis by a c-di-GMP-dependent process with high spatial resolution. *Elife* **11**: e73405.
Nan, B., Chen, J., Neu, J.C., Berry, R.M., Oster, G., and Zusman, D.R. (2011) Myxobacteria gliding motility requires cytoskeleton rotation powered by proton motive force. *Proc Natl Acad Sci U S A* **108**: 2498-503.
Nan, B., Mauriello, E.M., Sun, I.H., Wong, A., and Zusman, D.R. (2010) A multi-protein complex from *Myxococcus xanthus* required for bacterial gliding motility. *Mol Microbiol* **76**: 1539-54.

Naskar, S., Hohl, M., Tassinari, M., and Low, H.H. (2021) The structure and mechanism of the bacterial type II secretion system. *Mol Microbiol* **115**: 412-24.
Nassif, X., Beretti, J.L., Lowy, J., Stenberg, P., O'Gaora, P., Pfeifer, J., Normark, S., and So, M. (1994) Roles of pilin and PilC in adhesion of *Neisseria meningitidis* to human epithelial and endothelial cells. *Proc Natl Acad Sci U S A* **91**: 3769-73.
Navarro, M.V., De, N., Bae, N., Wang, Q., and Sondermann, H. (2009) Structural analysis of the GGDEF-EAL domain-containing c-di-GMP receptor FimX. *Structure* **17**: 1104-16.
Ng, D., Harn, T., Altindal, T., Kolappan, S., Marles, J.M., Lala, R., Spielman, I., Gao, Y., Hauke, C.A., Kovacikova, G., Verjee, Z., Taylor, R.K., Biais, N., and Craig, L. (2016) The *Vibrio cholerae* minor pilin TcpB initiates assembly and retraction of the toxin-coregulated pilus. *PLoS Pathog* **12**: e1006109.
Nguyen, Y., Harvey, H., Sugiman-Marangos, S., Bell, S.D., Buensuceso, R.N., Junop, M.S., and Burrows, L.L. (2015a) Structural and functional studies of the *Pseudomonas aeruginosa* minor pilin, PilE. *J Biol Chem* **290**: 26856-65.
Nguyen, Y., Sugiman-Marangos, S., Harvey, H., Bell, S.D., Charlton, C.L., Junop, M.S., and Burrows, L.L. (2015b) *Pseudomonas aeruginosa* minor pilins prime type IVa pilus assembly and promote surface display of the PilY1 adhesin. *J Biol Chem* **290**: 601-11.
Nudleman, E., Wall, D., and Kaiser, D. (2005) Cell-to-cell transfer of bacterial outer membrane lipoproteins. *Science* **309**: 125-7.
Nudleman, E., Wall, D., and Kaiser, D. (2006) Polar assembly of the type IV pilus secretin in *Myxococcus xanthus*. *Mol Microbiol* **60**: 16-29.
Nunn, D.N., and Lory, S. (1991) Product of the *Pseudomonas aeruginosa* gene *pilD* is a prepilin leader peptidase. *Proc Natl Acad Sci U S A* **88**: 3281-5.
O'Toole, G.A., and Wong, G.C. (2016) Sensational biofilms: surface sensing in bacteria. *Curr Opin Microbiol* **30**: 139-46.
Oeser, S., Wallner, T., Schuergers, N., Bucinska, L., Sivabalasarma, S., Bahre, H., Albers, S.V., and Wilde, A. (2021) Minor pilins are involved in motility and natural competence in the cyanobacterium *Synechocystis sp.* PCC 6803. *Mol Microbiol* **116**: 743-65.
Orans, J., Johnson, M.D., Coggan, K.A., Sperlazza, J.R., Heiniger, R.W., Wolfgang, M.C., and Redinbo, M.R. (2010) Crystal structure analysis reveals *Pseudomonas* PilY1 as an essential calcium-dependent regulator of bacterial surface motility. *Proc Natl Acad Sci U S A* **107**: 1065-70.
Overgaard, M., Wegener-Feldbrügge, S., and Søgaard-Andersen, L. (2006) The orphan response regulator DigR is required for synthesis of extracellular matrix fibrils in *Myxococcus xanthus*. *J Bacteriol* **188**: 4384-94.
Parge, H.E., Forest, K.T., Hickey, M.J., Christensen, D.A., Getzoff, E.D., and Tainer, J.A. (1995) Structure of the fibre-forming protein pilin at 2.6 A resolution. *Nature* **378**: 32-8.
Parker, J.K., Cruz, L.F., Evans, M.R., and De La Fuente, L. (2015) Presence of calcium-binding motifs in PilY1 homologs correlates with Ca-mediated twitching motility and evolutionary history across diverse bacteria. *FEMS Microbiol Lett* **362**: 1-9.
Pelicic, V. (2008) Type IV pili: e pluribus unum? *Mol Microbiol* **68**: 827-37.
Pérez-Burgos, M., and Søgaard-Andersen, L. (2020a) Biosynthesis and function of cell-surface polysaccharides in the social bacterium *Myxococcus xanthus*. *Biol Chem* **401**: 1375-87.
Pérez-Burgos, M., and Søgaard-Andersen, L., (2020b) Regulation by cyclic di-GMP in *Myxococcus xanthus*. In: Microbial Cyclic Di-Nucleotide Signaling. S.-H. Chou, N. Guiliani, V.T. Lee & U. Römling (eds). Cham: Springer International Publishing, pp. 293-309.
Petters, T., Zhang, X., Nesper, J., Treuner-Lange, A., Gomez-Santos, N., Hoppert, M., Jenal, U., and Søgaard-Andersen, L. (2012) The orphan histidine protein kinase SgmT is a c-di-GMP receptor and regulates composition of the extracellular matrix together with the orphan DNA binding response regulator DigR in *Myxococcus xanthus*. *Mol Microbiol* **84**: 147-65.
Piepenbrink, K.H., and Sundberg, E.J. (2016) Motility and adhesion through type IV pili in Gram-positive bacteria. *Biochem Soc Trans* **44**: 1659-66.
Pogue, C.B., Zhou, T., and Nan, B. (2018) PlpA, a PilZ-like protein, regulates directed motility of the bacterium *Myxococcus xanthus*. *Mol Microbiol* **107**: 214-28.
Potapova, A., Carreira, L.A.M., and Søgaard-Andersen, L. (2020) The small GTPase MglA together with the TPR domain protein SgmX stimulates type IV pili formation in *M. xanthus*. *Proc Natl Acad Sci U S A* **117**: 23859-68.
Qi, Y., Chuah, M.L., Dong, X., Xie, K., Luo, Z., Tang, K., and Liang, Z.X. (2011) Binding of cyclic diguanylate in the non-catalytic EAL domain of FimX induces a long-range conformational change. *J Biol Chem* **286**: 2910-7.
Randall, T.E., Eckartt, K., Kakumanu, S., Price-Whelan, A., Dietrich, L.E.P., and Harrison, J.J. (2022) Sensory Perception in Bacterial Cyclic Diguanylate Signal Transduction. *J Bacteriol* **204**: e0043321.
Reichenbach, H. (1999) The ecology of the myxobacteria. *Environ Microbiol* **1**: 15-21.
Reindl, S., Ghosh, A., Williams, G.J., Lassak, K., Neiner, T., Henche, A.L., Albers, S.V., and Tainer, J.A. (2013) Insights into FlaI functions in archaeal motor assembly and motility from structures, conformations, and genetics. *Mol Cell* **49**: 1069-82.
Rodriguez-Soto, J.P., and Kaiser, D. (1997) Identification and localization of the Tgl protein, which is required for *Myxococcus xanthus* social motility. *J Bacteriol* **179**: 4372-81.
Römling, U., Galperin, M.Y., and Gomelsky, M. (2013) Cyclic di-GMP: the first 25 years of a universal bacterial second messenger. *Microbiol Mol Biol Rev* **77**: 1-52.

Roux, N., Spagnolo, J., and de Bentzmann, S. (2012) Neglected but amazingly diverse type IVb pili. *Res Microbiol* **163**: 659-73.
Rudel, T., Scheurerpflug, I., and Meyer, T.F. (1995) Neisseria PilC protein identified as type-4 pilus tip-located adhesin. *Nature* **373**: 357-9.
Sampaleanu, L.M., Bonanno, J.B., Ayers, M., Koo, J., Tammam, S., Burley, S.K., Almo, S.C., Burrows, L.L., and Howell, P.L. (2009) Periplasmic domains of *Pseudomonas aeruginosa* PilN and PilO form a stable heterodimeric complex. *J Mol Biol* **394**: 143-59.
Satyshur, K.A., Worzalla, G.A., Meyer, L.S., Heiniger, E.K., Aukema, K.G., Misic, A.M., and Forest, K.T. (2007) Crystal structures of the pilus retraction motor PilT suggest large domain movements and subunit cooperation drive motility. *Structure* **15**: 363-76.
Savakis, P., De Causmaecker, S., Angerer, V., Ruppert, U., Anders, K., Essen, L.-O., and Wilde, A. (2012) Light-induced alteration of c-di-GMP level controls motility of *Synechocystis sp.* PCC 6803. *Mol Microbiol* **85**: 239-251.
Schuergers, N., Lenn, T., Kampmann, R., Meissner, M.V., Esteves, T., Temerinac-Ott, M., Korvink, J.G., Lowe, A.R., Mullineaux, C.W., and Wilde, A. (2016) Cyanobacteria use micro-optics to sense light direction. *Elife* **5**: e12620.
Schuergers, N., Nurnberg, D.J., Wallner, T., Mullineaux, C.W., and Wilde, A. (2015) PilB localization correlates with the direction of twitching motility in the cyanobacterium *Synechocystis sp.* PCC 6803. *Microbiology (Reading)* **161**: 960-966.
Schumacher, D., and Søgaard-Andersen, L. (2017) Regulation of cell polarity in motility and cell division in *Myxococcus xanthus*. *Annu Rev Microbiol* **71**: 61-78.
Seef, S., Herrou, J., de Boissier, P., My, L., Brasseur, G., Robert, D., Jain, R., Mercier, R., Cascales, E., Habermann, B.H., and Mignot, T. (2021) A Tad-like apparatus is required for contact-dependent prey killing in predatory social bacteria. *Elife* **10**: e72409.
Seidel, M., Skotnicka, D., Glatter, T., and Søgaard-Andersen, L. (2023) During heat stress in *Myxococcus xanthus,* the CdbS PilZ domain protein, in concert with two PilZ-DnaK chaperones, perturbs chromosome organization and accelerates cell death. *PLoS Genet* **19**: e1010819.
Sellner, B., Prakapaite, R., van Berkum, M., Heinemann, M., Harms, A., and Jenal, U. (2021) A new sugar for an old phage: a c-di-GMP-dependent polysaccharide pathway sensitizes *Escherichia coli* for bacteriophage infection. *mBio* **12**: e0324621.
Shi, W., and Zusman, D.R. (1993) The two motility systems of *Myxococcus xanthus* show different selective advantages on various surfaces. *Proc Natl Acad Sci U S A* **90**: 3378-82.
Siewering, K., Jain, S., Friedrich, C., Webber-Birungi, M.T., Semchonok, D.A., Binzen, I., Wagner, A., Huntley, S., Kahnt, J., Klingl, A., Boekema, E.J., Søgaard-Andersen, L., and van der Does, C. (2014) Peptidoglycan-binding protein TsaP functions in surface assembly of type IV pili. *Proc Natl Acad Sci U S A* **111**: E953-61.
Silhavy, T.J., Kahne, D., and Walker, S. (2010) The bacterial cell envelope. *Cold Spring Harb Perspect Biol* **2**: a000414.
Silva, Y.R.O., Contreras-Martel, C., Macheboeuf, P., and Dessen, A. (2020) Bacterial secretins: Mechanisms of assembly and membrane targeting. *Protein Sci* **29**: 893-904.
Siryaporn, A., Kuchma, S.L., O'Toole, G.A., and Gitai, Z. (2014) Surface attachment induces Pseudomonas aeruginosa virulence. *Proc Natl Acad Sci U S A* **111**: 16860-5.
Skerker, J.M., and Berg, H.C. (2001) Direct observation of extension and retraction of type IV pili. *Proc Natl Acad Sci U S A* **98**: 6901-4.
Skotnicka, D., Petters, T., Heering, J., Hoppert, M., Kaever, V., and Søgaard-Andersen, L. (2016a) Cyclic di-GMP regulates type IV pilus-dependent motility in *Myxococcus xanthus*. *J Bacteriol* **198**: 77-90.
Skotnicka, D., Smaldone, G.T., Petters, T., Trampari, E., Liang, J., Kaever, V., Malone, J.G., Singer, M., and Søgaard-Andersen, L. (2016b) A minimal threshold of c-di-GMP is essential for fruiting body formation and sporulation in *Myxococcus xanthus*. *PLoS Genet* **12**: e1006080.
Skotnicka, D., Steinchen, W., Szadkowski, D., Cadby, I.T., Lovering, A.L., Bange, G., and Søgaard-Andersen, L. (2020) CdbA is a DNA-binding protein and c-di-GMP receptor important for nucleoid organization and segregation in *Myxococcus xanthus*. *Nat Commun* **11**: 1791.
Smedley, J.G., 3rd, Jewell, E., Roguskie, J., Horzempa, J., Syboldt, A., Stolz, D.B., and Castric, P. (2005) Influence of pilin glycosylation on *Pseudomonas aeruginosa* 1244 pilus function. *Infect Immun* **73**: 7922-31.
Song, W.Y., Zang, S.S., Li, Z.K., Dai, G.Z., Liu, K., Chen, M., and Qiu, B.S. (2018) Sycrp2 Is essential for twitching motility in the cyanobacterium *Synechocystis sp*. strain PCC 6803. *J Bacteriol* **200**: 10.1128/jb.00436-18.
Stephens, D.S., Whitney, A.M., Rothbard, J., and Schoolnik, G.K. (1985) Pili of *Neisseria meningitidis*. Analysis of structure and investigation of structural and antigenic relationships to gonococcal pili. *J Exp Med* **161**: 1539-53.
Strom, M.S., Bergman, P., and Lory, S. (1993a) Identification of active-site cysteines in the conserved domain of PilD, the bifunctional type IV pilin leader peptidase/N-methyltransferase of *Pseudomonas aeruginosa*. *J Biol Chem* **268**: 15788-94.
Strom, M.S., and Lory, S. (1987) Mapping of export signals of *Pseudomonas aeruginosa* pilin with alkaline phosphatase fusions. *J Bacteriol* **169**: 3181-8.
Strom, M.S., Nunn, D.N., and Lory, S. (1993b) A single bifunctional enzyme, PilD, catalyzes cleavage and N-methylation of proteins belonging to the type IV pilin family. *Proc Natl Acad Sci U S A* **90**: 2404-8.
Sun, H., Zusman, D.R., and Shi, W. (2000) Type IV pilus of *Myxococcus xanthus* is a motility apparatus controlled by the *frz* chemosensory system. *Curr Biol* **10**: 1143-6.

Sun, M., Wartel, M., Cascales, E., Shaevitz, J.W., and Mignot, T. (2011) Motor-driven intracellular transport powers bacterial gliding motility. *Proc Natl Acad Sci U S A* **108**: 7559-64.

Szadkowski, D., Carreira, L.A.M., and Søgaard-Andersen, L. (2022) A bipartite, low-affinity roadblock domain-containing GAP complex regulates bacterial front-rear polarity. *PLoS Genet* **18**: e1010384.

Szadkowski, D., Harms, A., Carreira, L.A.M., Wigbers, M., Potapova, A., Wuichet, K., Keilberg, D., Gerland, U., and Søgaard-Andersen, L. (2019) Spatial control of the GTPase MglA by localized RomR-RomX GEF and MglB GAP activities enables *Myxococcus xanthus* motility. *Nat Microbiol* **4**: 1344-55.

Takhar, H.K., Kemp, K., Kim, M., Howell, P.L., and Burrows, L.L. (2013) The platform protein is essential for type IV pilus biogenesis. *J Biol Chem* **288**: 9721-8.

Talà, L., Fineberg, A., Kukura, P., and Persat, A. (2019) Pseudomonas aeruginosa orchestrates twitching motility by sequential control of type IV pili movements. *Nat Microbiol* **4**: 774-80.

Tammam, S., Sampaleanu, L.M., Koo, J., Manoharan, K., Daubaras, M., Burrows, L.L., and Howell, P.L. (2013) PilMNOPQ from the *Pseudomonas aeruginosa* type IV pilus system form a transenvelope protein interaction network that interacts with PilA. *J Bacteriol* **195**: 2126-35.

Tammam, S., Sampaleanu, L.M., Koo, J., Sundaram, P., Ayers, M., Chong, P.A., Forman-Kay, J.D., Burrows, L.L., and Howell, P.L. (2011) Characterization of the PilN, PilO and PilP type IVa pilus subcomplex. *Mol Microbiol* **82**: 1496-514.

Thiery, S., Turowski, P., Berleman, J.E., and Kaimer, C. (2022) The predatory soil bacterium *Myxococcus xanthus* combines a Tad- and an atypical type 3-like protein secretion system to kill bacterial cells. *Cell Rep* **40**: 111340.

Tomich, M., Planet, P.J., and Figurski, D.H. (2007) The tad locus: postcards from the widespread colonization island. *Nature Reviews Microbiology* **5**: 363-75.

Treuner-Lange, A., Chang, Y.W., Glatter, T., Herfurth, M., Lindow, S., Chreifi, G., Jensen, G.J., and Søgaard-Andersen, L. (2020) PilY1 and minor pilins form a complex priming the type IVa pilus in *Myxococcus xanthus*. *Nat Commun* **11**: 5054.

Treuner-Lange, A., Macia, E., Guzzo, M., Hot, E., Faure, L.M., Jakobczak, B., Espinosa, L., Alcor, D., Ducret, A., Keilberg, D., Castaing, J.P., Lacas Gervais, S., Franco, M., Søgaard-Andersen, L., and Mignot, T. (2015) The small G-protein MglA connects to the MreB actin cytoskeleton at bacterial focal adhesions. *J Cell Biol* **210**: 243-56.

Trindade, M.B., Job, V., Contreras-Martel, C., Pelicic, V., and Dessen, A. (2008) Structure of a widely conserved type IV pilus biogenesis factor that affects the stability of secretin multimers. *J Mol Biol* **378**: 1031-9.

Tsai, C.L., Tripp, P., Sivabalasarma, S., Zhang, C., Rodriguez-Franco, M., Wipfler, R.L., Chaudhury, P., Banerjee, A., Beeby, M., Whitaker, R.J., Tainer, J.A., and Albers, S.V. (2020) The structure of the periplasmic FlaG-FlaF complex and its essential role for archaellar swimming motility. *Nat Microbiol* **5**: 16-225.

Vaziri, F., and Brosch, R. (2019) ESX/Type VII secretion systems-an important way out for mycobacterial proteins. *Microbiol Spectr* **7**: 10.1128/microbiolspec.psib-0029-2019.

Viarre, V., Cascales, E., Ball, G., Michel, G.P., Filloux, A., and Voulhoux, R. (2009) HxcQ liposecretin is self-piloted to the outer membrane by its N-terminal lipid anchor. *J Biol Chem* **284**: 33815-23.

Waite, D.W., Chuvochina, M., Pelikan, C., Parks, D.H., Yilmaz, P., Wagner, M., Loy, A., Naganuma, T., Nakai, R., Whitman, W.B., Hahn, M.W., Kuever, J., and Hugenholtz, P. (2020) Proposal to reclassify the proteobacterial classes Deltaproteobacteria and Oligoflexia, and the phylum Thermodesulfobacteria into four phyla reflecting major functional capabilities. *Int J Syst Evol Microbiol* **70**: 5972-6016.

Wall, D., Wu, S.S., and Kaiser, D. (1998) Contact stimulation of Tgl and type IV pili in *Myxococcus xanthus*. *J Bacteriol* **180**: 759-61.

Wallner, T., Pedroza, L., Voigt, K., Kaever, V., and Wilde, A. (2020) The cyanobacterial phytochrome 2 regulates the expression of motility-related genes through the second messenger cyclic di-GMP. *Photochem Photobiol Sci* **19**: 631-43.

Wang, Y.C., Chin, K.H., Tu, Z.L., He, J., Jones, C.J., Sanchez, D.Z., Yildiz, F.H., Galperin, M.Y., and Chou, S.H. (2016) Nucleotide binding by the widespread high-affinity cyclic di-GMP receptor MshEN domain. *Nat Commun* **7**: 12481.

Weaver, S.J., Ortega, D.R., Sazinsky, M.H., Dalia, T.N., Dalia, A.B., and Jensen, G.J. (2020) CryoEM structure of the type IVa pilus secretin required for natural competence in *Vibrio cholerae*. *Nat Commun* **11**: 5080.

Webster, S.S., Lee, C.K., Schmidt, W.C., Wong, G.C.L., and O'Toole, G.A. (2021a) Interaction between the type 4 pili machinery and a diguanylate cyclase fine-tune c-di-GMP levels during early biofilm formation. *Proc Natl Acad Sci U S A* **118**: e2105566118.

Webster, S.S., Mathelie-Guinlet, M., Verissimo, A.F., Schultz, D., Viljoen, A., Lee, C.K., Schmidt, W.C., Wong, G.C.L., Dufrene, Y.F., and O'Toole, G.A. (2021b) Force-Induced Changes of PilY1 Drive Surface Sensing by *Pseudomonas aeruginosa*. *mBio* **13**: e0375421.

Wei, C., Wang, S., Liu, P., Cheng, S.T., Qian, G., Wang, S., Fu, Y., Qian, W., and Sun, W. (2021) The PdeK-PdeR two-component system promotes unipolar localization of FimX and pilus extension in *Xanthomonas oryzae pv. oryzicola*. *Sci Signal* **14**: eabi9589.

Wei, X., Pathak, D.T., and Wall, D. (2011) Heterologous protein transfer within structured myxobacteria biofilms. *Mol Microbiol* **81**: 315-26.

Whitchurch, C.B., Alm, R.A., and Mattick, J.S. (1996) The alginate regulator AlgR and an associated sensor FimS are required for twitching motility in *Pseudomonas aeruginosa*. *Proc Natl Acad Sci U S A* **93**: 9839-43.

Winther-Larsen, H.C., Hegge, F.T., Wolfgang, M., Hayes, S.F., van Putten, J.P., and Koomey, M. (2001) *Neisseria gonorrhoeae* PilV, a type IV pilus-associated protein essential to human epithelial cell adherence. *Proc Natl Acad Sci U S A* **98**: 15276-81.

Wolfgang, M., van Putten, J.P., Hayes, S.F., and Koomey, M. (1999) The *comP* locus of *Neisseria gonorrhoeae* encodes a type IV prepilin that is dispensable for pilus biogenesis but essential for natural transformation. *Mol Microbiol* **31**: 1345-57.

Worrall, L.J., Hong, C., Vuckovic, M., Deng, W., Bergeron, J.R.C., Majewski, D.D., Huang, R.K., Spreter, T., Finlay, B.B., Yu, Z., and Strynadka, N.C.J. (2016) Near-atomic-resolution cryo-EM analysis of the *Salmonella* T3S injectisome basal body. *Nature* **540**: 597-601.

Wright, T.A., Jiang, L., Park, J.J., Anderson, W.A., Chen, G., Hallberg, Z.F., Nan, B., and Hammond, M.C. (2020) Second messengers and divergent HD-GYP phosphodiesterases regulate 3',3'-cGAMP signaling. *Mol Microbiol* **113**: 222-36.

Xue, S., Mercier, R., Guiseppi, A., Kosta, A., De Cegli, R., Gagnot, S., Mignot, T., and Mauriello, E.M.F. (2022) The differential expression of PilY1 proteins by the HsfBA phosphorelay allows twitching motility in the absence of exopolysaccharides. *PLoS Genet* **18**: e1010188.

Yang, Z., Lux, R., Hu, W., Hu, C., and Shi, W. (2010) PilA localization affects extracellular polysaccharide production and fruiting body formation in *Myxococcus xanthus*. *Mol Microbiol* **76**: 1500-13.

Yin, M., Yan, Z., and Li, X. (2018) Structural insight into the assembly of the type II secretion system pilotin-secretin complex from enterotoxigenic *Escherichia coli*. *Nat Microbiol* **3**: 581-7.

Zhang, Y., Ducret, A., Shaevitz, J., and Mignot, T. (2012a) From individual cell motility to collective behaviors: insights from a prokaryote, *Myxococcus xanthus*. *FEMS Microbiol Rev* **36**: 149-64.

Zhang, Y., Franco, M., Ducret, A., and Mignot, T. (2010) A bacterial Ras-like small GTP-binding protein and its cognate GAP establish a dynamic spatial polarity axis to control directed motility. *PLoS Biol* **8**: e1000430.

Zhang, Y., Guzzo, M., Ducret, A., Li, Y.Z., and Mignot, T. (2012b) A dynamic response regulator protein modulates G-protein-dependent polarity in the bacterium *Myxococcus xanthus*. *PLoS Genet* **8**: e1002872.

8. Results

8.1 A noncanonical cytochrome *c* stimulates calcium binding by PilY1 for type IVa pili formation

This chapter contains our advances in the characterization of a novel component of one of the three minor pilin gene clusters of *M. xanthus* (Herfurth *et al.*, 2022). The article was reused under the CC BY 4.0 license. This part of the thesis is written in a manuscript style and was published in Proceedings of the National Academy of Science of the USA. I contributed to this work by designing, performing and analyzing experiments, preparing the figures and the manuscript.

I performed all experiments and analysis with the following exceptions: Acquisition of mass spectrometry data in Figure 3A, 4C, 6E and F was performed by Dr. Timo Glatter. UV-Vis spectroscopy measurements in Figure 5A, B, D and E were performed in collaboration with Prof. Dr. Antonio Pierik and Nadine Witmaak. EPR measurements in Figure 5D were done by Prof. Dr. Antonio Pierik.

A noncanonical cytochrome *c* stimulates calcium binding by PilY1 for type IVa pili formation

Marco Herfurth[a], Anke Treuner-Lange[a], Timo Glatter[b], Nadine Wittmaack[c], Egbert Hoiczyk[d], Antonio J. Pierik[c], and Lotte Søgaard-Andersen[a,1]

[a]Department of Ecophysiology, Max Planck Institute for Terrestrial Microbiology, 35043 Marburg, Germany; [b]Core Facility for Mass Spectrometry and Proteomics, Max Planck Institute for Terrestrial Microbiology, 35043 Marburg, Germany; [c]Biochemistry, Faculty of Chemistry, Technical University Kaiserslautern, D-67663 Kaiserslautern, Germany; and [d]Department of Molecular Biology and Biotechnology, The Krebs Institute, The University of Sheffield, Sheffield S10 2TN, United Kingdom

Edited by Christine Jacobs-Wagner, Department of Biology, Stanford University, Stanford, CA; received August 15, 2021; accepted December 28, 2021

Type IVa pili (T4aP) are versatile bacterial cell surface structures that undergo extension/adhesion/retraction cycles powered by the cell envelope–spanning T4aP machine. In this machine, a complex composed of four minor pilins and PilY1 primes T4aP extension and is also present at the pilus tip mediating adhesion. Similar to many several other bacteria, *Myxococcus xanthus* contains multiple minor pilins/PilY1 sets that are incompletely understood. Here, we report that minor pilins and PilY1 (PilY1.1) of cluster_1 form priming and tip complexes contingent on calcium and a noncanonical cytochrome *c* (TfcP) with an unusual His/Cys heme ligation. We provide evidence that TfcP is unlikely to participate in electron transport and instead stimulates calcium binding by PilY1.1 at low-calcium concentrations, thereby stabilizing PilY1.1 and enabling T4aP function in a broader range of calcium concentrations. These results not only identify a previously undescribed function of cytochromes *c* but also illustrate how incorporation of an accessory factor expands the environmental range under which the T4aP system functions.

type IV pili | cytochrome *c* | PilY1 | bacterial adhesin | minor pilin

In bacteria, motility is important for virulence, promotes colonization of habitats of diverse composition, and stimulates biofilm formation (1). Type IVa pili (T4aP) are filamentous cell surface structures that enable cell translocation across surfaces and also have critical functions in surface adhesion, surface sensing, host cell interaction, biofilm formation, predation, virulence, and DNA uptake (2–4). The versatility of T4aP is based on their ability to undergo cycles of extension, surface adhesion, and retraction (5, 6). Retractions generate a force up to 150 pN per pilus, pulling cells across surfaces (7).

In Gram-negative bacteria, the extension/retraction cycles of T4aP are driven by the T4aP machine (T4aPM), which consists of 15 conserved proteins that form a complex that spans from the outer membrane (OM) across the periplasm and inner membrane (IM) to the cytoplasm (8–10) (Fig. 1*A*). Pilus extension and retraction are powered by the PilB and PilT ATPases, respectively, that bind in a mutually exclusive manner to the cytoplasmic base of the T4aPM (8, 11–13). All 15 proteins are essential for T4aP extension except for PilT, which is only important for retraction (4). The so-called priming complex is an integral part of the T4aPM, composed of the major pilin, four minor pilins and the PilY1 protein, and incorporated into the machine independently of the PilB ATPase (10, 14) (Fig. 1*A*). The five pilins interact directly to form a short pilus that is capped by PilY1, which interacts directly with the minor pilins (10). Pilus extension is initiated by the incorporation of additional major pilin subunits from a reservoir in the IM to the base of the priming complex in a process stimulated by PilB (6, 10, 14). Conversely, during retractions, major pilin subunits are removed from the base of the pilus and reinserted into the IM in a process stimulated by PilT (12, 15). Because the major pilin is added to the priming complex during the initiation of the extension process, the priming complex remains at the tip of the extended pilus (10, 14, 16). Consistently, PilY1 is involved in surface adhesion, surface sensing, specificity in host cell recognition during infections, and virulence (14, 16–19).

Among the 15 proteins of the T4aPM, 9 are generally encoded by single-copy genes (20). Some species contain multiple PilT paralogs that enable retractions with different characteristics (21). The genes for the four minor pilins and PilY1 are also often present in multiple copies (10, 22–24). The multiplicity of minor pilins and PilY1 proteins has been suggested to allow individual species to assemble priming complexes and tip complexes of different composition and with different properties, thereby allowing the formation of T4aP that can function in a variety of different habitats (10, 14, 25). Minor pilins are low-abundance proteins that share overall structure and sequence homology with the major pilin and have a prepilin signal peptide, a hydrophobic N-terminal α-helix, and a C-terminal globular domain, which is less conserved (26). PilY1 proteins have a type I signal peptide, are secreted to the periplasm, and are composed of two domains. The conserved C-terminal PilY1 domain adopts a beta-propeller fold (27) that interacts with the minor pilins in the priming and tip complex (10) (Fig. 1*A*). The N-terminal domain is much less conserved

Significance

Type IVa pili (T4aP) are bacterial surface structures that function under different environmental conditions. In the machine for T4aP formation, a complex of minor pilins and PilY1 primes T4aP formation and is also present at the pilus tip mediating adhesion. Similar to several other bacterial adhesins, PilY1 depends on calcium binding for function. Here, we demonstrate that in *Myxococcus xanthus*, PilY1 at low levels of calcium depends on the accessory protein TfcP to bind calcium, thereby stabilizing the protein. TfcP is a noncanonical cytochrome *c* that does not participate in electron transport. Rather our data support that TfcP interacts transiently with PilY1 to stimulate calcium binding. In this way, TfcP expands the range of calcium levels under which T4aP functions.

Author contributions: M.H., A.T.-L., and L.S.-A. designed research; M.H., A.T.-L., T.G., N.W., and A.J.P. performed research; E.H. contributed new reagents/analytic tools; M.H., A.T.-L., T.G., A.J.P., and L.S.-A. analyzed data; and M.H., A.T.-L., T.G., N.W., E.H., A.J.P., and L.S.-A. wrote the paper.

The authors declare no competing interest.

This article is a PNAS Direct Submission.

[1]To whom correspondence may be addressed. Email: sogaard@mpi-marburg.mpg.de.

This article contains supporting information online at http://www.pnas.org/lookup/suppl/doi:10.1073/pnas.2115061119/-/DCSupplemental.

Published February 4, 2022.

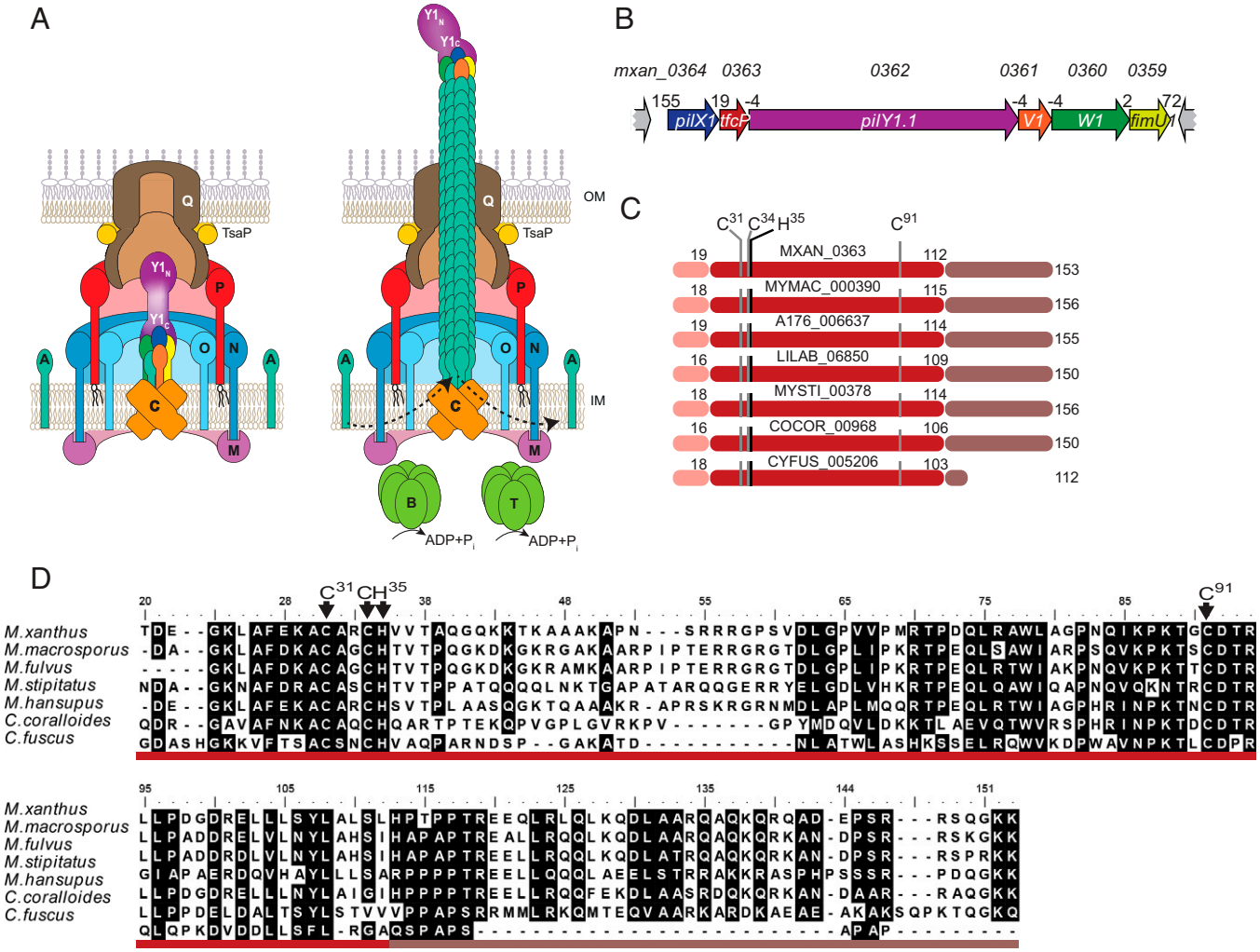

Fig. 1. TfcP is a noncanonical cytochrome *c*. (*A*) Architectural model of nonpiliated and piliated T4aPM. PilB and PilT associate with PilC in a mutually exclusive manner during extension and retraction, respectively. Bent arrows, incorporation and removal of the major pilin PilA from the pilus base during extension and retraction, respectively. Proteins labeled with single letters have the Pil prefix. $Y1_N$ and $Y1_C$ indicate the N- and C-terminal domains of PilY1, respectively. The color code for the four minor pilins is as in *B*. (*B*) Genetic organization of cluster_1 encoding minor pilins, PilY1.1 and TfcP. Locus tags are included *Above* and gene names within genes. Distances between start and stop codons are shown *Above*. (*C*) Domain architecture of TfcP and homologs. Pink, type I signal peptide; red, cytochrome *c* domain; and brown, C-terminal extension. The cytochrome *c* signature motif CxxCH and the distal Cys^{91} residue are indicated. Numbering of amino acids is according to the unprocessed, full-length TfcP. (*D*) Sequence alignment of TfcP homologs. Residues are highlighted based on >80% similarity. Domains are indicated using the color code from *C*. The cytochrome *c* signature motif CxxCH and the distal Cys^{91} residue are indicated. Numbering of amino acids is according to the unprocessed, full-length proteins.

and is the domain that mediates host cell recognition, adhesion, and surface sensing (10, 17, 28).

The soil-dwelling δ-proteobacterium *Myxococcus xanthus* uses T4aP-dependent motility (T4aPdM) and gliding motility to move on surfaces to generate spreading colonies in the presence of nutrients and spore-filled fruiting bodies in the absence of nutrients (29, 30). The *M. xanthus* genome contains three gene clusters (from here on cluster_1, _2, and _3; proteins labeled with suffixes 1, 2, and 3), each encoding four minor pilins and a PilY1 protein (8, 10). Cluster_1 alone and cluster_3 alone support T4aPdM under standard conditions (10). While the four respective minor pilins share overall sequence homology, the three PilY1 proteins are highly divergent in their N-terminal domains (10). Thus, *M. xanthus* has the potential to generate at least two, and possibly three, different T4aPM and T4aP that differ in their priming and tip complexes.

To understand the functional range of the three minor pilin/PilY1 protein sets, we focused on the proteins of cluster_1. Here, we provide evidence that these proteins form priming and tip complexes in a calcium-dependent manner. We identify the TfcP protein and show that it is a noncanonical cytochrome *c* with an unusual His/Cys heme ligation that is important for PilY1.1 stability under low-calcium conditions; PilY1.1, in turn, is important for the stability of the cluster_1 minor pilins. The effect of TfcP on PilY1.1 stability depends on calcium binding by PilY1.1 and is bypassed at high-calcium concentrations. Our data support a model whereby TfcP promotes calcium binding by PilY1.1 at low-calcium concentrations, thereby, allowing cluster_1 to support T4aP function in a broader range of environmental conditions.

Results

TfcP Is a Noncanonical Cytochrome *C* Important for Cluster_1-Based T4aP Formation. In addition to encoding four minor pilins (PilX1, PilW1, PilV1, and FimU1) and PilY1.1, cluster_1 contains an open reading frame (ORF) (locus tag=*mxan_0363*) (Fig. 1*B*), for which no homolog is present in cluster_2 and

cluster_3. This ORF is conserved in gene clusters encoding minor pilins and PilY1 in other Myxococcales genomes (*SI Appendix*, Fig. S1*A*). Mxan_0363 homologs contain three parts, including a type I signal peptide (Fig. 1*C*). The middle part has similarity to cytochromes *c*, including a single cytochrome *c* signature motif CxxCH (31) (Fig. 1 *C* and *D* and *SI Appendix*, Fig. S1*B*). *C*-type cytochromes are secreted to the periplasm in a Sec-dependent manner where they acquire the heme, which is covalently attached to the two Cys residues in the signature motif by thioether bonds, while the His residue is the proximal axial ligand of the heme iron (32). Approximately 90% of cytochromes *c*, the so-called canonical cytochromes *c*, have a Met or His residue ∼60 residues downstream of the signature motif that serves as the second axial ligand of the heme iron (31, 33, 34) (*SI Appendix*, Fig. S1*B*). Interestingly, in Mxan_0363 and homologs, this is a Cys residue (Cys^{91} in Mxan_0363) (Fig. 1 *C* and *D* and *SI Appendix*, Fig. S1*B*) that is rarely found as the second axial ligand in *c*-type cytochromes (34, 35). In the vicinity of Cys^{91}, no conserved Met or His residues are present and the alignment with canonical cytochromes *c* shows that Cys^{91} occupies the position of the conserved methionine distal ligand (*SI Appendix*, Fig. S1*B*). In an AlphaFold2 model together with ligand prediction using COACH (*SI Appendix*, *SI Materials and Methods*), this part of Mxan_0363 adopts a cytochrome *c*-like fold (36) that can readily be superimposed on the determined 1.5-Å structure (PDB 2B4Z) of *Bos taurus* cytochrome *c* (*SI Appendix*, Fig. S1*C*) and contains a heme c with His/Cys coordination (*SI Appendix*, Fig. S1*C*). Finally, Mxan_0363 and most of its homologs contain a C-terminal extension enriched in charged residues (Fig. 1 *C* and *D*), which does not occur in canonical cytochromes *c* (*SI Appendix*, Fig. S1 *B* and *C*). In the AlphaFold2 model, this extension is modeled as a 30-residue highly charged α-helix that is separated from the cytochrome *c* domain by a short Pro-rich region (*SI Appendix*, Fig. S1 *B* and *C*). Thus, Mxan_0363 homologs have features in common with canonical cytochromes *c* but also distinct features. Mxan_0363 homologs were not identified in species other than the listed Myxococcales (Fig. 1 *C* and *D*). From here on, we refer to Mxan_0363 as TfcP for T4aP formation cytochrome *c* protein.

Consistent with the overlap of or short distances between stop and start codons for neighboring genes in cluster_1 (Fig. 1*B*), they constitute an operon based on RT-PCR analyses (*SI Appendix*, Fig. S1*D*).

To test whether TfcP is important for T4aP formation or function, we generated in-frame deletions of *tfcP* and the remaining five cluster_1 genes. The deletions were generated in a strain in which cluster_2 and cluster_3 had been deleted (Δ2Δ3_cluster strain) because cluster_1 and _3 in the wild-type (WT) strain DK1622 function redundantly to support T4aP formation and T4aPdM (10). From here on, we used the Δ2Δ3_cluster strain as a reference strain and refer to it as the $WT_{\Delta2\Delta3}$ strain.

In motility assays for T4aPdM on 0.5% agar supplemented with 0.5% casitone broth (CTT), $WT_{\Delta2\Delta3}$ generated the flares at the colony edge characteristic of T4aPdM, while the Δ*pilA* mutant, which lacks the major pilin PilA, did not (Fig. 2*A*). As for cluster_3 genes (10), T4aPdM was abolished in the Δ*pilX1*, Δ*pilV1*, Δ*pilW1*, and Δ*pilY1.1* mutants and reduced in the Δ*fimU1* mutant. Strikingly, T4aPdM was also abolished in the Δ*tfcP* mutant. For all six in-frame deletion mutants, motility was complemented by ectopic expression of the relevant gene from a plasmid integrated in a single copy at the Mx8 *attB* site (Fig. 2 *A*, *Lower*).

To pinpoint the mechanism causing the T4aPdM defect in the cluster_1 mutants, we assessed T4aP formation in the six in-frame deletion mutants using an assay in which T4aP are sheared off the cell surface, and the level of the major pilin PilA in the sheared fraction quantified by immunoblot analysis (Fig. 2*B*). None of the five nonmotile mutants formed detectable T4aP, while the Δ*fimU1* mutant assembled T4aP at a much-reduced level compared to the parent strain. For all six in-frame deletion mutants, the total cellular level of PilA was similar or slightly lower than in the parent $WT_{\Delta2\Delta3}$ strain. T4aP formation in the Δ*tfcP* mutant was complemented by ectopic expression of *tfcP*.

To distinguish whether the defect in T4aP formation was caused by lack of extension or by hyperretractions, we examined T4aP formation in the in-frame deletion mutants additionally containing a Δ*pilT* mutation and, thus, lacking the PilT retraction ATPase (Fig. 2*C*). The $WT_{\Delta2\Delta3}$Δ*pilT* strain formed T4aP at a highly increased level compared to $WT_{\Delta2\Delta3}$, consistent with previous observations for the WTΔ*pilT* strain (12). In the absence of PilT, T4aP formation was partially restored in the Δ*tfcP* mutant, but at a much-reduced level compared to the $WT_{\Delta2\Delta3}$Δ*pilT* strain. By contrast, T4aP formation in the Δ*pilX1*, Δ*pilV1*, Δ*pilW1*, and Δ*pilY1.1* mutants was not restored. For all in-frame deletion mutants except for the Δ*fimU1* mutant, the total cellular level of PilA was lower than in the $WT_{\Delta2\Delta3}$Δ*pilT* strain. We conclude that TfcP is important but not essential for cluster_1-dependent T4aP extension while the minor pilins PilX1, -V1, and -W1 as well as PilY1.1 are essential for T4aP formation, and FimU1 plays a less important role. The observations are in agreement with similar experiments involving minor pilins and PilY1.3 of cluster_3 (10).

TfcP Is Important for PilY1.1 Stability. To understand how TfcP might be involved in T4aP extension, we used proteomics on whole-cell extracts to quantify the accumulation of T4aPM components in $WT_{\Delta2\Delta3}$ and $WT_{\Delta2\Delta3}$Δ*tfcP* strains. To increase sensitivity, we used targeted proteomics in which protein abundance is quantified relative to heavy-labeled reference peptides of the proteins of interest (*SI Appendix*, *SI Materials and Methods*). In the absence of TfcP, accumulation of 10 T4aPM components was largely unaffected, while the accumulation of the four minor pilins and PilY1.1 was significantly reduced (Fig. 3*A*). Because PilY1 of cluster_3 is important for the stability of cluster_3 minor pilins (10), we performed targeted proteomics on the $WT_{\Delta2\Delta3}$Δ*pilY1.1* strain. In this strain, accumulation of the four minor pilins was also significantly reduced, while TfcP accumulation was significantly increased (Fig. 3*A*). In immunoblot analysis, we observed that in the absence of individual cluster_1 minor pilins, accumulation of TfcP was increased and PilY1.1 unchanged (Fig. 3*B*). Immunoblot analysis also confirmed that PilY1.1 accumulation was strongly reduced in the absence of TfcP, while TfcP accumulation was increased in the absence of PilY1.1 (Fig. 3*B*).

To resolve whether the effect of the Δ*tfcP* mutation on PilY1.1 and the Δ*pilY1.1* mutation on minor pilin accumulation was due to altered transcription of the relevant genes or altered protein stability, we performed qRT-PCR analysis on total RNA from the $WT_{\Delta2\Delta3}$, $WT_{\Delta2\Delta3}$Δ*tfcP*, and $WT_{\Delta2\Delta3}$Δ*pilY1.1* strains. Transcript levels of the cluster_1 genes were significantly increased in the Δ*tfcP* and the Δ*pilY1.1* mutants (*SI Appendix*, Fig. S2), suggesting negative feedback regulation of cluster_1 genes as reported for the minor pilin/*pilY1* gene cluster of *Pseudomonas aeruginosa* (37). While the mechanism involved in this regulation remains unresolved, these results do not support the reduced levels of PilY1.1/minor pilins and minor pilins in the absence of TfcP and PilY1.1, respectively, being caused by reduced synthesis. Rather they support TfcP stabilizing PilY.1.1, which, in turn, stabilizes the four minor pilins. Accumulation dependencies have also been reported for the cluster_3 proteins in which PilY1.3 and minor pilins interact directly to mutually stabilize each other (10).

In *M. xanthus*, the T4aPM assembles at the two poles (10, 38–40). To exclude that lack of TfcP affects assembly of the

MICROBIOLOGY

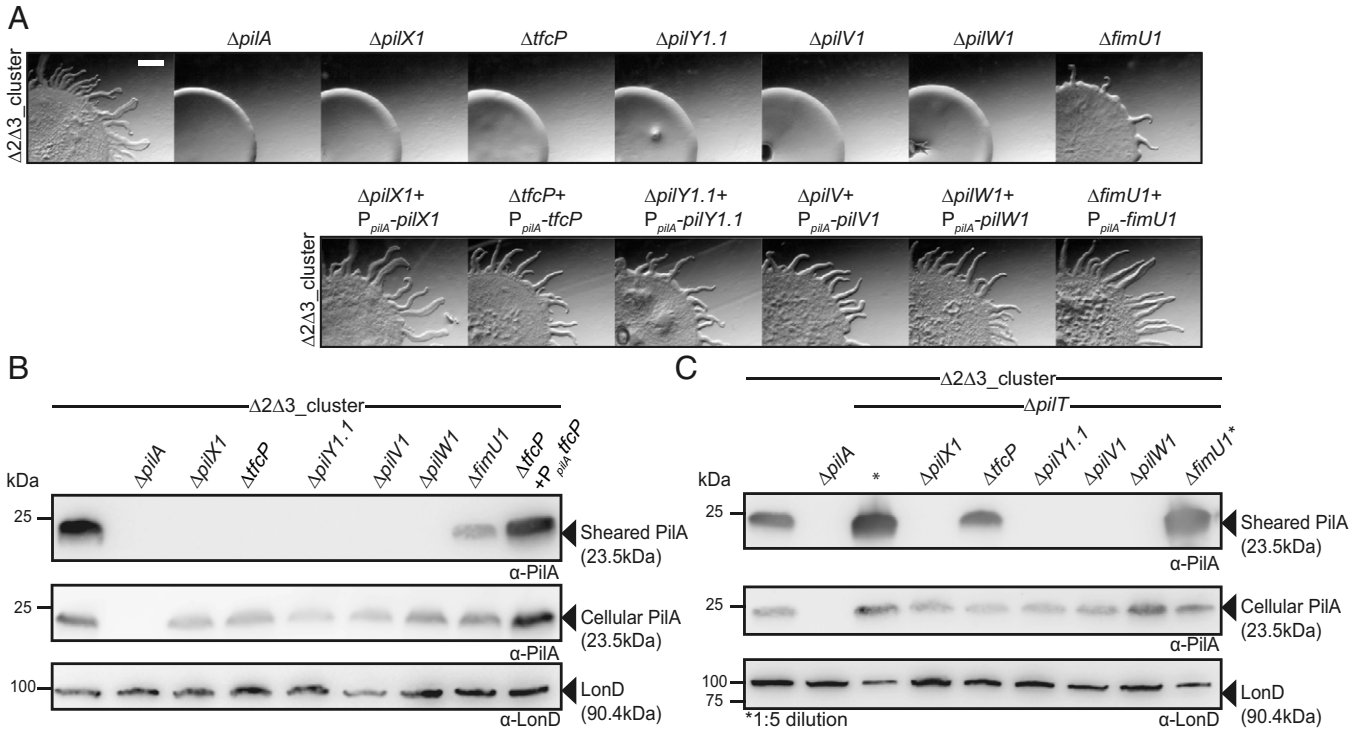

Fig. 2. TfcP, minor pilins, and PilY1.1 of cluster_1 are important for T4aPdM and T4aP formation. (*A*) Assay for T4aPdM. $WT_{\Delta2\Delta3}$ and strains with deletions of individual cluster_1 genes, and the corresponding complementation strains were spotted on 0.5% agar supplemented with 0.5% CTT and imaged after 24 h. (Scale bar, 1 mm.) (*B*) Shearing assay for T4aP formation. (*Top*) T4aP sheared off from ∼15 mg cells grown on 1.5% agar supplemented with 1.0% CTT were separated by sodium dodecyl sulphate-polyacrylamide gel electrophoresis (SDS-PAGE) and probed with α-PilA antibodies. (*Middle*) A total of 40 μg of total protein from total cell extracts separated by SDS-PAGE and probed with α-PilA antibodies and (*Lower*) after stripping, with α-LonD antibodies as a loading control. (*C*) Shearing assay for T4aP formation in retraction-deficient strains. T4aP formation was assayed as in *B*. In lanes labeled *, fivefold less total protein was loaded.

T4aPM, we used the bipolar localization of the cytoplasmic protein PilM as proxy for T4aPM assembly (39). We observed bipolar localization of an active mCherry-PilM fusion in most cells of the $WT_{\Delta2\Delta3}$ and $WT_{\Delta2\Delta3}\Delta tfcP$ strains but not in a mutant lacking the PilQ secretin, which is essential for T4aPM assembly (39) (Fig. 3*C*), supporting the idea that TfcP is not important for assembly of the remaining proteins into rudimentary T4aPM.

TfcP Is a Periplasmic Protein. To understand how TfcP stabilizes PilY1.1, we determined its subcellular localization using active TfcP-FLAG and TfcP-sfGFP fusions expressed from the endogenous locus; TfcP-FLAG accumulated at native levels while TfcP-sfGFP accumulated above native levels (*SI Appendix*, Fig. S3 *A* and *B*). After fractionation of $WT_{\Delta2\Delta3}$ synthesizing TfcP-FLAG into fractions enriched for soluble, IM and OM proteins, TfcP-FLAG was detected in the soluble fraction while the control proteins fractionated as described (12, 38) (Fig. 4*A*). After isolating proteins enriched in the periplasm, we detected TfcP-FLAG but not cytoplasmic PilB (Fig. 4*A*). In agreement with these observations, in fluorescence microscopy, TfcP-sfGFP localized along the entire cell periphery but polar clusters were not observed (Fig. 4*B*). Based on these observations and because TfcP has a type I signal peptide, we conclude that TfcP, similarly to other cytochromes *c* in Gram-negative bacteria and PilY1 proteins (10), is a periplasmic protein. Because all proteins that are incorporated into the T4aPM localize (bi)polarly (10, 38–40), the localization of TfcP-sfGFP also suggests that TfcP is not incorporated into the T4aPM.

To determine whether TfcP is present in pili, we purified pili from the $WT_{\Delta2\Delta3}\Delta pilT$ mutant (*SI Appendix*, Fig. S4) and used label-free quantitative proteomics to quantify cluster_1 proteins. TfcP was not detected in purified pili, while all minor pilins/PilY1 of cluster_1 were detected in low amounts relative to the PilA major pilin (Fig. 4*C*) as described for cluster_3 proteins (10).

Altogether, these observations support the idea that the minor pilins and PilY1.1 of cluster_1 form a priming complex in the T4aPM for T4aP extension as well as a pilus tip complex. The observations that TfcP stabilizes PilY1.1 but TfcP is incorporated into neither the T4aPM nor T4aP suggest that the stabilizing effect of TfcP on PilY1.1 occurs in the periplasm and before PilY1.1 incorporation into the T4aPM.

TfcP Is a Noncanonical Cytochrome *C* with a Low Redox Potential and Heme Binding Is Important for TfcP Stability In Vivo. We overexpressed and purified MalE-TfcP from *Escherichia coli* to assess TfcP's heme-binding and redox characteristics. In size exclusion chromatography (SEC), MalE-TfcP eluted in a symmetric peak as a protein with a size of ∼62 kDa supporting the idea that it is monomeric and adopts a stable conformation (*SI Appendix*, Fig. S5 *A* and *B*). MalE-TfcP exhibited a distinct red color, indicating that it binds heme (*SI Appendix*, Fig. S5*C*). Oxidized MalE-TfcP had strong peroxidase activity (*SI Appendix*, Fig. S5*C*) in agreement with heme-containing proteins having intrinsic peroxidase activity (41). Importantly, peroxidase activity was inhibited when MalE-TfcP was reduced by dithiothreitol (DTT), supporting this activity as resulting from oxidized heme bound to MalE-TfcP (42).

To assess the heme-binding properties of TfcP, we used UV-visible (UV-Vis) spectroscopy. MalE-TfcP has a cytochrome *c*-like spectrum with a strong Soret peak in the oxidized form and

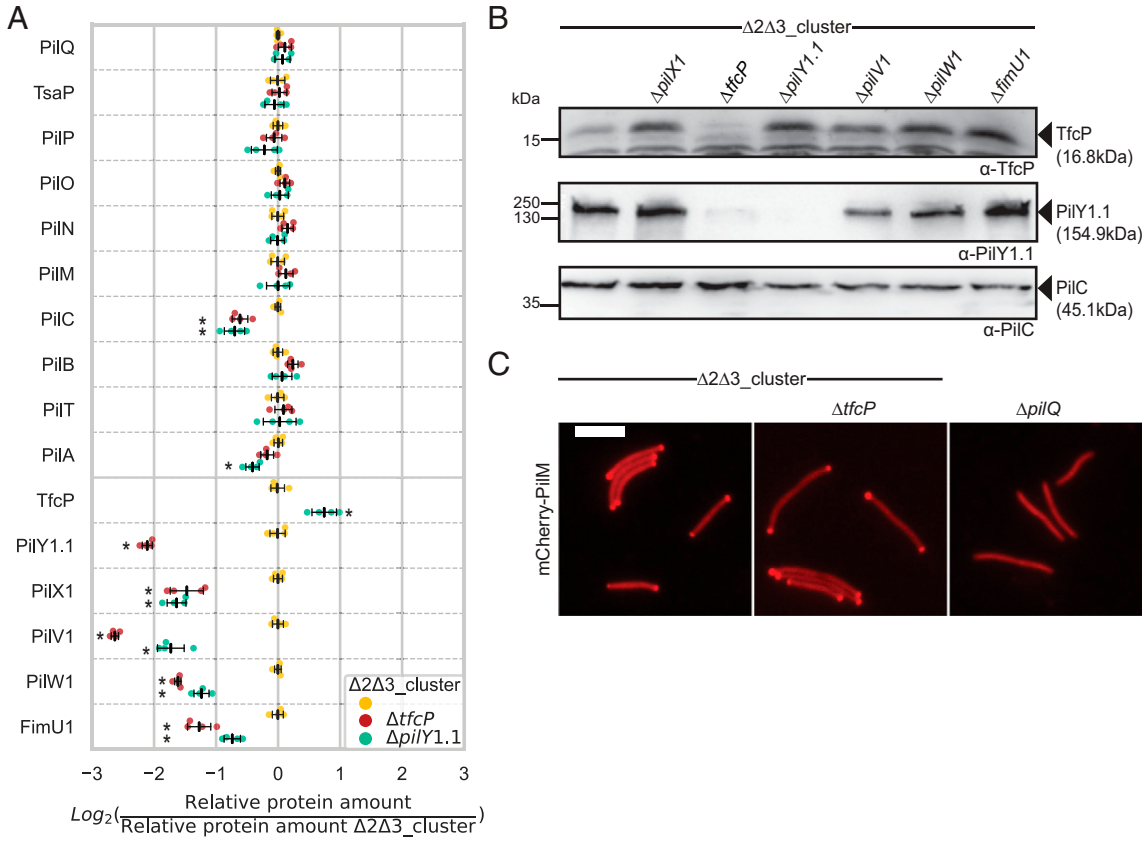

Fig. 3. TfcP is important for stability of PilY1.1 and minor pilins of cluster_1. (*A*) Accumulation of proteins of the T4aPM and cluster_1. Cells were grown in 1.0% CTT suspension culture. Relative protein amounts were determined using targeted proteomics with one to five heavy-labeled reference peptides for each protein spiked into the trypsin-digested cell lysates (*SI Appendix, SI Materials and Methods*). To calculate relative protein amounts, each light-to-heavy intensity ratio of the endogenous (light) and reference (heavy) peptide was calculated. Individual data points represent the mean of the $\log_2$ ratios of the relative amount of all peptides of one protein in one biological replicate to the mean relative amount of the same peptide in the $WT_{\Delta2\Delta3}$ strain. Center marker and error bars in black: Mean and SD from four biological replicates. Statistical analyses were performed by comparing $WT_{\Delta2\Delta3}$ to the mutants using Welch's test, $^*P < 0.01$. (*B*) Immunoblot analysis of TfcP and PilY1.1 accumulation. Cells were grown in 1.0% CTT suspension culture. Total cell extracts from the same number of cells were separated by SDS-PAGE and analyzed by immunoblotting with the indicated antibodies. PilC was used as loading control. (*C*) Localization of mCherry-PilM. Strains were grown in 1.0% CTT suspension culture, placed on 1.0% agarose supplemented with Tris/phosphate/magnesium (TPM) buffer, and immediately imaged by fluorescence microscopy. (Scale bar, 5 μm.)

after reduction with sodium-dithionite (Fig. 5*A*). In the spectrum of reduced TfcP, the α- and β-peaks become visible in the 550-nm region. This fits well to spectra of canonical cytochromes *c*. Interestingly, we did not observe a red shift of the Soret peak from the oxidized to the reduced spectrum. For canonical cytochromes *c* with His/His or His/Met coordination a 10-nm bathochromic shift is typically observed, while a semisynthetic cytochrome *c* with His/Cys coordination of the heme iron did not exhibit this shift (35, 43, 44), suggesting that Cys^{91} (Fig. 1 *C* and *D*) is the second axial ligand in TfcP and responsible for the lack of the red shift. This is also supported by the presence of a peak at 360 nm in the oxidized spectrum, which has been reported for His/Cys ligation (45). The presence of cysteine-to-Fe^{3+} charge transfer bands at ∼630 nm and ∼730 nm in the oxidized form, which disappear upon dithionite reduction (Fig. 5*A*, *Inset*), are also in full agreement with spectral properties of His/Cys coordinated *c*-type cytochromes (35). In control experiments, untagged TfcP also eluted from SEC as a monomeric protein (*SI Appendix*, Fig. S5 *D* and *E*) and was spectroscopically similar to MalE-TfcP (*SI Appendix*, Fig. S5 *F* and *G*). Therefore, to further support the special spectral properties of TfcP being due to Cys^{91}, we purified MalE-$TfcP^{C91M}$ (*SI Appendix*, Fig. S5*A*). In this variant, a red shift was observed upon reduction of the protein (Fig. 5*B*). In addition, the 360-nm peak was not detected in the oxidized form. We conclude that Cys^{91} is the second axial ligand of the heme iron in TfcP and that TfcP is a noncanonical cytochrome *c*.

We used electron paramagnetic resonance (EPR) spectroscopy to investigate the environment of the heme center. We obtained *g* values of 2.51, 2.26, and 1.88 (Fig. 5*C*) that fit well to the *g* values observed for multiple heme-containing proteins with a cysteine thiolate–ligated heme iron (46). Cytochromes *c* with a distal Cys were reported to have a very low midpoint potential in the range of −350 mV, while canonical cytochromes *c* have a potential of approximately +250 mV (35, 43, 44, 47). To determine whether TfcP has a similarly low redox potential, we used UV-Vis and EPR-monitored redox titrations (Fig. 5 *D* and *E*). For the UV-Vis redox titration, MalE-TfcP was incubated with a redox-mediator mixture. Spectra and potentials were recorded in 5-min intervals after addition of sodium-dithionite. After plotting the absorbance change at 550 nm versus the potential and fitting to the Nernst equation, the midpoint potential was determined as $E_m = -304 \pm 8$ mV, where 8 mV represent the intrinsic fitting error in one experiment. In the EPR-monitored redox titration, we followed the change of $g = 2.26$ EPR signal in frozen samples obtained by sequential reduction with sodium-dithionite in the presence of mediators and found a midpoint potential of $E_m = -320 \pm 15$ mV, where

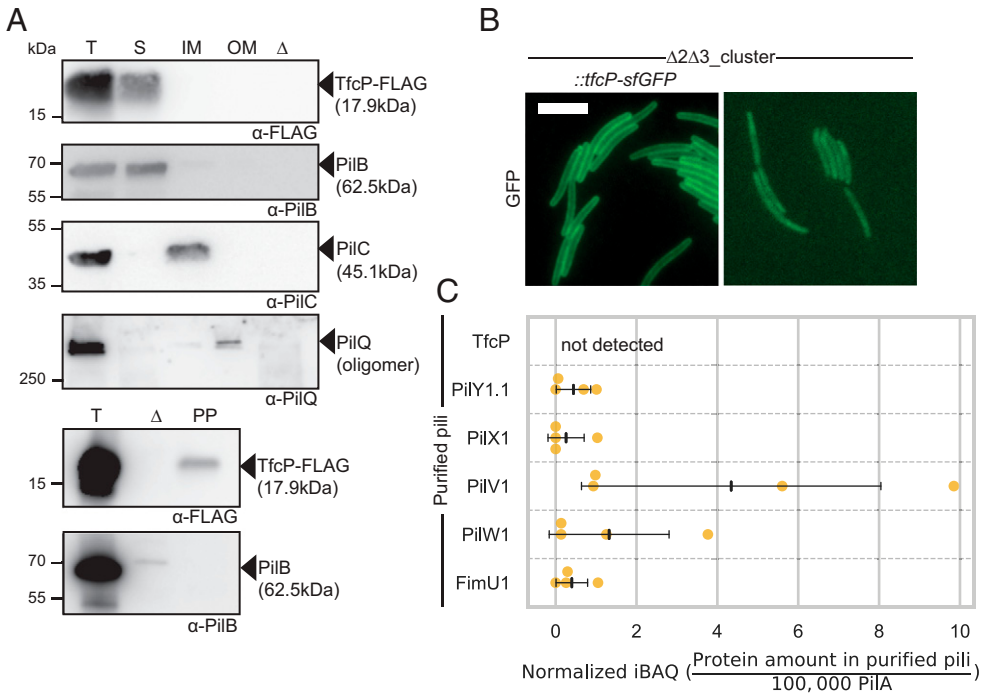

Fig. 4. TfcP is a periplasmic protein. (*A*) Subcellular localization of TfcP-FLAG. Cells were grown in 1.0% CTT suspension culture and fractionated into fractions enriched for soluble proteins (S), IM proteins, and OM proteins (four *Upper* panels) or the periplasmic fraction (PP) (two *Lower* panels). T indicates total cell extract. In the lanes marked Δ, total cell extract of the Δ*pilBTCMNOPQ* mutant was used as negative control. Protein from the same number of cells was loaded per lane and analyzed by immunoblotting. PilB, PilC, and PilQ serve as controls for the fractionation and localize to the cytoplasm, IM and OM, respectively (12, 38). For PilQ, only the heat- and detergent-resistant oligomeric form is shown (39). (*B*) Determination of TfcP-sfGFP localization. Cells were grown in 1.0% CTT suspension culture, and analyzed as in Fig. 3*C*. $WT_{\Delta2\Delta3}$ autofluorescence is shown as negative control. (Scale bar, 5 μm.) (*C*) Label-free quantification (LFQ) of cluster_1 proteins in purified pili. Pili were isolated from cells grown on 1.5% agar supplemented with 1.0% CTT. Normalized iBAQ (intensity based absolute quantification) values (*SI Appendix, SI Materials and Methods*) were determined in four biological replicates for $WT_{\Delta2\Delta3}$Δ*pilT* and the negative control $WT_{\Delta2\Delta3}$Δ*pilT*Δ*pilB*. iBAQ values of $WT_{\Delta2\Delta3}$Δ*pilT* were background corrected by subtraction of the mean iBAQ value of the four replicates of the negative control and rescaled to the iBAQ value of 100,000 PilA molecules in the same sample. Center marker and error bars: Mean and SD.

15 mV represents the intrinsic fitting error in one experiment. Overall, both experiments support the idea that TfcP has a very low redox potential. The slight difference between the two experiments is likely due to pH changes, which occur during freezing. The low redox potential (approximately −312 mV) indicates that TfcP is not likely to be part of a respiratory chain in *M. xanthus* (*Discussion*). Supporting this notion, $WT_{\Delta2\Delta3}$ and $WT_{\Delta2\Delta3}$Δ*tfcP* had similar growth rates (*SI Appendix*, Fig. S6*A*).

To clarify whether the heme-binding characteristics of TfcP are important in vivo, we substituted the two Cys residues to Ala in the C^{31}xxCH motif and Cys^{91} to His or Met (Fig. 1 *C* and *D*). The variants were synthesized ectopically as FLAG-tagged proteins in the Δ*tfcP* mutant from the strong *pilA* promoter. The three mutant variants accumulated at much-reduced levels compared to TfcP and TfcP-FLAG expressed from the native site, and supported neither PilY1.1 accumulation nor motility (*SI Appendix*, Fig. S6 *B* and *C*). We conclude that heme binding and distal coordination of the heme iron are important for TfcP stability.

A FLAG-tagged $TfcP^{\Delta118–153}$ variant lacking the C-terminal α-helical extension also accumulated at reduced levels and supported neither PilY1.1 accumulation nor motility (*SI Appendix*, Fig. S6 *B* and *C*), providing experimental support for the importance of this extension for protein stability.

Added Calcium Restores T4aP Formation in the Absence of TfcP. Several PilY1 proteins have been shown to bind calcium using an EF-hand–like motif in the C-terminal domain, and calcium binding is important for function (27, 48, 49). PilY1.1 and PilY1.2 contain the consensus EF-hand–like calcium binding Dx[DN]xDGxxD motif in the C-terminal PilY1 domain, while PilY1.3 has two calcium binding motifs in the N-terminal domain (Fig. 6*A*). In a homology model of the C-terminal domain of PilY1.1, the D^{1165}xDxDNxxD^{1173} motif is located in a surface exposed loop between two β-strands as described for the *P. aeruginosa* PilY1 domain (27) (Fig. 6*B*).

To address the effect of calcium on T4aPdM, we considered that the previous experiments were performed either in 1.0% CTT (targeted proteome analyses and qRT-PCR), which has a calcium concentration of ∼30 μM according to the manufacturer, or on 0.5% agar supplemented with 0.5% CTT (motility assays) or 1.5% agar supplemented with 1.0% CTT (T4aP purification). The estimated calcium concentration of 0.5% agar is ∼0.15 mM (50). To assess the effect of added $CaCl_2$ on T4aPdM, we used the $WT_{\Delta2\Delta3}$Δ*aglQ* strain, which lacks the AglQ motor for gliding (51, 52). In the presence of ≥0.25 mM added $CaCl_2$, $WT_{\Delta2\Delta3}$Δ*aglQ* exhibited a dramatic change of motility pattern from expansion in flares to a radial film-like expansion (Fig. 6*C*). Intriguingly, the $WT_{\Delta2\Delta3}$Δ*aglQ*Δ*tfcP* mutant also responded to external calcium, and at added $CaCl_2$ concentrations ≥0.5 mM, this mutant regained T4aPdM and at 1.0 mM displayed a motility pattern similar to that of the parent strain. By contrast, added $CaCl_2$ did not restore T4aPdM in the $WT_{\Delta2\Delta3}$Δ*pilY1.1* mutant even at 10 mM (Fig. 6*C* and *SI Appendix*, Fig. S7 *A* and *B*). Likewise, 10 mM $CaCl_2$ did not restore T4aPdM in the Δ*pilX1*, Δ*pilV1*, Δ*pilW1*, and Δ*pilA* mutants while the Δ*fimU1* mutant displayed the same radial motility pattern as the parent strain (*SI Appendix*, Fig. S7*A*).

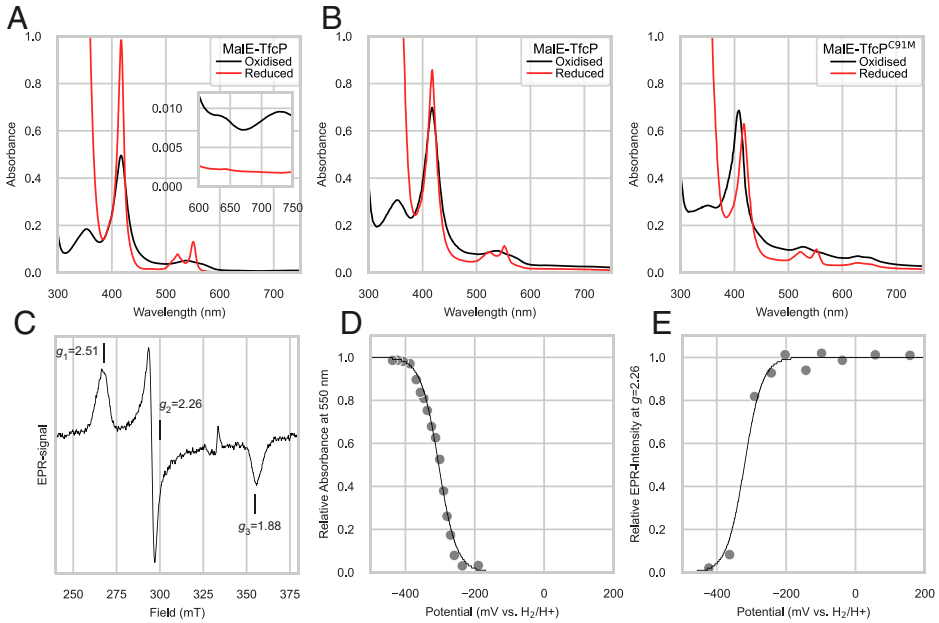

Fig. 5. TfcP is a redox active, heme-binding protein. (*A*) UV-Vis spectra of purified MalE-TfcP in the oxidized and reduced (after addition of sodium-dithionite) state. *Inset*, absorbance in the 600- to 750-nm region. Experiment was done using a Shimadzu 1900 spectrophotometer. (*B*) UV-Vis spectra of purified MalE-TfcP variants in the oxidized and reduced state. Experiments were done using a Tecan200Pro plate reader and, therefore, the spectrum of WT TfcP is included again. (*C*) EPR spectrum of MalE-TfcP. Spectra were recorded in the oxidized state at 12 K, 0.32-mW microwave power, 1.5-mT modulation amplitude (9.3523 GHz). (*D*) Redox titration of MalE-TfcP. The 550-nm absorbance at 23 °C is plotted versus the solution potential and fitted to the Nernst equation. (*E*) Redox titration of MalE-TfcP following the EPR intensity at $g = 2.26$ of samples poised at indicated solution redox potentials.

Additional experiments demonstrated that $WT_{\Delta2\Delta3}\Delta aglQ$ responded to added $CaCl_2$ concentrations as low as 0.025 mM while the $WT_{\Delta2\Delta3}\Delta aglQ\Delta tfcP$ only responded at ≥0.5 mM (*SI Appendix*, Fig. S7*B*). In control experiments, neither 5 mM NaCl nor 5 mM $MgCl_2$ restored motility in the $WT_{\Delta2\Delta3}\Delta tfcP$ mutant. A strain containing only cluster_3 responded to $CaCl_2$ with an altered expansion pattern; however, this pattern was only evident at added $CaCl_2$ concentrations ≥0.25 mM (*SI Appendix*, Fig. S7*B*). We conclude that $CaCl_2$ at an added concentration of 1.0 mM restores T4aPdM in the $WT_{\Delta2\Delta3}\Delta tfcP$ strain. From here on, we used an added $CaCl_2$ concentration of 1.0 mM.

Consistent with the effect of $CaCl_2$ on motility, $WT_{\Delta2\Delta3}\Delta tfcP$ formed T4aP in the presence of 1.0 mM $CaCl_2$, while the $WT_{\Delta2\Delta3}\Delta pilY1.1$ mutant did not (Fig. 6*D*). Added $CaCl_2$ also increased the amount of pili in $WT_{\Delta2\Delta3}$. The level of T4aP in the $WT_{\Delta2\Delta3}\Delta tfcP$ mutant was lower than in $WT_{\Delta2\Delta3}$ (Fig. 6*D*). Calcium also increased the amount of total cellular PilA in all strains (Fig. 6*D*). The retraction-deficient strains $WT_{\Delta2\Delta3}\Delta pilT$ and $WT_{\Delta2\Delta3}\Delta tfcP\Delta pilT$ assembled more T4aP in the presence of added $CaCl_2$ than in its absence, supporting the idea that calcium stimulates T4aP formation rather than counteracting retractions (Fig. 6*D*). Thus, 1.0 mM of added $CaCl_2$ can substitute for TfcP function in T4aP formation and T4aPdM.

TfcP Enhances Calcium-Dependent Stabilization of PilY1.1. To understand how a high concentration of calcium compensates for lack of TfcP, we used targeted proteomics. In $WT_{\Delta2\Delta3}$, 1.0 mM of $CaCl_2$ caused a significant increase in PilA abundance and a significant decrease in TfcP abundance, while accumulation of other T4aPM components including the remaining cluster_1 proteins was largely unaffected (Fig. 6*E*). In $WT_{\Delta2\Delta3}\Delta tfcP$, added $CaCl_2$ not only caused a significant increase in PilA abundance but also significantly increased the abundance of most remaining cluster_1 proteins including PilY1.1 (Fig. 6*E*). In $WT_{\Delta2\Delta3}\Delta pilY1.1$, extra $CaCl_2$ also caused increased PilA abundance, but a reduction in TfcP abundance as in the $WT_{\Delta2\Delta3}$ parent strain. PilW1 and FimU1 abundance was unaffected by added $CaCl_2$ in $WT_{\Delta2\Delta3}\Delta pilY1.1$, while PilV1 and PilX1 abundance significantly increased. We conclude that a high concentration of $CaCl_2$ causes increased PilY1.1 accumulation in the absence of TfcP. Extra $CaCl_2$ also caused 1) increased PilA accumulation independently of TfcP and PilY1.1, 2) decreased accumulation of TfcP independently of PilY1.1, and 3) increased accumulation of the minor pilins PilX1 and PilV1 independently of PilY1.1.

Because changes in extracellular calcium can cause altered gene expression (53), we performed qRT-PCR analyses to discriminate whether added $CaCl_2$ affects transcription or protein stability. We observed significant changes in the transcription of all cluster_1 genes as well as of *pilA* in response to added $CaCl_2$ (*SI Appendix*, Fig. S8); however, generally, these changes did not correlate with the altered protein accumulation profiles. For instance, in $WT_{\Delta2\Delta3}$, 1.0 mM added $CaCl_2$ caused increased PilA accumulation but *pilA* transcription was decreased, and decreased *pilY1.1* transcription but PilY1.1 abundance remained unchanged; and, in $WT_{\Delta2\Delta3}\Delta tfcP$, $CaCl_2$ caused decreased *pilY1.1* transcription but PilY1.1 abundance increased. We conclude that added $CaCl_2$ at 1.0 mM can substitute for TfcP in stabilizing PilY1.1.

Label-free quantitative proteomics of purified pili from $WT_{\Delta2\Delta3}\Delta pilT$ and $WT_{\Delta2\Delta3}\Delta pilT\Delta tfcP$ (*SI Appendix*, Fig. S4) revealed a strong increase in the abundance of cluster_1 minor pilins and PilY1.1 relative to PilA in the presence of calcium (Fig. 6*F*), suggesting that calcium also stabilizes minor pilins and PilY1.1 in the tip complex. Of note, TfcP was not detected in purified pili from $WT_{\Delta2\Delta3}\Delta pilT$ grown in the presence of added calcium (Fig. 6*F*).

To determine whether the effect of calcium on PilY1.1 stability depends on its binding to PilY1.1, we attempted to purify full-length PilY1.1 or its C-terminal domain but were unsuccessful, thus, precluding in vitro analyses of PilY1.1. Therefore, to assess calcium binding by PilY1.1 in vivo, we introduced the

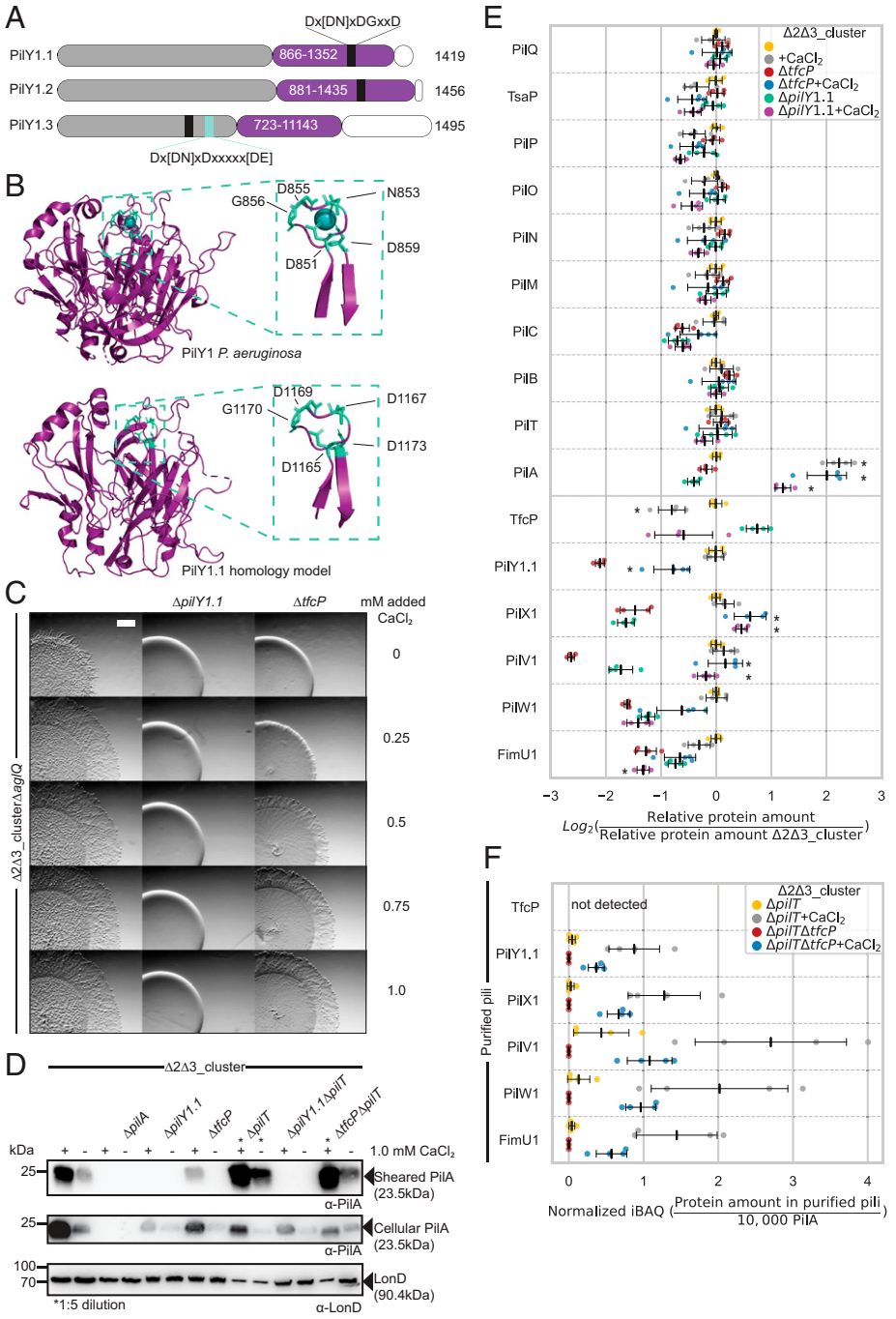

Fig. 6. Added $CaCl_2$ compensates for lack of TfcP. (*A*) Domain architecture of PilY1 proteins of *M. xanthus*. Purple, C-terminal PilY1 domain; gray, N-terminal domain; white; C-terminal sequences. EF-hand–like calcium binding motif is in black together with the consensus sequence; light blue box indicates second calcium binding motif in PilY1.3 together with the consensus sequence (25). (*B*) Comparison of PilY1 structure of *P. aeruginosa* (PDB 3HX6) (27) and a homology model of PilY1.1. *Inset*, zoom of calcium binding motif. (*C*) Assay for T4aPdM. Cells were grown in 1.0% CTT suspension culture and plated on 0.5% agar supplemented with 0.5% CTT and the indicated final concentrations of added $CaCl_2$, and imaged after 24 h. Note that the flares formed by $WT_{\Delta2\Delta3}$Δ*aglQ* are shorter than those formed by $WT_{\Delta2\Delta3}$ due to the Δ*aglQ* mutation. (Scale bar, 1 mm.) (*D*) Shearing assay for T4aP formation. T4aP sheared off from ∼15 mg cells grown on 1.5% agar supplemented with 1.0% CTT and 1.0 mM $CaCl_2$ as indicated, and analyzed as in Fig. 2*B*. (*E*) Accumulation of proteins of the T4aPM. Cells were grown in 1.0% CTT suspension culture without or with 1.0 mM added calcium as indicated. Proteins were quantified as in Fig. 3*A*. Data for samples without added $CaCl_2$ are the same as in Fig. 3*A* and included for comparison. Statistical analyses were done by comparing cells grown in the presence versus the absence of calcium using Welch's test, $^*P < 0.01$. (*F*) LFQ proteomics of cluster_1 proteins in purified pili. Pili were isolated as in Fig. 4*C* after growth without or with added $CaCl_2$ as indicated. Normalized iBAQ values were calculated as in Fig. 4*C* and background corrected by subtraction of the mean iBAQ value of the four replicates of the relevant negative control, and rescaled to 10,000 PilA molecules in the same sample. Data for $WT_{\Delta2\Delta3}$ without added $CaCl_2$ are the same as in Fig. 4*C* and included for comparison.

Asp^{1173} to Ala substitution in the EF-hand–like calcium binding D^{1165}xDxDNxxD^{1173} motif in PilY1.1 (Fig. 6 *A* and *B*) and expressed the protein from the native site in $WT_{\Delta2\Delta3}$ strains. The homologous substitution in other PilY1 proteins disrupts calcium binding without affecting the overall structure of the C-terminal beta-propeller domain (27, 48, 49).

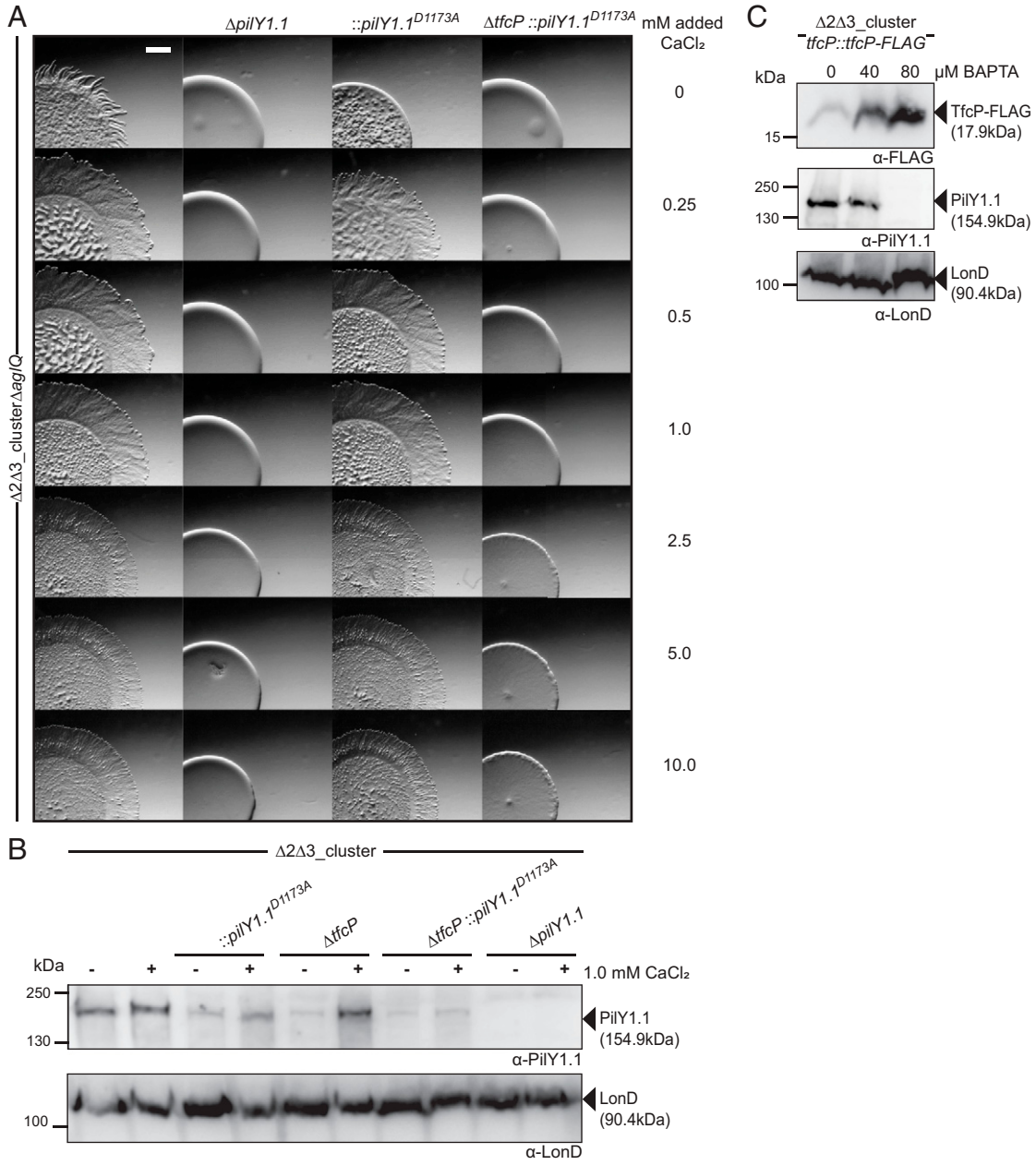

Fig. 7. Calcium binding by PilY1.1 is essential for TfcP function. (*A*) Assay for T4aPdM. Cells were grown in 1.0% CTT suspension culture and plated on 0.5% agar supplemented with 0.5% CTT and imaged after 24 h. The final concentration of added $CaCl_2$ is indicated. (Scale bar, 1 mm.) (*B*) Accumulation of PilY1.1 variants. Cells were grown in 1.0% CTT suspension culture without or with 1.0 mM $CaCl_2$, total cell extract isolated and analyzed by immunoblot as in Fig. 3*B*. (*C*) Accumulation of TfcP-FLAG and PilY1.1 in the presence of BAPTA. Cells were grown in 1.0% CTT in suspension, exposed to indicated concentrations of BAPTA for 16 h, and total cell extract was isolated and analyzed by immunoblot as in Fig. 3*B*.

The *pilY1.1*^{D1173A}*tfcP*$^{+}$ mutant was strongly reduced in T4aPdM in the absence of added $CaCl_2$ (Fig. 7*A*); however, this strain regained T4aPdM and was indistinguishable from the parent strain at ≥0.25 mM added $CaCl_2$. By contrast, the *pilY1.1*^{D1173A}Δ*tfcP* strain was nonmotile even at 10 mM of added $CaCl_2$. These observations support the notion that calcium binding is important for PilY1.1 function and that PilY1.1^{D1173A} is fully functional at elevated calcium concentrations but only if TfcP is present.

Consistent with the observations for T4aPdM, PilY1.1^{D1173A} accumulation was reduced in the *pilY1.1*^{D1173A}*tfcP*$^{+}$ mutant in the absence of added $CaCl_2$, and 1.0 of mM $CaCl_2$ at least partially restored its accumulation (Fig. 7*B*). By contrast, in the *pilY1.1*^{D1173A}Δ*tfcP* strain, PilY1.1^{D1173A} was detected at very low levels in the absence as well as in the presence of added $CaCl_2$. Thus, PilY1.1^{D1173A} depends on TfcP for stability and responds to added calcium only in the presence of TfcP. By comparison, PilY1.1^{WT} is fully functional at ≥1.0 mM added $CaCl_2$ in the absence of TfcP (Fig. 6*C*).

To determine whether TfcP can stabilize PilY1.1^{WT} independently of calcium, we analyzed PilY1.1 accumulation in the presence of the highly specific calcium chelator BAPTA (1,2-bis(*o*-aminophenoxy)ethane-N,N,N′,N′-tetraacetic acid). In WT$_{Δ2Δ3}$ expressing TfcP-FLAG from the endogenous site and grown in 1.0% CTT, PilY1.1 was detected in the presence of 40 μM but not in the presence of 80 μM BAPTA, while TfcP

was detected under all conditions and increased upon BAPTA addition (Fig. 7*C*). These observations strongly support the idea that TfcP can only stabilize PilY1.1 in the presence of calcium. Because $CaCl_2$ can stabilize PilY1.1 in the absence of TfcP, these observations suggest that the primary function of TfcP is to stimulate calcium binding by PilY1.1 at low-calcium concentrations.

Finally, using a fluorescence-based assay, we observed that purified untagged TfcP did not detectably bind calcium (*SI Appendix*, Fig. S9). Consistently, TfcP does not contain a conserved calcium binding motif.

Discussion

Here, we identify TfcP, a noncanonical cytochrome *c*, as important for cluster_1-dependent T4aP formation in *M. xanthus* at low-calcium concentrations. We demonstrate that TfcP stabilizes PilY1.1 at low-calcium concentrations. PilY1.1, in turn, stabilizes the four minor pilins of cluster_1 in that way enabling the formation of the cluster_1-based priming complex in the T4aPM and, thus, T4aP formation. Bacteria in their natural habitats experience large fluctuations in environmental conditions and depend on adaptive strategies to endure such changes. TfcP expands the range of calcium concentrations under which cluster_1 encoded minor pilins and PilY1.1 can support T4aPdM, thereby increasing fitness of *M. xanthus* under changing environmental conditions and enabling colonization of habitats with low-calcium concentrations (Fig. 8).

Several lines of evidence support the idea that the effect of TfcP on PilY1.1 stability is calcium dependent. First, under standard conditions, *M. xanthus* is exposed to ∼30 μM calcium in CTT suspension culture and ∼0.15 mM calcium on 0.5% agar plates for motility assays. Under these conditions, TfcP is important for PilY1.1 stability. However, at concentrations ≥1 mM of added $CaCl_2$, calcium alone is sufficient to stabilize PilY1.1 independently of TfcP. Second, in the complete absence of calcium, i.e., after addition of the calcium-specific chelator BAPTA, TfcP does not stabilize PilY1.1 while TfcP still accumulates. Third, the PilY1.1^{D1173A} variant, which is predicted to bind calcium with reduced affinity, depends on TfcP for stability at 1.0 mM added $CaCl_2$, and even at 10 mM $CaCl_2$, this protein is nonfunctional in the absence of TfcP. Thus, TfcP and calcium both function to stabilize PilY1.1. However, while high-calcium concentrations alone can stabilize PilY1.1, TfcP cannot stabilize PilY1.1 in the absence of calcium. Altogether, these findings support a model whereby calcium binding by PilY1.1 is the primary determinant for its stability and in which TfcP stabilizes PilY1.1 at low-calcium concentrations by stimulating calcium binding by PilY1.1. The functional outcome of this stimulation is that PilY1.1 accumulates at low-calcium concentrations and is able to support cluster_1-dependent T4aP formation and T4aPdM. Many myxobacteria, including *M. xanthus*, are found in terrestrial habitats in which calcium concentrations are described to vary from 0.1 to 1.0 mM at root–soil interfaces, 3.4 to 14 mM in some soils, and as low as 10 to 150 μM in other soils (54). Because the OM has been reported to be permeable to calcium, the environmental calcium concentration directly affects the periplasmic calcium concentration (55). We suggest that TfcP is key to enabling PilY1.1-dependent T4aP formation and T4aPdM in the lower range of environmental calcium concentrations. Interestingly, *Myxococcus stipitatus* and *Corallococcus coralloides* have only one gene cluster for minor pilins and PilY1, and this cluster encodes a TfcP ortholog (Fig. 1*C* and *SI Appendix*, Fig. S1*A*) emphasizing the importance of TfcP in T4aPdM in myxobacteria.

TfcP is a soluble, periplasmic protein and contains a noncanonical cytochrome *c* domain in which the second axial heme ligand is a Cys residue rather than the more common His and

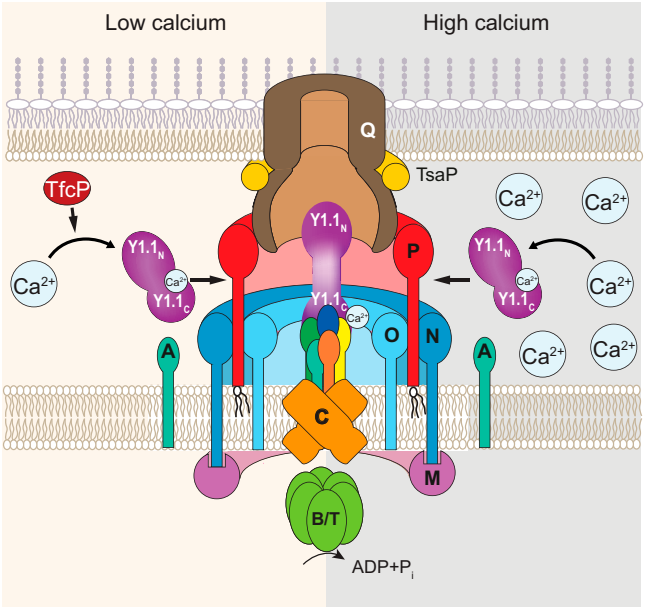

Fig. 8. Model of TfcP function at low- and high-calcium concentrations. For simplicity, PilB and PilT are not indicated separately. $Y1.1_N$ and $Y1.1_C$ indicate the N- and C-terminal domains of PilY1, respectively. The color code for the four minor pilins is as in Fig. 1*B*.

Met residues in canonical cytochromes *c*. Accordingly, TfcP has a very low redox potential of −304 to −320 mV based on two methods. Moreover, TfcP variants unable to bind heme or with altered heme-binding properties are unstable in vivo. *M. xanthus* is strictly aerobic and the genome encodes complex I through IV of the electron transport chain (56). Thus, the low redox potential of TfcP supports the idea that it is not part of the respiratory chain, which starts with a potential of −320 mV for the redox pair NAD/NADH (57). Some cytochromes *c* are involved in electron transport across the OM to external electron acceptors; however, these proteins are canonical cytochromes *c* (58), suggesting that TfcP also does not engage in this type of electron transport. Some *c*-type cytochromes with His/Cys ligation, e.g., the triheme DsrJ of *Allochromatium vinosum*, are involved in dissimilatory sulfur metabolism in which sulfate is used as the terminal electron acceptor (59), and some have been suggested to have a role in signaling (35, 60). Because *M. xanthus* does not respire on sulfate, it is unlikely that TfcP would be involved in dissimilatory sulfur metabolism. While we cannot rule out a function of TfcP in signaling, our data support a scenario in which TfcP is a repurposed cytochrome *c* that is no longer involved in electron transport, and in which the covalently bound heme serves a structural function to stabilize TfcP. This "inert" cytochrome *c* then stimulates calcium binding by PilY1.1 at low-calcium concentrations. TfcP also differs from canonical cytochromes *c* by having a highly charged C-terminal extension. This extension is important for TfcP stability; however, its precise function remains to be uncovered.

An Asp to Ala substitution in the calcium binding motif in the PilY1 proteins of *P. aeruginosa*, *Kingella kingae*, and *Neisseria gonorrhoeae* abolishes calcium binding and renders the proteins nonfunctional while still folding correctly and accumulating (27, 48, 49). The corresponding PilY1.1^{D1173A} variant was also functionally impaired, supporting the idea that PilY1.1 binds calcium as described for other PilY1 proteins. Compared to PilY1.1^{WT}, PilY1.1^{D1173A} had an increased dependency on TfcP and calcium for stability, indicating that PilY1.1 depends more strongly on calcium binding for stability than other PilY1

proteins. More importantly, PilY1.1^{D1173A} was still functional at high-calcium concentrations but only in the presence of TfcP. Thus, TfcP can rescue the PilY1.1^{D1173A} calcium-binding mutant, emphasizing the role of TfcP in stimulating calcium binding by PilY1.1.

The observation that PilY1.1 is unstable in the absence of TfcP at low-calcium concentrations suggest that the two proteins interact directly. However, such an interaction remains to be shown and will be addressed in future experiments. Nevertheless, some inferences can be made. PilY1.1 and the four minor pilins of cluster_1 were detected in purified pili. By contrast, TfcP was not detected in purified pili. We previously showed that sfGFP-tagged PilY1.3 and the sfGFP-tagged minor pilin PilW3 of cluster_3 localize polarly, are incorporated into the T4aPM but do not support pilus extension, likely because the sfGFP-tag jams the machine by precluding passage of PilY1.3-sfGFP and PilW3-sfGFP through the secretin channel in the OM (10). By contrast, TfcP-sfGFP was fully active and did not localize polarly. These observations strongly support TfcP as neither part of the pilus nor the T4aPM. They also strengthen the hypothesis that the suggested direct interaction between PilY1.1 and TfcP is transient and only occurs in the periplasm before PilY1.1 incorporation into the T4aPM (Fig. 8). The observations that added calcium stabilizes PilY1.1 in the absence of TfcP and that TfcP does not bind calcium supports TfcP as not acting as a metallochaperone to deliver calcium to PilY1.1. We, therefore, suggest that TfcP interacts transiently with calcium-free PilY1.1 prior to PilY1.1 incorporation into the T4aPM. We suggest that TfcP either supports correct PilY1.1 folding or induces conformational changes in PilY1.1, thereby enabling efficient calcium binding by PilY1.1. Subsequently, calcium-bound PilY1.1, but not TfcP, is incorporated into the priming complex of the T4aPM to support T4aP formation (Fig. 8). This mechanism of protein stabilization is reminiscent of that of periplasmic chaperones, which in an ATP-independent manner transiently interact with their periplasmic clients to enable folding (61), except that the suggested TfcP/PilY1.1 interaction promotes calcium binding by PilY1.1, which then stabilizes PilY1.1. Altogether, these findings also provide evidence for a previously undescribed function of a cytochrome *c* in protein folding and/or stabilization.

In addition to the conserved proteins of the T4aPM, T4aP extension in several species depends on accessory factors that are much less conserved. For instance, the c-di-GMP binding protein FimX in *P. aeruginosa* and SgmX in *M. xanthus* stimulate T4aP extension (62–64). TfcP adds to the list of such regulators and also acts at the level of extension; however, in contrast to these cytoplasmic regulators, TfcP acts in the periplasm.

In the presence of added $CaCl_2$ at 1.0 mM, more T4aP are formed and the ratio between minor pilins and PilY1.1 to PilA is increased. These observations support calcium as not only helping to stabilize PilY1.1, but may also stabilize the pilus, including the minor pilin/PilY1.1 tip complex in extracellular space. In this context, it is interesting to note that calcium binding has been reported to stabilize the interactions between major pseudopilin subunits in the pseudopilus of the type II secretion system of *Klebsiella oxytoca* (65). In future experiments, this effect of calcium will be addressed.

Materials and Methods

Bacterial Strains and Growth Media. All *M. xanthus* strains are derivatives of DK1622 (66) and listed in *SI Appendix*, Table 1. Plasmids are listed in *SI Appendix*, Table 2. In-frame deletion mutants were generated using double homologous recombination using a *galK*-containing plasmid (67). Genes were ectopically expressed from the *pilA* promoter in plasmids integrated by site-specific recombination at the *attB* site. All plasmids were verified by sequencing. All strains were confirmed by PCR. Oligonucleotides are listed in *SI Appendix*, Table 3. *M. xanthus* suspension cultures were grown in 1% CTT broth (1% Bacto Casitone [Gibco], 10 mM Tris·HCl pH 8.0, 1 mM KPO_4 pH 7.6, 8 mM $MgSO_4$) or on 1% CTT 1.5% agar plates. When required, media were supplemented with kanamycin (50 $\mu g\ mL^{-1}$) or oxytetracyclin (10 $\mu g\ mL^{-1}$).

Data Availability. All study data are included in the article and/or supporting information.

ACKNOWLEDGMENTS. We thank Steffi Lindow for excellent help with plasmid and strain constructions, Bazlur Rashid for help with preparation of the EPR samples, and Seigo Shima as well as Rolf Thauer for many helpful discussions. This work was supported by the NIH Grant GM85024 (to E.H.) and the Max Planck Society (to L.S.-A.).

1. R. M. Harshey, Bacterial motility on a surface: Many ways to a common goal. *Annu. Rev. Microbiol.* **57**, 249–273 (2003).
2. L. L. Burrows, *Pseudomonas aeruginosa* twitching motility: Type IV pili in action. *Annu. Rev. Microbiol.* **66**, 493–520 (2012).
3. K. J. Evans, C. Lambert, R. E. Sockett, Predation by *Bdellovibrio bacteriovorus* HD100 requires type IV pili. *J. Bacteriol.* **189**, 4850–4859 (2007).
4. L. Craig, K. T. Forest, B. Maier, Type IV pili: Dynamics, biophysics and functional consequences. *Nat. Rev. Microbiol.* **17**, 429–440 (2019).
5. A. J. Merz, M. So, M. P. Sheetz, Pilus retraction powers bacterial twitching motility. *Nature* **407**, 98–102 (2000).
6. J. M. Skerker, H. C. Berg, Direct observation of extension and retraction of type IV pili. *Proc. Natl. Acad. Sci. U.S.A.* **98**, 6901–6904 (2001).
7. M. Clausen, V. Jakovljevic, L. Søgaard-Andersen, B. Maier, High-force generation is a conserved property of type IV pilus systems. *J. Bacteriol.* **191**, 4633–4638 (2009).
8. Y. W. Chang *et al.*, Architecture of the type IVa pilus machine. *Science* **351**, aad2001 (2016).
9. V. A. Gold, R. Salzer, B. Averhoff, W. Kühlbrandt, Structure of a type IV pilus machinery in the open and closed state. *eLife* **4**, e07380 (2015).
10. A. Treuner-Lange *et al.*, PilY1 and minor pilins form a complex priming the type IVa pilus in *Myxococcus xanthus*. *Nat. Commun.* **11**, 5054 (2020).
11. M. McCallum, S. Tammam, A. Khan, L. L. Burrows, P. L. Howell, The molecular mechanism of the type IVa pilus motors. *Nat. Commun.* **8**, 15091 (2017).
12. V. Jakovljevic, S. Leonardy, M. Hoppert, L. Søgaard-Andersen, PilB and PilT are ATPases acting antagonistically in type IV pilus function in *Myxococcus xanthus*. *J. Bacteriol.* **190**, 2411–2421 (2008).
13. J. M. Mancl, W. P. Black, H. Robinson, Z. Yang, F. D. Schubot, Crystal structure of a type IV pilus assembly ATPase: Insights into the molecular mechanism of PilB from *Thermus thermophilus*. *Structure* **24**, 1886–1897 (2016).
14. Y. Nguyen *et al.*, *Pseudomonas aeruginosa* minor pilins prime type IVa pilus assembly and promote surface display of the PilY1 adhesin. *J. Biol. Chem.* **290**, 601–611 (2015).
15. A. M. Misic, K. A. Satyshur, K. T. Forest, *P. aeruginosa* PilT structures with and without nucleotide reveal a dynamic type IV pilus retraction motor. *J. Mol. Biol.* **400**, 1011–1021 (2010).
16. T. Rudel, I. Scheurerpflug, T. F. Meyer, *Neisseria* PilC protein identified as type-4 pilus tip-located adhesin. *Nature* **373**, 357–359 (1995).
17. M. D. Johnson *et al.*, *Pseudomonas aeruginosa* PilY1 binds integrin in an RGD- and calcium-dependent manner. *PLoS One* **6**, e29629 (2011).
18. V. A. Marko, S. L. N. Kilmury, L. T. MacNeil, L. L. Burrows, *Pseudomonas aeruginosa* type IV minor pilins and PilY1 regulate virulence by modulating FimS-AlgR activity. *PLoS Pathog.* **14**, e1007074 (2018).
19. S. L. Kuchma *et al.*, Cyclic-di-GMP-mediated repression of swarming motility by *Pseudomonas aeruginosa*: The *pilY1* gene and its impact on surface-associated behaviors. *J. Bacteriol.* **192**, 2950–2964 (2010).
20. V. Pelicic, Type IV pili: e pluribus unum? *Mol. Microbiol.* **68**, 827–837 (2008).
21. R. Zöllner, T. Cronenberg, B. Maier, Motor properties of PilT-independent type 4 pilus retraction in *Gonococci*. *J. Bacteriol.* **201**, e00778-18 (2019).
22. T. Feng *et al.*, Interspecies and intraspecies signals synergistically regulate *Lysobacter enzymogenes* twitching motility. *Appl. Environ. Microbiol.* **85**, e01742-19 (2019).
23. L. F. Cruz, J. K. Parker, P. A. Cobine, L. De La Fuente, Calcium-enhanced twitching motility in *Xylella fastidiosa* is linked to a single PilY1 homolog. *Appl. Environ. Microbiol.* **80**, 7176–7185 (2014).
24. C. E. A. Engel, D. Vorländer, R. Biedendieck, R. Krull, K. Dohnt, Quantification of microaerobic growth of *Geobacter sulfurreducens*. *PLoS One* **15**, e0215341 (2020).
25. J. K. Parker, L. F. Cruz, M. R. Evans, L. De La Fuente, Presence of calcium-binding motifs in PilY1 homologs correlates with Ca-mediated twitching motility and evolutionary history across diverse bacteria. *FEMS Microbiol. Lett.* **362**, 1–9 (2015).
26. C. L. Giltner, Y. Nguyen, L. L. Burrows, Type IV pilin proteins: Versatile molecular modules. *Microbiol. Mol. Biol. Rev.* **76**, 740–772 (2012).
27. J. Orans *et al.*, Crystal structure analysis reveals *Pseudomonas* PilY1 as an essential calcium-dependent regulator of bacterial surface motility. *Proc. Natl. Acad. Sci. U.S.A.* **107**, 1065–1070 (2010).

28. J. Hoppe *et al.*, PilY1 promotes *Legionella pneumophila* infection of human lung tissue explants and contributes to bacterial adhesion, host cell invasion, and twitching motility. *Front. Cell. Infect. Microbiol.* **7**, 63 (2017).
29. Y. Zhang, A. Ducret, J. Shaevitz, T. Mignot, From individual cell motility to collective behaviors: Insights from a prokaryote, *Myxococcus xanthus. FEMS Microbiol. Rev.* **36**, 149–164 (2012).
30. D. Schumacher, L. Søgaard-Andersen, Regulation of cell polarity in motility and cell division in *Myxococcus xanthus. Annu. Rev. Microbiol.* **71**, 61–78 (2017).
31. S. Zaidi, M. I. Hassan, A. Islam, F. Ahmad, The role of key residues in structure, function, and stability of cytochrome-*c. Cell. Mol. Life Sci.* **71**, 229–255 (2014).
32. L. Thöny-Meyer, Cytochrome c maturation: A complex pathway for a simple task? *Biochem. Soc. Trans.* **30**, 633–638 (2002).
33. R. P. Ambler, Sequence variability in bacterial cytochromes c. *Biochim. Biophys. Acta* **1058**, 42–47 (1991).
34. C. Fufezan, J. Zhang, M. R. Gunner, Ligand preference and orientation in *b*- and *c*-type heme-binding proteins. *Proteins* **73**, 690–704 (2008).
35. L. Zuccarello *et al.*, Protonation of the Cysteine axial ligand investigated in His/Cys c-type cytochrome by UV-Vis and Mid- and Far-IR spectroscopy. *J. Phys. Chem. Lett.* **11**, 4198–4205 (2020).
36. I. Bertini, G. Cavallaro, A. Rosato, Cytochrome c: Occurrence and functions. *Chem. Rev.* **106**, 90–115 (2006).
37. Y. Luo *et al.*, A hierarchical cascade of second messengers regulates *Pseudomonas aeruginosa* surface behaviors. *MBio* **6**, e02456-14 (2015).
38. I. Bulyha *et al.*, Regulation of the type IV pili molecular machine by dynamic localization of two motor proteins. *Mol. Microbiol.* **74**, 691–706 (2009).
39. C. Friedrich, I. Bulyha, L. Søgaard-Andersen, Outside-in assembly pathway of the type IV pilus system in *Myxococcus xanthus. J. Bacteriol.* **196**, 378–390 (2014).
40. E. Nudleman, D. Wall, D. Kaiser, Polar assembly of the type IV pilus secretin in *Myxococcus xanthus. Mol. Microbiol.* **60**, 16–29 (2006).
41. Y. Y. Londer, "Expression of recombinant cytochromes c in *E. coli*" in *Heterologous Gene Expression in E. coli: Methods and Protocols*, J. T. C. Evans, M.-Q. Xu, Eds. (Humana Press, 2011), **vol. 705**, pp. 123–150.
42. T. L. Poulos, Heme enzyme structure and function. *Chem. Rev.* **114**, 3919–3962 (2014).
43. A. L. Raphael, H. B. Gray, Axial ligand replacement in horse heart cytochrome *c* by semisynthesis. *Proteins* **6**, 338–340 (1989).
44. A. L. Raphael, H. B. Gray, Semisynthesis of axial-ligand (position 80) mutants of cytochrome *c. J. Am. Chem. Soc.* **113**, 1038–1040 (2002).
45. A. T. Smith *et al.*, Identification of Cys94 as the distal ligand to the Fe(III) heme in the transcriptional regulator RcoM-2 from *Burkholderia xenovorans. J. Biol. Inorg. Chem.* **17**, 1071–1082 (2012).
46. M. R. Cheesman, P. J. Little, B. C. Berks, Novel heme ligation in a *c*-type cytochrome involved in thiosulfate oxidation: EPR and MCD of SoxAX from *Rhodovulum sulfidophilum. Biochemistry* **40**, 10562–10569 (2001).
47. E. J. Reijerse *et al.*, The unusal redox centers of SoxXA, a novel c-type heme-enzyme essential for chemotrophic sulfur-oxidation of *Paracoccus pantotrophus. Biochemistry* **46**, 7804–7810 (2007).
48. Y. Cheng *et al.*, Mutation of the conserved calcium-binding motif in *Neisseria gonorrhoeae* PilC1 impacts adhesion but not piliation. *Infect. Immun.* **81**, 4280–4289 (2013).
49. E. A. Porsch *et al.*, Calcium binding properties of the *Kingella kingae* PilC1 and PilC2 proteins have differential effects on type IV pilus-mediated adherence and twitching motility. *J. Bacteriol.* **195**, 886–895 (2013).
50. J. M. Kuner, D. Kaiser, Fruiting body morphogenesis in submerged cultures of *Myxococcus xanthus. J. Bacteriol.* **151**, 458–461 (1982).
51. M. Sun, M. Wartel, E. Cascales, J. W. Shaevitz, T. Mignot, Motor-driven intracellular transport powers bacterial gliding motility. *Proc. Natl. Acad. Sci. U.S.A.* **108**, 7559–7564 (2011).
52. B. Nan *et al.*, Myxobacteria gliding motility requires cytoskeleton rotation powered by proton motive force. *Proc. Natl. Acad. Sci. U.S.A.* **108**, 2498–2503 (2011).
53. K. Bilecen, F. H. Yildiz, Identification of a calcium-controlled negative regulatory system affecting *Vibrio cholerae* biofilm formation. *Environ. Microbiol.* **11**, 2015–2029 (2009).
54. S. B. McLaughlin, R. Wimmer, Tansley Review No. 104. Calcium physiology and terrestrial ecosystem processes. *New Phytol.* **142**, 373–417 (1999).
55. H. E. Jones, I. B. Holland, A. K. Campbell, Direct measurement of free Ca(2+) shows different regulation of Ca(2+) between the periplasm and the cytosol of *Escherichia coli. Cell Calcium* **32**, 183–192 (2002).
56. B. Goldman, S. Bhat, L. J. Shimkets, Genome evolution and the emergence of fruiting body development in *Myxococcus xanthus. PLoS One* **2**, e1329 (2007).
57. F. Kracke, I. Vassilev, J. O. Krömer, Microbial electron transport and energy conservation—The foundation for optimizing bioelectrochemical systems. *Front. Microbiol.* **6**, 575 (2015).
58. M. J. Edwards, G. F. White, J. N. Butt, D. J. Richardson, T. A. Clarke, The crystal structure of a biological insulated transmembrane molecular wire. *Cell* **181**, 665–673.e10 (2020).
59. F. Grein *et al.*, DsrJ, an essential part of the DsrMKJOP transmembrane complex in the purple sulfur bacterium *Allochromatium vinosum*, is an unusual triheme cytochrome *c. Biochemistry* **49**, 8290–8299 (2010).
60. T. Shimizu, Binding of cysteine thiolate to the Fe(III) heme complex is critical for the function of heme sensor proteins. *J. Inorg. Biochem.* **108**, 171–177 (2012).
61. C. Goemans, K. Denoncin, J. F. Collet, Folding mechanisms of periplasmic proteins. *Biochim. Biophys. Acta* **1843**, 1517–1528 (2014).
62. R. Jain, O. Sliusarenko, B. I. Kazmierczak, Interaction of the cyclic-di-GMP binding protein FimX and the Type 4 pilus assembly ATPase promotes pilus assembly. *PLoS Pathog.* **13**, e1006594 (2017).
63. A. Potapova, L. A. M. Carreira, L. Søgaard-Andersen, The small GTPase MglA together with the TPR domain protein SgmX stimulates type IV pili formation in *M. xanthus. Proc. Natl. Acad. Sci. U.S.A.* **117**, 23859–23868 (2020).
64. R. Mercier *et al.*, The polar Ras-like GTPase MglA activates type IV pilus via SgmX to enable twitching motility in *Myxococcus xanthus. Proc. Natl. Acad. Sci. U.S.A.* **117**, 28366–28373 (2020).
65. A. López-Castilla *et al.*, Structure of the calcium-dependent type 2 secretion pseudopilus. *Nat. Microbiol.* **2**, 1686–1695 (2017).
66. D. Kaiser, Social gliding is correlated with the presence of pili in *Myxococcus xanthus. Proc. Natl. Acad. Sci. U.S.A.* **76**, 5952–5956 (1979).
67. X. Shi *et al.*, Bioinformatics and experimental analysis of proteins of two-component systems in *Myxococcus xanthus. J. Bacteriol.* **190**, 613–624 (2008).

PNAS
www.pnas.org

Supplementary Information

A non-canonical cytochrome *c* stimulates calcium binding by PilY1 for type IVa pili formation

Marco Herfurth, Anke Treuner-Lange, Timo Glatter, Nadine Wittmaack, Egbert Hoiczyk, Antonio J. Pierik and Lotte Søgaard-Andersen

This PDF file includes:

- Supplementary Materials & Methods
- Supplementary Figures 1-9
- Supplementary Tables 1-4
- Supplementary References

Corresponding author: Lotte Søgaard-Andersen[1]

E-mail: sogaard@mpi-marburg.mpg.de

Supplementary Materials & Methods

Bacterial strains and growth media. *E. coli* strains were grown in LB broth (1). Plasmids were propagated using *E. coli* NEB-Turbo. All media and buffers were prepared with ultrapure water using an ELGA Pureflex 2, that reduces the calcium concentration to <2.5 nM according to the manufacturer.

Bioinformatics. Homologs of TfcP were searched using BlastP (2). Pairwise sequence alignments were calculated using EMBOSS-Needle (3). Protein domains were identified using InterPro (4). Alignments were computed using MUSCLE (3). The homology model of PilY1.1 was generated using the Phyre2 server (5). Protein structure of TfcP was predicted using AlphaFold2 (6) and ColabFold (7). Ligand prediction was done using COACH (8). Structures were superimposed using PyMol (http://www.pymol.org/pymol).

Motility assay. T4aPdM was assayed as described (9). Briefly, exponentially growing *M. xanthus* cultures were harvested and concentrated in 1% CTT to a density of 7×10^9 cells ml^{-1}. 5 µl of the concentrated cell suspension were spotted on soft-agar CTT plates (0.5% CTT, 10 mM Tris-HCl pH 8.0, 1 mM KPO_4 pH 7.6, 8 mM $MgSO_4$, 0.5% select-agar (Invitrogen)) and incubated at 32°C for 24 hrs. Colonies were imaged using a Leica MZ75 stereomicroscope equipped with a Leica MC120 HD camera.

T4aP shearing assay. T4aP were sheared off *M. xanthus* cells as described (10). Briefly, cells were grown on CTT 1.5% agar plates at 32°C for three days, then scraped off, and resuspended in pili resuspension buffer (100 mM Tris-HCl pH 7.6, 150 mM NaCl) (1 ml per 60 mg cells). Cell suspensions were vortexed 10 min at maximum speed. A 100 µl aliquot was harvested and resuspended in 200 µl sodium dodecyl sulfate (SDS) lysis buffer (50 mM Tris-HCl pH 6.8, 2% SDS, 10% glycerol, 0.1 M DTT, 1.5 mM EDTA, 0.001% Bromophenol Blue), and denatured at 95°C for 10 min and used to determine the cellular PilA amount. The remaining cell suspension was cleared three times by 20 min centrifugation at 20,000 *g* at 4°C. Pili in the cleared supernatant were precipitated by adding 10× pili-precipitation buffer (final concentration: 100 mM $MgCl_2$, 2% PEG 6000, 100 mM Tris-HCl pH 7.6, 150 mM NaCl), incubation on ice for 4 hrs and centrifugation at 20,000 *g* for 30 min, 4°C. The pellet was resuspended in 1 µl SDS lysis buffer per mg cells and boiled for 10 min at 95°C. The samples were separated by SDS-PAGE and analysed for PilA accumulation by immuno-blot using PilA antibodies.

Immuno-blot and peroxidase staining. Immuno-blot analysis was carried out as described (1). Samples were prepared by harvesting exponentially growing *M. xanthus* cells and subsequently resuspension in SDS lysis buffer to an equal concentration of cells. Immuno-blot was done using as primary antibodies α-PilB, α-PilC, α-PilQ (11), α-PilA, α-LonD (12), α-

FLAG (Rockland; 600-401-383), α-GFP (Roche; 11814460001), α-MalE (New England Biolabs), α-PilY1.1 (13) and α-TfcP. Antibodies against TfcP were generated by Eurogentec against TfcP$^{\Delta 1\text{-}18}$-His$_6$ purified from *E. coli* Rosetta 2(DE3) containing plasmid pMH6 using native Ni-NTA affinity purification. As secondary antibodies, goat α-rabbit immunoglobulin G peroxidase conjugate (Sigma-Aldrich, A8275) and sheep α-mouse immunoglobulin G peroxidase conjugate (Amersham, NXA931) were used. Antibodies and conjugates were used in the following dilutions: 1:500 α-TfcP; 1:1000 α-PilY1.1; 1:3000 α-PilB; α-PilC; 1:5000 α-PilQ; α-PilA; 1:6000 α-LonD; 1:2000 α-GFP, α-MalE, α-FLAG and α-mouse peroxidase conjugate; and, 1:10,000 α-rabbit peroxidase conjugate. Blots were developed using Luminata™Western HRP substrate (Millipore). Unless otherwise noted, protein from 3×10^8 cells were loaded per lane. For peroxidase staining, protein was separated by SDS-PAGE, blotted on a nitrocellulose membrane and developed using Luminata™Western HRP substrate.

Fractionation of *M. xanthus*. *M. xanthus* was fractionated into fractions enriched for soluble, IM and OM proteins as described (14). Briefly, an exponentially growing *M. xanthus* culture was harvested and the pellet resuspended in lysis buffer (50 mM Tris-HCl pH7.6, Protease inhibitor cocktail (Roche)) (1 ml per 80 mg cells). A 75 µl aliquot was taken as the whole cell sample, suspended with SDS-lysis buffer and boiled 10 min at 95°C. Cells were lysed using sonication and lysates cleared by centrifugation at 8000 *g* for 1 min. The cleared lysate was subjected to ultra-centrifugation using an Air-Fuge (Beckman) at ~150,000 *g* for 1 hr. The resulting supernatant contains soluble proteins and was mixed with SDS-lysis buffer. The pellet was resuspended in detergent-lysis buffer (50 mM Tris-HCl pH 7.6, 2% Triton X-100) and subjected to ultra-centrifugation as described. The resulting supernatant is enriched for IM proteins while the pellet is enriched for OM proteins. The supernatant was mixed with SDS lysis buffer and the pellet resuspended in SDS-lysis buffer. The samples were analysed by SDS-PAGE and immuno-blot.

To identify proteins enriched in the periplasm, 100 ml of exponentially growing *M. xanthus* cells inCTT suspension culture were harvested and resuspended in 300 µl TSE8-buffer (200 mM Tris-HCl pH 8.0, 1 mM EDTA, 20% sucrose) supplemented with a Protease inhibitor cocktail (Roche) (15). Cells were incubated on a rotary shaker for 30 min at 4°C and harvested at 16,000 *g,* 4°C for 30 min. The supernatant containing periplasmic proteins was subjected to ultracentrifugation using an Air-Fuge at 150,000 *g* for 30 min. The cleared supernatant was precipitated with acetone and resuspended in SDS-lysis buffer.

Fluorescence microscopy. Exponentially growing *M. xanthus* cells were spotted on 1% agarose pads supplemented with TPM (10 mM Tris-HCl pH 8.0, 1 mM KPO_4 pH 7.6, 8 mM

$MgSO_4$) and incubated for 30 min at 32°C before microscopy. Cells were imaged using a Leica DMI600B microscope with a Hamamatsu Flash 4.0 camera. Images were recorded with Leica MM AF software and processed with Metamorph.

Targeted proteomics. To identify peptides of T4aPM proteins suitable for targeted-mass spectrometry (MS) analysis, we performed sample preparation on *M. xanthus* cell pellets for total proteome analysis as described (12). Briefly, proteins were extracted from cell pellets by heat exposure in the presence of 2% sodium-lauroylsarcosinate. Extracts were then reduced, alkylated and digested overnight using trypsin (Promega). Peptides were purified using C18 solid phase extraction and analysed on a Q-Exactive Plus mass spectrometer connected to an Ultimate 3000 RSLC and a nanospray flex ion source (all Thermo Scientific). The peptides were analysed using data dependent acquisition with settings as described (12). MS raw data were searched using Mascot (Matrix Science) and loaded into Scaffold 4 (Proteome software) for further data evaluation. Peptides considered most amenable for targeted MS were chosen for reference peptide synthesis (JPT Peptide Technologies, Berlin) containing heavy labelled (^{13}C and ^{15}N) C-terminal Lys or Arg residues with a resulting mass shift of +8 Da and +10 Da, respectively. Sequences of reference peptides are listed in Supplementary Table 4. For targeted MS experiments, reference peptides and iRT retention calibration peptides (Biognosys) were spiked into the *M. xanthus* total proteome peptide samples (generated as described), and analysed by liquid chromatography (LC)-MS.

Peptides were separated on a 90 min gradient from 2-50% acetonitrile at a flow rate of 300 nl min^{-1}, and analysed by MS in targeted parallel reaction monitoring (PRM) mode. The mass spectrometer first acquired a full MS-Selected Ion Monitoring (SIM) scan with an MS1 resolution of 70,000, AGC (automatic gain control) target setting of $1e^6$ and 100 ms max injection time. Then PRM scans were carried out with a MS2 resolution of 35,000, AGC target setting of $2e^5$, 100 ms maximum injection time with a quadrupole isolation window of 1.6 m/z. Normalised collision energy was set to 27%. All stages of targeted MS data analysis was carried out in Skyline (20.2.1.384) (16). Results with dot-product <0.85 or $ratio_{heavy/light}$<0.005 were excluded from the analysis.

Proteome analysis of T4aP. Label-free quantification (LFQ) MS of the pili proteome was carried out as described (12). Briefly, pili were purified following the shearing assay protocol with the modification that after precipitation, pili were resuspended in pili-resuspension buffer and re-precipitated with pili-precipitation buffer three times. Pili were resuspended in pili-resuspension buffer to 1 µl buffer per 1 mg cells. 25% of the pili sample was mixed with SDS-lysis buffer and analysed by SDS-PAGE and subsequent staining with Coomassie

Blue. The remaining 75% were precipitated with acetone. The dried acetone pellets were resuspended, reduced, alkylated and digested with trypsin as described (12). Pili LFQ proteomics analysis was carried out on an Exploris 480 mass spectrometer (Thermo Scientific), connected to an Ultimate 3000 RSLC. Peptides were separated on a 60 min gradient from 2-50% acetonitrile at a flow rate of 300 nl min^{-1}. The Exploris 480 mass spectrometer first acquired a full MS scan with an MS1 resolution of 60,000, AGC target setting of $3e^6$ and 60 ms max injection time, followed by MS/MS scans of Top-20 most abundant signals. For MS/MS scans a resolution of 7,500 was set, with an AGC of $2e^5$ and 30 ms max. injection time. Normalised collision energy was set to 27% and the isolation window of the quadrupole was 1.6 m/z. All MS raw data was analysed by MaxQuant (1.6.17.0). iBAQ values were calculated as described (12) as the sum of all peptide intensities for a given protein divided by the number of theoretically MS observable peptides. Following MaxQuant analysis, the iBAQ values were normalised by the total iBAQ sum independently of the highly abundant PilA.

Purification of MalE-TfcP. For purification of MalE-TfcP/MalE-TfcP^{C91M}, gene expression was done in *E. coli* strain BL21 containing the helper plasmid pEC86, which encodes the *ccm* genes for cytochrome *c* maturation of *E. coli*, as well as pMH31 (MalE-TfcP) or pMH39 (MalE-TfcP^{C91M}) using auto-induction in buffered 5052-Terrific-Broth (0.5% glycerol, 0.05% glucose, 0.2% lactose, 2.4% yeast extract, 2% tryptone, 25 mM Na_2HPO_4, 25 mM KH_2PO_4, 50 mM NH_4Cl, 5 mM Na_2SO_4, 2 mM $MgSO_4$) (17) containing chloramphenicol (25 µg ml^{-1}) and carbenicillin (100 µg ml^{-1}). After 24 hrs incubation at 37°C, cells were harvested, and resuspended in MBP-lysis buffer (100 mM Tris-HCl pH 7.0, 200 mM NaCl) supplemented with EDTA-free protease inhibitor cocktail (Roche) and lysed using sonication. The lysate was cleared by centrifugation at 20,000 *g*, 4°C for 30 minutes and loaded onto a 5 ml HighTrap MBP column (GE Healtcare) using an Äkta-Pure system (GE Healthcare). The column was washed with lysis buffer and protein eluted with 10 column volumes MBP-elution buffer (100 mM Tris-HCl pH 7.0, 200 mM NaCl, 10 mM maltose). The elution fractions containing MalE-TfcP/MalE-TfcP^{C91M} were pooled and diluted four fold in 100 mM Tris-HCl pH 7.0. The pooled and diluted samples were loaded onto a HighTrap SP ion exchange column. The column was washed with IEX-wash buffer (100 mM Tris-HCl pH 7.0) and protein eluted in a linear gradient with IEX-elution buffer (100 mM Tris-HCl pH 7.0, 2 M NaCl). Samples were concentrated using an Amicon Ultra filter with 10 kDa cutoff and loaded on a HiLoad 16/600 Superdex 200 pg (GE Healthcare) size exclusion chromatography column equilibrated with SEC-buffer (50 mM Tris-HCl pH 7.6, 50 mM NaCl). Protein was either used fresh or snap-frozen in buffer containing SEC-buffer with 10% glycerol.

Purification of TfcP. For purification of tag-free TfcP, *E. coli* BL21 was transformed with plasmids pMH41 and pEC86 and synthesis of TfcP induced using auto-induction in buffered 5052-Terrific-Broth as described for MalE-TfcP. pMH41 encodes untagged TfcP in which the native type I signal peptide is replaced with the MalE signal peptide for efficient secretion to the periplasm. Expression cultures were grown at 37°C until reaching turbidity and further incubated at 22°C over-night. Cells were harvested and the periplasmic fraction extracted using the TSE-method as described (15). In brief, cells were resuspended in TSE7-buffer (200 mM Tris-HCl pH 7, 1 mM EDTA, 20% Sucrose) and incubated 30 min following by harvesting of cells 30 min at 16,000 *g*. Subsequently, periplasmic proteins are present in the supernatant. TfcP was enriched from the periplasmic fraction using a HiTrap SP HP column on an Äkta pure system using the same buffers as for MalE-TfcP. Fractions were pooled, concentrated and loaded on a Superdex75 10/300 size exclusion chromatography column (GE Healthcare) equilibrated with SEC-buffer (50 mM Tris-HCl pH 7.6, 50 mM NaCl).

UV-Vis spectroscopy. UV-Vis measurements of purified (oxidised) and reduced MalE-TfcP/MalE-TfcP^{C91M} was conducted on a Tecan M200Pro platereader or a Shimadzu 1900 spectrophotometer. Protein was diluted to an absorbance of ~0.7. After measurement of the oxidised spectrum, protein was reduced by adding a few crystals of sodium-dithionite, equilibrated for 15 min and the reduced spectrum recorded.

Redox titrations. Redox titrations were carried out in a Coy anaerobic tent (3% H_2, <5 ppm O_2). MalE-TfcP in HEPES buffer, pH 7.0, was mixed with 20 µM (final concentration) of the following redox mediators: Phenosafranin, safranin T, neutral red, benzyl viologen, and methyl viologen. The solution potential was measured with an InLab redox micro combination electrode (Mettler Toledo) under anaerobic conditions. Correction to redox potentials vs. H_2/H^+ was done by addition of 207 mV to the reading of the potentiometer. Stirring was done using a 8 mm teflon coated stirrer bar. For redox titration using visible spectroscopy (using a Shimadzu 1900 spectrophotometer), automated addition of 15 µl buffered 0.2 mM sodium-dithionite solution was done using a remotely controlled peristaltic pump (Pharmacia P1) for 60 sec followed by 2 min equilibration and 2 min recording of the spectra in the 600-460 nm range. The normalised absorbance increase at 550 nm (corrected by the absorbance for titration of mediators only) was fitted to the Nernst equation for n=1 at 298 K. For the EPR titration, manual addition of aliquots of buffered sodium-dithionite was used. After stabilisation of the solution potential, 300 µl samples were withdrawn, transferred to EPR tubes, which were capped with rubber tubing and an acrylic glass stick. Samples were shock-frozen and stored in liquid nitrogen until the EPR measurements.

EPR spectroscopy. EPR spectra were recorded with an X-band EPR spectrometer (Bruker Elexsys E580) in a 4122HQE-W1/1017 resonator. The temperature of the samples in Ilmasil PN quartz tubes (4.7±0.2 mm outer diameter, 0.45±0.05 mm wall thickness) was maintained at 12 K with an ESR900 continuous flow helium cryostat (Oxford Instruments). The modulation frequency was 100 kHz and the modulation amplitude 1.5 mT. Spectra were averages for four 90 sec scans. For the titration, the normalised amplitude of the derivative-shaped feature of the low spin EPR signal of the ferric state at *g*=2.26 was used for a fit to the Nernst equation (n=1, T=298 K).

Operon mapping. Total RNA was isolated from exponentially growing *M. xanthus* cultures using the Monarch Total RNA Miniprep Kit (NEB). 10^9 cells were harvested and resuspended in 200 µl lysis-buffer (100 mM Tris-HCl pH 7.6, 1 mg ml^{-1} lysozyme). After incubation at 25°C for 5 min cells were lysed and RNA purified according to manufacturer's protocol with the exception that the on-column DNase treatment was omitted. RNA was eluted in RNase-free water and subsequently treated with Turbo DNase and purified using the Monarch RNA Cleanup Kit (50 µg) (NEB) and eluted in RNase-free water. 1 µg of RNA was used for cDNA synthesis using the LunaScript RT SuperMix Kit (NEB) with and without reverse transcriptase (RT). cDNA was diluted 1:5 with water and 1 µl of diluted cDNA used for PCR reactions.

qRT-PCR. For qRT-PCR RNA was isolated and cDNA synthesised as described for operon mapping. qPCRs were carried out using the Luna Universal qPCR MasterMix (NEB) with the primers listed in Supplementary Table 3 and measured on an Applied Biosystems 7500 Real-Time PCR system. Relative gene expression levels were calculated using the comparative C_T method (18). *Mxan_3298* (*tuf2*), which encodes elongation factor Tu, and *mxan_3303* (*rpsS*), which encodes the small ribosomal subunit protein S19, were used as internal controls. All experiments were done with three biological replicates and two technical replicates.

Growth curve. Three independent precultures were diluted to an OD_{550} 0.05 and incubated at 32°C shaking for 72 hrs. Growth was monitored by taking samples at indicated time points and measuring the OD_{550}.

Calcium binding assay. Calcium binding of TfcP was assayed as described (19). Briefly, purified TfcP and bovine heart cytochrome *c* (Sigma) was passed over a Chelex-100 column (Bio-Rad) and subsequently buffer exchanged using a PD MiniTrap G-25 equilibrated with 50 mM Tris pH7.6; 50 mM NaCl. Protein was serially diluted and titration reactions with 20 µM OregonGreen-BAPTA5N, 2 µM $CaCl_2$ measured on a Tecan M200. Binding curves were fitted using GraphPad Prism.

Statistics and reproducibility. Data shown for operon mapping, T4aP-dependent motility, T4aP shearing assays, immuno-blot experiments, UV-Vis spectroscopy, growth curves, size exclusion chromatography, and fluorescence microscopy were obtained in at least two biological replicates with similar results. For targeted proteomics and LFQ-analysis of the pili proteome, four biological replicates were analysed. qRT-PCR analysis were conducted with three biological replicates each with two technical replicates. Calcium-binding, redox titrations and EPR-spectroscopy where done in a single experiment.

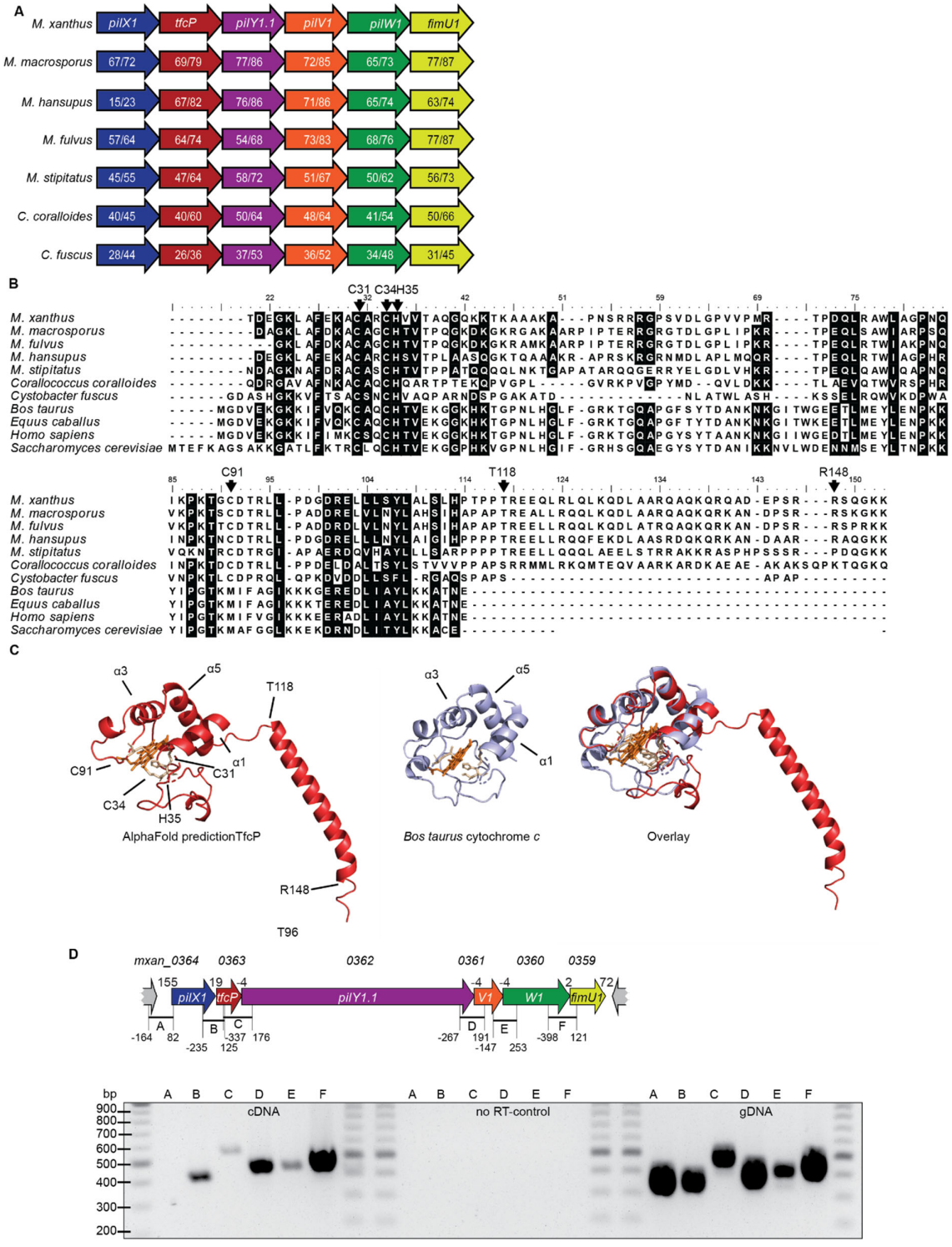

Figure S1. Analysis of cluster_1 and TfcP.
A Comparison of cluster_1 gene clusters in myxobacteria. All six proteins in the listed species are encoded at the same locus. Arrows indicate direction of transcription. Numbers within genes represent identity/similarity determined by pairwise alignment with the respective *M. xanthus* protein. **B** Multiple sequence alignment of TfcP and homologs as well as canonical cytochromes *c.* Shading represents >70% conservation. The cytochrome *c*

signature motif CxxCH and the distal Cys^{91} residue in TfcP are indicated. T118 and R148 indicate the N-terminal and C-terminal residues in the C-terminal α-helix. Numbering of amino acids is according to the unprocessed, full-length TfcP protein. **C** Structure of TfcP predicted by AlphaFold2 with the cytochrome *c* signature motif CxxCH and the distal Cys^{91} residue indicated (left), crystal structure of *Bos taurus* cytochrome *c* (PDB 2B4Z) (middle) and overlay of the TfcP AlphaFold2 model (red) with the crystal structure of *B. taurus* cytochrome *c (*blue*)* (right). Orange: Heme; brown: Heme-binding residues; α1, α3 and α5 make up the typical cytochrome *c* fold (20). **D** Operon mapping of cluster_1 in *M. xanthus*. Upper panel, genetic organization of cluster_1. Locus tags are included above genes and gene names within genes. Distances between start and stop codons are shown above. Letters below arrows indicate the fragments amplified by PCR. Numbers indicate the distance from the 5'-end of a primer to the first base of the stop codon or the first base of the start codon as appropriate. The PCR products amplified using cDNA, an enzyme free reverse transcription reaction and genomic DNA as templates were separated on a 1% agarose gel. Letters above the individual lanes correspond to the letters of the primer combinations depicted above. Molecular size markers in base-pairs are shown on the left.

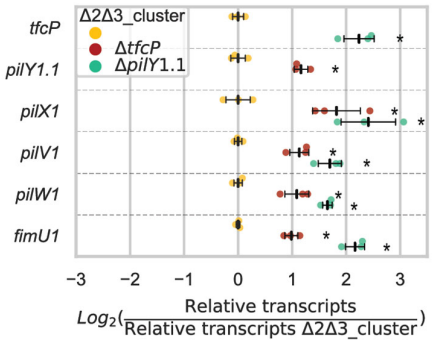

Figure S2. qRT-PCR analysis of transcript levels of cluster_1 genes.
Total RNA was isolated from cells grown in 1.0% CTT suspension culture. Individual data points represent three biological replicates with each two technical replicates, and in which the ratio of the relative transcript level in a mutant over the transcript level in the $WT_{\Delta 2\Delta 3}$ strain is plotted. Center marker and error bars: Mean and STDEV. Statistical analyses were performed as in Fig. 3A. *,*P*< 0.05.

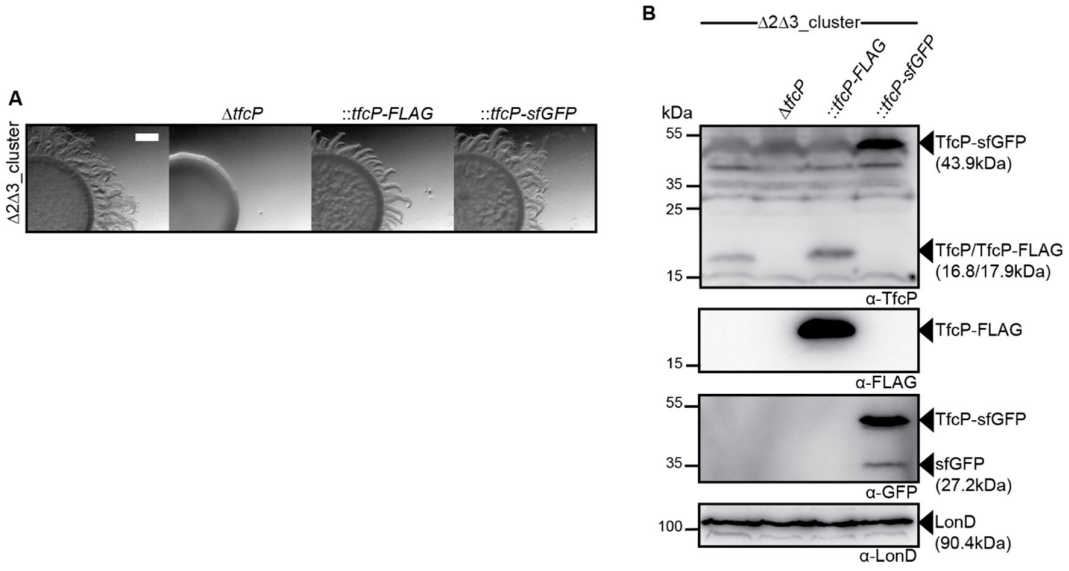

Figure S3. Analysis of TfcP-FLAG and TfcP-GFP.
A Assay for T4aPdM. Strains were assayed as in Fig. 2A. Scale bar, 1 mm. **B** Immuno-blot analysis of TfcP-FLAG and TfcP-sfGFP accumulation. Cells were grown in 1.0% CTT suspension culture and analysed as in Fig. 3B. Note that immuno-blots probed with α-TfcP contain a cross-reacting band at the size of TfcP-sfGFP.

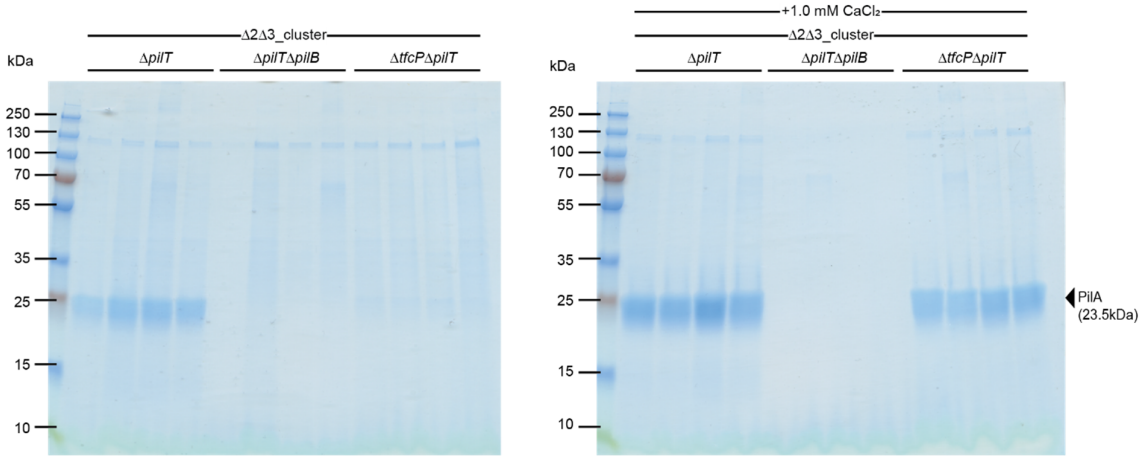

Figure S4. Analysis of purified pili

Pili from 15 mg of cells of the indicated strains were loaded on SDS-PAGE and stained with Coomassie Blue. The left and right gels show pili from cells grown on 1.5% agar supplemented with 1.0%CTT in the absence and presence of 1.0 mM additional $CaCl_2$, respectively.

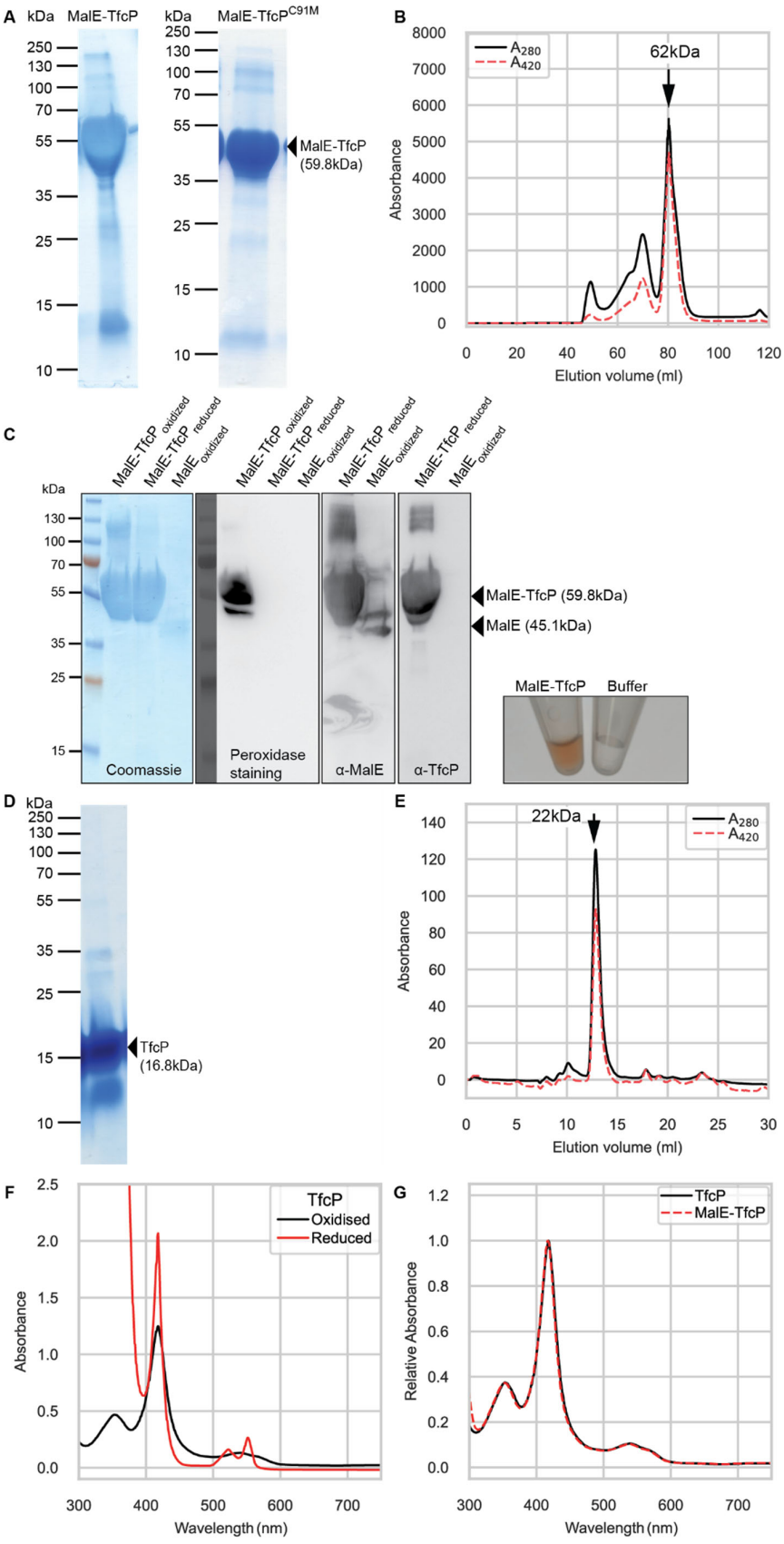
A
kDa
MalE-TfcP
kDa
MalE-TfcP^C91M
250
130
100
70
55
35
25
15
10
MalE-TfcP
(59.8kDa)
B
A280
A420
62kDa
Absorbance
Elution volume (ml)
C
MalE-TfcP oxidized
MalE-TfcP reduced
MalE oxidized
kDa
Coomassie
Peroxidase staining
α-MalE
α-TfcP
MalE-TfcP (59.8kDa)
MalE (45.1kDa)
MalE-TfcP
Buffer
D
TfcP
(16.8kDa)
E
22kDa
Absorbance
Elution volume (ml)
F
TfcP
Oxidised
Reduced
Absorbance
Wavelength (nm)
G
TfcP
MalE-TfcP
Relative Absorbance
Wavelength (nm)

Figure S5. *In vitro* analysis of TfcP
A Purified MalE-TfcP variants used for spectroscopic analysis. ~5 µg of purified proteins were separated by SDS-PAGE and stained by Coomassie Blue. The fusions for overexpression contains the MalE type I signal peptide and lacks the TfcP signal peptide. The molecular mass is indicated for full-length unprocessed proteins. **B** Absorbance at 280 nm and 420 nm during size exclusion chromatography of MalE-TfcP. Calculated molecular weight of MalE-TfcP based on the elution volume is indicated. **C** TfcP heme-binding assay. Panels from left-to-right**,** MalE-TfcP in oxidised (as purified) and reduced state (after addition of DTT) stained with Coomassie Blue, analysed for heme-binding by peroxidase staining using a luminescent horse radish peroxidase (HRP) substrate and MalE as negative control, detected by immuno-blotting with α-MalE and α-TfcP as indicated, and image of purified MalE-TfcP in buffer. **D** Purified TfcP used for spectroscopic analysis and the calcium binding experiment. Molecular mass is indicated for the full-length unprocessed protein. **E** Absorbance at 280 nm and 420 nm during size exclusion chromatography of TfcP. Calculated molecular weight of TfcP based on the elution volume is indicated. **F** UV-Vis spectra of purified TfcP in the oxidised and reduced state. Experiments were performed on a Tecan200Pro platereader. **G** Comparison of UV-Vis spectra of MalE-TfcP and TfcP. Spectra were normalized to the Soret-Peak.

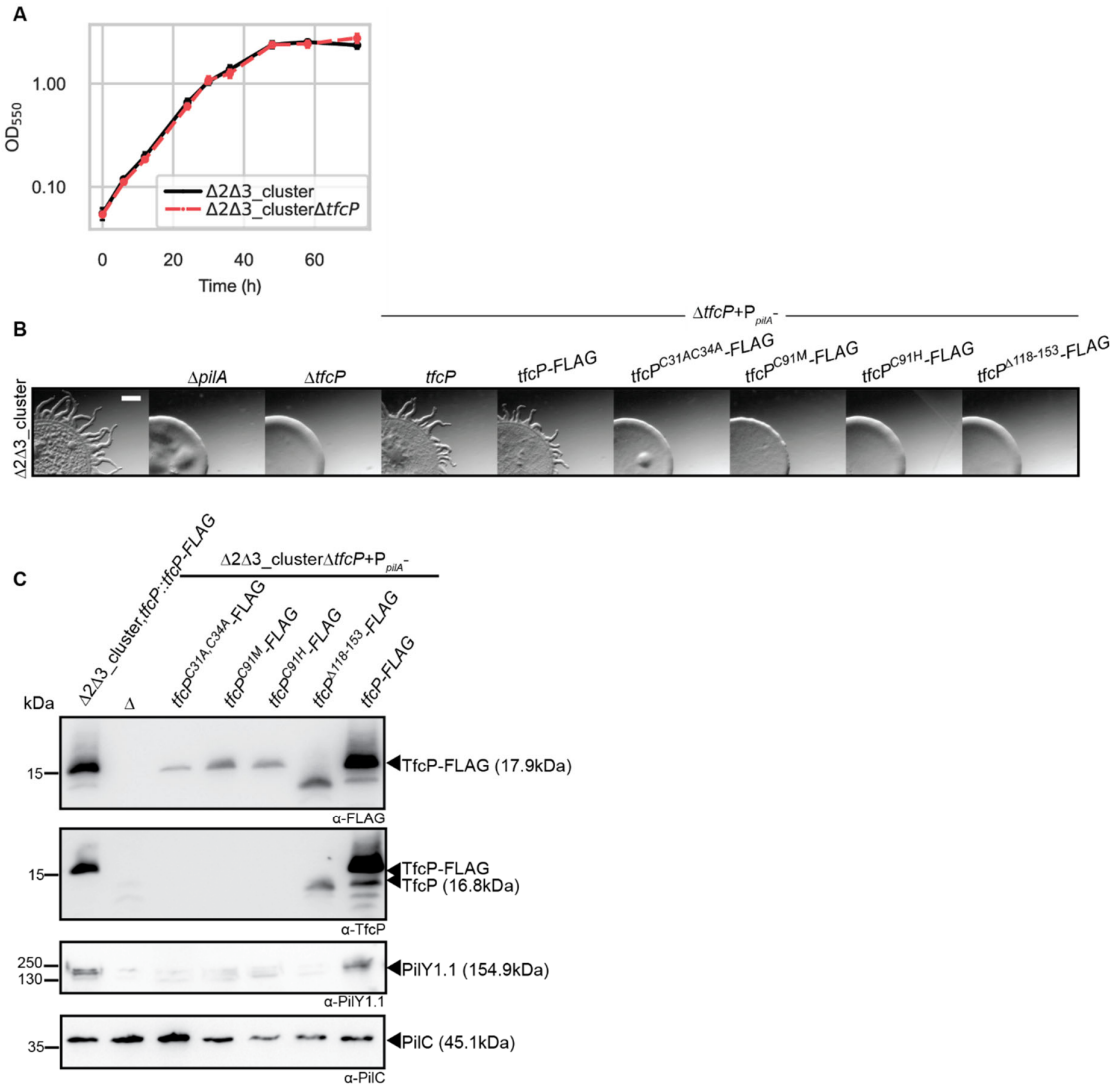

Figure S6. Amino acid substitution in heme-binding residues of TfcP or deletion of the C-terminal extension affect protein stability

A Growth curves of $WT_{\Delta2\Delta3}$ and $WT_{\Delta2\Delta3}\Delta$*tfcP*. Points represent mean and STDEV from three biological replicates. **B** Assays for T4aPdM. $WT_{\Delta2\Delta3}$ and strains expressing mutant TfcP variants were spotted on 0.5% agar supplemented with 0.5% CTT and imaged after 24 hrs. Scale bar, 1 mm. **C** Accumulation of TfcP and PilY1.1 in strains expressing TfcP variants. Protein from the same number of cells grown in 1.0% CTT suspension culture was separated by SDS-PAGE and analysed by immuno-blotting. The lane labeled with Δ contains whole cell lysate of a Δ1Δ2_cluster strain as a negative control. PilC was used as a loading control.

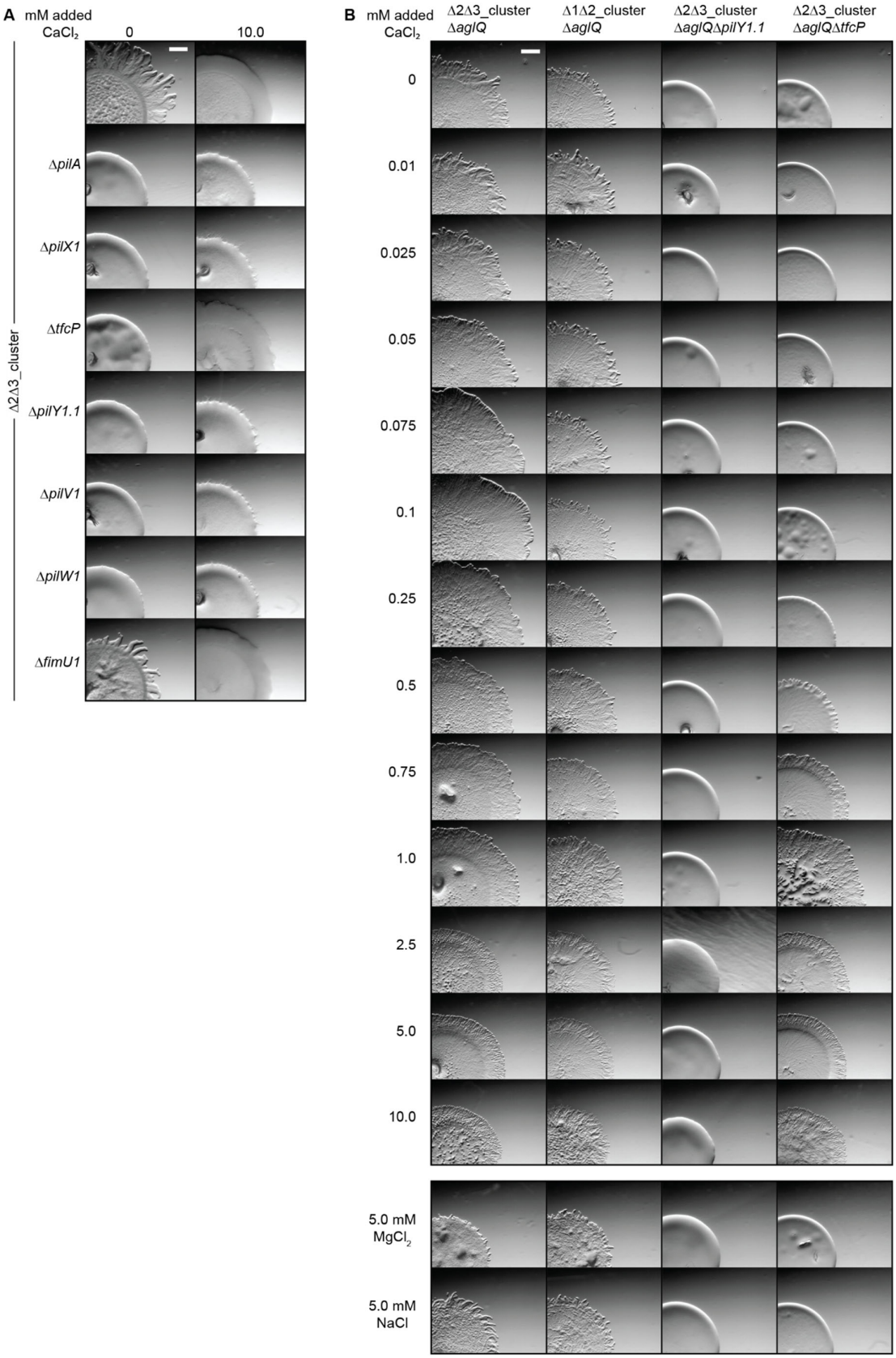

Figure S7. $CaCl_2$ affects T4aPdM of *M. xanthus*

A Assay for T4aPdM. Cells were grown in 1.0% CTT suspension culture and plated on 0.5% agar supplemented with 0.5% CTT and imaged after 24 hrs. The final concentration of added $CaCl_2$ is indicated. Scale bar, 1 mm. **B** Assay for T4aPdM. Cells were grown in 1.0% CTT suspension culture and plated on 0.5% agar supplemented with 0.5% CTT and imaged after 24 hrs. The final concentration of added $CaCl_2$, $MgCl_2$ and NaCl is indicated. Scale bar, 1 mm.

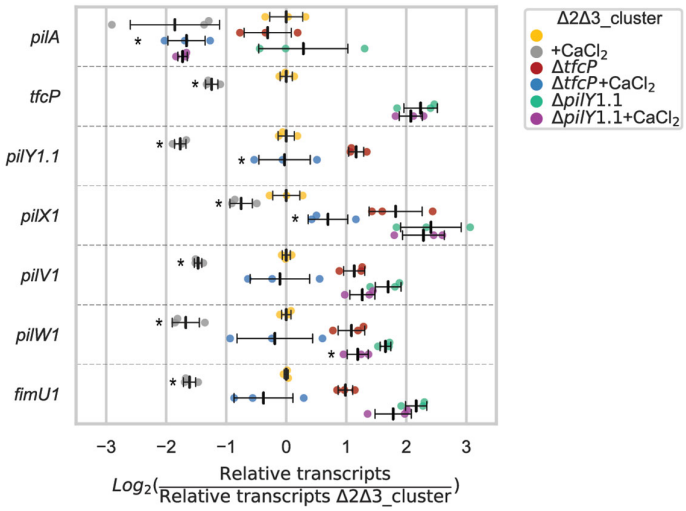

Figure S8. qRT-PCR analysis of transcript levels of cluster_1 genes and *pilA*.
Total RNA was isolated from cells grown in 1.0% CTT suspension culture without or with added calcium as indicated. Individual data points represent three biological replicates with each two technical replicates, and in which the ratio of the relative transcript level in a mutant over the transcript level in the $WT_{\Delta 2\Delta 3}$ strain is plotted. Data for samples without added $CaCl_2$ are the same as in Fig. S2 and included for comparison. Center marker and error bars: Mean and STDEV. Statistical analyses were performed as in Fig. 6E. *,$P< 0.05$.

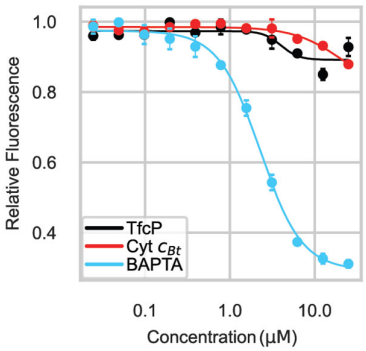

Figure S9. TfcP does not detectably bind calcium.
Calcium binding by purified TfcP was assayed by titration against a fluorescent calcium reporter. *Bos taurus* cytochrome *c* (Cyt C_{Bt}) was used as negative and BAPTA as positive control. Points represent mean and STDEV from two technical replicates.

Supplementary Table 1. Strains used in this study

Name	Description	Reference
	***M. xanthus* strains**	
SA6892	Δ*cluster_2 (mxan_1021-1017)* Δ*cluster_3 (mxan_1369-1365)*	(12)
SA6888	Δ*cluster_1* (*mxan_0364-0359)* Δ*cluster_2*	(12)
SA8754	Δ*cluster_2* Δ*cluster_3* Δ*pilT* (*mxan_5787*) Δ*pilB* (*mxan_5788*)	This study
SA7717	Δ*cluster_2* Δ*cluster_3* Δ*pilT*	This study
SA7698	Δ*cluster_2* Δ*cluster_3* Δ*aglQ* (*mxan_6861*)	This study
SA7703	Δ*cluster_1* Δ*cluster_2* Δ*aglQ*	This study
SA7649	Δ*cluster_2* Δ*cluster_3* Δ*pilX1* (*mxan_0364*)	This study
SA7648	Δ*cluster_2* Δ*cluster_3* Δ*tfcP* (*mxan_0363*)	This study
SA7647	Δ*cluster_2* Δ*cluster_3* Δ*pilY1.1* (*mxan_0362*)	This study
SA7646	Δ*cluster_2* Δ*cluster_3* Δ*pilV1* (*mxan_0361*)	This study
SA7645	Δ*cluster_2* Δ*cluster_3* Δ*pilW1* (*mxan_0360*)	This study
SA7644	Δ*cluster_2* Δ*cluster_3* Δ*fimU1* (*mxan_0359*)	This study
SA7672	Δ*cluster_2* Δ*cluster_3* Δ*pilT* Δ*pilX1*	This study
SA7673	Δ*cluster_2* Δ*cluster_3* Δ*pilT* Δ*tfcP*	This study
SA7674	Δ*cluster_2* Δ*cluster_3* Δ*pilT* Δ*pilY1.1*	This study
SA7675	Δ*cluster_2* Δ*cluster_3* Δ*pilT* Δ*pilV1*	This study
SA7676	Δ*cluster_2* Δ*cluster_3* Δ*pilT* Δ*pilW1*	This study
SA7677	Δ*cluster_2* Δ*cluster_3* Δ*pilT* Δ*fimU1*	This study
SA9004	Δ*cluster_2* Δ*cluster_3 tfcP::tfcP-FLAG*	This study
SA9009	Δ*cluster_2* Δ*cluster_3 tfcP::tfcP-sfGFP*	This study
SA9012	Δ*cluster_2* Δ*cluster_3* Δ*pilY1.1* Δ*aglQ*	This study
SA9016	Δ*cluster_2* Δ*cluster_3* Δ*tfcP* Δ*aglQ*	This study
SA9017	Δ*cluster_2* Δ*cluster_3* Δ*pilA* (*mxan_5783*)	This study
SA9019	Δ*cluster_2* Δ*cluster_3* Δ*tfcP pilM (mxan_5776)::mCherry-pilM*	This study
SA7680	Δ*cluster_2* Δ*cluster_3* Δ*tfcP attB::*P_{pilA}*-tfcP*	This study
SA9040	Δ*cluster_2* Δ*cluster_3* Δ*tfcP attB::*P_{pilA}*-tfcP-FLAG*	This study
SA9041	Δ*cluster_2* Δ*cluster_3* Δ*tfcP attB::*P_{pilA}*-tfcP*^{C91H}*-FLAG*	This study
SA9042	Δ*cluster_2* Δ*cluster_3* Δ*tfcP attB::*P_{pilA}*-tfcP*^{C91M}*-FLAG*	This study
SA9043	Δ*cluster_2* Δ*cluster_3* Δ*tfcP attB::*P_{pilA}*-tfcP*$^{\Delta 118\text{-}153}$*-FLAG*	This study
SA9031	Δ*cluster_2* Δ*cluster_3* Δ*pilY1.1 attB::*P_{pilA}*-pilY1.1*	This study
SA9032	Δ*cluster_2* Δ*cluster_3* Δ*fimU1 attB::*P_{pilA}*-fimU1*	This study
SA9033	Δ*cluster_2* Δ*cluster_3* Δ*pilV1 attB::*P_{pilA}*-pilV1*	This study
SA9044	Δ*cluster_2* Δ*cluster_3* Δ*tfcP attB::*P_{pilA}*-tfcP*^{C31A,C34A}*-FLAG*	This study
SA9034	Δ*cluster_2* Δ*cluster_3* Δ*pilW1 attB::*P_{pilA}*-pilW1*	This study
SA9055	Δ*cluster_2* Δ*cluster_3* Δ*pilX1 attB::*P_{pilA}*-pilX1*	This study
SA9051	Δ*cluster_2* Δ*cluster_3 pilM::mCherry-pilM*	This study
SA9064	Δ*cluster_2* Δ*cluster_3 pilY1.1::pilY1.1*^{D1173A}	This study
SA9066	Δ*cluster_2* Δ*cluster_3* Δ*tfcP pilY1.1::pilY1.1*^{D1173A}	This study
SA9068	Δ*cluster_2* Δ*cluster_3* Δ*aglQ pilY1.1::pilY1.1*^{D1173A}	This study
SA9069	Δ*cluster_2* Δ*cluster_3* Δ*tfcP* Δ*aglQ pilY1.1::pilY1.1*^{D1173A}	This study
SA6024	Δ*pilBTCMNOPQ*	(21)
SA8721	Δ*pilQ; pilM::mcherry-pilM*	(12)

	***E. coli* strains**	
NEB-Turbo	F' *proA*$^{+}$*B*$^{+}$ *lacI*^{q} Δ*lacZM15 / fhuA2* Δ*(lac-proAB) glnV galK16 galE15 R(zgb-210::Tn10)*Tet^{S} *endA1 thi-1* Δ*(hsdS-mcrB)5*	New England Biolabs
BL21	*fhuA2 [lon] ompT gal [dcm] ΔhsdS*	New England Biolabs

Supplementary Table 2. Plasmids used in this study

Name	Description	Reference
pBJ114	*galK* containing vector for generation of in-frame deletions in *M. xanthus*, Kan^R	(22)
pSW105	P_{pilA} , Kan^R, *attP*	(23)
pMal-p5x	Expression vector for periplasmic MalE fusions	NEB
pET24b+	Expression vector for His_6-tagged protein	Novagen
pMAT150	pBJ114, in-frame deletion of *pilT*	(12)
pBJd*aglQ*	pBJ114, in-frame deletion of *aglQ*	(24)
pMH12	pBJ114, endogenous *tfcP*-sfGFP	This study
pMH41	pMAL-p5x derived, MalE-signal peptide TfcP	This study
pMAT167	pBJ114, in-frame deletion of *pilX1*	(12)
pMAT164	pBJ114, in-frame deletion of *pilY1.1*	(12)
pMAT163	pBJ114, in-frame deletion of *pilB*	(12)
pMAT162	pBJ114, in-frame deletion of *pilA*	(12)
pMAT170	pBJ114, in-frame deletion of *pilB* and *pilT*	This study
pMAT336	pBJ114, endogenous mCherry-PilM	(12)
pMAT407	pSW105, P_{pilA} -*tfcP*-FLAG	This study
pMAT409	pSW105, P_{pilA} -$tfcP^{C91H}$-FLAG	This study
pMAT408	pSW105, P_{pilA} -$tfcP^{C91M}$-FLAG	This study
pMAT410	pSW105, P_{pilA} -$tfcP^{\Delta 118-153}$-FLAG	This study
pMAT210	pSW105, P_{pilA} -*pilY1.1*	This study
pMAT220	pSW105, P_{pilA} -*fimU1*	This study
pMAT222	pSW105, P_{pilA} -*pilV1*	This study
pMAT310	pSW105, P_{pilA} -*pilX1*	This study
pMH45	pSW105, P_{pilA} -$tfcP^{C31A,C34A}$-FLAG	This study
pMAT221	pSW105, P_{pilA} -*pilW1*	This study
pMH60	pBJ114, endogenous $pilY1.1^{D1173A}$	This study
pMH1	pBJ114, in-frame deletion of *tfcP*	This study
pMH2	pBJ114, in-frame deletion of *fimU1*	This study
pMH3	pBJ114, in-frame deletion of *pilW1*	This study
pMH4	pBJ114, in-frame deletion of *pilV1*	This study
pMH5	pET24b+, *tfcP-*His_6	This study
pMH7	pSW105, P_{pilA} -*tfcP*	This study
pMH10	pBJ114, endogenous *tfcP*-FLAG	This study
pMH31	pMAL-p5x, MalE-TfcP	This study
pMH39	pMAL-p5x, MalE-$TfcP^{C91M}$	This study
pMH45	pSW105, $tfcP^{C31A,C34A}$-FLAG	This study
pEC86	Constitutive expression of *ccm* genes of *E. coli*	(25)

Supplementary Table 3. Oligonucleotides used in this study

	Oligonucleotides used for cloning	
Name	**Sequence**[1]	**Brief description**
0359-A-HindIII	**GCGCAAGCTT**GCATGGTGACGCTGAGTCCC	Δ*fimU1*
0359-B-XbaI	**GCGCTCTAGAT**CCGCGTGTGTGCCTCATG	Δ*fimU1*
0359-C-XbaI	**GCGCTCTAGAT**GAGCACTGCCGGCACCTGAAG	Δ*fimU1*
0359-D-BamHI	**GCGCGGATCC**CGGAGGTGGAGCTGCTGC	Δ*fimU1*
0360-A-HindIII	**GCGCAAGCTT**AAGGTCTACGCGACCACGGC	Δ*pilW1*
0360-B-XbaI	**GCGCTCTAGA**CGTCTTCACGGCGCCATCCT	Δ*pilW1*
0360-C-XbaI	**GCGCTCTAGA**ACGGAAAATTGAGCATGAGG	Δ*pilW1*
0360-D-BamHI	**GCGCGGATCC**GGAAGTGGCGCAGGCCTTCG	Δ*pilW1*
0361-A-HindIII	**GCGCAAGCTT**CACGGGCTCTGGCATCGCCG	Δ*pilV1*
0361-B-XbaI	**GCGCTCTAGA**CGCTGTCACTGCGGCATCCT	Δ*pilV1*
0361-C-XbaI	**GCGCTCTAGA**ATGGCGCCGTGAAGACGACT	Δ*pilV1*
0361-D-BamHI	**GCGCGGATCC**CAGGTACTCCAGCGTCGGTA	Δ*pilV1*
0363-A-HindIII	**GCGCAAGCTT**GTGCCGCCGCTCAGGCATG	Δ*tfcP*
0363-Bflag-KpnI	**GCGCGGTACC**CTTCTTCCCCTGCGAACG	*tfcP-FLAG*
0363-Cflag-KpnI	**GCGCGGTACC**CTTCTTCCCCTGCGAACG	*tfcP-FLAG*
0363-B-XbaI	**GCGCTCTAGA**GATGAGTCGGTTCATGGG	Δ*tfcP*
0363-C-XbaI	**GCGCTCTAGA**TCGCAGGGGAAGAAGTGA	Δ*tfcP*
0363-D-BamHI	**GCGCGGATCC**GCGACAGGTTTCCGTAGG	Δ*tfcP*
sfGFP-B overlay	GCGCGGATGAGGGTGCGCATCATTTGTAGAGCTC	*tfcP-sfGFP*
0363-C overlay	TGATGCGCACCCTCATCCAGACACTGGCCG	*tfcP-sfGFP*
0363 AvaI FactorXa - SP	**GCGCCTCGGG**ATCGAGGGAAGGACGGATGAAGGCAAGCTCGCCTTC	MalE-TfcP/MalE-TfcP^{C91M}
0363 Stop HindIII	**CGCGAAGCTT**TCACTTCTTCCCCTGCGAACG	MalE-TfcP/MalE-TfcP^{C91M}/TfcP
MalE start NdeI*	**GCGCCATATG**AAAATAAAAACAGGTGCACGC	MalE-TfcP/MalE-TfcP^{C91M}
0363 Start XbaI	**GCGCTCTAGA**AACCGACTCATCCTGTTG	PpilA-tfcP
0363 nostop BamHI	**GCGCGGATCC**CTTCTTCCCCTGCGAACG	P$_{pilA}$-*tfcP*-FLAG/sfGFP
0363 Δ118-153 BamHI	**GCGCGGATCC**AGGAGGTGTGGGGTGGAGGCT	P$_{pilA}$-*tfcP*$^{\Delta 118\text{-}153}$-FLAG
0363-Bmut-XmaI	**GCGCCCCGGG**CGGCGGCCTTCTCGAAGGCGAG	*tfcP*^{C31A,C34A}
0363-Cmut-XmaI	**GCGCCCCGGG**CTCACGTCGTCACCGCGCAAG	*tfcP*^{C31A,C34A}
0363-Short-B	**GCGCTCTAGAG**TGGAGGCTGAGCGCCAG	*tfcP*$^{\Delta 118\text{-}153}$

0363-Short-C	**GCGCTCTAGA**TGATGCGCACCCTCATCCAGAC	*tfcP*$^{\Delta 118\text{-}153}$
PilY1_1 mut fwd HindIII	**GCGCAAGCTT**CAATCAAAACCAGATCAACAG	*pilY1.1*^{D1173A}
PilY1_1_mut rev BamHI	**GCGCGGATCC**GATGAACAAGTGATTGTCATG	*pilY1.1*^{D1173A}
0363-E	GTCTCTTGAGACCAACC	Δ*tfcP*
0363-F	GTCGTAGGGGGAGATTC	Δ*tfcP*
0363-G	CACGGATGAAGGCAAGC	Δ*tfcP*
0363-H	GACGGTTCATCCGCCTG	Δ*tfcP*
0361-0359-E	GCTCACCGGCTGGCGCCATG	Δ*fimU1/pilV1/pilW1*
0361-0359-F	CTTCGACCCGGCGAAGCACG	Δ*fimU1/pilV1/pilW1*
0361-0359-G	CATCGTCTTCAGTGACACGC	Δ*pilW1*
0361-0359-H	GGCGCGACAAGTTCATTGGG	Δ*pilW1*
0363 C91M C	**GCGCACCGGT**ATGGATACGCGC	*tfcP*^{C91M}
0363 C91H C	**GCGCACCGGT**CATGATACGCGCCTGC	*tfcP*^{C91H}
0363 C91X B	**GCGCACCGGT**CTTGGGTTTGATCTGG	*tfcP*$^{C91M/H}$
pilY1.1$^{D1173A+}$	CGAGACGGCAACTACGCCGTCATGTACGTGCCG	*pilY1.1*^{D1173A}
pilY1.1$^{D1173A-}$	CGGCACGTACATGACGGCGTAGTTGCCGTCTCG	*pilY1.1*^{D1173A}
0361-G_n	CCACCATGGCCATCCTGCTG	Δ*pilV1*
0361-H_n	CAGCTCAGGACGACGCGTAC	Δ*pilV1*
0359-G	CGGTGGCCATCGCCTCCATC	Δ*fimU1*
0359-H_n	GATGGCCTGGTTCTGGGTCG	Δ*fimU1*
0359 start XbaI	**GCGCTCTAGA**ATGAGGCACACACGCGGAATC	P_{pilA}-*fimU1*
0359 stop HindIII	**GCGCAAGCTT**TCAGTTCACGCACTCGATGGC	P_{pilA}-*fimU1*
0360 start XbaI	**GCGCTCTAGA**GTGAAGACGACTTTGACGC	P_{pilA}–*pilW1*
0360 stop HindIII	**GCGCAAGCTT**TCAATTTTCCGTCAGGAG	P_{pilA}–*pilW1*
0361 start XbaI	**GCGCTCTAGA**GTGAAGACGACTTTGACGCG	P_{pilA}-*pilV1*
0361 stop HindIII	**GCGCAAGCTT**TCACGGCGCCATCCTCGTC	P_{pilA}-*pilV1*
0362 start XbaI	**GCGCTCTAGA**GTGATGCGCACCCTCATCCAG	P_{pilA}-*pilY1.1*
0362 stop HindIII	**GCGCAAGCTT**TCACTGCGGCATCCTCCCGTC	P_{pilA}-*pilY1.1*
0364 start XbaI	**GCGCTCTAGA**GTGCAACGTCCCACAACC	P_{pilA}–*pilX1*
0364 stop HindIII	**GCGCAAGCTT**TCAAGGGGCGGGGGTGATG	P_{pilA}–*pilX1*
MalE Mfe	GCGC**CAATTG**ACCAACAAGGAC	Signal peptide MalE
MalE-SP rev	CTTGCCTTCATCCGTCGCGAGAGCCGAGGCGGAAA	Signal peptide MalE
0363_MalE-SP_fwd	GCCTCGGCTCTCGCGACGGATGAAGGCAAGCTCGC	TfcP untagged

	Oligonucleotides used for operon mapping	
Name	**Sequence**	**Combination**
0365 map-fwd	CCGAGCCATCCGAGGTG	A
pilX1 map-rev	GTGGGACGTTGCACCATGT	A
pilX1 q-1 fwd	AGGTCTCGACGATGACAATGG	B
tfcP q-1 rev	CCGCGGCCTTTGTTTTCTTC	B
tfcP q-2 fwd	ACAGAAGAAAACAAAGGCCGC	C
PilY1 map rev	CGGTGATTCCTCGGTGATG	C
PilY1 map fwd	CTGAGCCAGGACGAGAGCG	D
PilV map rev	AGCGTGATGTTCTCCATCGC	D
pilV1 q-2 fwd	CCCTCCATCCTCAGCACTATC	E
PilW map rev	TGAAGACGATGGGGGCATTC	E
pilW1 q-1 fwd	ATGTCGAACGTCTCTCGGTG	F
fimU1 q-1 rev	CATTCTCGCGTTGACGGTTG	F
	Oligonucleotides used for qRT-PCR	
Name	**Sequence**	**Gene**
fimU1_q-2_fwd	CTCCGGTGCGACAATGAATG	*fimU1*
fimU1_q-2_rev	TGTAGCAGAGCCCGTGAATC	*fimU1*
pilV1_q-1_fwd	GGACTGGATGAGAGCTACGTC	*pilV1*
pilV1_q-1_rev	GCTCGATAGTGCTGAGGATGG	*pilV1*
pilW1_q-1_fwd	ATGTCGAACGTCTCTCGGTG	*pilW1*
pilW1_q-1_rev	CGACAAGTTCATTGGGGTGC	*pilW1*
pilY1.1_q-2_fwd	GACGTCTCCCATTACGACCC	*pilY1.1*
pilY1.1_q-2_rev	AAGATGACTTCCTTCCCGCC	*pilY1.1*
rpsS_q-1_rev	GACGAACACCGGGATGAACT	*rpsS*
rpsS_q-2_fwd	GTTCGATCAAGAAGGGTCCGT	*rpsS*
tfcP_q-1_fwd	CCGACTCATCCTGTTGTCCC	*tfcP*
tfcP_q-1_rev	CCGCGGCCTTTGTTTTCTTC	*tfcP*
pilA_q-1_fwd	GATTCAACCCCCGCAACCG	*pilA*
pilA_q-1_rev	GTTCGTCTTCGCCTCGGAC	*pilA*
PilX1_q-6_fwd	GGTCGGAGGCTGGAACTC	*pilX1*
PilX1_q-6_rev	TCGTTTGGAGCGGGAAGG	*pilX1*
Tau_q-3_fwd	AGTGGAAGTCGTTGGTCTGC	*tuf2 (mxan_3298)*
Tau_q-3_rev	TTGGTGTGCGGGGTGATG	*tuf2 (mxan_3298)*

[1]Restriction sites are underlined. Oligonucleotide sequences that are not complementary to the template are indicated in bold.

Supplementary Table 4. Heavy labelled (^{13}C and ^{15}N) reference peptides with C-terminal Lys or Arg residue

Peptide Name	Peptide Sequence
FimU1_1	DFLDDLPALDAAAPGNLR
FimU1_2	IVVEENVPR
FimU1_3	SLIQVEPR
PilA_1	FGANSAIDDPTPVVAR
PilA_2	NAADLPVPAAGVPCISNDSFR
PilA_3	VSAAAGDCEVR
PilA_4	YSDFANEIGFAPER
PilB_1	ENLISVQQLR
PilB_2	HLVVPVNR
PilB_3	LGMSSLR
PilC_1	DILVFTR
PilC_2	KGEMEAMDVEAVNAR
PilC_3	TLGTMISSGVPILDALDVTAK
PilC_4	TVEDAIIYVR
PilM_1	DVTIGGNQFTEEIQK
PilM_2	QLNVSYEEAEALK
PilM_3	SLDFYAGTAADSNFSK
PilM_4	VLSSVAEQVAGEIQR
PilN_1	INLLPVR
PilN_2	LAVLDALR
PilN_3	MMDALASATPK
PilN_4	QSELEAHQAGVASTK
PilN_5	QVGGAQVGVPILVEFK
PilO_1	DIEELLAQINDIGKK
PilO_2	LSEALTELPEQR
PilO_3	VVLQSEFQATTFR
PilP_1	LVAVVTGDASPVAMVEDPAGR
PilP_2	QDPAYNMMTGR
PilQ_1	ALGKEEFGNIIR
PilQ_2	NIVVADDVSGK
PilQ_3	TNVLIVK
PilT_1	GASDLHVTTGSPPQLR
PilT_2	VHQIYSSMQVGQAK
PilV1_1	DLVPGVPDTAGNIANVR
PilW1_1	AGSGMGNAPIVFSDTR
PilW1_2	ALFEEQTMLAQVTGR
PilW1_3	INVVPGTGIETTTTDR
PilW1_4	LQPTTAPTTPALLVNPAR
PilW1_5	NLACHVEVTNVDAAGR
PilX1_1	QSPSGDAYAAFPLQTNVR
PilX1_2	YKEAYFAAEAGLAEGR
PilY1.1_1	SATVSGDLSPDIANDFVITK
PilY1.1_3	SSNIEHAFSTAK

PilY1.1_4	VNLDQVNPNAPLGQK
TfcP_1	AWLAGPNQIKPK
TfcP_2	GPSVDLGPVVPMR
TsaP_1	GDLVGPVGER
TsaP_2	IGVDLANSVPVTTQGFVTQR
TsaP_3	SLEELVPGDR
TsaP_4	YVVYHTTQAVK

Supplementary References

1. J. Sambrook, E. F. Fritsch, T. Maniatis, *Molecular Cloning: A Laboratory Manual* (Cold Spring Harbor Laboratory Press, 1989).

2. S. F. Altschul, W. Gish, W. Miller, E. W. Myers, D. J. Lipman, Basic local alignment search tool. *J. Mol. Biol.* **215**, 403-410 (1990).

3. F. Madeira *et al.*, The EMBL-EBI search and sequence analysis tools APIs in 2019. *Nucl. Acids Res.* **47**, W636-W641 (2019).

4. M. Blum *et al.*, The InterPro protein families and domains database: 20 years on. *Nucl. Acids Res.* **49**, D344-D354 (2021).

5. L. A. Kelley, S. Mezulis, C. M. Yates, M. N. Wass, M. J. Sternberg, The Phyre2 web portal for protein modeling, prediction and analysis. *Nat. Protoc.* **10**, 845-858 (2015).

6. J. Jumper *et al.*, Highly accurate protein structure prediction with AlphaFold. *Nature* **596**, 583-589 (2021).

7. M. Mirdita, S. Ovchinnikov, M. Steinegger, ColabFold - Making protein folding accessible to all. *bioRxiv* 10.1101/2021.08.15.456425, 2021.2008.2015.456425 (2021).

8. J. Yang, A. Roy, Y. Zhang, Protein-ligand binding site recognition using complementary binding-specific substructure comparison and sequence profile alignment. *Bioinformatics* **29**, 2588-2595 (2013).

9. W. Shi, D. R. Zusman, The two motility systems of *Myxococcus xanthus* show different selective advantages on various surfaces. *Proc Natl Acad Sci U S A* **90**, 3378-3382 (1993).

10. S. S. Wu, J. Wu, D. Kaiser, The *Myxococcus xanthus pilT* locus is required for social gliding motility although pili are still produced. *Mol. Microbiol.* **23**, 109-121 (1997).

11. I. Bulyha *et al.*, Regulation of the type IV pili molecular machine by dynamic localization of two motor proteins. *Mol. Microbiol.* **74**, 691-706 (2009).

12. A. Treuner-Lange *et al.*, PilY1 and minor pilins form a complex priming the type IVa pilus in *Myxococcus xanthus*. *Nat. Comm.* **11**, 5054 (2020).

13. S. Agrawal (2013) Identification and characterization of novel factors needed for two aspects of *Myxococcus xanthus* physiology: Social motility and osmoregulation. in *Bloomberg School of Public Health* (Johns Hopkins University), p 196.

14. B. Thomasson *et al.*, MglA, a small GTPase, interacts with a tyrosine kinase to control type IV pili-mediated motility and development of *Myxococcus xanthus*. *Mol. Microbiol.* **46**, 1399-1413 (2002).

15. S. Quan, A. Hiniker, J. F. Collet, J. C. Bardwell, Isolation of bacteria envelope proteins. *Methods Mol Biol* **966**, 359-366 (2013).

16. B. MacLean *et al.*, Skyline: an open source document editor for creating and analyzing targeted proteomics experiments. *Bioinformatics* **26**, 966-968 (2010).

17. F. W. Studier, Stable expression clones and auto-induction for protein production in *E. coli*. *Methods Mol. Biol.* **1091**, 17-32 (2014).

18. T. D. Schmittgen, K. J. Livak, Analyzing real-time PCR data by the comparative CT method. *Nat. Protoc.* **3**, 1101-1108 (2008).

19. J. Orans *et al.*, Crystal structure analysis reveals *Pseudomonas* PilY1 as an essential calcium-dependent regulator of bacterial surface motility. *Proc. Natl. Acad Sci. U S A* **107**, 1065-1070 (2010).

20. I. Bertini, G. Cavallaro, A. Rosato, Cytochrome c: occurrence and functions. *Chem Rev* **106**, 90-115 (2006).

21. C. Friedrich, I. Bulyha, L. Søgaard-Andersen, Outside-in assembly pathway of the type IV pilus system in *Myxococcus xanthus*. *J. Bacteriol.* **196**, 378-390 (2014).

22. B. Julien, A. D. Kaiser, A. Garza, Spatial control of cell differentiation in *Myxococcus xanthus*. *Proc Natl Acad Sci U S A* **97**, 9098-9103 (2000).

23. V. Jakovljevic, S. Leonardy, M. Hoppert, L. Søgaard-Andersen, PilB and PilT are ATPases acting antagonistically in type IV pilus function in *Myxococcus xanthus*. *J. Bacteriol.* **190**, 2411-2421 (2008).

24. M. Sun, M. Wartel, E. Cascales, J. W. Shaevitz, T. Mignot, Motor-driven intracellular transport powers bacterial gliding motility. *Proc. Natl. Acad Sci. U S A* **108**, 7559-7564 (2011).

25. E. Arslan, H. Schulz, R. Zufferey, P. Kunzler, L. Thöny-Meyer, Overproduction of the *Bradyrhizobium japonicum* c-type cytochrome subunits of the cbb3 oxidase in *Escherichia coli*. *Biochem Biophys Res Commun* **251**, 744-747 (1998).

8.2 Mechanism of polar localization of the type IVa pilus machine

This chapter contains our analysis of the mechanism and timing of the polar localization of the PilQ secretin of *M. xanthus.* This part of the thesis is written in a manuscript style and was in press at time of submission of the thesis. I contributed to this work by designing, performing and analyzing experiments, preparing the figures and the manuscript.

I performed experiments and analysis in Fig. 2B-F, 3B-E, 4A, 5A-B, 6A-B, 7A-G, 8A-I, S1A and C-D, S4A-G, S5.

The mechanism for polar localization of the type IVa pilus machine

Marco Herfurth[a, b], María Pérez-Burgos[a, b] and Lotte Søgaard-Andersen[a, #]

[a]Max Planck Institute for Terrestrial Microbiology, Department of Ecophysiology,

35043 Marburg, Germany

[b] contributed equally to this work. Author order was determined alphabetically.

[#] Corresponding author

Tel. +49-(0)6421-178201

Fax +49-(0)6421-178209

E-mail: sogaard@mpi-marburg.mpg.de

Abstract

Type IVa pili (T4aP) are important for bacterial motility, adhesion, biofilm formation and virulence. This versatility is based on their cycles of extension, adhesion, and retraction. The conserved T4aP machine (T4aPM) drives these cycles, however the piliation pattern varies between species. To understand how these patterns are established, we focused on the T4aPM in *Myxococcus xanthus* that assembles following an outside-in pathway, starting with the polar incorporation of the PilQ secretin forming a multimeric T4aP conduit in the outer membrane. We demonstrate that PilQ recruitment to the nascent poles initiates during cytokinesis, but most is recruited to the new poles in the daughters after completion of cytokinesis. This recruitment depends on the peptidoglycan-binding AMIN domains in PilQ. Moreover, the pilotin Tgl stimulates PilQ multimerization in the outer membrane, is transiently recruited to the nascent and new poles in a PilQ-dependent manner, and dissociates after completion of secretin assembly. Altogether, our data support a model whereby PilQ polar recruitment and multimerization occur in two steps: The PilQ AMIN domains bind septal and polar peptidoglycan, thereby enabling polar Tgl localization, which then stimulates secretin multimerization in the outer membrane. Using computational analyses, we provide evidence for a conserved mechanism of T4aPM pilotins whereby the pilotin transiently interacts with the unfolded β-lip, i.e. the region that eventually inserts into the outer membrane, of the secretin monomer. Finally, we suggest that the presence/absence of AMIN domain(s) in T4aPM secretins determines the different T4aPM localization patterns across bacteria.

Importance

Type IVa pili (T4aP) are widespread bacterial cell surface structures with important functions in motility, surface adhesion, biofilm formation and virulence. Different bacteria have adapted different piliation patterns. To address how these patterns are established, we focused on the bipolar localization of the T4aP machine in the model organism *M. xanthus* by studying the localization of the PilQ secretin, the first component of this machine that assembles at the poles. Based on experiments using a combination of fluorescence microscopy, biochemistry and computational structural analysis, we propose that PilQ, and specifically its AMIN domains, binds septal and polar peptidoglycan, thereby enabling polar Tgl localization, which then stimulates PilQ multimerization in the outer membrane. We also propose that the presence and absence of AMIN domains in T4aP secretins determine the different piliation patterns across bacteria.

Keywords: Secretin, pilotin, type IV pili, AMIN domain, PilQ, peptidoglycan, *Myxococcus xanthus*

Introduction

In bacteria, motility is important for a wide range of processes, including virulence, colonization of habitats, and biofilm formation (1, 2). Two large non-homologous envelope-spanning machines drive the two most common bacterial motility mechanisms, i.e. the extension/retraction of surface-exposed type IVa pili (T4aP) that enable cells to translocate across solid surfaces and the rotation of surface-exposed flagella that enable cells to swim through liquids or swarm across semisolid surfaces (2). Interestingly, the patterns in which these machines are positioned in cells vary between species (2-4). For both flagella and T4aP, these distinct patterns are important for efficient motility, biofilm formation and virulence (3, 5, 6). How these patterns are established is poorly understood.

T4aP are highly versatile and not only important for motility but also for surface sensing, adhesion to and colonization of host cells and abiotic surfaces, biofilm formation, virulence, predation, and DNA uptake (4, 7). The versatility of T4aP is based on their cycles of extension, surface adhesion, and retraction that are driven by the T4aP machine (T4aPM), a multiprotein complex that consists of at least 15 different proteins and spans from the outer membrane (OM) to the cytoplasm (Fig. 1) (4, 8-12). Cryo-electron tomography of the piliated and non-piliated forms of the T4aPM of *Myxococcus xanthus* and *Thermus thermophilus* revealed that both forms are multilayered structures (8, 9) (Fig. 1). However, while the architecture of the T4aPM is conserved, bacteria have adapted different piliation patterns. Specifically, in the rod-shaped cells of *Pseudomonas aeruginosa* (13, 14) and *Myxococcus xanthus* (15, 16), T4aP localization alternates between the two cell poles, while in the rod-shaped *Thermosynechococcus vulcanus* cells, they localize at both cell poles simultaneously (17). They localize in a “line along the long cell axis” (from hereon, lateral pattern) in the coccobacillus-shaped *Acinetobacter baylyi* cells (6), to the junctions between cells in the hormogonium of *Nostoc punctiforme* (18), and peritrichously in the rods of *Burkholderia cepacia* (19) and in the coccoid-shaped cells of *Neisseria meningitidis* (20), *Neisseria gonorrhoeae* (21), *Moraxella catarrhalis* (22) and *Synechocystis* sp. PCC6803 (23). Accordingly, the T4aPM has specifically been shown to localize to both poles in *P. aeruginosa* (14, 24, 25) and *M. xanthus* (26-29), laterally in *A. baylyi* (6), and to the intercellular junctions in *N. punctiforme* (18). To address how and when these T4aPM localization and piliation patterns are established, we focused on its bipolar localization in the model organism *M. xanthus*.

As noted, *M. xanthus* assembles T4aPM at both poles, but the T4aPM are only active at one pole at a time and this pole changes on average every 10-15 min (30, 31). The assembly of the T4aPM at the two poles in *M. xanthus* depends on the OM secretin PilQ (Fig. 1) and follows an outside-in pathway (8, 27). Without the secretin, the remaining components either do not

accumulate or are not incorporated into the T4aPM (27). Moreover, assembly of the T4aPM was suggested to occur at the nascent and new cell pole during and immediately after the completion of cytokinesis (27). The secretin forms the conduit for the T4aP in the OM (8, 9) (Fig. 1). In contrast to canonical OM β-barrel proteins in which a single polypeptide forms the β-barrel, the β-barrel formed by a secretin is generated from 12-15 subunits and most of the secretin pore is periplasmic (8, 32-36). Secretin protomers comprise two major subdomains, an N-terminal species-specific region and the C-terminal conserved pore-forming region (32). The N-terminal region contains at least two N-domains and, in the case of T4aPM secretins, also occasionally one or more PG-binding AMIN domains (24, 32, 34). The C-terminal region comprises the secretin domain and the β-lip region and forms most of the barrel and a gate that closes the pore (34, 37). The periplasmic part of the secretin oligomer forms a large vestibule, which is open towards the periplasm and closed towards the OM by the gate (32). Secretins also facilitate substrate translocation across the OM in diverse other T4P systems and in type II secretion systems (T2SS) as well as type III secretion systems (T3SS) (32, 33). For their assembly in the OM, secretins rely on a cognate pilotin protein that assists in (1) secretin monomer transport to OM (38-40), (2) secretin insertion in the OM (37, 41), (3) secretin oligomerization in the OM (27, 29, 37, 39, 42), and/or (4) protection of the secretin monomer from proteolytic degradation (43, 44). Pilotins are OM periplasmic lipoproteins (33). In *M. xanthus,* the OM lipoprotein Tgl is the cognate PilQ pilotin (45-48). Lack of Tgl causes a defect in PilQ multimerization (27, 29). Consequently, in the absence of Tgl, the remaining parts of the T4aPM do not accumulate or not assemble (27). Interestingly, the lack of PilQ assembly in Δ*tgl* cells can be extracellularly complemented by Tgl$^+$ cells in a process referred to as OM-exchange, in which OM proteins are exchanged between cells (45, 48-50).

To understand how T4aPM becomes polarly localized in *M. xanthus*, we investigated when and how the PilQ secretin is recruited to the poles. We show that PilQ recruitment to the nascent pole initiates during cytokinesis, but most is recruited to the new poles in the daughter cells after completion of cytokinesis. We also demonstrate that Tgl is transiently recruited to the nascent and new poles during and after cytokinesis in a PilQ-dependent manner, and that Tgl dissociates after secretin assembly is completed. Based on a dissection of PilQ, our data support that its N-terminal PG-binding AMIN domains are crucial for its septal and polar recruitment likely via binding to PG specific to the septum and cell poles. Our data support a model whereby PilQ monomers are recruited to the nascent and new cell poles by specific septal and polar PG via their AMIN domains, thereby enabling Tgl localization, and, consequently, secretin assembly in the OM. We also propose that the presence/absence of PG-binding AMIN domain(s) in T4aPM secretins is responsible for the different localization patterns of T4aPM across bacteria.

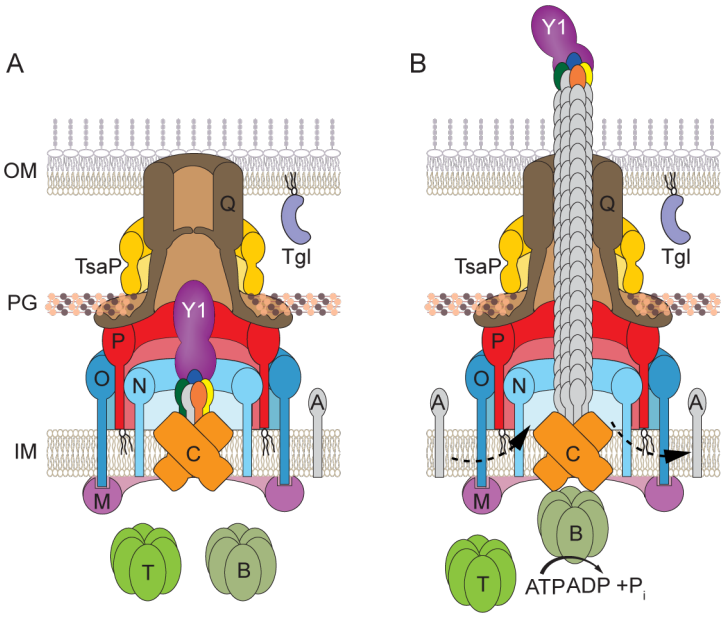

Figure 1. Architectural model of the T4aPM

Architectural model of the cell envelope-spanning non-piliated (A) and (B) piliated T4aPM (B) of *M. xanthus* with the 15 core proteins (8). The T4aPM is divided into five parts: (1) The OM secretin channel is formed by PilQ and stabilized by the LysM domain protein TsaP (28). (2) The PilN/-O/-P periplasmic alignment complex is anchored in the inner membrane (IM) and interact with PilQ. (3) The IM/cytoplasmic platform complex is composed of PilC/-M. (4) The extension/retraction ATPases PilB/-T bind to the cytoplasmic base of the T4aPM in a mutually exclusive manner (8, 95, 96). (5) The pilus fiber is formed by PilA subunits and a priming complex , composed of PilY1 and four minor pilins (blue: PilX, green: PilW, orange: PilV, yellow: FimU), that remains at the tip of the extended T4aP (8, 12). Tgl is an OM lipoprotein that is required for PilQ secretin assembly (27, 29). Bent arrows indicate incorporation of and removal from the pilus base of PilA during extension and retraction, respectively. Proteins labeled with single letters have the Pil prefix.

Results

The secretin PilQ is stably recruited to the nascent and new poles

Previously, PilQ was suggested to be recruited to the nascent and new poles of *M. xanthus* cells during and immediately after completion of cytokinesis (27). In those experiments, a partially active PilQ-sfGFP fusion that accumulated at a reduced level was used (27). To reassess PilQ recruitment to the nascent pole, we used a strain, in which an active PilQ-sfGFP fusion protein was expressed from the native site (5) (Fig. S1A). In immunoblots, the heat- and SDS-resistant PilQ multimer accumulated at close to native levels while the monomer was only detected at a very low level (Fig. 2A). Of note, a small fraction of PilQ-sfGFP was cleaved to PilQ and sfGFP (Fig. 2A).

In agreement with previous observations that the *M. xanthus* T4aPM assembles at both cell poles (8, 26-29), PilQ-sfGFP overall localized in a bipolar pattern (Fig. 2B) and ~19±6% of the fluorescent signal is polar (5). However, we noticed that long cells had more symmetric bipolar PilQ-sfGFP clusters, while short cells had a higher degree of asymmetry and a few short cells

even only had a unipolar signal (Fig. 2B and C). We did not reliably identify dividing cells with PilQ-sfGFP at the nascent poles at the constriction site at mid-cell.

To determine whether PilQ-sfGFP can be recruited to the nascent cell poles during cytokinesis, we treated cells with cephalexin to inhibit FtsI that catalyzes PG cross-linking at the septum (51), and blocks cytokinesis after the initiation of constriction in *M. xanthus* (52, 53). In cells treated with cephalexin for 4-5 h, largely corresponding to one doubling time, the cell length had increased, the bipolar PilQ-sfGFP signals were more symmetrical, unipolar PilQ-sfGFP localization was not observed, and, importantly, PilQ-sfGFP localized at the constriction site at mid-cell in two-thirds of the cells (Fig. 2B). The cluster at the constriction site was stable when treated cells were followed by time-lapse fluorescence microscopy (Fig. 2D). These observations demonstrate that PilQ-sfGFP can be stably incorporated into the nascent poles during cytokinesis. Consistent with these findings, we observed by time-lapse fluorescence microscopy of untreated PilQ-sfGFP-expressing cells that ~20% of cells had a very faint PilQ-sfGFP cluster at the constriction site at mid-cell up to 50 min prior to completion of cytokinesis (Fig. 2E). However, most of the clusters only became clearly visible at the new poles after completion of cytokinesis, and on average, a polar cluster became reliably visible 20 min after completion of cytokinesis. In the daughter cells, the PilQ-sfGFP clusters at the new poles increased in intensity over time, and mostly during the first 60-90 min after completion of cytokinesis, ultimately resulting in the more symmetric bipolar localization pattern (Fig. 2E and F).

We conclude that recruitment of PilQ to the nascent poles initiates during cytokinesis but most of PilQ is recruited over the first 60-90 min after completion of cytokinesis resulting in a symmetric bipolar localization of PilQ. We speculate that we did not detect a PilQ-sfGFP signal at the site of division in the analysis of snapshots (Fig. 2B) because the PilQ-sfGFP signal before completion of cytokinesis is too faint to be reliably detected and only becomes reliably detected when cells are followed in time-lapse microscopy experiments.

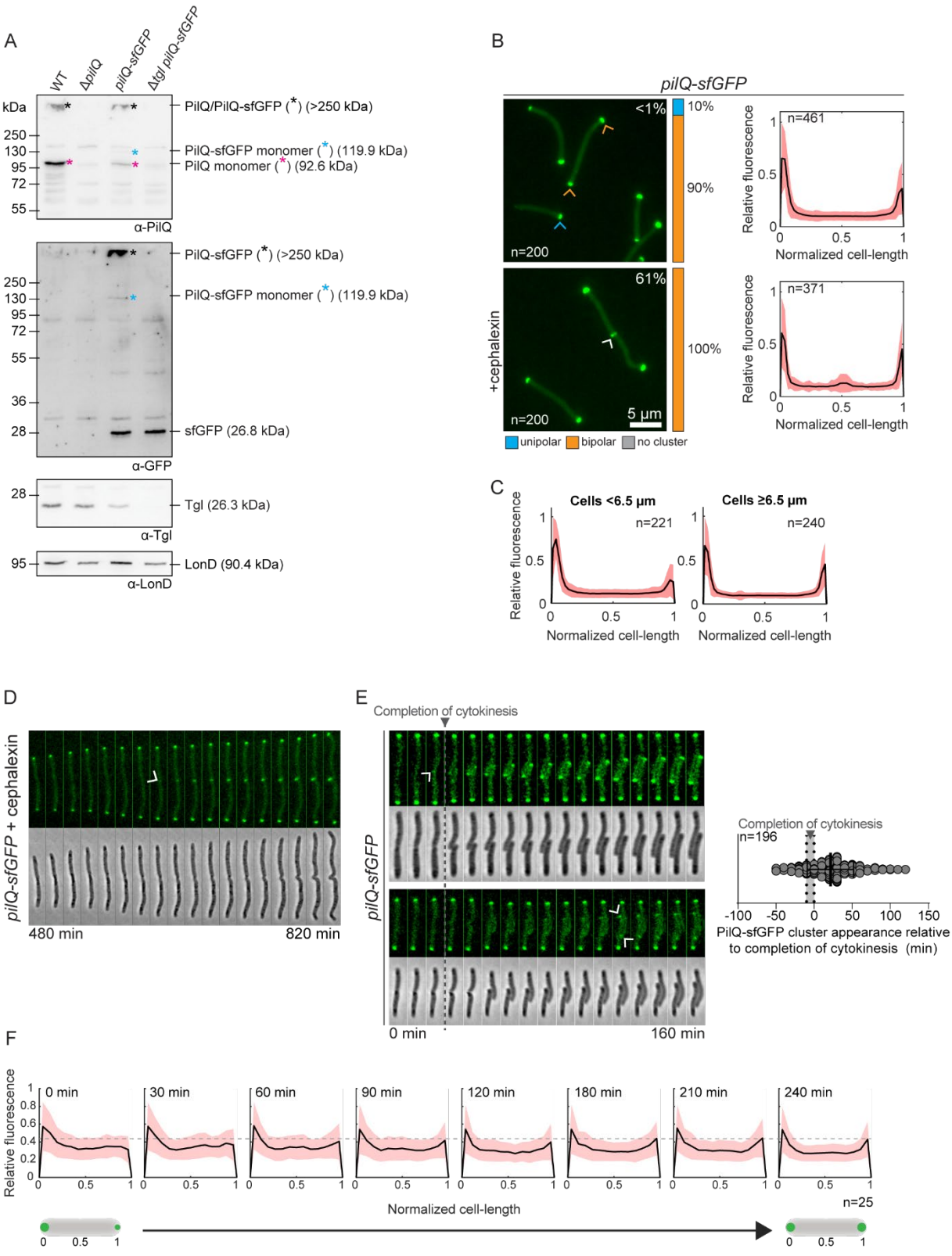

Figure 2. Accumulation of PilQ variants and localization of PilQ-sfGFP

(A) Immunoblot detection of PilQ/PilQ-sfGFP. Protein from the same number of cells from exponentially growing suspension cultures was loaded per lane. Blot was probed with the indicated antibodies. The blot was stripped before applying a new antibody. LonD served as a loading control. Monomeric and oligomeric forms of PilQ/PilQ-sfGFP are marked with an asterisk. Calculated molecular weights of proteins without signal peptide (if relevant) are indicated. (B) Localization of PilQ-sfGFP in the presence and absence of cephalexin. Left panels, representative epifluorescence images of cells expressing PilQ-sfGFP. The percentage of cells with a unipolar (blue), bipolar (orange) cluster localization pattern or no cluster (grey) is indicated. Blue, orange and white arrowheads indicate unipolar, bipolar and mid-cell

clusters. Percentage of cells with a mid-cell cluster is indicated in white. Right panels, normalized fluorescence profiles of cells, for which a cluster was detected, as a function of the relative cell length. Mean (black line) and standard deviation (SD) (orange) of the relative fluorescence along the normalized cell are depicted. Cell length was normalized from 0 to 1, where 0 is assigned to the pole with the highest fluorescent value. (C) Localization of PilQ-sfGFP in short (<6.5 µm) and long (≥6.5 µm) cells. Same cells analyzed as in untreated cells in B. Signals are shown as in B, right panel. (D) Time-lapse microscopy of a PilQ-sfGFP expressing cell treated with cephalexin. Epifluorescence and phase-contrast images are shown. Arrow indicates first time point at which the PilQ-sfGFP cluster is clearly visible at mid-cell. Time indicates time point after the addition of cephalexin (t=0). (E) Polar recruitment of PilQ-sfGFP during the cell cycle. Left panels, epifluorescence and phase-contrast images from time-lapse microscopy of cells expressing PilQ-sfGFP. PilQ-sfGFP clusters are visible at the nascent poles during (upper panel) or after completion (lower panel) of cytokinesis. Arrowheads indicate first time point at which the PilQ-sfGFP cluster is clearly visible. Right panel, analysis of appearance of the PilQ-sfGFP cluster relative to completion of cytokinesis for each daughter cell. The first time point after completion of cytokinesis is defined as t=0 and indicated by the grey vertical bar. The black line and error bars represent the mean ± SD. The appearance of PilQ-sfGFP clusters was studied in 196 daughter cells. (F) Analysis of polar incorporation of PilQ-sfGFP after completion of cytokinesis. The cellular fluorescence was quantified at different time points after completion of cytokinesis and the relative fluorescence along a normalized cell was plotted. Mean (black line) and SD (orange) are indicated. Cell length was normalized from 0 to 1, where 0 was assigned to the old pole. n=25. In D-F, to follow cells on hard agar by time-lapse microscopy for extended periods of time and avoid that they move out of the field of view, all strains contain an in-frame deletion of *gltB* (Δ*gltB),* which encodes a component of the *M. xanthus* gliding motility machine (85, 97).

The pilotin Tgl is transiently recruited to the nascent and new poles

Next, we investigated the localization of the pilotin Tgl. We previously analyzed Tgl localization using a strain overexpressing an active Tgl-sfGFP protein and found that it localized to the cell envelope but not specifically at the cell poles or the division site (27). By contrast, Nudleman et al. found by immunostaining that Tgl localized unipolarly in ~30% of the cells (29). To resolve the localization of Tgl, we generated a strain expressing the active Tgl-sfGFP fusion (Fig. S1A) from the native site at native levels (Fig. 3A) and reevaluated its localization.

In all cells, Tgl-sfGFP localized along the entire cell periphery in a pattern typical of proteins localizing to the cell envelope (Fig. 3B). Moreover, in 14% of the cells, Tgl-sfGFP also localized in a unipolar cluster, and these cells were typically short in length (Fig. 3B and C). Additionally, in 4% of the cells, Tgl-sfGFP localized at the constriction site, and these were typically long cells (Fig. 3B and C). In the remaining cells, Tgl-sfGFP did not form clusters (Fig. 3B). We note that Tgl-sfGFP localization is very different from the bipolar localization of the T4aPM in *M. xanthus* cells. We speculate that in our previous analysis of Tgl-sfGFP localization, its overexpression and the resulting strong cell envelope signal likely masked the weak Tgl-sfGFP clusters at the nascent and new poles.

Treatment of Tgl-sfGFP-expressing cells with cephalexin caused a significant increase in the fraction of cells with a mid-cell cluster, and while the fraction of cells with a unipolar signal remained unchanged, this signal was substantially weaker than in untreated cells (Fig. 3B). Of note, the fraction of cells with Tgl-sfGFP at mid-cell was significantly lower than in the case of PilQ-sfGFP in cephalexin-treated cells (Fig. 2B). When cephalexin-treated cells were followed

by time-lapse fluorescence microscopy, we observed Tgl-sfGFP clusters appear at mid-cell in cells with constrictions, and these clusters disintegrated after ~100 min (Fig. 3D). Similarly, time-lapse fluorescence microscopy of untreated Tgl-sfGFP-expressing cells showed that the protein on average appeared at mid-cell in constricting cells ~10 min before completion of cytokinesis but in a few cells the cluster appeared up to 50 min prior to completion of cytokinesis (Fig. 3E). Upon completion of cytokinesis, the two daughters each inherited a cluster at the new pole that eventually disintegrated (Fig. 3E).The lifetime of a cluster from its first appearance until it permanently disintegrated was ~70 min (Fig. 3E). Given a generation time of 5-6 h, this lifetime correlates well with the percentage of cells with unipolar and mid-cell clusters quantified in snapshots of cells expressing Tgl-sfGFP (Fig. 3B). Interestingly, the lifetime of a Tgl-sfGFP cluster coincides with the time (60-90 min) required for polar incorporation of PilQ-sfGFP at the nascent and new poles (Fig. 2E and F).

The observations that the PilQ-sfGFP cluster stably remains at mid-cell in cephalexin-treated cells (Fig. 2D), while the Tgl-sfGFP cluster disintegrates in the presence or absence of cephalexin, support that Tgl is transiently localized to the nascent and new poles to promote secretin assembly in the OM and is not part of the fully assembled T4aPM.

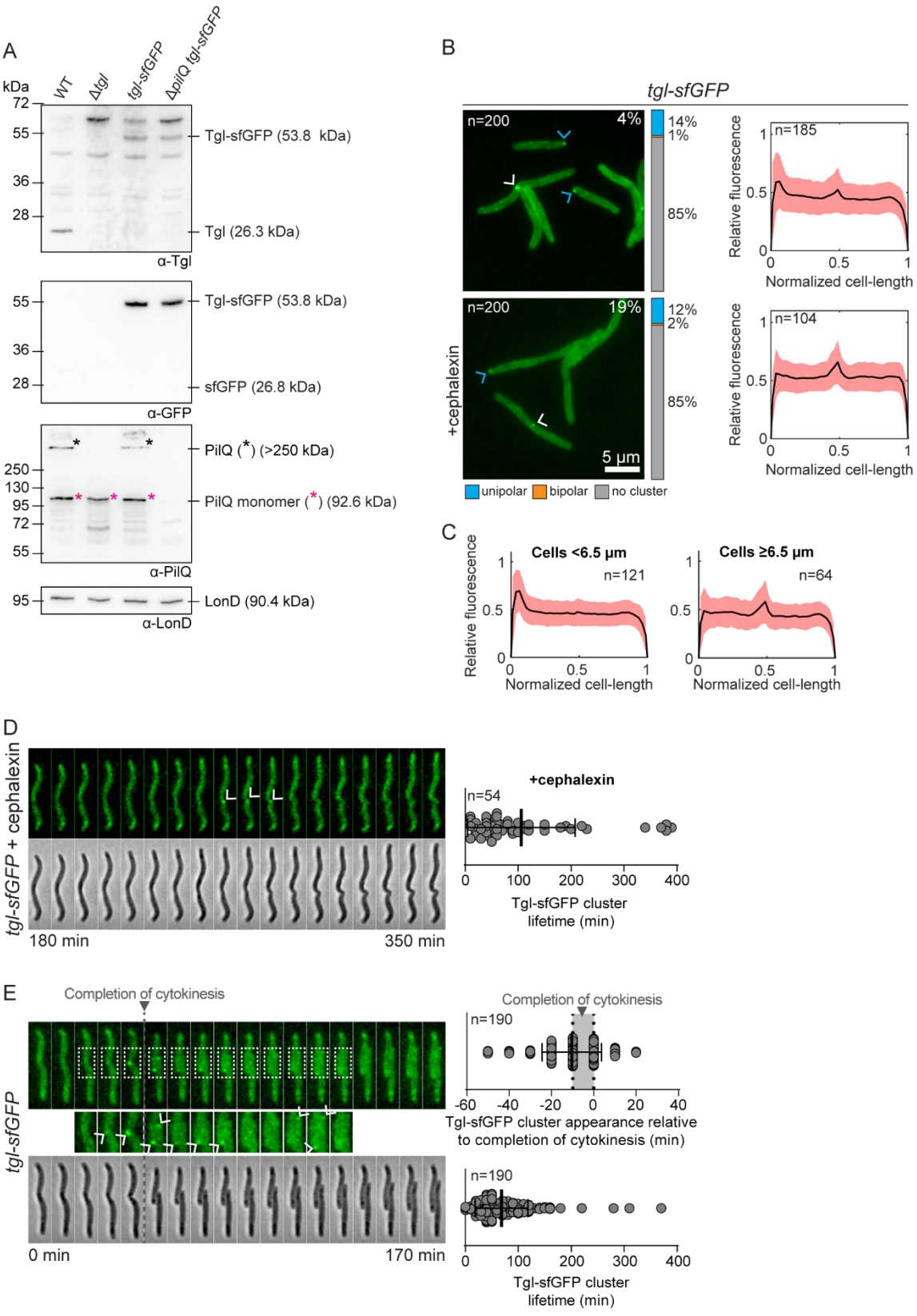

Figure 3. Accumulation of Tgl variants and localization of Tgl-sfGFP
(A) Immunoblot detection of Tgl/Tgl-sfGFP. Protein from the same number of cells from exponentially growing suspension cultures was loaded per lane. Blot was probed with the indicated antibodies. The blot was stripped before applying a new antibody. LonD served as a loading control. Monomeric and oligomeric forms of PilQ are marked with an asterisk. Calculated molecular weights of proteins without signal peptide (if relevant) are indicated. (B) Localization of Tgl-sfGFP in the presence and absence of cephalexin as in Fig. 2B. (C) Localization of Tgl-sfGFP in short (<6.5 µm) and long (≥6.5 µm) cells. Same

cells analyzed as in untreated cells in panel B. Signals are shown as in Fig. 2B, right panel. (D) Time-lapse microscopy of cells expressing Tgl-sfGFP treated with cephalexin. Left panel, epifluorescence and phase-contrast images are shown. Arrows indicate time points at which the Tgl-sfGFP cluster is clearly visible. Time indicates time point after the addition of cephalexin (t=0). Right diagram shows lifetime of Tgl-sfGFP clusters. The black line and error bars represent the mean ± SD. n=54. (E) Recruitment of Tgl-sfGFP to the nascent and new poles during the cell cycle. Left panel, epifluorescence and phase-contrast images from time-lapse microscopy of a cell expressing Tgl-sfGFP. Tgl-sfGFP clusters generally appear at the nascent poles during cytokinesis. Arrows indicate time points, at which the Tgl-sfGFP cluster is clearly visible. The boxed areas are shown below in a higher magnification. Right panels, analysis of appearance of a Tgl-sfGFP cluster relative to completion of cytokinesis for each daughter cell and lifetime of the Tgl-sfGFP cluster relative to completion of cytokinesis for each daughter cell. The first time point after completion of cytokinesis is defined as t=0 and indicated by the grey vertical bar. The black line and error bars represent the mean ± SD. The appearance of Tgl-sfGFP clusters was studied in 190 daugther cells. In D-E, strains analyzed contain the Δ*gltB* mutation.

Tgl is important for multimerization and stability of PilQ and PilQ is important for polar recruitment of Tgl

Our fluorescence microscopy analyses showed that Tgl-sfGFP on average formed a visible cluster at mid-cell slightly earlier than PilQ-sfGFP (Fig. 2E vs Fig. 3E). We, therefore hypothesized that Tgl could be responsible for recruiting PilQ to mid-cell during cytokinesis. To this end, we analyzed protein accumulation and localization of each fluorescent fusion in the absence of the other.

In agreement with previous observations (27, 29), only the monomer fraction of PilQ and PilQ-sfGFP accumulated in the Δ*tgl* mutant (Fig. 2A and 3A), confirming that Tgl is important for multimerization of PilQ. We also noticed that the total level of the PilQ variants, and especially of PilQ-sfGFP, was reduced in the absence of Tgl (Fig. 2A and Fig. 3A), arguing that Tgl is also important for PilQ stability. Accordingly, the PilQ-sfGFP fluorescent signal was strongly reduced, and as reported (27), polar and mid-cell clusters were not detected (Fig. 4A). In previous immunofluorescence studies using a Δ*tgl*:: *tet*^{R} strain, PilQ was reported to localize to the poles in the absence of Tgl (29), however, we did also not observe PilQ-sfGFP clusters in this strain background (Fig. S1B and C).

In the inverse experiment, we observed that Tgl and Tgl-sfGFP accumulated at the same level in the presence and absence of PilQ (Fig. 2A and Fig. 3A) and that Tgl-sfGFP localized at the cell envelope (Fig. 4A). However, Tgl-sfGFP neither formed unipolar nor mid-cell clusters in the absence of PilQ (Fig. 4A). Because Tgl-sfGFP accumulates at native levels but does not form polar or mid-cell clusters in the absence of PilQ, these data support that PilQ recruits Tgl to mid-cell and the poles rather than the other way around. We note that the time-lapse fluorescence microscopy analyses showed that Tgl-sfGFP on average formed a visible cluster at mid-cell slightly earlier than PilQ-sfGFP (Fig. 2E vs Fig. 3E). Because cells expressing PilQ-sfGFP also accumulate a fraction of untagged PilQ monomer (Fig. 2A), we speculate that the slight delay (30 min) in the average timing of PilQ-sGFP recruitment to the nascent/new poles

relative to the average recruitment of Tgl-sfGFP could originate from a preference of untagged PilQ for the constriction site.

PilQ recruitment to the nascent and new poles depend on the AMIN domains

Next, we addressed how PilQ is recruited to the nascent poles. In *P. aeruginosa*, localization to the division site of the inner membrane (IM) protein PilO (Fig. 1), and therefore the T4aPM, to the nascent poles at the constriction site depends on the PG-binding AMIN domains of PilQ (24). The *M. xanthus* PilQ contains three AMIN domains, one of which is sufficient for the correct assembly and polar localization of the T4aPM (8). We, therefore, speculated that deletion of all three AMIN domains would prevent PilQ from being recruited to the nascent and new poles.

To this end, we generated a strain expressing a PilQ variant lacking all three AMIN domains fused to sfGFP (PilQ$^{\Delta AMIN\times3}$-sfGFP) from the native site. In immunoblots with α-GFP antibodies, monomeric PilQ$^{\Delta AMIN\times3}$-sfGFP accumulated at high levels, although a significant fraction of the protein was also cleaved to generate free sfGFP, and no heat-resistant multimers were detected (Fig. 4B). Consistently, cells expressing PilQ$^{\Delta AMIN\times3}$-sfGFP were non-motile (Fig. S1A). Because PilQ$^{\Delta AMIN\times3}$-sfGFP was not detected by the PilQ antibodies (Fig. 4B), we suggest that the epitopes detected by these antibodies are within the AMIN domains. Consistent with the three AMIN domains being essential for polar PilQ recruitment, PilQ$^{\Delta AMIN\times3}$-sfGFP did not generate mid-cell and polar clusters (Fig. 4A). We conclude that the three AMIN domains are required for recruitment of PilQ to the nascent and new poles and multimer formation.

Next, to test whether the three AMIN domains are sufficient for polar recruitment, we generated a fusion in which the three AMIN domains were fused to sfGFP (PilQ^{AMINs}-sfGFP). However, immunoblot analysis and fluorescence microscopy revealed that PilQ^{AMINs}-sfGFP did not accumulate thus precluding further analyses (Fig. 4B and Fig. S1D).

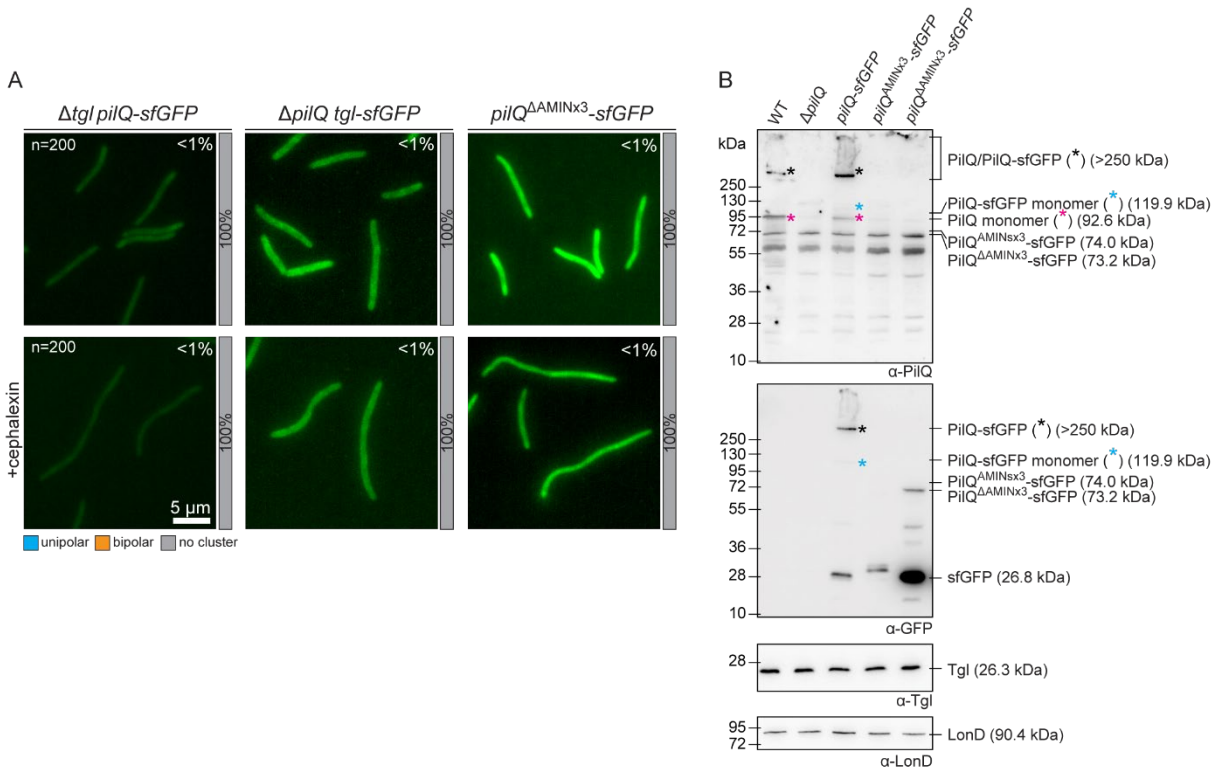

Figure 4. Polar Tgl-sfGFP localization depends on PilQ and polar PilQ-sfGFP localization depends on its AMIN domains.
(A) Localization of PilQ-sfGFP and Tgl-sfGFP in the absence of the other as well as localization of PilQ$^{\Delta AMINx3}$-sfGFP in the presence and absence of cephalexin as in Fig. 2B, left panel. (B) Immunoblot detection of PilQ$^{AMIN\times3}$-sfGFP and PilQ$^{\Delta AMIN\times3}$-sfGFP. Protein from the same number of cells from exponentially growing suspension cultures was loaded per lane. The same blot was stripped before applying a new antibody. LonD served as a loading control. Monomeric and oligomeric forms of the PilQ-sfGFP variants are marked with an asterisk. Calculated molecular weights of proteins without signal peptide (if relevant) are indicated.

Cell division-independent polar recruitment of PilQ

Generally, septal and polar PG contains fewer stem peptides, is considered metabolically mostly inert and modifications acquired during cytokinesis are retained at the poles indefinitely (54, 55). Moreover, it has been shown that the AMIN domain of the cell division protein AmiC in *Escherichia coli* binds to septal PG during cytokinesis (56-58). Based on these considerations, and because the three PilQ AMIN domains are required for polar recruitment of PilQ, we hypothesized that the old cell poles would have the properties required for recruitment and incorporation of the PilQ secretin in the OM independently of a cell division event. To test this hypothesis, we expressed PilQ-sfGFP in a Δ*pilQ* mutant under the control of the vanillate-inducible promoter (P_{van}) and then followed its polar recruitment (Fig. 5A and Fig. S2A). Remarkably, we observed that PilQ-sfGFP was recruited to both poles independently of cell division as well as to mid-cell when cells started constricting (Fig. 5A). As expected, neither polar nor mid-cell PilQ-sfGFP recruitment was observed in the absence of Tgl (Fig. 5A and Fig. S2A). Consistently, we also observed that upon induction of untagged PilQ synthesis in the Δ*pilQ* strain additionally expressing Tgl-sfGFP from the native site, Tgl-

sfGFP transiently formed clusters at both poles (Fig. 5B and Fig. S2B). Finally, to determine whether PilQ recruited to the poles independently of cell division was competent to guide the assembly of the remaining components of the T4aPM, we repeated the PilQ induction experiment in a strain additionally expressing an active mCherry-PilM fusion (12) from the native site. The cytoplasmic PilM protein (Fig. 1) is the last component to be incorporated into the polar T4aPM in *M. xanthus* (27). Before induction of PilQ synthesis, mCherry-PilM localized diffusely to the cytoplasm; importantly, upon induction of *pilQ* expression, PilM also localized in a bipolar pattern (Fig. 5B and Fig. S2C).

Based on these observations, we conclude that the polar recruitment and OM incorporation of PilQ can occur at both poles independently of cell division, and that these secretins support the assembly of the remaining components of the T4aPM. Because this incorporation depends on Tgl, we also conclude that the cell division-independent PilQ incorporation into the OM follows the same mechanism as in the case of its incorporation at nascent and new poles.

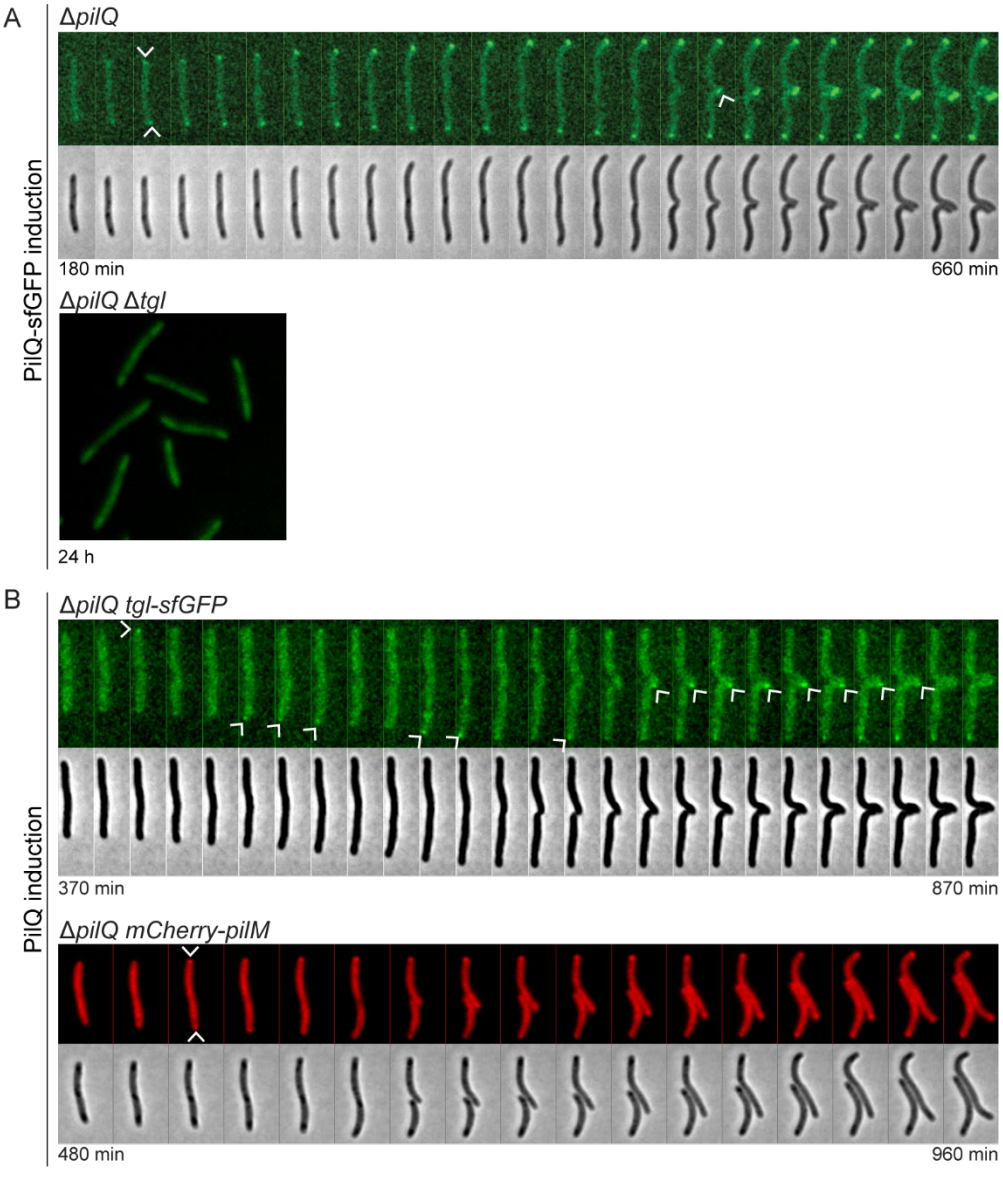

Figure 5. Cell division-independent assembly of T4aP machines
(A, B) Induction of expression of *pilQ-sfGFP* (A) or *pilQ* (B) from P_{van} in the indicated strains followed by time-lapse epifluorescence microscopy. Time indicates interval after the addition of vanillate (t=0). In A, upper panel, the arrows indicate the first appearance of fluorescent clusters of PilQ-sfGFP. In A, lower panel, cells are shown after 24 hrs of PilQ-sfGFP induction in the Δ*tgl* mutant. In A, 10 µM vanillate was used for inducing PilQ-sfGFP accumulation at WT levels in the Δ*pilQ* background (Fig. S4A), and 500 µM vanillate was used to highly induce PilQ-sfGFP accumulation in the Δ*tgl* Δ*pilQ* background (Fig. S4A). In B, upper panel, 20 µM vanillate was used for inducing PilQ accumulation at WT levels in Δ*pilQ* cells expressing *tgl-sfGFP* (Fig. S4B). Arrows indicate time points at which the Tgl-sfGFP cluster is clearly visible. In B, lower panel 1mM vanillate was used to rapidly induce *pilQ* expression in cells co-expressing *mCherry-pilM* (Fig. S4C). Arrows indicate the first appearance of fluorescent clusters of mCherry-PilM. Localization of mCherry-PilM at the poles is used as a proxy to study correct assembly of the T4aPM. In A and B, strains analyzed contain the Δ*gltB* mutation.

Tgl is not important for PilQ transport across the periplasm

To evaluate whether OM localization of Tgl is important for its function, we generated a strain expressing Tgl^{C20G}-sfGFP (using the numbering of the full-length protein), in which the conserved Cys residue (+1 in the mature protein) (Fig. S3A) was substituted to Gly to prevent its acylation and, therefore, transport to and anchoring in the OM. Additionally, because an Asp in position +2 of mature lipoproteins in *Escherichia coli* can cause their retention in the IM (59), we also generated a strain expressing Tgl^{S21D}-sfGFP. Expression of Tgl^{C20G}-sfGFP and Tgl^{S21D}-sfGFP from the native site or under the control of P_{van} only resulted in very low levels of accumulation of the proteins (Fig. S3B), thus precluding their further analyses.

Therefore, to obtain more insights into the function of Tgl, we determined the subcellular localization of PilQ in cell fractionation experiments in the presence and absence of Tgl. In wild-type (WT) cells, the PilQ monomer and multimer were enriched in the membrane fraction (Fig. 6A). Similarly, in Δ*tgl* cell extracts, monomeric PilQ was enriched in the membrane fraction. Control proteins previously shown to localize to the IM, OM or cytoplasm documented that the fractionation procedure worked properly (Fig. 6A).

To determine whether monomeric PilQ is integrated in the IM or OM, we isolated the OM of WT and Δ*tgl* cells after osmotic shock with sucrose and EDTA treatment. Monomeric PilQ was detected in the OM fraction of both strains (Fig. 6B). As expected, in WT extracts, the heat- and detergent-resistant oligomers were also enriched in the OM fraction, while controls fractionated as expected (Fig. 6B). These results demonstrate that Tgl is not required for the transport of monomeric PilQ across the periplasm to the OM, and that monomeric PilQ is at to the OM.

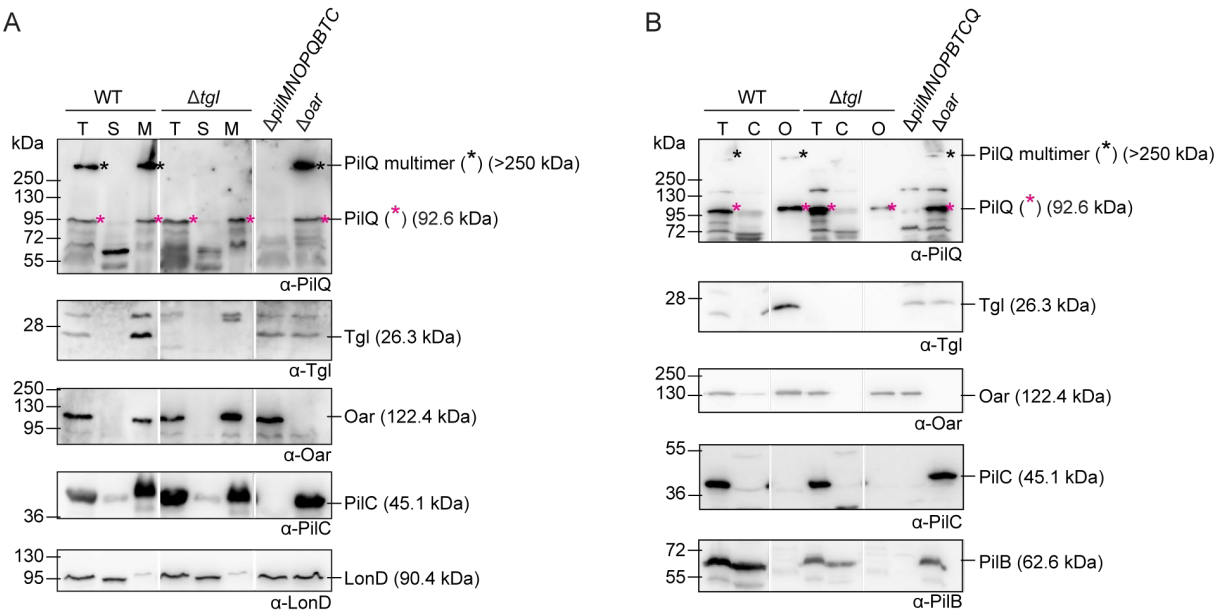

Figure 6. Subcellular localization of monomeric and multimeric PilQ as well as Tgl.
(A) Total cell extracts (T) were fractionated into fractions enriched for soluble (S) and membrane (M) proteins. (B) Total cell extracts (T) were fractionated into fractions enriched for cytoplasmic (C), and OM (O) proteins. Protein from the same number of cells was loaded per lane and analyzed by immunoblotting. Oar is an OM protein (98), PilC is an IM protein (26), and LonD and PilB are cytoplasmic proteins (26, 99). These proteins served as controls that the fractionation procedure worked properly. Monomeric and oligomeric forms of PilQ are marked with an asterisk. Calculated molecular weights of proteins without signal peptide (if relevant) are indicated. Gaps indicate lanes removed for presentation purposes.

A computational structural model of the Tgl/PilQ complex

To evaluate how Tgl interacts with monomeric PilQ to promote its stability and multimerization in the OM, we analyzed the two proteins *in silico*. While the sequences of T4aPM pilotins are not well conserved (39) (Fig. S3A), it was previously suggested that they all share a similar superhelix structure composed of six TPR motifs (45, 60), which are typically involved in protein-protein interactions (61). In agreement with this suggestion, a high-confidence AlphaFold-based structure of monomeric Tgl includes 13 anti-parallel α-helices, among which helices 1 to 12 fold into six TPR motifs forming a superhelix (Fig. 7A and Fig. S3C). Additionally, the Tgl structural model could readily be superimposed on the solved structures of PilF and PilW (pilotins of the secretin of the T4aPM in *P. aeruginosa* and *N. meningitidis,* respectively (60, 62)) (Fig. 7B). While PilF does not contain disulfide bridges and PilW contains one, which is crucial for its function and connects TPR domains 3 and 4 (Fig. S3A) (60, 63), Tgl is predicted to contain three disulfide bridges that link TPR domains 5 and 6 as well as TPR 6 and α-helix 13 (Fig. 7A and Fig. S3A). Conservation analysis of the amino acid sequence of Tgl homologs using ConSurf revealed two conserved hydrophobic surfaces, one in the N-terminal TPR1 (from hereon CS1) and one within the concave groove of Tgl close to CS1 (from hereon CS2) (Fig. 7C).

In secretins, the two or more conserved N-terminal N-domains are involved in oligomerization (64), interaction with IM components of the T4aPM (65), and also form part of the periplasmic vestibule, while the AMIN domains, if present, bind PG (24, 32, 34) (Fig. 7D). In the C-terminal region, the secretin domain (PF00263) forms β-sheets, which in the secretin oligomer form the gate, part of the periplasmic vestibule, and the amphipathic helical loop (AHL) (34, 37) (Fig. 7D). The hydrophobic surface of the AHL associates with the inner leaflet of the OM (Fig. 7D and E) (37). The amphipathic β-lip region in the C-terminal region forms part of the β-barrel (34), but mainly forms the β-stranded region with which the secretin spans the OM (Fig. 7D and E) (37).

Similar to other T4aPM secretins, PilQ from *M. xanthus* ($PilQ_{Mxa}$) is divided into four main regions: the three AMIN domains connected by flexible linkers, the N0- and N3-domains, the β-lip region and the C-terminal secretin domain (Fig. 7F). Monomeric $PilQ_{Mxa}$ was modeled with high confidence using AlphaFold (Fig. 7F and Fig. S3C) and could readily be superimposed on a protomer from the cryo-electron microscopy-based structure of *P. aeruginosa* PilQ ($PilQ_{Pae}$) (35) (Fig. 7D and Fig. S4A). Similar results were obtained when using monomeric $PilQ_{Pae}$ modeled with AlphaFold (Fig. S3C and Fig. S4A), supporting that the predicted structures are modeled with high confidence.

It is currently not known how pilotins of T4aPM secretins interact with their cognate secretin monomer. Therefore, to gain insights into how T4aPM secretins and their pilotins interact, we started with the *M. xanthus* proteins and used AlphaFold-Multimer to predict heterodimeric structures of TgI and monomeric $PilQ_{Mxa}$. Surprisingly, in the high-confidence heterodimer model, the amphipathic β-sheet of the β-lip observed in the structural model of the $PilQ_{Mxa}$ monomer (Fig. 7F and Fig. S3C) is unfolded into (1) a hydrophobic α-helix and (2) an unstructured region (Fig. 7G). Remarkably, TgI is modeled to specifically interact with this hydrophobic α-helix and this unstructured region via the conserved hydrophobic surfaces CS1 in TPR1 and CS2 in the concave groove, respectively (Fig. 7C and G). Underscoring the validity of this structural model of the heterodimer, PilF and PilW are also modeled with high confidence to associate with their partner secretin in the same way, i.e. using the same interfaces as in TgI to contact the unfolded β-lip (Fig. S4B-D). Moreover, these specific interactions appear to depend on the cognate pilotin-secretin pair, because heterodimer modeling of TgI with the *P. aeruginosa* or the *N. meningitidis* secretin yielded structural models of lower confidence, and in which some of these interactions were lost (Fig. S4E-G).

In conclusion, we suggest that T4aPM pilotins by associating with the unfolded β-lip of their cognate monomeric secretin keep this region, part of which will ultimately be inserted into the OM, in a conformation optimal for oligomerization and OM insertion. Once the secretin monomers multimerize and the correctly folded β-lip integrates into the OM, the interaction

with the pilotin would be lost, thus explaining why the pilotin only transiently associates with the secretin.

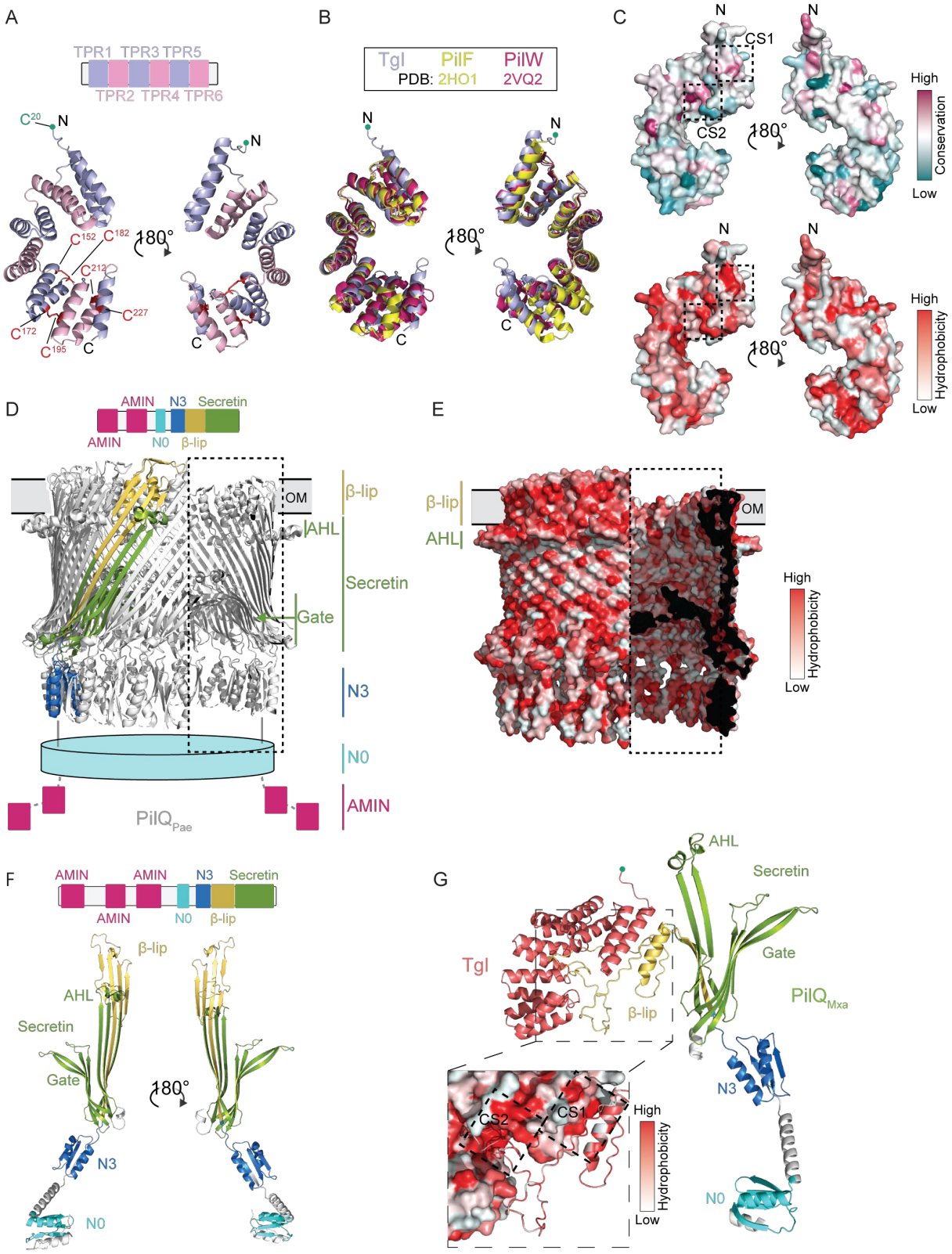

Figure 7. Structural characterization of Tgl alone and in complex with its PilQ secretin partner
(A) AlphaFold model of mature Tgl. Upper panel, TPR domains 1 to 6 in Tgl are indicated to scale. Lower panel, AlphaFold structure of Tgl. Cys residues (Cys152/Cys182, Cys172/Cys195, Cys212/Cys227, numbering for unprocessed protein) engaged in disulfide bridge formation are

indicated in red. Amino acids are indicated using the numbering of the full-length protein. (B) Superposition of the AlphaFold Tgl structure with the solved structures of PilF (PDB: 2HO1) (39) and PilW (PDB: 2VQ2) (60). (C) Surface representation of the sequence conservation calculated with ConSurf using 279 homolog sequences (upper panel) and hydrophobicity of Tgl (lower panel). The conserved hydrophobic surfaces CS1 in TPR1 and CS2 in the concave groove are marked with dashed squares. (D) CryoEM structure of the tetradecameric PilQ secretin of *P. aeruginosa* (PDB: 6VE2) (35). Upper panel, domain architecture of $PilQ_{Pae}$. Lower panel, CryoEM structure, in which the different domains of one $PilQ_{Pae}$ protomer are indicated as in (34) are colored as N3 (marine blue), secretin (green), and β-lip region (yellow). The N0 and two AMIN domains, which are not resolved in the structure, are represented by a cyan cylinder and magenta boxes, respectively. In the part of the secretin marked by the dashed box, the front part of the barrel structure has been removed to show the inside of the barrel with the gate.
(E) Surface representation of the hydrophobicity of the cryoEM solved structure of the tetradecameric $PilQ_{Pae}$ secretin. Note the amphipathic AHL and β-lip. In the part of the secretin marked by the dashed box, the front part of the barrel structure has been removed to show the inside of the barrel with the gate. Regions in which the protein structure was sliced are colored black. (F) AlphaFold model of *M. xanthus* PilQ monomer. Upper panel, domain architecture of PilQ. Lower panel, AlphaFold model with regions colored according to the domains and as described for panel D. For clarity, AMIN domains are not shown. (G) AlphaFold model of heterodimer of *M. xanthus* PilQ monomer and Tgl. Inset: Interaction interface between Tgl (surface representation) and PilQ (cartoon) colored according to hydrophobicity. The conserved hydrophobic surfaces CS1 in TPR1 and CS2 in the concave groove are marked with a dashed square. In A, B and G, the acylated N-terminal Cys residue of mature Tgl (residue Cys20 in the unprocessed protein) that places the protein at the inner leaflet of the OM is indicated by a green circle.

The presence and absence of AMIN domains in T4aPM secretins correlate with the piliation pattern

As shown here, septal and polar recruitment of the PilQ secretin, and therefore the T4aPM, in *M. xanthus* depends on its AMIN domains. Because AMIN domains are not universally conserved in T4aPM secretins (34), we wondered whether their presence or absence correlated with the localization pattern of the T4aP/T4aPM in other species. To this end, we selected bacteria with different T4aP localization patterns and studied the domain architecture of their secretin.

The PilQ secretins of *M. xanthus*, *P. aeruginosa*, *T. vulcanus* and *N. punctiforme* that localize to the cell poles (17, 18, 24) have three, two, one and one AMIN domains, respectively (Fig. 8A-D, Fig. S3C and Fig. S5). By contrast, the spherical cells of *Synechocystis* sp. PCC6803*, M. catarrhalis* as well as the rod-shaped cells of *B. cepacia* have PilQ homologs without AMIN domain (Fig. 8E-G and Fig. S5) and these species have peritrichous T4aP localization patterns (19, 22, 23). Interestingly, the coccoid *N. meningitidis* and *N. gonorrhoeae,* which assemble peritrichous T4aP (20, 21), both have PilQ homologs with two AMIN domains (Fig. 8H and Fig. S5). Finally, the PilQ homolog of *A. baylyi* contains two AMIN domains (Fig. 8I and Fig. S5), and has the unique lateral T4aP localization pattern (6).

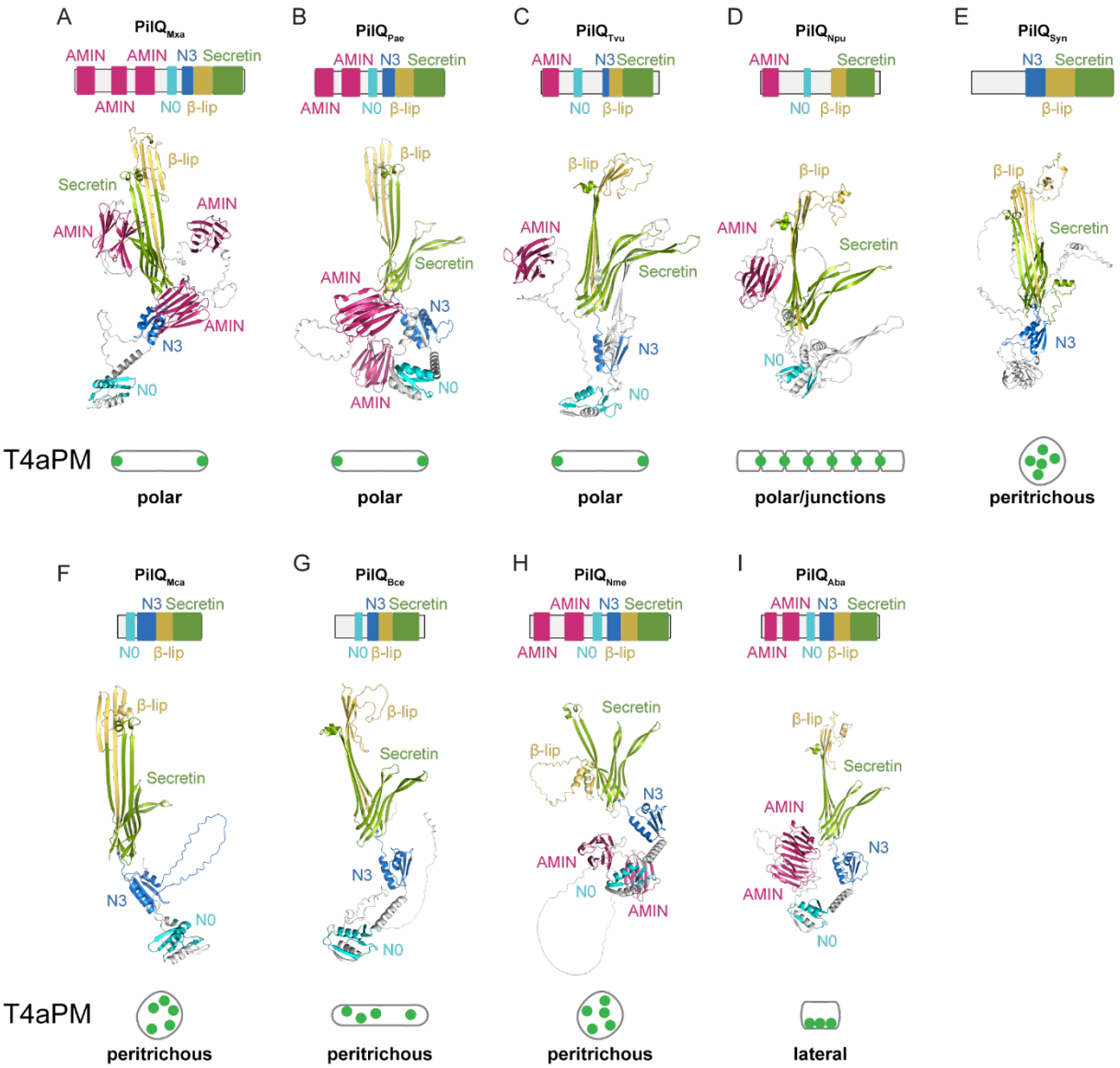

Figure 8. Characterization of PilQ secretins in other bacteria

(A-I) Domain architecture and AlphaFold models of secretin monomers from (A) *M. xanthus* ($PilQ_{Mxa}$), (B) *P. aeruginosa* ($PilQ_{Pae}$) (GenBank: AAA16704.1), (C) *T. vulcanus* ($PilQ_{Tvu}$) (GenBank: BAY52454.1), (D) *N. punctiforme* ($PilQ_{Npu}$) (GenBank: RCJ37220.1), (E) *Synechocystis* sp. PCC6803 ($PilQ_{Syn}$) (GenBank: BAA18278.1), (F) *M. catarrhalis* ($PilQ_{Mca}$) (GenBank: ADG61696.1), (G) *B. cepacia* ($PilQ_{Bce}$) (GenBank: ALK17307.1), (H) *N. meningitidis* ($PilQ_{Nme}$) (GenBank: AHW75028.1), and (I) *A. baylyi* ($PilQ_{Aba}$) (GenBank: AAK00351.1). The domains of PilQ are colored as described in Fig. 7D. T4aPM distribution within the cell is indicated (see text).

Discussion

Here, we focused on the polar incorporation of the T4aPM in the rod-shaped cells of *M. xanthus* to understand how different localization patterns of T4aP are ultimately established. *M. xanthus* is an ideal system to address this question because the T4aPM assembly pathway is well-understood and initiates with the PilQ secretin in the OM (8, 27). Thus, using PilQ as a proxy for the T4aPM allowed us to examine how the specific localization of the T4aPM is determined. We demonstrate that PilQ is recruited to and begins to assemble in the OM at the nascent pole during cytokinesis, and these processes continue for 60-90 min in the two daughter cells after completion of cytokinesis. The recruitment and assembly eventually result in the symmetric localization of PilQ at the two cell poles. Consistent with the pilotin Tgl being important for PilQ multimer formation (27, 29), we observed that Tgl transiently associated with the nascent and new cell poles in a PilQ-dependent manner and largely in parallel with PilQ recruitment and OM assembly. Moreover, we demonstrate that PilQ recruitment to and assembly at the nascent and new poles depends on its PG-binding AMIN domains.

How, then, does PilQ assembled at the nascent and new poles? Several lines of evidence support that this assembly is a two-step process that crucially depends on the PG-binding AMIN domains in PilQ in concert with Tgl. Firstly, a PilQ variant lacking all three AMIN domains accumulated but was not recruited to the nascent and new poles and did not assemble to form multimers, while a PilQ variant with only one AMIN domain is sufficient for correct assembly and polar localization of the T4aPM (8). In agreement with this observation, recruitment of the PilQ secretin in *P. aeruginosa* to the nascent poles was suggested to depend on its AMIN domains (24). AMIN domains also have crucial functions in the recruitment of the amidases AmiB and AmiC to the site of cell division in *E. coli* (56, 66) and the AmiC AMIN domain specifically binds to septal PG during cytokinesis (56-58). Secondly, previous work concluded that PG modifications acquired during cytokinesis are retained at the poles indefinitely (55). Thirdly, the pilotin Tgl, which is an OM lipoprotein, is important for PilQ stability and multimerization in the OM. Fourthly, in cells lacking PilQ, Tgl still accumulated; however, it did not localize to the nascent and new poles. Fifthly, the PilQ multimerization defect in Δ*tgl* cells can be extracellularly complemented by transfer of Tgl from Tgl^+ cells (45, 48-50). Based on these lines of evidence, we suggest a model for the polar recruitment and OM incorporation of PilQ and, consequently, the complete T4aPM. In this model, PilQ monomers and Tgl are translocated to the OM independently of each other (Fig. 9, step 1). During and immediately after cytokinesis, PilQ monomers specifically recognize and stably bind to septal and polar PG via their AMIN domains (Fig. 9, step 2). These PilQ monomers either bring along Tgl or recruit Tgl to the poles (Fig. 9, step 2). The high local concentration of PilQ/Tgl complexes at the nascent and new poles, facilitates Tgl-dependent OM incorporation and multimerization of PilQ eventually resulting in the release of Tgl (Fig. 9, step 3-4). Upon assembly of the PilQ multimer

in the OM, the remaining components of the T4aPM are incorporated (Fig. 9, step 5). In agreement with our model, PilQ can be recruited to both poles and assemble multimers in a cell-division independent manner supporting that both cell poles have the properties required for recruitment and incorporation of the PilQ secretin in the OM independently of a cell division event. We note that not all PilQ is localized to the cell poles. We, therefore, suggest that PilQ monomer recruitment to the nascent and new poles represents an example of a diffusion-and-capture mechanism for polar protein localization (67, 68). In this mechanism, OM-associated PilQ monomers and TgI diffuse in two dimensions until the PilQ monomers recognize and bind septal and polar PG that serve as a polar landmark, thereby enabling polar TgI localization (Fig. 9, step 1-2). We speculate that the number of assembled PilQ multimers in the OM at the cell poles, and therefore the number of T4aPM at the cell poles, is limited by the availability of the specific septal and polar PG recognized by the PilQ AMIN domains. In the future, it will be important to determine the exact PG recognized by the PilQ AMIN domains. Similarly, it will be important to determine whether monomeric PilQ and TgI are recruited as a complex or sequentially. The assembled T4aPM in *M. xanthus* has a width of 15-20 nm (8, 12) while the average pore size of PG has been estimated to ~2 nm (69). While the incorporation of T4aPM in parallel with cytokinesis is compatible these different dimensions, it is more difficult to understand how the T4aPM would be incorporated after completion of cytokinesis and independently of cell division. Thus, it will also be important to address how the T4aPM is assembled post-divisionally.

How then does TgI stimulate PilQ multimer formation in the OM? TgI is important for PilQ stability and multimerization in the OM. In cellular fraction experiments, we found that the PilQ monomer is associated with the OM in a TgI-independent manner demonstrating that TgI is not required for translocating monomeric PilQ from the IM across the periplasm to the OM. We note that whether PilQ is associated with the OM or integrated into the OM cannot be distinguished based on these experiments. High confidence *in silico* structural models of monomeric TgI, monomeric PilQ, and heterodimeric TgI/PilQ complexes, support that TgI interacts with monomeric PilQ via hydrophobic interfaces. Specifically, our structural models suggest that two conserved hydrophobic surfaces, i.e. CS1 in TPR1 and CS2 in the concave groove, in TgI interact with the hydrophobic parts of the unfolded amphipathic β-lip of monomeric PilQ. Therefore, our results suggest that TgI at the OM binds the OM associated PilQ monomer thereby (1) stimulating multimerization by maintaining an oligomerization-ready conformation of the PilQ monomer, (2) protecting monomeric PilQ from proteolytic degradation, and (3) ensuring that the assembled secretin only forms at the OM. Because TgI is associated with the OM via its acylated N-terminus, CS1 and CS2 are close to the OM and, therefore, ideally positioned to assist in PilQ secretin integration into the OM. Once PilQ monomers multimerize and integrate into the OM, the interaction with TgI would be lost

because the β-lip is integrated into the OM and the interaction surfaces no longer available for interaction with TgI (Fig. 9, step 3-4). *In silico* structural models of PilF/PilQ and PilW/PilQ heterodimers support that they form complexes similar to that of TgI/PilQ. These models of the heterodimers are also supported by the observations that PilF interacts with the C-terminal region of monomeric $PilQ_{Pae}$ and that loss-of-function PilF variants have substitutions in TPR1 (70). We, therefore, propose that T4aPM pilotins and their cognate monomeric secretin use the same conserved mechanism in which the pilotin interacts with the unfolded β-lip of the monomeric secretin to aid its OM integration. Lending further support for this generalized mechanism of the cognate T4aPM pilotin/secretin pairs, cognate pilotin/secretin pairs of the T2SS and T3SS interact via the so-called S-domain at the C-terminus of the secretin monomer (32, 33). However, T4aPM pilotins are structurally different from T2SS and T3SS pilotins (71), and T4aPM secretins lack the S-domain (32, 33).

Because different species have different T4aP patterns and the PilQ AMIN domains in polarly piliated *M. xanthus* (here) and *P. aeruginosa* (24) are essential for the polar assembly of the T4aPM, we asked whether there is a correlation between piliation patterns and the presence/absence of AMIN domains in the relevant secretins. Interestingly, we found that not only the PilQ secretins of *M. xanthus* and *P. aeruginosa* but also of the polarly piliated *T. vulcanus* and *N. punctiforme* contain AMIN domains, while the secretins of the peritrichiously piliated *Synechocystis* sp. PCC6803*, M. catarrhalis* and *B. cepacia* cells do not contain AMIN domains. In this survey, three species did not follow the overall correlation between piliation pattern and the presence/absence of AMIN domain(s) in the relevant secretin. Specifically, *N. meningitidis* and *N. gonorrhoeae* assemble peritrichous T4aP and both have secretins that contain AMIN domains. Notably, it has been suggested that these two species have a rod-shaped ancestor and that the emergence of their coccoid cell shape derives from relatively recent gene losses from the genome of this ancestor (72, 73). Thus, we speculate that the AMIN domains in the *N. meningitidis* and *N. gonorrhoeae* T4aPM secretins are remnants from the rod-shaped ancestor. The third species in which the piliation pattern and absence /presence of AMIN domain(s) correlation did not match was *A. baylyi.* This species has a unique lateral piliation pattern and its T4aPM secretin contains two AMIN domains, suggesting that *A. baylyi* may potentially accumulate a specific form of PG laterally that is recognized by its T4aPM secretin. Interestingly, the secretins of T2SS and T3SS lack AMIN domains and have been reported to have a dispersed localization (74-76). Thus, the presence/absence of AMIN domains in the relevant secretin for the localization of the relevant macromolecular structure may extend beyond the T4aPM.

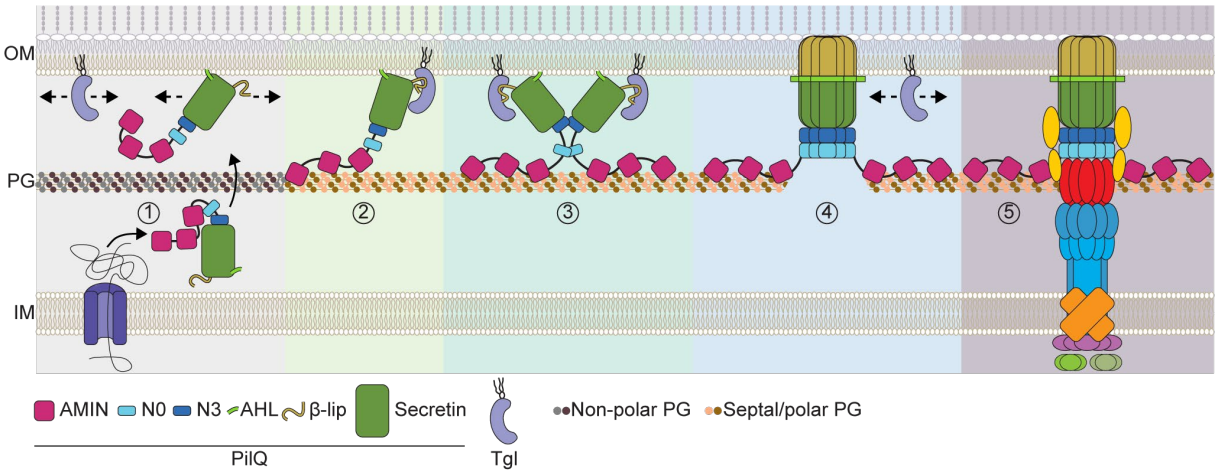

Figure 9. Model of polar incorporation and OM assembly of the PilQ secretin as well as polar assembly of the T4aPM in *M. xanthus*

See main text for details. Note that in step 1, PilQ monomers and Tgl away from the septal and polar PG are shown not to interact; however, it is possible that the two proteins interact prior to their polar localization. In step 1 and 4, the arrows indicate that the proteins can diffuse in the OM. In step 1-3, PilQ is shown to associate with the OM via its AHL domain; however, it is not known how PilQ monomers associate with/integrate into the OM. In step 3, while the secretin oligomerizes from 12-15 PilQ monomers, only two are shown for illustration purposes. In step 5, all T4aPM components except for PilQ are colored as in Fig. 1.

Acknowledgment

The authors thank Martin Thanbichler for helpful discussions, Luís Antonío Menezes Carreira for constructing pLC220 and Anke Treuner-Lange for generating strain SA11377. This work was generously supported by the Max Planck Society (to LS-A).

Conflict of Interest

The authors declare no conflict of interest.

Availability of data and materials

The authors declare that all data supporting this study are available within the article and its Supplementary Information files.

Materials and Methods

Bacterial strains and growth media. All *M. xanthus* strains are derivatives of the wild type DK1622 (15) and are listed in Table 1. In-frame deletions and gene replacements were generated as described (77) and were verified by PCR. Point mutation replacements were confirmed by DNA sequencing. *M. xanthus* cells were grown at 32°C in 1% CTT broth (1% (w/v) Bacto Casitone, 10 mM Tris-HCl pH 8.0, 1 mM K_2HPO_4/KH_2PO_4 pH 7.6, and 8 mM $MgSO_4$) or on 1% CTT 1.5% agar (50) supplemented when required with kanamycin (50 µg ml^{-1}) or oxytetracycline (10 µg ml^{-1}).
Plasmids used in this study are listed in Table 2. Plasmids were propagated in *E. coli* Mach1 (Δ*recA*1398 *endA*1 *tonA* Φ80Δ*lacM*15 Δ*lacX*74 *hsdR* (r_K^- m_K^+); Invitrogen), which was grown at 37°C in lysogeny broth (10 mg tryptone ml^{-1}, 5 mg yeast extract ml^{-1} and 10 mg NaCl ml^{-1}) supplemented when required with kanamycin (50 µg ml^{-1}).

Plasmid construction. All oligonucleotides used are listed in Table S1. All constructed plasmids were verified by DNA sequencing.

For **pLC220** (plasmid for replacement of *tgl* with *tgl-sfGFP* in the native site): the *tgl-sfGFP* fragment was amplified from pSC104 (27) using primers tgl_fw_hindiii/sfgfp_rv_xbaI. The downstream fragment was amplified from genomic DNA from *M. xanthus* DK1622 using the primer pair tgl_ds_fw_xbaI/ tgl_ds_rv. To generate the full-length insert, both DNA fragments were digested with XbaI and ligated. Next, the insert was digested with HindIII and EcoRI, and cloned into pBJ114.

For **pMH111** (plasmid for replacement of *tgl* with *tgl*^{C20G} at the native site): up- and downstream fragments were amplified using genomic DNA from *M. xanthus* DK1622 as DNA template and the primer pairs tgl_CtoG_A_HindIII/tgl_CtoG_Bov and tgl_CtoG_Cov/ tgl_CtoG_D_BamHI, respectively. To generate the full-length insert, an overlapping PCR using the two fragments as DNA templates and the primer pair tgl_CtoG_A_HindIII/ tgl_CtoG_D_BamHI was performed. Subsequently, the fragment was digested with HindIII and BamHI, and cloned into pBJ114.

For **pMH118** (plasmid for expression of *pilQ-sfGFP* from the *18-19* site under the control of the vanillate promoter): *pilQ-sfGFP* was amplified using genomic DNA from *M. xanthus* SA7192 (*pilQ::pilQ-sfGFP*) (5) as DNA template and the primer pair Pvan_PilQ_fwd_NdeI/ sfGFP_rev_pilQ_EcoRI. The fragment was digested with NdeI and EcoRI, and cloned into pMR3690.

For **pMH119** (plasmid for expression of *tgl-sfGFP* from the *18-19* site under the control of the vanillate promoter): *tgl-sfGFP* was amplified using genomic DNA from *M. xanthus* SA12016 (*tgl::tgl-sfGFP*) as DNA template and the primer pair Pvan_tgl_fw_NdeI/ sfGFP_rv_tgl_EcoRI. The fragment was digested with NdeI and EcoRI, and cloned into pMR3690.

For **pMH120** (plasmid for expression of *tgl*^{C20G}*-sfGFP* from the *18-19* site under the control of the vanillate promoter): *tgl*^{C20G}*-sfGFP* was amplified using genomic DNA from *M. xanthus* SA12035 (*tgl*^{C20G}*::tgl-sfGFP*) as DNA template and the primer pair Pvan_tgl_fw_NdeI/ sfGFP_rv_tgl_EcoRI. The fragment was digested with NdeI and EcoRI, and cloned into pMR3690.

For **pMH121** (for generation of an in-frame deletion of the AMIN×3 domains of native *pilQ*): up- and downstream fragments were amplified from genomic DNA from *M. xanthus* DK1622 using the primer pairs PilQ_dAMIN_A_XbaI/ PilQ_dAMIN_B and PilQ_dAMIN_C/ pilQ_dAMIN_D_HindIII, respectively. Subsequently, the up- and downstream fragments were used as a template for an overlapping PCR with the primer pair PilQ_dAMIN_A_XbaI/ pilQ_dAMIN_D_HindIII, to generate the AD fragment. The AD fragment was digested with XbaI and HindIII, and cloned in pBJ114.

For **pMH122** (for generation of an in-frame deletion of *tgl*): up- and downstream fragments were amplified from genomic DNA of SA6053 (Δ*tgl*) (27) using the primer pair tgl-A_XbaI/tgl-D_EcoRI to generate the AD fragment as described in (77). The AD fragment was digested with XbaI/EcoRI and cloned in pBJ114.

For **pMH125** (for replacement of *pilQ* with *pilQ*$^{AMINs\times3\ (1\text{-}475)}$*-sfGFP* in the native site of the *pilQ::pilQ-sfGFP* strain): up- and downstream fragments were amplified from pMH118 using the primer pairs PilQAMIN_A_KpnI/ PilQAMIN_sfGFP_overlay_rev and PilQamin_sfGFP_overlay_fwd/ sfGFP_rev_pilQ_EcoRI, respectively. Subsequently, the up- and downstream fragments were used as a template for an overlapping PCR with the primer pair PilQAMIN_A_KpnI/ sfGFP_rev_pilQ_EcoRI, to generate the AD fragment. The AD fragment was digested with KpnI and EcoRI, and cloned in pBJ114.

For **pMH127** (plasmid for expression of *tgl*^{S21D}*-sfGFP* from the *18-19* site under the control of the vanillate promoter): *tgl*^{S21D}*-sfGFP* was amplified using pMH119 as DNA template and the primer pairs Pvan forw/Tgl_S21G_overlay_rev and Tgl_S21G_overlay_fwd/sfGFP_rv_tgl_EcoRI to introduce the point mutation. Subsequently, both PCR fragments were used as a template for an overlapping PCR with the primer pair Pvan forw/sfGFP_rv_tgl_EcoRI, to generate the full-length fragment. The fragment was digested with NdeI and EcoRI, and cloned into pMR3690.

For **pMP183** (plasmid for expression of *pilQ* from the *18-19* site under the control of the vanillate promoter): *pilQ* was amplified using pMH118 as DNA template and the primer pair Pvan_PilQ_fwd_NdeI/ PilQ_rev_EcoRI. The fragment was digested with NdeI and EcoRI, and cloned into pMR3690.

Motility assays. T4aP-dependent motility assays were performed as described (78). Briefly, exponentially growing *M. xanthus* cultures were harvested (6,000 *g*, 3 min, RT) and resuspended in 1% CTT to a calculated density of 7×10^9 cells ml^{-1}. 5 µl aliquots were spotted on 0.5% CTT 0.5% select-agar (Invitrogen). After 24 h incubation at 32°C, cells were imaged using an M205FA Stereomicroscope (Leica) equipped with a Hamamatsu ORCA-flash V2 Digital CMOS camera (Hamamatsu Photonics), and images were analyzed using Metamorph® v 7.5 (Molecular Devices).

Epifluorescence microscopy. Cells were visualized following a slightly modified protocol (79). Briefly, exponentially growing cells were placed on a glass coverslip attached to a metal frame. Cells were covered with a thick 1% agarose pad supplemented with 0.2% (w/v) Bacto Casitone and TPM (10 mM Tris-HCl pH 8.0, 1 mM K_2HPO_4/KH_2PO_4 pH 7.6, 8 mM MgSO4), and supplemented with vanillate or cephalexin as indicated. For long time-lapse microscopy, the pad was additionally sealed with parafilm to reduce evaporation. Cells were imaged using a DMi8 inverted microscope and a Hamamatsu ORCA-Flash4.0 V2 Digital CMOS C11440 or a DFC9000 GT (Leica) camera. Images were analyzed using Metamorph® v 7.5 (Molecular Devices) and ImageJ (Schindelin et al., 2012). Image segmentation was done using Omnipose (80) and cell outlines were transformed to Oufti-compatible meshes using Matlab R2020a (The MathWorks). Segmentation was manually curated using Oufti (81). For signal detection and background correction, a previously published Matlab script was used (82). Because the Tgl-sfGFP fluorescent clusters have low fluorescence intensity, the script was modified to detect the strongest pixel intensity in each cell segment assigned by Oufti. Specifically, each pixel intensity in each segment was normalized to the maximum pixel intensity within the cell. Next, to identify cells with one or more fluorescent cluster(s), cells were only considered to have a cluster if less than 10% of the selected pixel intensities had a normalized fluorescence above 0.75. Hence identifying cells with an intense and narrow fluorescent peak.

Immunoblot analysis. Immunoblots were carried out as described (83). Rabbit polyclonal α-Tgl (dilution: 1:2,000) (27), α-PilQ (dilution, 1:5,000) (26), α-PilB (dilution: 1:2,000) (84), α-PilC (dilution: 1:2000) (26), α-Oar (1:10,000) (85) and α-LonD (dilution: 1:5,000) (12), were used together with a horseradish peroxidase-conjugated goat anti-rabbit immunoglobulin G (1:15,000) (Sigma) as a secondary antibody. Mouse α-GFP antibodies (dilution: 1:2,000) (Roche) were used together with horseradish peroxidase-conjugated sheep α-mouse immunoglobulin G (dilution: 1:2,000) (GE Healthcare) as a secondary antibody. Blots were developed using Luminata Forte Western HRP Substrate (Millipore) on a LAS-4000 imager (Fujifilm).

Fractionation of *M. xanthus* cells. To fractionate *M. xanthus* cells into fractions enriched for soluble or membrane proteins, 20 ml of an exponentially growing *M. xanthus* suspension

culture were harvested by centrifugation (8,000 *g*, 10 min, RT) and concentrated to an optical density at 550 nm (OD_{550}) of 28 in resuspension buffer (50 mM Tris-HCl pH 7.6, 250 mM NaCl supplemented with Complete EDTA-free protease inhibitor (Roche)). Cells were lysed by sonication with 5×30 pulses, pulse 60%, amplitude 60% with a UP200St sonifier and microtip (Hielscher), and the lysate was cleared by centrifugation (12,000 *g,* 5 min, RT). As a sample for total cellular protein, an aliquot of the cleared lysate was taken and mixed with 4×SDS lysis buffer (200 mM Tris-HCl pH 6.8, 8% SDS, 40% glycerol, 400 mM DTT, 6 mM EDTA, 0.4% bromphenol blue). A 200 µl aliquot of the remaining supernatant was subjected to ultracentrifugation using an Air-Fuge (Beckman) (100,000 *g*, 20 min, RT). The resulting supernatant is enriched in soluble proteins and a sample was taken and mixed with 4×SDS lysis buffer. The pellet was washed by resuspension in 200 µl resuspension buffer and was subjected to ultracentrifugation as above. The remaining pellet, which is enriched in IM and OM membrane proteins, was resuspended in 100 µl 1×SDS lysis buffer. All samples were heated for 10 min at 95°C, separated by SDS-PAGE and analyzed by immunoblot.

OM protein enrichment. As a sample for total cellular protein (total fraction), 2 ml of an exponentially growing *M. xanthus* cell suspension were harvested by centrifugation (8,000 *g*, 3 min, RT) and concentrated to an OD_{550} of 7 in 1× SDS lysis buffer. To isolate a fraction enriched for OM proteins, 50 ml of the cell suspension were harvested (4,700 *g*, 25 min, 4°C), and the pellet was gently resuspended in TSE8-buffer (100 mM Tris-HCl pH 8, 1 mM EDTA, 20% (w/v) sucrose, protease inhibitor cocktail (Roche)) to a concentration corresponding to OD_{550}=50. The sample was incubated for 30 min at 4°C to release the OM, followed by centrifugation of the samples (16,000 *g*, 30 min*,* 4°C). The resulting supernatant is enriched in OM and periplasmic proteins and was recovered for the following steps, while the pellet, containing cells without OM or where the OM had not been released, was frozen at -20°C. Next, 150 µl of the supernatant was ultra-centrifuged using an Air-Fuge (Beckman) (~133,000 *g*, 1 h, RT) to separate the OM from periplasmic proteins. The resulting supernatant was discarded and the OM-enriched pellet (OM fraction) was resuspended in 150 µl 1×SDS lysis buffer. The frozen pellet was thawed, resuspended to OD=50 in resuspension buffer (50 mM Tris pH 7.6, 10 mM $MgICl_2$) and lysed by sonication. Cell debris was removed by centrifugation (16,000 *g*, 15 min, 4°C). The cell-free supernatant (~150 µl) was subjected to ultra-centrifugation as described above. The resulting supernatant contained cytoplasmic proteins and was mixed with 4×SDS lysis buffer (cytoplasmic fraction). All samples were boiled 10 min at 95°C, separated by SDS-PAGE, and analyzed by immunoblot.

Bioinformatics. Full-length protein sequences or sequences in which the signal peptide was identified with SignalP 6.0 (86) and removed, were used for AlphaFold and AlphaFold-Multimer modeling via ColabFold (1.3.0) (87-89). The predicted Local Distance Difference Test (pLDDT)

and predicted Alignment Error (pAE) graphs of the five models generated were made using a custom Matlab R2020a (The MathWorks) script (90). Ranking of the models was performed based on combined pLDDT and pAE values, with the best-ranked models used for further analysis and presentation. Per residue model accuracy was estimated based on pLDDT values (>90, high accuracy; 70-90, generally good accuracy; 50-70, low accuracy; <50, should not be interpreted) (87). Relative domain positions were validated by pAE. The pAE graphs indicate the expected position error at residue X if the predicted and true structures were aligned on residue Y; the lower the pAE value, the higher the accuracy of the relative position of residue pairs and, consequently, the relative position of domains/subunits/proteins (87). PyMOL version 2.4.1 (http://www.pymol.org/pymol) was used to analyze and visualize the models. Structural alignments were performed using the PyMOL Alignment plugin with default settings. Hydrophobicity was calculated in PyMol according to the hydrophobicity scale (91). Conservation of Tgl residues was assessed using the ConSurf server with default settings (92). Protein domains were identified using the Interpro server (93) and the predicted AlphaFold structures. The alignment of Tgl, PilF, and PilW was generated using Muscle5 (5.1) (94).

References

1. Harshey RM. 2003. Bacterial motility on a surface: many ways to a common goal. Annu Rev Microbiol 57:249-73.
2. Wadhwa N, Berg HC. 2022. Bacterial motility: machinery and mechanisms. Nat Rev Microbiol 20:161-173.
3. Schuhmacher JS, Thormann KM, Bange G. 2015. How bacteria maintain location and number of flagella? FEMS Microbiol Rev 39:812-22.
4. Craig L, Forest KT, Maier B. 2019. Type IV pili: dynamics, biophysics and functional consequences. Nat Rev Microbiol 17:429-440.
5. Potapova A, Carreira LAM, Søgaard-Andersen L. 2020. The small GTPase MglA together with the TPR domain protein SgmX stimulates type IV pili formation in *M. xanthus*. Proc Natl Acad Sci U S A 117:23859-23868.
6. Ellison CK, Fei C, Dalia TN, Wingreen NS, Dalia AB, Shaevitz JW, Gitai Z. 2022. Subcellular localization of type IV pili regulates bacterial multicellular development. Nat Commun 13:6334.
7. Berry JL, Pelicic V. 2015. Exceptionally widespread nanomachines composed of type IV pilins: the prokaryotic Swiss Army knives. FEMS Microbiol Rev 39:134-54.
8. Chang YW, Rettberg LA, Treuner-Lange A, Iwasa J, Søgaard-Andersen L, Jensen GJ. 2016. Architecture of the type IVa pilus machine. Science 351:aad2001.
9. Gold VA, Salzer R, Averhoff B, Kuhlbrandt W. 2015. Structure of a type IV pilus machinery in the open and closed state. Elife 4:e07380.
10. Merz AJ, So M, Sheetz MP. 2000. Pilus retraction powers bacterial twitching motility. Nature 407:98-102.
11. Skerker JM, Berg HC. 2001. Direct observation of extension and retraction of type IV pili. Proc Natl Acad Sci U S A 98:6901-4.
12. Treuner-Lange A, Chang YW, Glatter T, Herfurth M, Lindow S, Chreifi G, Jensen GJ, Søgaard-Andersen L. 2020. PilY1 and minor pilins form a complex priming the type IVa pilus in *Myxococcus xanthus*. Nat Commun 11:5054.
13. Weiss RL. 1971. The structure and occurrence of pili (fimbriae) on *Pseudomonas aeruginosa*. J Gen Microbiol 67:135-43.
14. Chiang P, Habash M, Burrows LL. 2005. Disparate subcellular localization patterns of *Pseudomonas aeruginosa* type IV pilus ATPases involved in twitching motility. J Bacteriol 187:829-39.
15. Kaiser D. 1979. Social gliding is correlated with the presence of pili in *Myxococcus xanthus*. Proc Natl Acad Sci U S A 76:5952-6.
16. Sun H, Zusman DR, Shi W. 2000. Type IV pilus of *Myxococcus xanthus* is a motility apparatus controlled by the *frz* chemosensory system. Curr Biol 10:1143-6.
17. Nakane D, Enomoto G, Bahre H, Hirose Y, Wilde A, Nishizaka T. 2022. *Thermosynechococcus* switches the direction of phototaxis by a c-di-GMP-dependent process with high spatial resolution. Elife 11:e73405.
18. Khayatan B, Meeks JC, Risser DD. 2015. Evidence that a modified type IV pilus-like system powers gliding motility and polysaccharide secretion in filamentous cyanobacteria. Mol Microbiol 98:1021-36.
19. Sajjan US, Sun L, Goldstein R, Forstner JF. 1995. Cable (Cbl) type II pili of cystic fibrosis-associated *Burkholderia* (*Pseudomonas*) *cepacia*: nucleotide sequence of the *cblA* major subunit pilin gene and novel morphology of the assembled appendage fibers. J Bacteriol 177:1030-8.
20. Stephens DS, Whitney AM, Rothbard J, Schoolnik GK. 1985. Pili of *Neisseria meningitidis*. Analysis of structure and investigation of structural and antigenic relationships to gonococcal pili. J Exp Med 161:1539-53.
21. Marathe R, Meel C, Schmidt NC, Dewenter L, Kurre R, Greune L, Schmidt MA, Muller MJ, Lipowsky R, Maier B, Klumpp S. 2014. Bacterial twitching motility is coordinated by a two-dimensional tug-of-war with directional memory. Nat Commun 5:3759.
22. Ahmed K, Rikitomi N, Nagatake T, Matsumoto K. 1990. Electron microscopic observation of *Branhamella catarrhalis*. Microbiol Immunol 34:967-75.
23. Bhaya D, Watanabe N, Ogawa T, Grossman AR. 1999. The role of an alternative sigma factor in motility and pilus formation in the cyanobacterium *Synechocystis* sp. strain PCC6803. Proc Natl Acad Sci U S A 96:3188-93.
24. Carter T, Buensuceso RN, Tammam S, Lamers RP, Harvey H, Howell PL, Burrows LL. 2017. The type IVa pilus machinery is recruited to sites of future cell division. mBio 8.

25. Cowles KN, Moser TS, Siryaporn A, Nyakudarika N, Dixon W, Turner JJ, Gitai Z. 2013. The putative Poc complex controls two distinct *Pseudomonas aeruginosa* polar motility mechanisms. Mol Microbiol 90:923-38.
26. Bulyha I, Schmidt C, Lenz P, Jakovljevic V, Hone A, Maier B, Hoppert M, Søgaard-Andersen L. 2009. Regulation of the type IV pili molecular machine by dynamic localization of two motor proteins. Mol Microbiol 74:691-706.
27. Friedrich C, Bulyha I, Søgaard-Andersen L. 2014. Outside-in assembly pathway of the type IV pilus system in *Myxococcus xanthus*. J Bacteriol 196:378-90.
28. Siewering K, Jain S, Friedrich C, Webber-Birungi MT, Semchonok DA, Binzen I, Wagner A, Huntley S, Kahnt J, Klingl A, Boekema EJ, Søgaard-Andersen L, van der Does C. 2014. Peptidoglycan-binding protein TsaP functions in surface assembly of type IV pili. Proc Natl Acad Sci U S A 111:E953-61.
29. Nudleman E, Wall D, Kaiser D. 2006. Polar assembly of the type IV pilus secretin in *Myxococcus xanthus*. Mol Microbiol 60:16-29.
30. Schumacher D, Søgaard-Andersen L. 2017. Regulation of cell polarity in motility and cell division in *Myxococcus xanthus*. Annu Rev Microbiol 71:61-78.
31. Carreira LAM, Szadkowski D, Müller F, Søgaard-Andersen L. 2022. Spatiotemporal regulation of switching front-rear cell polarity. Curr Opin Cell Biol 76:102076.
32. Majewski DD, Worrall LJ, Strynadka NC. 2018. Secretins revealed: structural insights into the giant gated outer membrane portals of bacteria. Curr Opin Struct Biol 51:61-72.
33. Silva YRO, Contreras-Martel C, Macheboeuf P, Dessen A. 2020. Bacterial secretins: Mechanisms of assembly and membrane targeting. Protein Sci 29:893-904.
34. Weaver SJ, Ortega DR, Sazinsky MH, Dalia TN, Dalia AB, Jensen GJ. 2020. CryoEM structure of the type IVa pilus secretin required for natural competence in *Vibrio cholerae*. Nat Commun 11:5080.
35. McCallum M, Tammam S, Rubinstein JL, Burrows LL, Howell PL. 2021. CryoEM map of *Pseudomonas aeruginosa* PilQ enables structural characterization of TsaP. Structure 29:457-466 e4.
36. Koo J, Lamers RP, Rubinstein JL, Burrows LL, Howell PL. 2016. Structure of the *Pseudomonas aeruginosa* type IVa pilus secretin at 7.4 Å. Structure 24:1778-1787.
37. Worrall LJ, Hong C, Vuckovic M, Deng W, Bergeron JRC, Majewski DD, Huang RK, Spreter T, Finlay BB, Yu Z, Strynadka NCJ. 2016. Near-atomic-resolution cryo-EM analysis of the *Salmonella* T3S injectisome basal body. Nature 540:597-601.
38. Majewski DD, Okon M, Heinkel F, Robb CS, Vuckovic M, McIntosh LP, Strynadka NCJ. 2021. Characterization of the pilotin-secretin complex from the *Salmonella enterica* type III secretion system using hybrid structural methods. Structure 29:125-138 e5.
39. Koo J, Tammam S, Ku SY, Sampaleanu LM, Burrows LL, Howell PL. 2008. PilF is an outer membrane lipoprotein required for multimerization and localization of the *Pseudomonas aeruginosa* type IV pilus secretin. J Bacteriol 190:6961-9.
40. Collin S, Guilvout I, Nickerson NN, Pugsley AP. 2011. Sorting of an integral outer membrane protein via the lipoprotein-specific Lol pathway and a dedicated lipoprotein pilotin. Mol Microbiol 80:655-65.
41. Hardie KR, Lory S, Pugsley AP. 1996. Insertion of an outer membrane protein in *Escherichia coli* requires a chaperone-like protein. EMBO J 15:978-88.
42. Carbonnelle E, Helaine S, Prouvensier L, Nassif X, Pelicic V. 2005. Type IV pilus biogenesis in *Neisseria meningitidis*: PilW is involved in a step occurring after pilus assembly, essential for fibre stability and function. Mol Microbiol 55:54-64.
43. Hardie KR, Seydel A, Guilvout I, Pugsley AP. 1996. The secretin-specific, chaperone-like protein of the general secretory pathway: separation of proteolytic protection and piloting functions. Mol Microbiol 22:967-76.
44. Daefler S, Guilvout I, Hardie KR, Pugsley AP, Russel M. 1997. The C-terminal domain of the secretin PulD contains the binding site for its cognate chaperone, PulS, and confers PulS dependence on pIVf1 function. Mol Microbiol 24:465-75.
45. Rodriguez-Soto JP, Kaiser D. 1997. The *tgl* gene: social motility and stimulation in *Myxococcus xanthus*. J Bacteriol 179:4361-71.
46. Rodriguez-Soto JP, Kaiser D. 1997. Identification and localization of the Tgl protein, which is required for *Myxococcus xanthus* social motility. J Bacteriol 179:4372-81.
47. Wei X, Pathak DT, Wall D. 2011. Heterologous protein transfer within structured myxobacteria biofilms. Mol Microbiol 81:315-26.
48. Nudleman E, Wall D, Kaiser D. 2005. Cell-to-cell transfer of bacterial outer membrane lipoproteins. Science 309:125-7.

49. Wall D, Wu SS, Kaiser D. 1998. Contact stimulation of Tgl and type IV pili in *Myxococcus xanthus*. J Bacteriol 180:759-61.
50. Hodgkin J, Kaiser D. 1977. Cell-to-cell stimulation of movement in nonmotile mutants of *Myxococcus*. Proc Natl Acad Sci U S A 74:2938-42.
51. Eberhardt C, Kuerschner L, Weiss DS. 2003. Probing the catalytic activity of a cell division-specific transpeptidase in vivo with beta-lactams. J Bacteriol 185:3726-34.
52. Schumacher D, Bergeler S, Harms A, Vonck J, Huneke-Vogt S, Frey E, Søgaard-Andersen L. 2017. The PomXYZ proteins self-organize on the bacterial nucleoid to stimulate cell division. Dev Cell 41:299-314 e13.
53. Treuner-Lange A, Aguiluz K, van der Does C, Gomez-Santos N, Harms A, Schumacher D, Lenz P, Hoppert M, Kahnt J, Munoz-Dorado J, Søgaard-Andersen L. 2013. PomZ, a ParA-like protein, regulates Z-ring formation and cell division in *Myxococcus xanthus*. Mol Microbiol 87:235-53.
54. Priyadarshini R, de Pedro MA, Young KD. 2007. Role of peptidoglycan amidases in the development and morphology of the division septum in *Escherichia coli*. J Bacteriol 189:5334-47.
55. de Pedro MA, Quintela JC, Holtje JV, Schwarz H. 1997. Murein segregation in *Escherichia coli*. J Bacteriol 179:2823-34.
56. Bernhardt TG, de Boer PA. 2003. The *Escherichia coli* amidase AmiC is a periplasmic septal ring component exported via the twin-arginine transport pathway. Mol Microbiol 48:1171-82.
57. Rocaboy M, Herman R, Sauvage E, Remaut H, Moonens K, Terrak M, Charlier P, Kerff F. 2013. The crystal structure of the cell division amidase AmiC reveals the fold of the AMIN domain, a new peptidoglycan binding domain. Mol Microbiol 90:267-77.
58. Heidrich C, Templin MF, Ursinus A, Merdanovic M, Berger J, Schwarz H, de Pedro MA, Holtje JV. 2001. Involvement of N-acetylmuramyl-L-alanine amidases in cell separation and antibiotic-induced autolysis of *Escherichia coli*. Mol Microbiol 41:167-78.
59. Grabowicz M. 2019. Lipoproteins and their trafficking to the outer membrane. EcoSal Plus 8.
60. Trindade MB, Job V, Contreras-Martel C, Pelicic V, Dessen A. 2008. Structure of a widely conserved type IV pilus biogenesis factor that affects the stability of secretin multimers. J Mol Biol 378:1031-9.
61. D'Andrea LD, Regan L. 2003. TPR proteins: the versatile helix. Trends Biochem Sci 28:655-62.
62. Kim K, Oh J, Han D, Kim EE, Lee B, Kim Y. 2006. Crystal structure of PilF: functional implication in the type 4 pilus biogenesis in *Pseudomonas aeruginosa*. Biochem Biophys Res Commun 340:1028-38.
63. Szeto TH, Dessen A, Pelicic V. 2011. Structure/function analysis of *Neisseria meningitidis* PilW, a conserved protein that plays multiple roles in type IV pilus biology. Infect Immun 79:3028-35.
64. Huysmans GHM, Guilvout I, Pugsley AP. 2013. Sequential steps in the assembly of the multimeric outer membrane secretin PulD. J Biol Chem 288:30700-30707.
65. Tammam S, Sampaleanu LM, Koo J, Manoharan K, Daubaras M, Burrows LL, Howell PL. 2013. PilMNOPQ from the *Pseudomonas aeruginosa* type IV pilus system form a transenvelope protein interaction network that interacts with PilA. J Bacteriol 195:2126-35.
66. Peters NT, Dinh T, Bernhardt TG. 2011. A fail-safe mechanism in the septal ring assembly pathway generated by the sequential recruitment of cell separation amidases and their activators. J Bacteriol 193:4973-83.
67. Rudner DZ, Losick R. 2010. Protein subcellular localization in bacteria. Cold Spring Harb Perspect Biol 2:a000307.
68. Treuner-Lange A, Søgaard-Andersen L. 2014. Regulation of cell polarity in bacteria. J Cell Biol 206:7-17.
69. Demchick P, Koch AL. 1996. The permeability of the wall fabric of *Escherichia coli* and *Bacillus subtilis*. J Bacteriol 178:768-73.
70. Koo J, Tang T, Harvey H, Tammam S, Sampaleanu L, Burrows LL, Howell PL. 2013. Functional mapping of PilF and PilQ in the *Pseudomonas aeruginosa* type IV pilus system. Biochemistry 52:2914-23.
71. Koo J, Burrows LL, Howell PL. 2012. Decoding the roles of pilotins and accessory proteins in secretin escort services. FEMS Microbiol Lett 328:1-12.
72. Nyongesa S, Weber PM, Bernet E, Pulido F, Nieves C, Nieckarz M, Delaby M, Viehboeck T, Krause N, Rivera-Millot A, Nakamura A, Vischer NOE, vanNieuwenhze M, Brun YV, Cava F, Bulgheresi S, Veyrier FJ. 2022. Evolution of longitudinal division in multicellular bacteria of the Neisseriaceae family. Nat Commun 13:4853.

73. Veyrier FJ, Biais N, Morales P, Belkacem N, Guilhen C, Ranjeva S, Sismeiro O, Pehau-Arnaudet G, Rocha EP, Werts C, Taha MK, Boneca IG. 2015. Common cell shape evolution of two nasopharyngeal pathogens. PLoS Genet 11:e1005338.
74. Buddelmeijer N, Krehenbrink M, Pecorari F, Pugsley AP. 2009. Type II secretion system secretin PulD localizes in clusters in the *Escherichia coli* outer membrane. J Bacteriol 191:161-8.
75. Lybarger SR, Johnson TL, Gray MD, Sikora AE, Sandkvist M. 2009. Docking and assembly of the type II secretion complex of *Vibrio cholerae*. J Bacteriol 191:3149-61.
76. Diepold A, Wiesand U, Cornelis GR. 2011. The assembly of the export apparatus (YscR,S,T,U,V) of the *Yersinia* type III secretion apparatus occurs independently of other structural components and involves the formation of an YscV oligomer. Mol Microbiol 82:502-14.
77. Shi X, Wegener-Feldbrugge S, Huntley S, Hamann N, Hedderich R, Søgaard-Andersen L. 2008. Bioinformatics and experimental analysis of proteins of two-component systems in *Myxococcus xanthus*. J Bacteriol 190:613-24.
78. Shi W, Zusman DR. 1993. The two motility systems of *Myxococcus xanthus* show different selective advantages on various surfaces. Proc Natl Acad Sci U S A 90:3378-82.
79. Schumacher D, Søgaard-Andersen L. 2018. Fluorescence live-cell imaging of the complete vegetative cell cycle of the slow-growing social bacterium *Myxococcus xanthus*. J Vis Exp doi:doi:10.3791/57860:e57860.
80. Cutler KJ, Stringer C, Lo TW, Rappez L, Stroustrup N, Brook Peterson S, Wiggins PA, Mougous JD. 2022. Omnipose: a high-precision morphology-independent solution for bacterial cell segmentation. Nat Methods 19:1438-1448.
81. Paintdakhi A, Parry B, Campos M, Irnov I, Elf J, Surovtsev I, Jacobs-Wagner C. 2016. Oufti: an integrated software package for high-accuracy, high-throughput quantitative microscopy analysis. Mol Microbiol 99:767-77.
82. Schumacher D, Harms A, Bergeler S, Frey E, Søgaard-Andersen L. 2021. PomX, a ParA/MinD ATPase activating protein, is a triple regulator of cell division in *Myxococcus xanthus*. Elife 10:e66160.
83. Sambrook J, Russell DW. 2001. Molecular cloning: a laboratory manual, 3rd ed. Cold Spring Harbor Laboratory Press, Cold Spring Harbor, N.Y.
84. Jakovljevic V, Leonardy S, Hoppert M, Søgaard-Andersen L. 2008. PilB and PilT are ATPases acting antagonistically in type IV pilus function in *Myxococcus xanthus*. J Bacteriol 190:2411-21.
85. Jakobczak B, Keilberg D, Wuichet K, Søgaard-Andersen L. 2015. Contact- and protein transfer-dependent stimulation of assembly of the gliding motility machinery in *Myxococcus xanthus*. PLoS Genet 11:e1005341.
86. Teufel F, Almagro Armenteros JJ, Johansen AR, Gislason MH, Pihl SI, Tsirigos KD, Winther O, Brunak S, von Heijne G, Nielsen H. 2022. SignalP 6.0 predicts all five types of signal peptides using protein language models. Nat Biotechnol 40:1023-1025.
87. Jumper J, Evans R, Pritzel A, Green T, Figurnov M, Ronneberger O, Tunyasuvunakool K, Bates R, Zidek A, Potapenko A, Bridgland A, Meyer C, Kohl SAA, Ballard AJ, Cowie A, Romera-Paredes B, Nikolov S, Jain R, Adler J, Back T, Petersen S, Reiman D, Clancy E, Zielinski M, Steinegger M, Pacholska M, Berghammer T, Bodenstein S, Silver D, Vinyals O, Senior AW, Kavukcuoglu K, Kohli P, Hassabis D. 2021. Highly accurate protein structure prediction with AlphaFold. Nature 596:583-589.
88. Evans R, O'Neill M, Pritzel A, Antropova N, Senior A, Green T, Žídek A, Bates R, Blackwell S, Yim J, Ronneberger O, Bodenstein S, Zielinski M, Bridgland A, Potapenko A, Cowie A, Tunyasuvunakool K, Jain R, Clancy E, Kohli P, Jumper J, Hassabis D. 2022. Protein complex prediction with AlphaFold-Multimer. bioRxiv doi:10.1101/2021.10.04.463034:10.1101/2021.10.04.463034.
89. Mirdita M, Schutze K, Moriwaki Y, Heo L, Ovchinnikov S, Steinegger M. 2022. ColabFold: making protein folding accessible to all. Nat Methods 19:679-682.
90. Schwabe J, Pérez-Burgos M, Herfurth M, Glatter T, Søgaard-Andersen L. 2022. Evidence for a widespread third system for bacterial polysaccharide export across the outer membrane comprising a composite OPX/beta-barrel translocon. mBio 13:e0203222.
91. Eisenberg D, Schwarz E, Komaromy M, Wall R. 1984. Analysis of membrane and surface protein sequences with the hydrophobic moment plot. J Mol Biol 179:125-42.
92. Ashkenazy H, Abadi S, Martz E, Chay O, Mayrose I, Pupko T, Ben-Tal N. 2016. ConSurf 2016: an improved methodology to estimate and visualize evolutionary conservation in macromolecules. Nucleic Acids Res 44:W344-50.

93. Blum M, Chang HY, Chuguransky S, Grego T, Kandasaamy S, Mitchell A, Nuka G, Paysan-Lafosse T, Qureshi M, Raj S, Richardson L, Salazar GA, Williams L, Bork P, Bridge A, Gough J, Haft DH, Letunic I, Marchler-Bauer A, Mi H, Natale DA, Necci M, Orengo CA, Pandurangan AP, Rivoire C, Sigrist CJA, Sillitoe I, Thanki N, Thomas PD, Tosatto SCE, Wu CH, Bateman A, Finn RD. 2021. The InterPro protein families and domains database: 20 years on. Nucleic Acids Res 49:D344-D354.
94. Edgar RC. 2022. Muscle5: High-accuracy alignment ensembles enable unbiased assessments of sequence homology and phylogeny. Nat Commun 13:6968.
95. Bischof LF, Friedrich C, Harms A, Søgaard-Andersen L, van der Does C. 2016. The type IV pilus assembly ATPase PilB of *Myxococcus xanthus* interacts with the inner membrane platform protein PilC and the nucleotide-binding protein PilM. J Biol Chem 291:6946-57.
96. Takhar HK, Kemp K, Kim M, Howell PL, Burrows LL. 2013. The platform protein is essential for type IV pilus biogenesis. J Biol Chem 288:9721-9728.
97. Luciano J, Agrebi R, Le Gall AV, Wartel M, Fiegna F, Ducret A, Brochier-Armanet C, Mignot T. 2011. Emergence and modular evolution of a novel motility machinery in bacteria. PLoS Genet 7:e1002268.
98. Gómez-Santos N, Glatter T, Koebnik R, Świątek-Połatyńska MA, Søgaard-Andersen L. 2019. A TonB-dependent transporter is required for secretion of protease PopC across the bacterial outer membrane. Nat Commun 10:1360.
99. Gill RE, Bornemann MC. 1988. Identification and characterization of the *Myxococcus xanthus bsgA* gene product. J Bacteriol 170:5289-97.
100. Wu SS, Wu J, Kaiser D. 1997. The *Myxococcus xanthus pilT* locus is required for social gliding motility although pili are still produced. Mol Microbiol 23:109-21.
101. Wall D, Kolenbrander PE, Kaiser D. 1999. The *Myxococcus xanthus pilQ* (*sglA*) gene encodes a secretin homolog required for type IV pilus biogenesis, social motility, and development. J Bacteriol 181:24-33.
102. Julien B, Kaiser AD, Garza A. 2000. Spatial control of cell differentiation in *Myxococcus xanthus*. Proc Natl Acad Sci U S A 97:9098-103.
103. Iniesta AA, Garcia-Heras F, Abellon-Ruiz J, Gallego-Garcia A, Elias-Arnanz M. 2012. Two systems for conditional gene expression in *Myxococcus xanthus* inducible by isopropyl-beta-D-thiogalactopyranoside or vanillate. J Bacteriol 194:5875-85.
104. Carreira LAM, Tostevin F, Gerland U, Søgaard-Andersen L. 2020. Protein-protein interaction network controlling establishment and maintenance of switchable cell polarity. PLoS Genet 16:e1008877.

Table 1. *M. xanthus* strains used in this work

Strain	Genotype	Reference
DK1622	WT	(15)
DK10410	Δ*pilA*	(100)
DK8615	Δ*pilQ*	(101)
DK10405	Δ*tgl::tet*^{R}	(46, 49)
SA6053	Δ*tgl*	(27)
SA6024	Δ*pilBTCMNOPQ*	(27)
SA3922	Δ*gltB*	(85)
SA7192	*pilQ::pilQ-sfGFP*	(5)
SA11377	Δ*oar*	This study
SA12016	*tgl::tgl-sfGFP*	This study
SA12017	*pilQ::pilQ-sfGFP* Δ*gltB*	This study
SA12021	*tgl::tgl-sfGFP* Δ*gltB*	This study
SA12031	Δ*tgl::tet*^{R} *pilQ::pilQ-sfGFP*	This study
SA12032	Δ*pilQ tgl::tgl-sfGFP*	This study
SA12035	*tgl::tgl*^{C20G}*-sfGFP*	This study
SA12047	Δ*tgl 18-19::*P$_{van}$ *tgl-sfGFP*	This study
SA12048	Δ*tgl 18-19::*P$_{van}$ *tgl*^{C20G}*-GFP*	This study
SA12049	*pilQ::pilQ*$^{\Delta AMIN\times3\ (\Delta31\text{-}475)}$*-sfGFP*	This study
SA12050	Δ*tgl pilQ::pilQ-sfGFP*	This study
SA12054	Δ*pilQ* Δ*gltB 18-19::*P$_{van}$ *pilQ-sfGFP*	This study
SA12073	Δ*tgl 18-19*::P$_{van}$ *tgl*^{S21D}*-sfGFP*	This study
SA12074	*pilQ::pilQ*$^{AMIN\times3\ (1\text{-}475)}$*-sfGFP*	This study
SA12078	Δ*pilQ tgl::tgl-sfGFP* Δ*gltB 18-19::*P$_{van}$ *pilQ*	This study
SA12085	Δ*gltB* Δ*tgl* Δ*pilQ 18-19::*P$_{van}$ *pilQ-sfGFP*	This study
SA12088	Δ*pilQ* Δ*gltB pilM::mCherry-pilM 18-19*::P$_{van}$ *pilQ*	This study

Table 2. Plasmids used in this work

Plasmid	Description	Reference
pBJ114	Km^r *galK*	(102)
pMR3690	Km^r, P_{van}	(103)
pDK25	pBJ114, for generation of a *gltB* in-frame deletion, Km^r	(85)
pNG020	pBJ114, for generation of an *oar* in-frame deletion, Km^r	(98)
pAP37	pBJ114, for native site replacement of *pilQ* with *pilQ-sfGFP*, Km^r	(5)
pMAT123	pBJ114, for generation of a *pilQ* in-frame deletion, Km^r	(104)
pMAT336	pBJ114, for native site replacement of *pilM* with *mCherry-pilM*, Km^r	(12)
pLC220	pBJ114, for native site replacement of *tgl* with *tgl-sfGFP*, Km^r	This study
pMH111	pBJ114, for native site replacement of *tgl* with *tgl*^{C20G}, Km^r	This study
pMH118	pMR3690, induction construct of *pilQ-sfGFP* expressed from the vanillate promoter, Km^R	This study
pMH119	pMR3690, induction construct of *tgl-sfGFP* expressed from the vanillate promoter, Km^R	This study
pMH120	pMR3690, induction construct of *tgl*^{C20G}*-sfGFP* expressed from the vanillate promoter, Km^R	This study
pMH121	pBJ114, for generation of an in-frame deletion of the three AMIN domains of *pilQ-sfGFP* (Δ31-475), Km^r	This study
pMH122	pBJ114, for generation of a *tgl* in-frame deletion, Km^r	This study
pMH125	pBJ114, for native site replacement of *pilQ-sfGFP* with *pilQ*$^{AMIN\times3\ (1\text{-}475)}$-sfGFP, Km^r	This study
pMH127	pMR3690, induction construct of *tgl*^{S21D}*-sfGFP* expressed from the vanillate promoter, Km^R	This study
pMP183	pMR3690, induction construct of *pilQ* expressed from the vanillate promoter, Km^R	This study

Supplementary Information for

The mechanism for polar localization of the type IVa pilus machine

Marco Herfurth, María Pérez-Burgos and Lotte Søgaard-Andersen

This file contains:

- Supplementary Figures 1-5
- Table S1

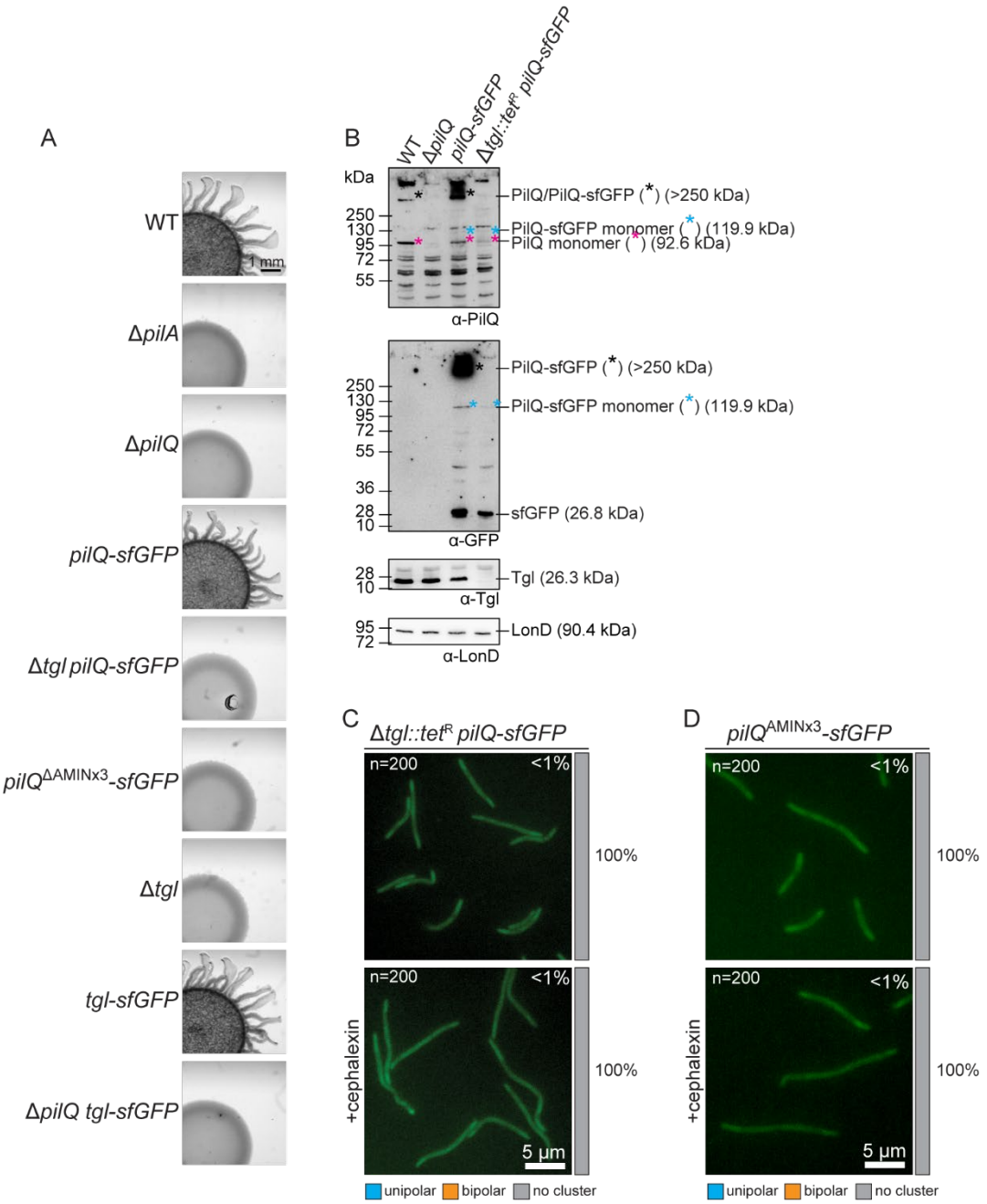

Figure S1. Analysis of PilQ-sfGFP and Tgl-sfGFP variants functionality and localization. (A) Colony-based motility assay of the indicated strains. T4aP-dependent motility was analyzed on 0.5% agar and images were recorded after 24 h. The Δ*pilA* mutant is deficient in T4aP-dependent motility and was used as the negative control. Scale bar: 1 mm. (B) Immunoblot detection of PilQ-sfGFP in the Δ*tgl::Tet*^{R} background strain. Protein from the same number of cells from exponentially growing suspension cultures was loaded per lane. Blot was probed with the indicated antibodies. The blot was stripped before applying a new antibody. LonD served as a loading control. Monomeric and oligomeric forms of PilQ/PilQ-sfGFP are marked with an asterisk. Calculated molecular weights of proteins without signal peptide (if relevant) are indicated. (C-D) Localization of PilQ-sfGFP in the Δ*tgl::Tet*^{R} background strain or of PilQ^{AMINx3}-sfGFP, and in the presence and absence of cephalexin as in Fig. 2B left panel.

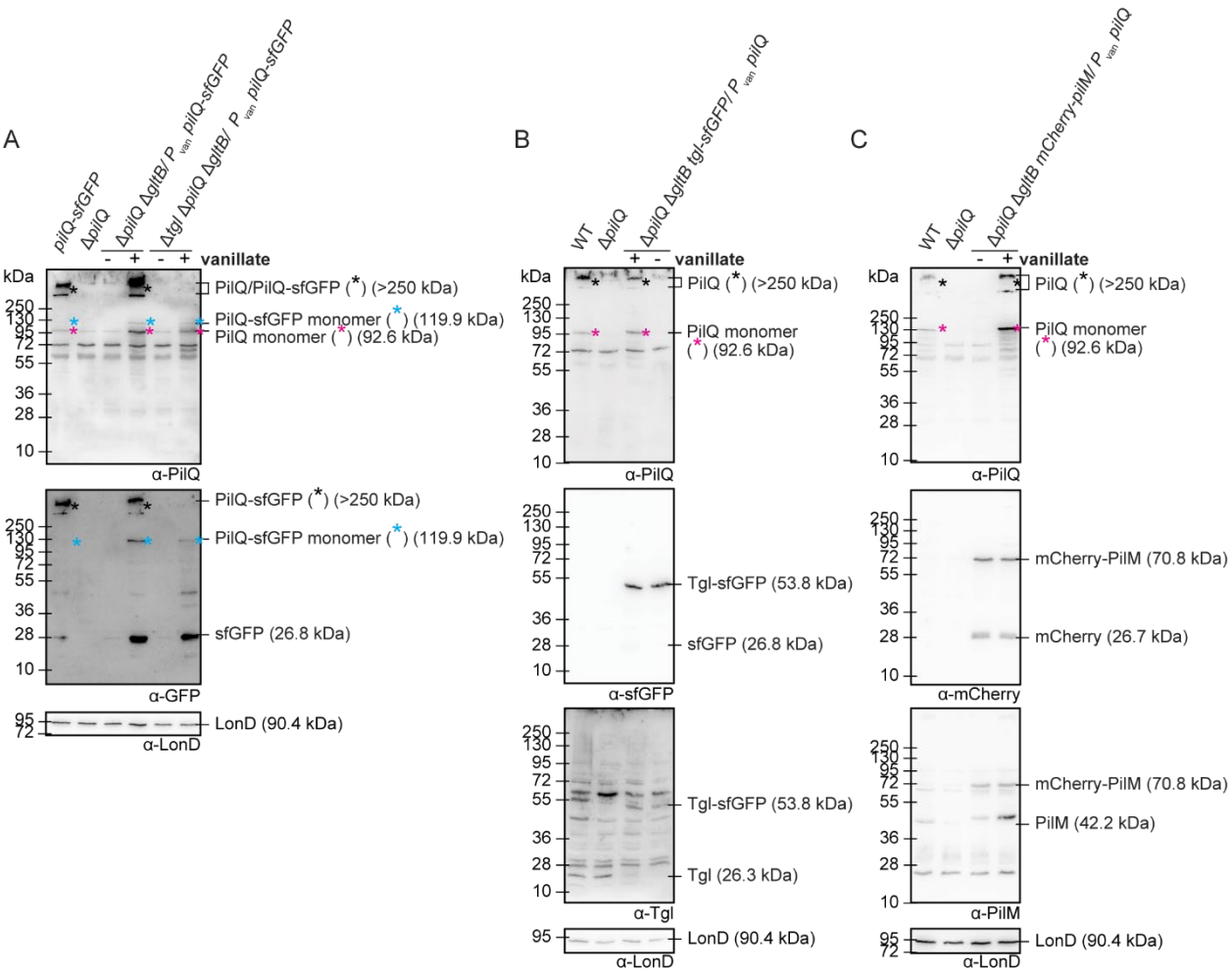

Figure S2. Induction of PilQ synthesis. (A-C) Immunoblot detection of (A) PilQ-sfGFP or (C, D) PilQ protein expression in the indicated strains. Protein from the same number of cells from exponentially growing suspension cultures was loaded per lane. To induce protein expression from P_{van}, cells were treated with vanillate for 24 h. In A, 10 µM vanillate was used for inducing PilQ-sfGFP accumulation at WT levels in the Δ*pilQ* background, and 500 µM vanillate was used to highly induce PilQ-sfGFP accumulation in the Δ*tgl* Δ*pilQ* background. In B, 20 µM vanillate was used for inducing PilQ accumulation at WT levels in Δ*pilQ* cells expressing *tgl-sfGFP*. In C, 1mM vanillate was used to rapidly induce *pilQ* expression in cells co-expressing *mCherry-pilM* (Fig. S4C). The blot was stripped before applying a new antibody. LonD served as a loading control. Monomeric or oligomeric forms of PilQ/PilQ-sfGFP are marked with an asterisk. Calculated molecular weights of proteins without signal peptide (if relevant) are indicated.

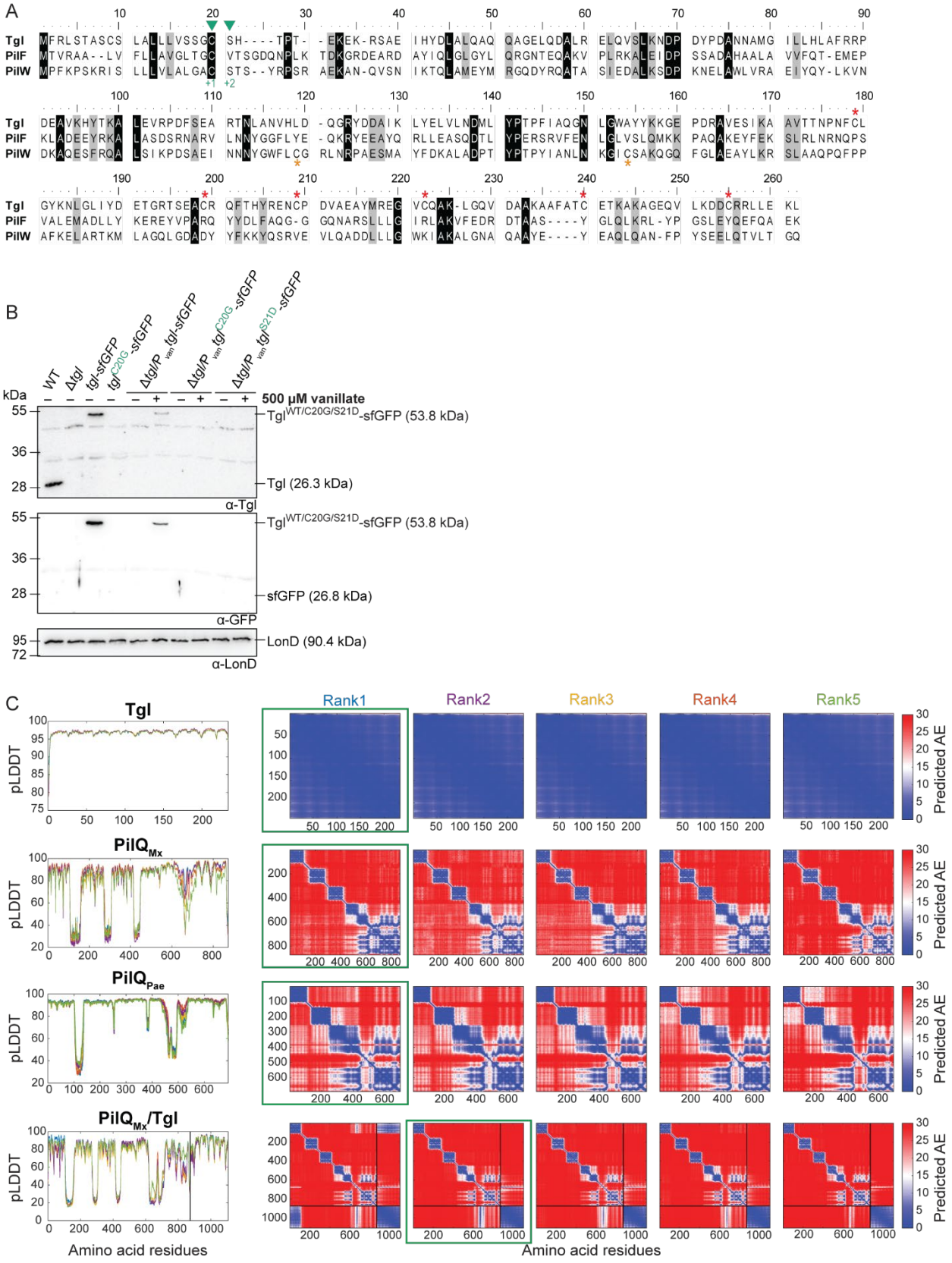

Figure S3. Amino acid and structural characterization of TgI alone and in complex with its PilQ secretin partner, and accumulation of TgI-sfGFP variants. (A) Alignment of full-length amino acid sequences of TgI, PilF from *P. aeruginosa,* and PilW from *N. meningitides*, where the acylated N-terminal Cys residue +1 of the mature lipoprotein and residue +2, important for retention of lipoproteins in the IM in *Escherichia coli*, are marked with a green arrow. The Cys residues within TgI predicted by AlphaFold to form disulfide bridges are marked with a red asterisk (Fig. 7A). The Cys residues within

PilW that form a disulfide bridge are marked with an orange asterisk. (B) Immunoblot detection of Tgl variants. Protein from the same number of cells from exponentially growing suspension cultures was loaded per lane. To induce gene expression from P_{van}, cells were incubated with 500 µM vanillate for 24 h when indicated. Blot was probed with the indicated antibodies. The blot was stripped before applying a new antibody. LonD served as a loading control. Calculated molecular weights of proteins without signal peptide (if relevant) are indicated. (C) pLDDT and pAE plots for five models of the indicated proteins or protein complexes in Fig. 7A, F and Fig. S5A, predicted by AlphaFold. The model marked by a green box was used for further analysis. Signal peptides were removed before generating a model.

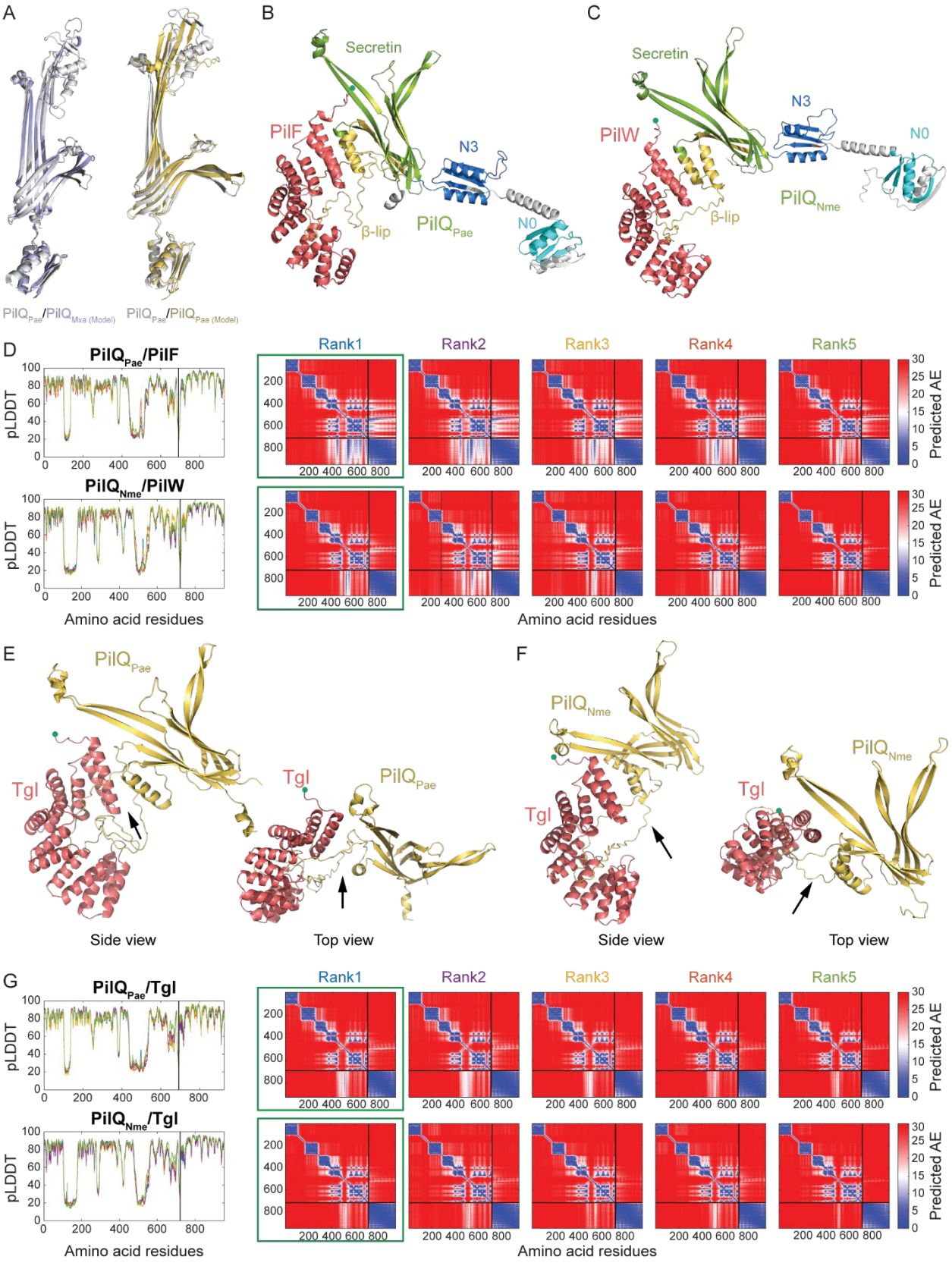

Figure S4. Structural characterization of pilotin/secretin complexes. (A) Superposition of the AlphaFold modeled PilQ structures of *M. xanthus* (lilac) or *P. aeruginosa* (yellow) with a PilQ protomer (gray) of the CryoEM structure of the secretin of *P. aeruginosa* in Fig. 7D. (B, C, E, F) Modeled AlphaFold heterodimer of PilF/PilQ$_{Pae}$ (B), PilW/PilQ$_{Nme}$ (C), Tgl/PilQ$_{Pae}$ (E) and Tgl/PilQ$_{Nme}$ (F). The the acylated N-terminal Cys residue of mature Tgl (residue Cys20 in the unprocessed protein) that places the protein at the inner leaflet of the OM is indicated by a green circle. The domains of PilQ are colored as described

in Fig. 7F. (D, G) pLDDT and pAE plots for five models of the indicated proteins or protein complexes in panels B-C, E-F predicted by AlphaFold. The model marked by a green box was used for further analysis. Signal peptides were removed before generating a model.

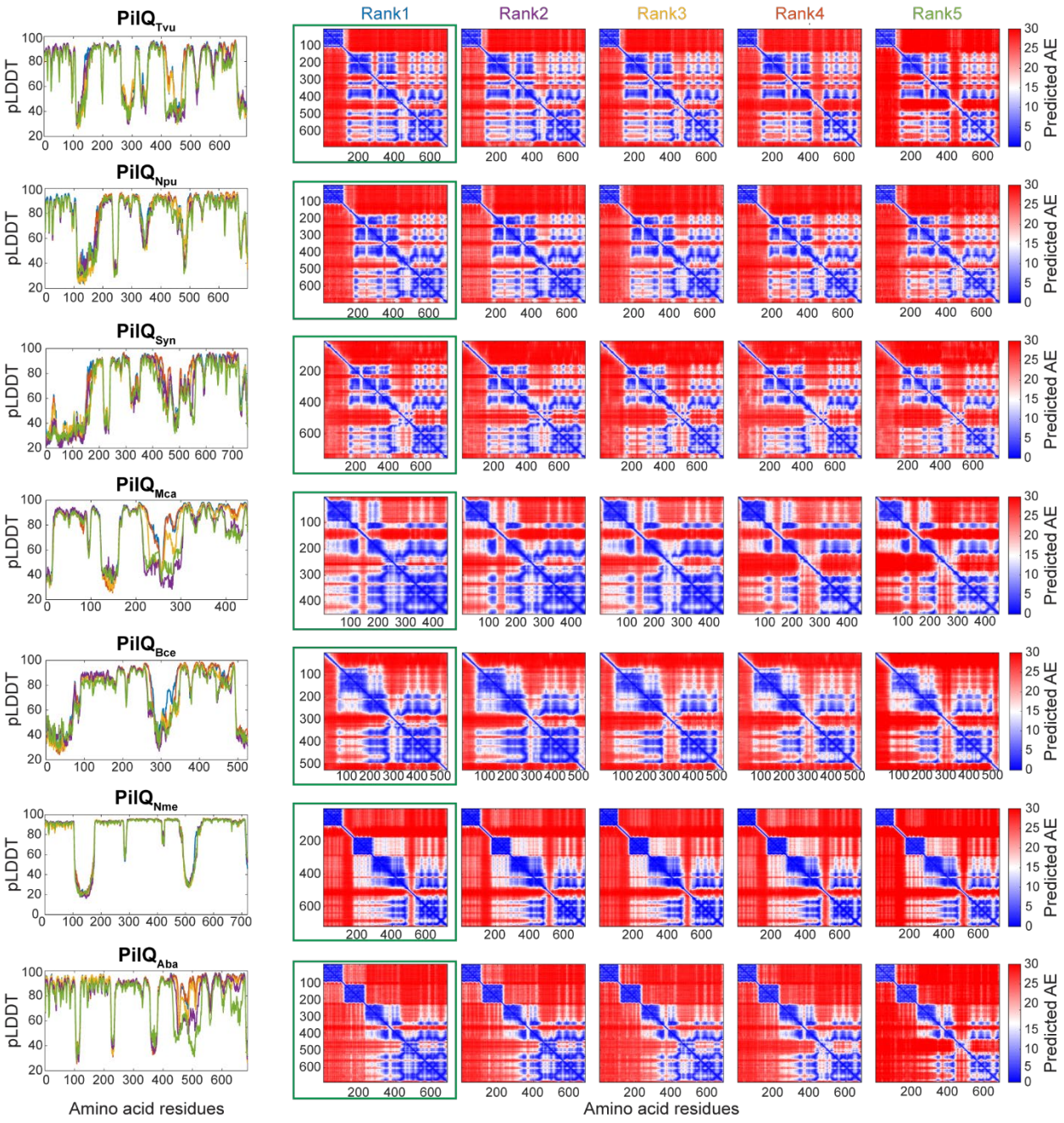

Figure S5. pLDDT and pAE plots of the Alphafold models of PilQ secretins in other bacteria. pLDDT and pAE plots for five models of the indicated proteins in Fig. 8 C-I predicted by AlphaFold. The model marked by a green box was used for further analysis. Signal peptides were removed before generating a model.

Table S1. Oligonucleotides used in this work[1]

Primer name	Sequence 5‘-3‘	Brief description
tgl_fw_hindiii	ATCAAGCTTATGTTCCGCCTTTCCACCGCGTCC	For replacement of *tgl* with *tgl*-sfGFP
sfgfp_rv_xbaI	ATCTCTAGATTATTTGTAGAGCTCATCCATGCCAT	
tgl_ds_fw_xbaI	ATCTCTAGACGCGTTGGGTATCTGGGGACCCGT	
tgl_ds_rv	ATCGAATTCGGAGCGCCGCCACACAGCGAGCAC	
tgl_CtoG_A_HindIII	GCGCAAGCTTGTGATGATCGACAATCCCAT	For replacement of *tgl* with *tgl*^{C20G}
tgl_CtoG_Bov	GGGCGTGTGGGAGCCACCGGAGGACACCAGCAGCA	
tgl_CtoG_Cov	GTGTCCTCCGGTGGCTCCCACACGCCCACGGAGAA	
tgl_CtoG_D_BamHI	GCGCGGATCCCCAGCTTTCGCCTTGGTCTCA	
Pvan_PilQ_fwd_NdeI	AGTCCATATGCTCGAGGAGAGCGCTGT	For expression of *pilQ or pilQ-sfGFP* from the *18-19* site under control of P_{van}
sfGFP_rev_pilQ_EcoRI	TCAGGAATTCTTAGGATCCTTTGTAGAGC	
PilQ_rev_EcoRI	GCGTGAATTCTTACAGAGTCTGCGCAATGG	
Pvan_tgl_fw_NdeI	GATCCATATGTTCCGCCTTTCCACCGCG	For expression of tgl, *tgl-sfGFP*, *tgl*^{C20G}*-sfGFP or tgl*^{S21D}*-sfGFP* from the *18-19* site under control of P_{van}
sfGFP_rv_tgl_EcoRI	CACTGAATTCTTATTTGTAGAGCTCATCCATGCCAT	
Pvan forw	TGGACTCTAGCCGACCGACTGAGACGC	
Tgl_S21G_overlay_rev	TGGGCGTGTGGTCGCAACCGGAGGACACCA	
Tgl_S21G_overlay_fwd	CTCCGGTTGCGACCACACGCCCACGGAGAA	
PilQ_dAMIN_A_XbaI	ATATTCTAGACGCTGCGTCGACCGCGGGCA	For deletion of the AMIN domains of PilQ
PilQ_dAMIN_B	TCCCACGGTAGCGGGCACCATGCACCCTGGCGCCC	
PilQ_dAMIN_C	GGTGCATGGTGCCCGCTACCGTGGGAAGCGCGTAT	
pilQ_dAMIN_D_HindIII	GAATAAGCTTCGCAGGTTGAGCTGAAGCGCCC	
tgl-A_XbaI	ATATTCTAGATACCGCGGGCTGCCCGCC	For Δ*tgl*
tgl-D_EcoRI	TGACGAATTCACGAGCCGGTCGGACTCG	

PilQAMIN_A_KpnI	TATAGGTACCATGCAGACAAGGTTCGCCT	For generation of *pilQ*$^{AMINs\ (1-475)}$*-sfGFP* using the *pilQ::pilQ-sfGFP* strain
PilQAMIN_sfGFP_overlay_rev	ggagccgccgccgccGGCCTGCTGGGGCGCGCCCT	
PilQamin_sfGFP_overlay_fwd	GCGCCCCAGCAGGCCggcggcggcggctccatgag	
sfGFP_rev_pilQ_EcoRI	TCAGGAATTCTTAGGATCCTTTGTAGAGC	

[1] Underlined sequences indicate restriction sites.

8.3 A burst of c-di-GMP during cytokinesis ensures the generation of phenotypically identical and symmetrical daughter cells

This chapter contains our analysis of the function of DmxA in motility of *M. xanthus.* This part of the thesis is written in a manuscript style and is in preparation for publication. I contributed to this work by designing, performing and analyzing experiments, preparing the figures and the manuscript.

I performed experiments and analysis in Fig. 1A-C, 2A-H, 3B and D, 4A-D, 5A-C, 6A-C, 7, S1C-D and F, S2A-E, S3D, S4A-B, S5.

A burst of c-di-GMP during cytokinesis ensures the generation of phenotypically identical and symmetrical daughter cells

María Pérez-Burgos[1, #], Marco Herfurth[1, #], Andreas Kaczmarczyk[4], Katrin Huber[1], Timo Glatter[3], Urs Jenal[4], Roland Seifert[5], and Lotte Søgaard-Andersen[1,6]

[1]Max Planck Institute for Terrestrial Microbiology, Department of Ecophysiology,

35043 Marburg, Germany

[#] contributed equally to this work.

[3] Core Facility for Mass Spectrometry & Proteomics, Max Planck Institute for Terrestrial Microbiologygrid.419554.8, Marburg, Germany.

[4] Biozentrum, University of Basel, Basel, Switzerland.

[5] Institute of Pharmacology and RCU Metabolomics, Hannover Medical School, Carl-Neuberg Str. 1, D-30625 Hannover

[6] Corresponding author

Tel. +49-(0)6421-178201

Fax +49-(0)6421-178209

E-mail: sogaard@mpi-marburg.mpg.de

Abstract

C-di-GMP is a ubiquitous and highly versatile second messenger that regulates numerous processes in response to cellular or environmental signals in bacteria. The rod-shaped *Myxococcus xanthus* cells move in the direction of their long axis with well-defined leading and lagging cell poles and using type IV pili (T4P)-dependent motility and gliding motility. The motility machines are polarized, and their activity is only stimulated at the leading cell pole. However, in response to signaling by the Frz chemosensory system, the cells reverse their direction of movement, and the polarity of the two motility systems is inverted. *M. xanthus* synthesizes the second messenger c-di-GMP and systematic inactivation of genes encoding diguanylate cyclases (DGCs), showed that only a lack of DmxA causes a defect in motility. Here we show that Δ*dmxA* cells hyper-reverse leading to the defect in both motility systems. Additionally, we report that DmxA is recruited by the divisome to mid-cell during cytokinesis, thereby activating DmxA DGC activity and resulting in a brief burst in the c-di-GMP level. Our experiments support that during this short period of the cell cycle, DmxA and c-di-GMP establish the symmetric distribution of proteins at the nascent and new cell poles of the two daughter cells. In the absence of DmxA, this symmetric distribution is deficient resulting in abnormal cell polarity and an increase in the reversal frequency. Thus, *M. xanthus* represents an example in which c-di-GMP regulates the generation of phenotypically similar daughter cells.

Keywords: c-di-GMP, diguanylate cyclase, phosphodiesterase, divisome, polarity, type IV pili, type IV pili-dependent motility, gliding motility, heterogeneity, cell cycle regulation

Introduction

Bis-(3'-5')-cyclic dimeric GMP (c-di-GMP) is a ubiquitous and versatile nucleotide-based second messenger that regulates multiple processes in bacteria (Jenal *et al.*, 2017, Römling *et al.*, 2013). At the population-level, these processes are often associated with lifestyle transitions between motile and sessile behaviors with high levels of c-di-GMP stimulating adhesion as well as the synthesis of secreted polysaccharides and inhibiting motility, thereby promoting biofilm formation and virulence (Jenal *et al.*, 2017, Römling *et al.*, 2013). However, at the level of individual cells, c-di-GMP can also play an essential role in the generation of cellular heterogeneity within a population of genetically identical cells (Kreiling & Thormann, 2023). Specifically, during the *Caulobacter crescentus* cell cycle, a hardwired, deterministic genetic program drives oscillations in the cellular c-di-GMP concentration that upon cell division results in the formation of a non-motile stalked daughter cell with a high level of c-di-GMP and a motile swarmer cell with a low level of c-di-GMP (Lori *et al.*, 2015, Abel *et al.*, 2013, Kaczmarczyk *et al.*, 2020, Kaczmarczyk *et al.*, 2022, Christen *et al.*, 2010). Similarly, in response to surface contact by *Pseudomonas aeruginosa* cells, a deterministic genetic program is initiated that also results in the formation of a non-motile stalked daughter cell that has a high level of c-di-GMP and a motile swarmer cell with a low level of c-di-GMP (Laventie *et al.*, 2019b, Kaczmarczyk *et al.*, 2022). Here, we report that a c-di-GMP-based, deterministic genetic program is hardwired into the cell cycle of *Myxococcus xanthus* to reduce heterogeneity and guarantee the formation of phenotypically identical daughter cells.

The cellular level of c-di-GMP is determined by the opposing activities of diguanylate cyclases (DGC), which synthesize c-di-GMP from two GTP molecules, and phosphodiesterases (PDE), which degrade c-di-GMP (Jenal *et al.*, 2017, Römling *et al.*, 2013). DGCs contain a catalytic GGDEF domain named after the GG[E/D]EF motif in the active site (A-site) (Paul *et al.*, 2004). Additionally, they often contain an allosteric binding site for c-di-GMP, the so-called I-site, that is responsible for allosteric feedback inhibition of DGC activity (Christen *et al.*, 2006). PDEs contain either an EAL or an HD-GYP domain (Jenal *et al.*, 2017, Römling *et al.*, 2013). The effects of changing c-di-GMP levels are implemented by the binding of d-di-GMP to downstream effectors (Jenal *et al.*, 2017, Römling *et al.*, 2013). Importantly, the genetic programs driving the generation of cellular heterogeneity in *C. caulobacter* and *P. aeruginosa* depend on the spatial separation of the relevant DGC and PDE to opposite cell poles (Lori *et al.*, 2015, Laventie *et al.*, 2019b). As a consequence of this localization, one daughter cell inherits the cell pole with the PDE and, therefore, has a low level of c-di-GMP, and this daughter cell becomes the motile daughter cell. By contrast, the other daughter cell inherits the pole with the DGC and, therefore, has a high level of c-di-GMP, and this daughter cell becomes the non-motile daughter cell.

The rod-shaped cells of *Myxococcus xanthus* translocate across surfaces using two motility systems, one for gliding and one for type IV pili (T4P)-dependent motility (Fig. S1A-B) (Carreira *et al.*, 2022, Schumacher & Søgaard-Andersen, 2017, Zhang *et al.*, 2012a). Motility is important for the social behaviors of *M. xanthus* including the formation of predatory, spreading colonies in the presence and spore-filled fruiting bodies in the absence of nutrients (Konovalova *et al.*, 2010, Muñoz-Dorado *et al.*, 2016). Both motility systems are highly polarized, i.e. the T4P machine (T4PM) is present at both cell poles (Nudleman *et al.*, 2006, Bulyha *et al.*, 2009, Friedrich *et al.*, 2014, Siewering *et al.*, 2014). However, it is only active at one pole at a time and, therefore, T4P only assemble at one pole at a time (Kaiser, 1979, Chang *et al.*, 2016, Sun *et al.*, 2000, Bulyha *et al.*, 2009). Along the same lines, the Agl/Glt machine for gliding only assembles at one pole at a time (Jakobczak *et al.*, 2015, Luciano *et al.*, 2011, Mignot *et al.*, 2007, Nan *et al.*, 2013, Nan *et al.*, 2011, Nan *et al.*, 2010, Sun *et al.*, 2011, Wartel *et al.*, 2013, Treuner-Lange *et al.*, 2015). Importantly, the two machines are active at the same pole (Carreira *et al.*, 2022, Schumacher & Søgaard-Andersen, 2017, Zhang *et al.*, 2012a). This polarity enables *M. xanthus* cells to move unidirectionally with a piliated leading and a non-piliated lagging cell pole (Sun *et al.*, 2000, Mercier *et al.*, 2020, Potapova *et al.*, 2020) and is essential for efficient translocation across surfaces (Potapova *et al.*, 2020, Treuner-Lange *et al.*, 2015). Occasionally, and in response to signaling by the Frz-chemosensory system, the polarity of the two motility machines is inverted and in parallel cells reverse their direction of movement (Carreira *et al.*, 2022, Schumacher & Søgaard-Andersen, 2017, Zhang *et al.*, 2012a, Dinet & Mignot, 2023). Regulation of the reversal frequency is essential for the formation the predatory spreading colonies and spore-filled fruiting bodies (Blackhart & Zusman, 1985).

The activity and polarity of the two motility machines is regulated by the so-called polarity module (Carreira *et al.*, 2022, Dinet & Mignot, 2023, Carreira *et al.*, 2023, Szadkowski *et al.*, 2022). The output of this module is generated by the small Ras-like GTPase MglA, which is a nucleotide-dependent molecular switch that is inactive in the GDP-bound and active in the GTP-bound state (Leonardy *et al.*, 2010, Zhang *et al.*, 2010). In its GTP-bound state MglA localizes to and defines the leading cell pole (Leonardy *et al.*, 2010, Zhang *et al.*, 2010). At the leading pole, MglA interacts with effectors to stimulate the T4PM resulting in T4P formation (Potapova *et al.*, 2020, Mercier *et al.*, 2020) and is essential for T4aP-dependent motility (Hodgkin & Kaiser, 1979, Hartzell & Kaiser, 1991). Similarly, MglA at the leading cell pole stimulates the assembly of the Agl/Glt machine (Treuner-Lange *et al.*, 2015, Zhang *et al.*, 2012b, Mauriello *et al.*, 2010). The remaining polarly localized proteins of the polarity module regulate the nucleotide-bound state of MglA by acting as a guanine nucleotide exchange factor (GEF) in case of the RomR/RomX complex (Szadkowski *et al.*, 2019) or as a GTPase activating protein (GAP) in case of the MglB/RomY complex (Leonardy *et al.*, 2010,

Szadkowski *et al.*, 2022, Zhang *et al.*, 2010). In particular, the MglB/RomY complex, via its GAP activity, excludes MglA from the lagging pole (Carreira *et al.*, 2020, Zhang *et al.*, 2012a, Szadkowski *et al.*, 2022, Leonardy *et al.*, 2010, Keilberg *et al.*, 2012, Zhang *et al.*, 2010).

M. xanthus synthesizes c-di-GMP during growth and development, and it encodes 11 GGDEF domain proteins that are predicted to be enzymatically active (Skotnicka *et al.*, 2015). The systematic inactivation of the 11 corresponding genes identified DmxA as the only DGC implicated in the regulation of motility in the presence of nutrients (Skotnicka *et al.*, 2015). However, the mechanism by which DmxA regulates motility is not understood.

Here, we show that DmxA regulates both motility systems by establishing correct cell polarity. DmxA is recruited to mid-cell during cytokinesis and during this brief period of the cell cycle, DGC activity is stimulated resulting in a dramatic but brief increase in the cellular c-di-GMP concentration. By focusing on the T4PM, we show that the spike in the c-di-GMP level ensures the equal incorporation of proteins at the incipient cell poles during cytokinesis as well as the new cell poles of the two daughter cells. As a consequence, the two daughter cells are created equally, both inheriting the same amount of T4PM structural components and correct polarity. In the absence of DmxA, the daughter cells inherit unequal amounts of T4PM structural components and have incorrect polarity. Mislocalization of proteins at the poles, in turn, results in an abnormal polarity and an increase in the reversal frequency and a defect in motility. Thus, we show for the first time that, during cell division, c-di-GMP not only regulates the generation of phenotypically distinct offspring but also phenotypically identical offspring.

Results

Δ*dmxA* cells have a defect in the regulation of the reversal frequency

We previously showed that disruption of the *dmxA* gene by a plasmid insertion (Ω*dmxA*) caused reduced T4P-dependent motility (Skotnicka *et al.*, 2015). To understand the molecular mechanism underlying the mechanism of DmxA, we generated an in-frame deletion mutation of *dmxA* (Δ*dmxA*) and tested the mutant for motility using population-based assays as well as single cell assays. In the population-based motility assays, cells were spotted on 0.5% and 1.5% agar supplemented with 0.5% casitone broth (CTT), which are favorable for T4P-dependent and gliding motility, respectively (Shi & Zusman, 1993).

On 0.5% agar, wild-type (WT) cells generated colonies with the long characteristic flares while the Δ*pilA* mutant, which lacks the major pilin of T4P (Fig. S1B) (Wu & Kaiser, 1995) and served as a negative control, generated smooth colony edges without flares (Fig. 1A). The Δ*dmxA* mutant formed significantly shorter flares than WT and was significantly reduced in colony expansion (Fig. 1A). Importantly, this motility defect was complemented by the ectopic expression of *dmxA* from its native promoter from a plasmid integrated in a single copy at the Mx8 *attB* site (Fig. 1A). Because the Δ*gltB* mutant, which has a defect in gliding motility due to the lack of a component of the Agl/Glt machine for gliding (Fig. S1A) (Jakobczak *et al.*, 2015), also exhibited reduced flare formation on 0.5% agar, we compared flare formation and colony expansion of the Δ*gltB* mutant and the Δ*dmxA* Δ*gltB* double mutant. The Δ*dmxA* Δ*gltB* mutant exhibited significantly shorter flares and reduced colony expansion compared to the Δ*gltB* mutant (Fig. 1A), supporting that the Δ*dmxA* mutation causes a T4aP-dependent motility defect.

On 1.5% agar, WT displayed single cells at the edge of the colony, which was not the case for the Δ*gltB* mutant, which served as a negative control (Fig. 1A). The Δ*dmxA* mutant also exhibited single cells at the colony edge but was significantly reduced in colony expansion (Fig. 1A) and this motility defect was complemented by the ectopic expression of *dmxA* (Fig. 1A). Because the Δ*pilA* mutant, while still displaying single cells at the colony edge, also had reduced colony expansion on 1.5% agar, we compared its motility characteristics with those of a Δ*dmxA* Δ*pilA* double mutant. Δ*dmxA* Δ*pilA* cells had a stronger expansion defect on 1.5% agar than the Δ*pilA* control (Fig. 1A), supporting that the Δ*dmxA* mutation causes a gliding motility defect. In total, we conclude that DmxA is important but not essential for T4aP-dependent motility as well as for gliding motility. We previously reported that the Ω*dmxA* mutant only had a defect in T4P-dependent motility (Skotnicka *et al.*, 2015). However, in those experiments, we exclusively focused on whether single cells could move by gliding motility and not the overall colony expansion.

Because motility defects in the population-based assay can be caused by *bona fide* motility defects or by an altered reversal frequency, we analyzed the single-cell behavior of Δ*dmxA* cells to distinguish between these two possibilities. In the single-cell assays for T4aP-dependent motility and gliding motility, the Δ*dmxA* cells reversed with a higher frequency than WT (Fig. 1B-C). The reversal defect was complemented in the complementation strain (Fig. 1B-C). To determine whether the increase in the reversal frequency of the Δ*dmxA* cells depended on a higher activity of the Frz chemosensory system, we deleted the *frzE* gene, which encodes the FrzE kinase and is essential for Frz-induced reversals (Bustamante *et al.*, 2004). While the reversal frequency of Δ*frzE* cells, as expected, was strongly reduced, the Δ*dmxA* Δ*frzE* cells reversed with a higher frequency than the Δ*frzE* cells but lower than the Δ*dmxA* cells (Fig. 1B-C). Together, these results suggest that the motility defects caused by the Δ*dmxA* mutation are caused by a Frz-independent increase in the reversal frequency rather than a *bona fide* motility defect. Consistent with the observation that motility *per se* is not affected by the the Δ*dmxA* mutation, the structural proteins of the two motility machines accumulated at the same level in WT and the Δ*dmxA* mutant (Fig. S1C-D).

Previously, the T4P-dependent motility defect of the Ω*dmxA* mutant was suggested to arise from a slight increase in the biosynthesis of the secreted polysaccharide exopolysaccharide (EPS) (Skotnicka *et al.*, 2015). In a plate-based colorimetric assay for EPS accumulation with Congo red and Trypan blue, we observed that the Δ*dmxA* mutation also resulted in a slight increase in EPS synthesis compared to WT (Fig. S1E). Because a slight increase in EPS synthesis would not explain the defects in gliding motility, we suggest that the slightly increased EPS accumulation is not causing the reversal defect in the Δ*dmxA* mutant.

Δ*dmxA* cells have a defect in cell polarity

Mutants with a Frz-independent increase in the reversal frequency, generally, have aberrant regulation of the polarity module causing MglA to localize to both cell poles (e.g. Δ*mglB*) (Zhang *et al.*, 2010, Leonardy *et al.*, 2010, Keilberg *et al.*, 2012, Szadkowski *et al.*, 2022). In the case of the T4P-dependent motility system, this causes formation of T4P at both cell poles (Potapova *et al.*, 2020). Because T4P are easily scored, we used T4P-dependent motility as a readout to understand the mechanism of DmxA. Therefore, we determined the localization of T4P in the Δ*dmxA* cells. While 82% of WT cells has T4P at one pole and the remaining cells were unpiliated, 10% of Δ*dmxA* cells had T4P at both poles (Fig. 1D). Moreover, the percentage of piliated Δ*dmxA* cells was slightly higher than for WT. Consistently, in a T4P shear-off assay, in which T4P are sheared off the cell surface followed by quantification of PilA levels by immunoblotting, PilA was present in the sheared fraction from the Δ*dmxA* mutant at a slightly higher level than in WT cells (Fig. S1F). The Frz-independent hyper-reversal

phenotype with formation of T4P at both poles caused by the Δ*dmxA* mutation is somewhat reminiscent of the one caused by lack of the MglB/RomY GAP complex (Potapova *et al.*, 2020, Szadkowski *et al.*, 2022, Leonardy *et al.*, 2010, Zhang *et al.*, 2010). Interestingly, the Δ*dmxA* cells reverse in a heterogenous manner with some cells reversing up to 8 times in 15 min, and some not reversing. In contrast, all Δ*mglB* cells showed a significant increase in the reversal frequency (Fig. 1B) and more cells were bipolarly piliated (Fig. 1D) suggesting that the polarity defect of the Δ*dmxA* mutant is different from that of the Δ*mglB* mutant.

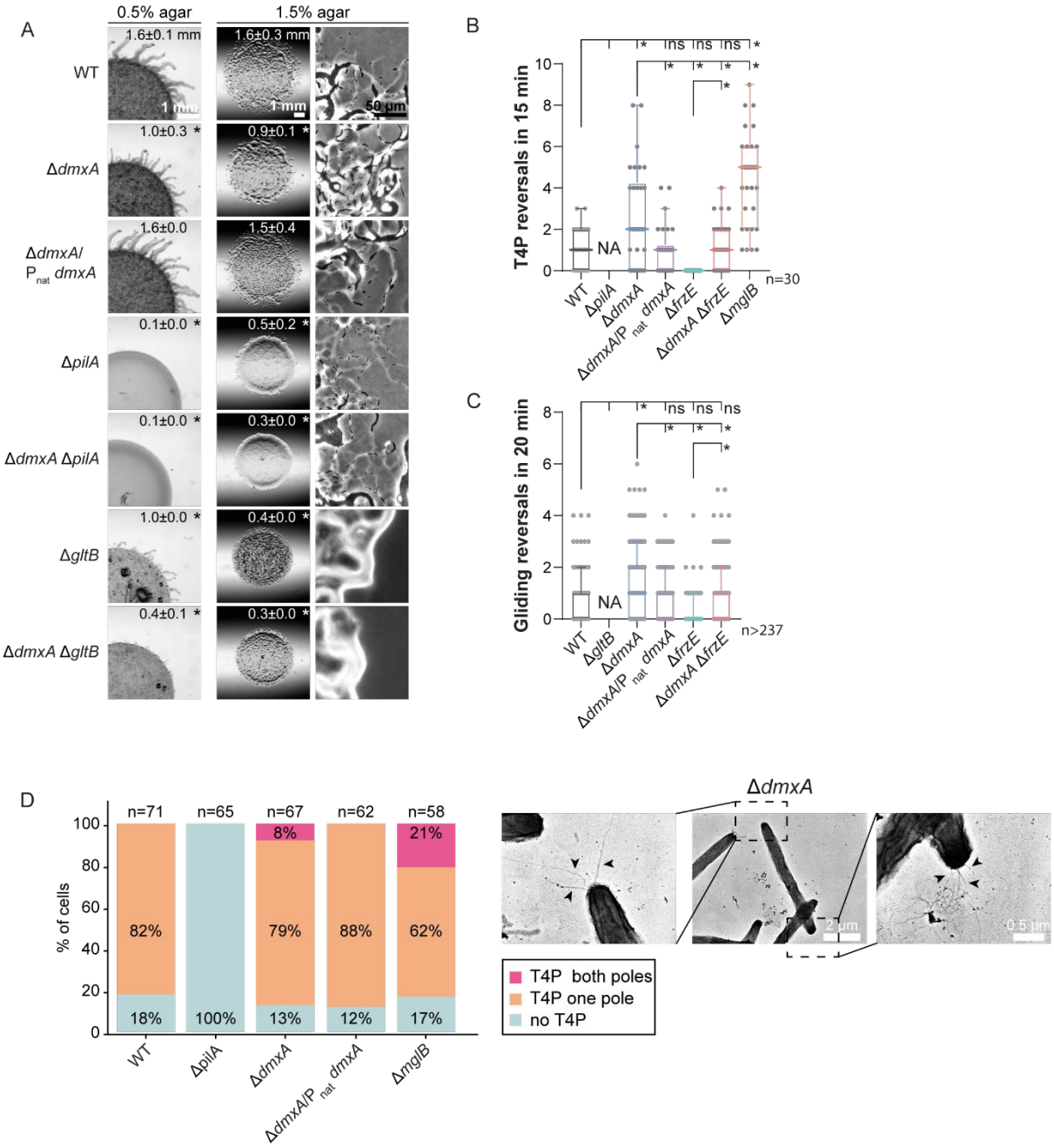

Figure 1. The Δ*dmxA* mutant has a defect in polarity. (A) T4P-dependent and gliding motility were analyzed on 0.5% and 1.5% agar respectively. Numbers indicate the colony expansion in 24 h as mean ± standard deviation (SD) (*n* = 3). *p<0.05, one-way ANOVA with multiple comparison test against WT. Scale bars, 1 mm (left), 1 mm (middle), 50 µm (right). (B-C) Movement of single cells by (B) T4P-

dependent or (C) gliding in 1% methylcellulose or on 1.5% agar supplemented with 0.5% CTT, respectively. Cells were imaged for 15 min or 20 min with 30 s intervals and number of reversals was analyzed. Only cells moving during the entire recording interval were included. In the box plot, boxes enclose the 25th and 75th percentile with the thick horizontal line representing the median; whiskers represent the 1.5 times the interquartile range. Additionally, individual data points are shown. NA, not applicable because cells are non-motile. * p<0.05, ns, not significant; one-way ANOVA multiple comparison test. (D) Transmission electron microscopy analysis of T4P formation pattern. Left panel, quantification of cells with no T4P, T4P at one pole or at both poles. Right panel, example of a Δ*dmxA* cell, with T4P at both poles. T4P are indicated by black arrowheads. The picture in the middle (size bar is 2 µm) shows the complete cell and the pictures on the left and right (size bar is 0.5 µm) show the first and second pole.

DmxA is an active DGC and with a low affinity I-site

To understand how DmxA regulates cell polarity, we analyzed its biochemical properties *in vitro*. Based on sequence analysis, DmxA has six N-terminal trans-membrane α-helices, followed by two GAF domains (GAF1 and GAF2), and the catalytic GGDEF domain, which contains a GGEEF motif as well as an I-site (Fig. 2A). We previously showed that a soluble His_6-DmxA variant comprising the two GAF domains and the GGDEF domain is enzymatically active and binds c-di-GMP *in vitro* (Skotnicka *et al.*, 2015). To understand how the different parts of DmxA contribute to its catalytic activity, we purified soluble variants of DmxA fused to MalE (Fig. 2B) and tested for DGC activity and c-di-GMP binding. Specifically, we purified truncated MalE-tagged WT variants containing the two GAF domains and the GGDEF domains ($DmxA^{WT}$), only the two GAF domains ($DmxA^{GAF\times2}$), or only the GGDEF domain ($DmxA^{GGDEF}$). Moreover, we purified MalE-tagged $DmxA^{WT}$ variants with a substitution either in the catalytic A-site ($DmxA^{E626A}$) or in the I-site ($DmxA^{R615A}$). Interestingly, in size exclusion chromatography (SEC), the $DmxA^{WT}$ and $DmxA^{GAF\times2}$ variants eluted as dimers, while the $DmxA^{GGDEF}$ variant eluted as a monomer (Fig. 2B and Fig. S2A-B), indicating that the GAF domains are important for dimer formation. DGCs have to dimerize to be active (Jenal *et al.*, 2017, Römling *et al.*, 2013). Indeed, a high-confidence Alphafold structural model showed that as for other DGCs, DmxA forms a symmetric dimer with the active sites of the two GGDEF domains facing each other (Fig. 2C and Fig. S2C). Interestingly, in this structure, the protomers bind to each other via the two long α-helices connecting GAF1 to GAF2, and GAF2 to the GGDEF domain within each protomer (Fig. 2C), supporting that the GAF domains are important for dimer formation.

As expected, $DmxA^{WT}$ was active and synthetized c-di-GMP, while the $DmxA^{E626A}$ variant did not (Fig. 2D). The $DmxA^{R615A}$ variant also had DGC activity (Fig. 2D), whereas $DmxA^{GAF\times2}$ as expected did not. Importantly, the $DmxA^{GGDEF}$ variant did not have DGC activity (Fig. 2D) supporting that the GAF domains are necessary for the efficient dimerization and, therefore, activity of DmxA. Next, we used Bio-Layer Interferometry to test the affinity of $DmxA^{WT}$ for c-di-GMP. $DmxA^{WT}$ bound c-di-GMP with a K_D of ~3.5 µM (Fig. 2E-F and Fig. S2D), whereas $DmxA^{R615A}$ did not detectably bind c-di-GMP (Fig. 2E). The $DmxA^{E626A}$ variant also bound c-di-

GMP while the DmxA$^{GAF\times2}$ variant did not (Fig. 2E). Surprisingly, the DmxA^{GGDEF} only generated a weaker wavelength shift than DmxA^{WT}, which could either result from the smaller size of this variant, or suggest that it binds c-di-GMP with a lower affinity (Fig. 2E). Because the c-di-GMP binding affinity of the I-site was only moderate, we wondered whether the I-site would even regulate DGC activity of DmxA at physiological concentrations. To this end, we determined the initial reaction velocity (V_0) of DmxA^{WT} and DmxA^{R615A} and observed that V_0 of DmxA^{R615A} was only slightly higher at very high concentrations of GTP (400µM) (Fig. 3G). Because inhibition of DmxA^{WT} DGC activity by c-di-GMP was relatively minor, we determined the inhibitory constant of DmxA^{WT} by measuring V_0 of DmxA^{WT} and DmxA^{R615A} in the presence of different c-di-GMP concentrations. As expected, DmxA^{R615A} was not inhibited by c-di-GMP, while DmxA^{WT} was inhibited with a K_i of ~15 µM (Fig. 7H). This concentration is 10-fold higher than the average c-di-GMP concentration in *M. xanthus* cells (i.e. 1.4±0.5 µM) (Skotnicka *et al.*, 2020).

Finally, because GAF domains of eukaryotic PDEs mediate oligomerization and also bind to nucleotides, e.g. cAMP, cGMP, to regulate catalytic activity (e.g. the activity of human PDE2A is stimulated by cGMP binding) (Pandit *et al.*, 2009, Heikaus *et al.*, 2009), we wondered whether the GAF domains of DmxA would bind other nucleotides. To this end, we tested DGC activity of DmxA^{WT} in the presence of different nucleotides, but did not observe any significant effect on c-di-GMP synthesis, demonstrating that the GAF domains of DmxA may not bind nucleotides (Fig. S2E).

Altogether, our results demonstrate that DmxA is a DGC with a low affinity for c-di-GMP, suggesting that it can be highly active before product inhibition regulates activity. Moreover, while DGC activity and c-di-GMP binding is dispensable for dimer formation, the two GAF domains are essential for dimerization.

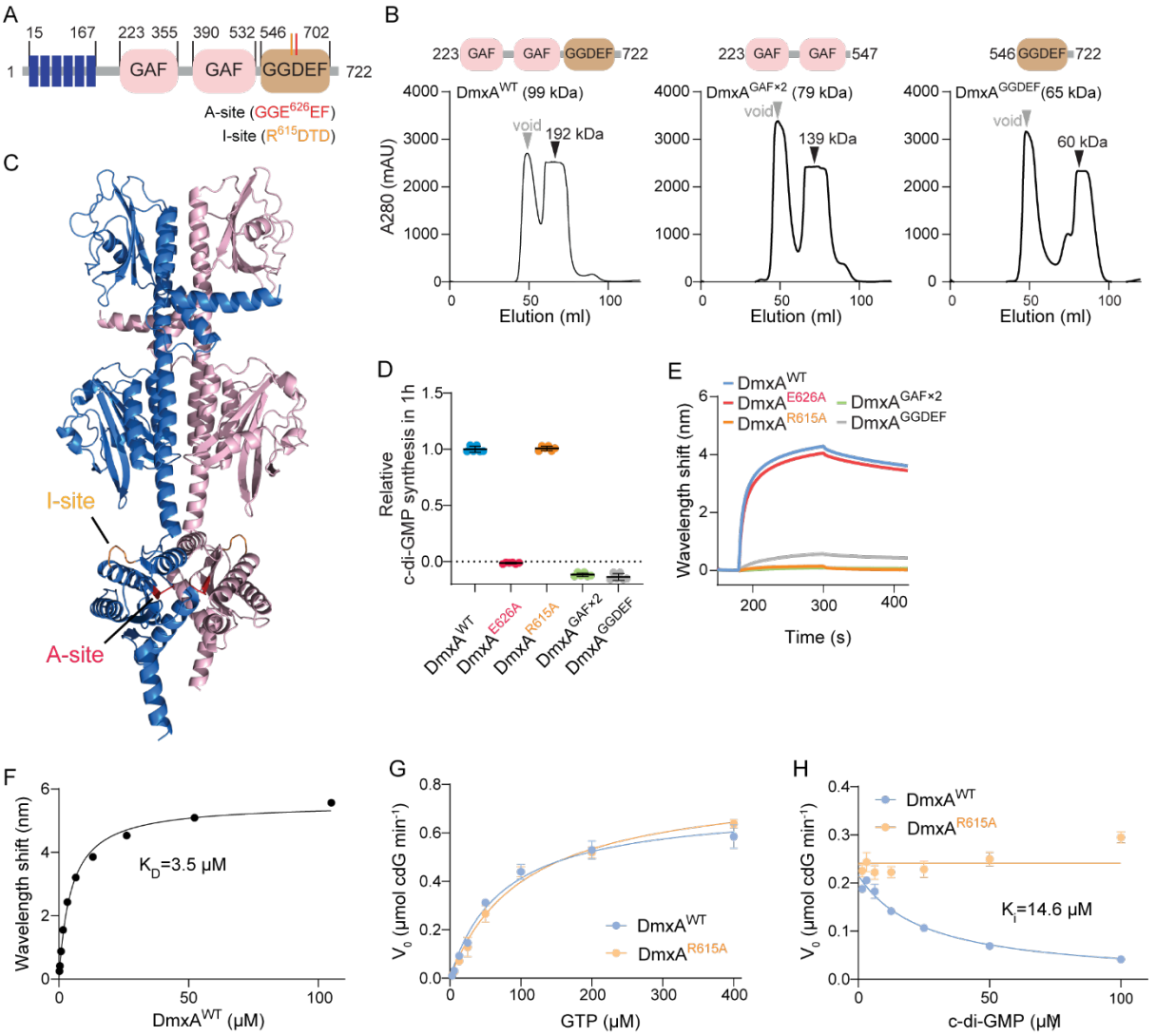

Figure 2. DmxA is an active DGC with weak substrate inhibition. (A) Domain architecture of DmxA is indicated. (B) SEC of $_{MalE}$DmxA variants. Domain architectures of truncated DmxA variants are shown above chromatograms. Gray arrows indicate the void volume and black arrows the elution volume with the corresponding calculated molecular weight. (C) AlphaFold structure of a DmxA dimer. The transmembrane helices were removed before generating a model. (D) *In vitro* DGC assay of the indicated MalE-tagged DmxA variants. The relative amount of c-di-GMP synthesized after 1 h was determined by measuring the release of inorganic pyrophosphate using a modified Pyrophosphate Assay Kit. Measurements of five technical replicates are plotted relative to the mean of the DmxA^{WT} variant. Error bars indicate mean ± SD. (E) Bio-Layer Interferometric analysis of the binding of the indicated MalE-tagged DmxA variants to c-di-GMP. Streptavidin-coated sensors were loaded with 500 nM biotinylated c-di-GMP and probed with 10 μM of the indicated protein variant. The interaction kinetics were followed by monitoring the wavelength shifts resulting from changes in the optical thickness of the sensor surface during association or dissociation of the analyte. (F) Analysis of c-di-GMP binding kinetics of different concentrations of DmxA^{WT}. Plot shows the equilibrium levels measured at the indicated DmxA^{WT} concentrations of data in Fig S2D. The data were fitted to a non-cooperative one-site specific-binding model. The calculated K_D for DmxA^{WT} is shown in the graph. (G) Initial reaction velocity of DmxA^{WT} and DmxA^{R615A} DGC activity in the presence of different GTP concentrations. DGC activity over time was measured as described in (D). Points and error bars represent the mean ± SD of three technical replicates measured at the indicated concentration of GTP. The data were fitted to a Michaelis-Menten kinetic. (H) Inhibition of the initial reaction velocity of DmxA^{WT} and DmxA^{R615A} of DGC activity in the presence of different c-di-GMP concentrations. DGC activity over time was measured as described in (D). The calculated K_i for DmxA^{WT} is shown in the graph. Points and error bars represent the mean ± SD of three technical replicates measured at the indicated concentration of c-di-GMP. The data were fitted to a tight-binding inhibition model.

DmxA localizes to mid-cell late during cytokinesis

To study how DmxA influences motility and polarity, we determined the localization of an active DmxA-mVenus fusion expressed from the native site (Fig. 3A). Remarkably, DmxA-mVenus localized to mid-cell in ~5% of the cells (Fig. 3A). All cells with a mid-cell cluster had initiated cytokinesis and the clusters co-localized with the cell division constrictions, but not all cells with a constriction had a DmxA-mVenus cluster at mid-cell. Additionally, DmxA-mVenus localized in speckles along the cell body (Fig. 3A). The DmxA-mVenus localization pattern suggested that it is recruited to the site of cell division late during cytokinesis. To test this hypothesis, we treated cells with cephalexin to inhibit PG cross-linking at the septum by FtsI (Eberhardt *et al.*, 2003). Treatment of *M. xanthus* with cephalexin inhibits cytokinesis after the initiation of constriction (Schumacher *et al.*, 2017, Treuner-Lange *et al.*, 2013). In cells treated with cephalexin for one doubling time (~5 h), the number of cells with a constriction and a DmxA-mVenus cluster at mid-cell significantly increased (Fig. 3A). Time-lapse fluorescence microscopy of untreated cells expressing DmxA-mVenus supported that the cluster only appeared at mid-cell after initiation of constriction, and then disintegrated upon completion of cytokinesis (Fig. 3B). DmxA-mVenus accumulated at the same level in treated and untreated cells (Fig. S3A) suggesting that DmxA-mVenus synthesis is not cell cycle regulated. Importantly, cluster formation was visible in each division event. The 5 h doubling time of *M. xanthus* and a cluster lifetime of ~30 min per cell cycle (Fig. 3B), is in overall agreement with the low percentage of cells with a cluster in a growing cell population.

The *dmxA* gene is located downstream of *ftsB* (*MXAN_3704*) (Fig. S3B), which encodes the FtsB divisome protein, which has been shown to localize to mid-cell during cell division (Goley *et al.*, 2011, Buddelmeijer *et al.*, 2002, Katis *et al.*, 1997). This genetic organization is conserved in the suborders Cystobacterineae and Nannocystineae, but not in the Sorangineae (Fig. S3C). Additionally, *MXAN_3702* and *MXAN_3703* are located in the same orientation and immediately upstream of *ftsB* (Fig. S3B). RNA-seq and Cappable-seq (Kuzmich *et al.*, 2021) (Fig. S3D) and operon mapping (Fig. S3E) support that *dmxA* and *ftsB* form a bicistronic operon. Because of this genetic organization, we determined whether DmxA is implicated in cell growth. Our analysis showed that Δ*dmxA* cells had a growth rate (Fig. S4A) and cell length distribution (Fig. S4B) similar to WT cells, supporting that DmxA is not implicated in cell growth or division.

DmxA is recruited to mid-cell by the divisome

Based on the localization of DmxA-mVenus to the site of cell division in constricting cells and the localization of *dmxA* downstream of *ftsB*, we hypothesized that DmxA-mVenus is recruited to the site of cell division by the divisome. To test this hypothesis, we depleted cells expressing *dmxA-mVenus* from its native site of the essential cell division protein FtsZ, which is essential

for the assembly of the divisome (Treuner-Lange *et al.*, 2013). In these experiments, *ftsZ* was expressed from a vanillate-inducible promoter and accumulated at WT levels in the presence of vanillate and was largely depleted 10 h after removal of vanillate (Fig. S4C). In the presence of vanillate, DmxA-mVenus localized at mid-cell in 3% of cells, and all these cells had a constriction (Fig. 3C). Upon FtsZ depletion, fewer and fewer cells had DmxA-mVenus at mid-cell and after 10 h of FtsZ depletion, when FtsZ was largely undetectable by immunoblotting, no cells had DmxA-mVenus at mid-cell (Fig. 3C) despite the protein accumulating at the same level in immunoblots (Fig. S4C). We conclude that DmxA-mVenus localization to mid-cell during cytokinesis depends on FtsZ and likely on the assembly of the divisome.

To further investigate the potential interaction of DmxA with the divisome, we performed biotin-based proximity labeling in the presence of cephalexin. To this end, we fused DmxA to the promiscuous biotin ligase miniTurboID and expressed the fusion from the *pilA* promoter (P_{pilA}). As a control, we expressed sfGFP-miniTurboID from the P_{van}. Interestingly, in the DmxA-miniTurboID samples, the cell division protein FtsK was significantly enriched (Fig. 3D, Table S2). Similarly, in the reciprocal experiment using an FtsK-miniTurboID construct, DmxA was enriched (Fig. 3E, Table S2), supporting that DmxA interacts with proteins of the divisome and is recruited to the site of cell division by the divisome. .

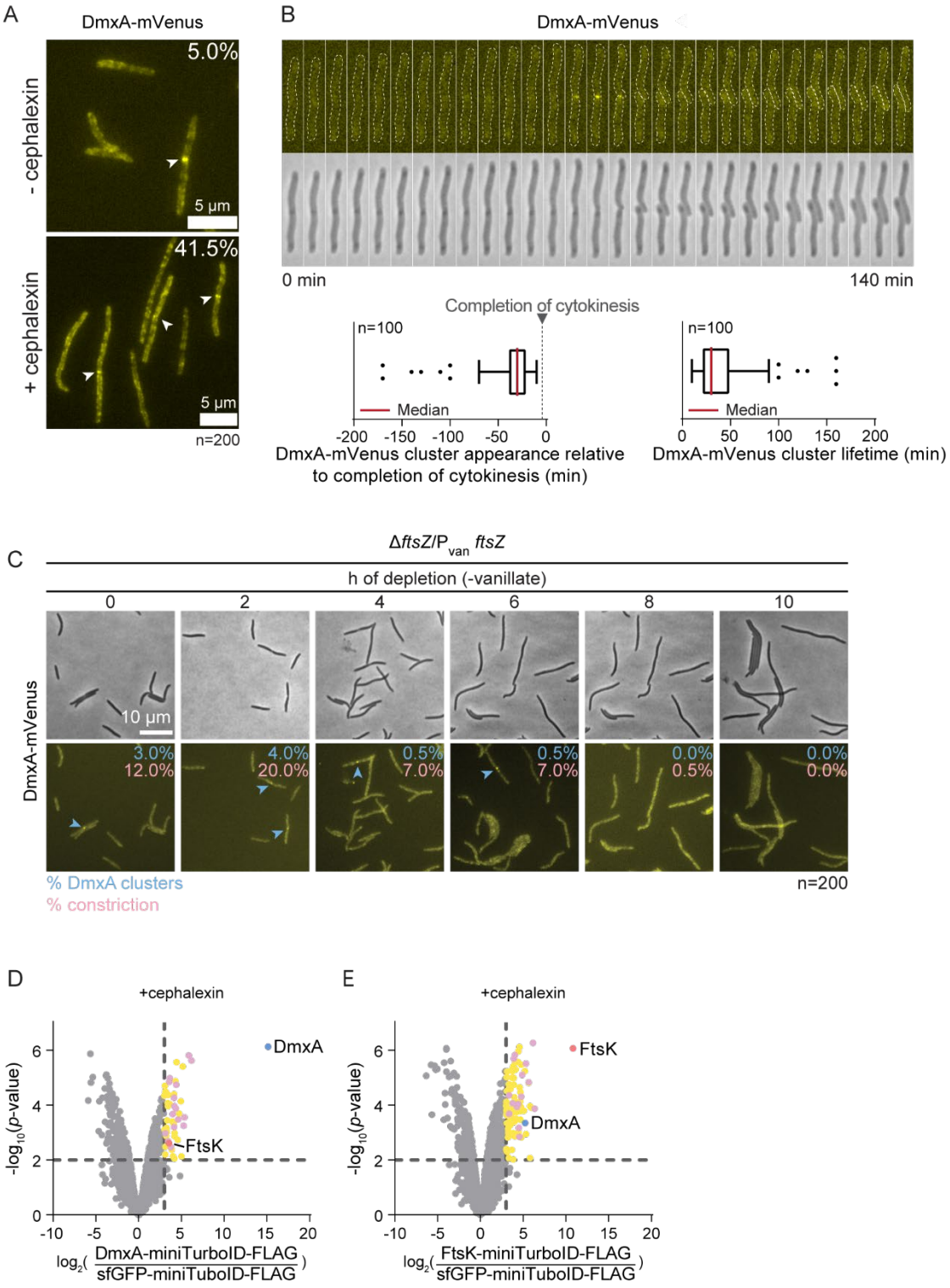

Figure 3. DmxA is recruited to mid-cell during cytokinesis by the divisome. (A) Localization of DmxA-mVenus by epifluorescence microscopy in the presence or absence of cephalexin. The percentage of cells with a cluster is indicated. White arrowheads indicate clusters. (B) DmxA-mVenus localization during the cell cycle. Upper panels, epifluorescence and phase-contrast images from time-lapse microscopy of cells expressing DmxA-mVenus. DmxA-mVenus cluster is visible at mid-cell during cytokinesis. Bottom panels, analysis of the appearance and lifetime of the DmxA-mVenus cluster relative to completion of cytokinesis. The first time point after completion of cytokinesis is defined as t=0 and indicated by the grey vertical bar. In the box plot, boxes enclose the 25th and 75th percentile with the red line representing the median; whiskers represent the 1.5 times the interquartile range. *n* = 100. To follow cells on hard agar by time-lapse microscopy for extended periods of time and to avoid that they move out of the field of view, the strain contains an in-frame deletion of *gltB* (Δ*gltB),* which encodes a

component of the *M. xanthus* gliding motility machine (Fig. S1A) (Luciano *et al.*, 2011, Jakobczak *et al.*, 2015). (C) Localization of DmxA-mVenus by epifluorescence microscopy in presence and absence of FtsZ. Cells were exponentially grown in the presence of 10 µM vanillate for ~8 generations in suspension culture before the start of the experiment. The percentage of cells with a cluster (blue) or a constriction (pink) are indicated. Blue arrowheads indicate DmxA-mVenus clusters. (D-E) Volcano plot visualizing enriched proteins in DmxA-miniTurboID-FLAG (D) and FtsK-miniTurboID-FLAG (E). Proximity labeling using DmxA-miniTurboID-FLAG or FtsK-miniTurboID-FLAG as bait compared to GFP-miniTurboID-FLAG (negative control). DmxA-miniTurboID-FLAG and FtsK-miniTurboID-FLAG were expressed from the P_{pilA}, and GFP-miniTurboID-FLAG was expressed from the P_{van} using 100 µM vanillate that was added to the suspension culture 18 h prior to the addition of biotin. Samples from three biological replicates were collected after incubating the cells for 4 h in the presence of cephalexin as well as 100 µM biotin and were analyzed by label-free mass spectrometry-based quantitative proteomics. Log_2-fold enrichment in experimental samples compared to GFP-miniTurboID-FLAG samples was calculated based on normalized intensities. X-axis, log_2-fold enrichment of proteins with the indicated bait protein versus the control sample. Y-axis, $-log_{10}$ of P-value. Significantly enriched proteins in the experimental samples (log_2 ratio ≥ 3; *p*-value ≤ 0.01 ($-log_{10}$ ≥ 2.0) are indicated by the stippled lines. Proteins that were enriched in both experiments in (D) and (E) are shown in pink, DmxA and FtsK are shown in blue and red, respectively, and other enriched proteins are yellow.

DmxA function depends on DGC activity and mid-cell localization, but not on c-di-GMP binding

To determine which DmxA domains and if DGC activity contribute to the localization of the protein and regulation of motility, we replaced the native *dmxA* with *mVenus*-fused versions of *dmxA*^{E626A}, *dmxA*^{R615A}, *dmxA*$^{\Delta GAF\times2}$ (full length DmxA lacking the two GAF domains), *dmxA*$^{\Delta TMH}$ (full-length DmxA lacking the six transmembrane α-helices) or *dmxA*^{TMH} (only the transmembrane α-helices) (Fig. 4A-B). Immunoblot analysis showed that all variants accumulated at a similar level except DmxA$^{\Delta GAF\times2}$-mVenus, which accumulated at a slightly reduced level (Fig.S4D), and DmxA^{TMH}-mVenus, which was partially cleaved (Fig. S4D). Fluorescense microscopy analysis showed that mid-cell localization of DmxA-mVenus was independent of DGC activity, the I-site and the two GAF domains (Fig. 4A). By contrast, the transmembrane domain with the six α-helices was not only essential but also sufficient for DmxA-mVenus localization to mid-cell (Fig. 4A). Interestingly, when strains expressing the different DmxA-mVenus variants were tested for motility, all of them, except for the *dmxA-mVenus* strain and the *dmxA*^{R615A}*-mVenus* mutant, had a motility defect similar to that of the Δ*dmxA* mutant (Fig. 4C).

Based on these findings, we conclude that mere localization to mid-cell is insufficient for DmxA function and that this also relies on DGC activity. Conversely, because the DmxA$^{\Delta TMH}$-mVenus construct is similar to the MalE-DmxA^{WT} construct analyzed *in vitro* and this construct has DGC activity (Fig. 2D), we concluded that DGC activity is likely not sufficient for function. Rather, the protein must also localize to mid-cell to promote DmxA activity.

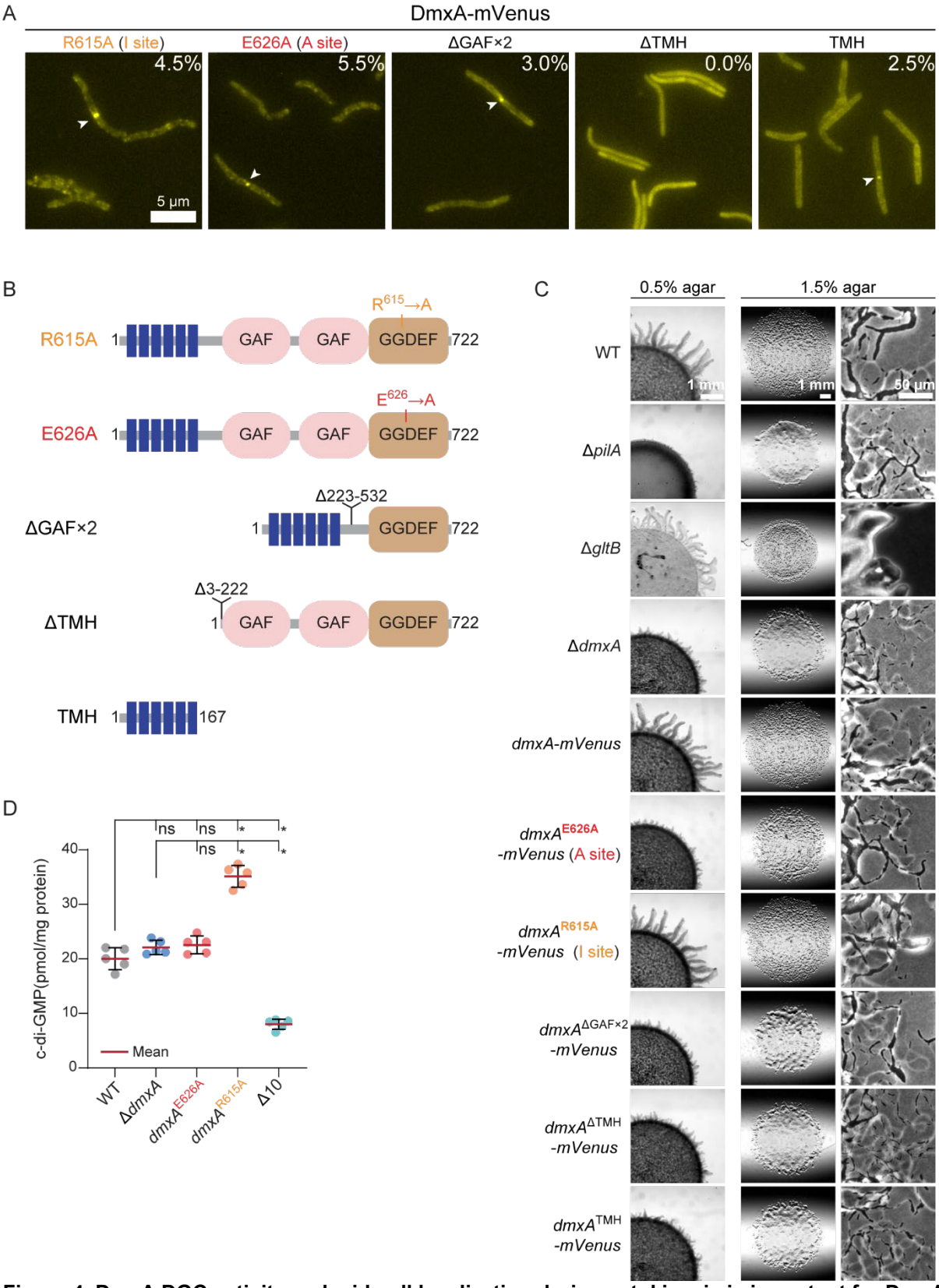

Figure 4. DmxA DGC activity and mid-cell localization during cytokinesis is important for DmxA function. (A) Localization of the indicated DmxA-mVenus variants by epifluorescence microscopy. The percentage of cells with a cluster is indicated. White arrowheads indicate clusters. (B) Domain architecture of the DmxA variants fused to mVenus is indicated. (C) T4P-dependent and gliding motility were analyzed on 0.5% and 1.5% agar respectively. Scale bars, 1 mm (left), 1 mm (middle), 50 μm (right). (D) c-di-GMP level of indicated strains during growth. The level of c-di-GMP is shown as the mean ± SD from five biological replicates. *dmxA*^{E626A} and *dmxA*^{R615A} are fused to *mVenus.* Individual data points are shown. * p<0.05; ns, not significant, one-way ANOVA multiple comparison test.

DmxA does not contribute to the global level of c-di-GMP and is only active during cytokinesis

To understand how DGC activity and c-di-GMP contributes to DmxA function, we measured the global level of c-di-GMP in WT and different *dmxA* mutants. Unexpectedly, no differences in the c-di-GMP level were observed between WT, Δ*dmxA* cells and cells expressing the A-site variant DmxA^{E626A}. By contrast, cells expressing the I-site variant DmxA^{R615A} had a two-fold higher level of c-di-GMP (Fig. 4D). Thus, DmxA does not significantly contribute to the global level of c-di-GMP.

Because DmxA (i) localizes to mid-cell late during cytokinesis, (ii) DGC activity is essential for function, and (iii) DmxA does not significantly contribute to the global level of c-di-GMP, we hypothesized that DmxA activity could be cell cycle-regulated and that DmxA would only be active when localizing late at the constriction site. To test this hypothesis, we took advantage of the genetically-encoded c-di-GMP biosensor cdGreen2 (Kaczmarczyk *et al.*, 2022) to follow c-di-GMP dynamics and more specifically DmxA DGC activity during the cell cycle. Binding of c-di-GMP to cdGreen2 results in conformational changes that lead to an increase in its green fluorescence intensity. Additionally, for normalization of the cdGreen2 fluorescence signal, we co-expressed mScarlet (Kaczmarczyk *et al.*, 2022).

WT cells expressing cdGreen2 revealed a heterogeneous fluorescent signal; however, long cells with a constriction had the highest fluorescence (Fig. 5A). Moreover, in a mutant in which all ten DGCs except for DmxA were inactivated (hereon the Δ10 strain) and which accumulated significantly less c-di-GMP (Fig. 4D), the population was more homogeneous and only long cells with a constriction had a high fluorescent signal (Fig. 5A) strongly supporting that the peak in c-di-GMP in constricting cells is caused by DmxA DGC activity at mid-cell. In agreement with this notion, treatment of WT and Δ10 cells with cephalexin for 5 h, corresponding to one generation, resulted in an increase in the percentage of long cells with constrictions and these cells had a high fluorescent signal. Of note, treatment of WT cells with cephalexin also caused a decrease in the number of cells with a moderate signal (Fig. 5A). Finally, in time-lapse fluorescence microscopy of Δ10 cells expressing cdGreen2, we observed that c-di-GMP increased shortly before completion of cytokinesis (~20 min) and decreased rapidly after completion of cytokinesis (Fig. 5B). These results suggest DmxA is only active during its localization to mid-cell during cytokinesis.

To understand if the increase in c-di-GMP occurred before or after the separation of the cytoplasm in the two daughter cells, we performed fluorescence recovery after photobleaching (FRAP) experiments in which we bleached one half of a pre-divisional cell with a high fluorescent signal, and then analyzed the fluorescence recovery (Fig. 5C). In 50% of cells (Fig.

5C, left), the bleaching event only affected the fluorescence signal in the bleached half of the pre-divisional cell. By contrast, in the remaining 50% of cells (Fig. 5C, right), the bleaching event caused a decrease in the fluorescence signal in both halves of the pre-divisional cell.

Based on these analyses, we suggest that DmxA is only active during its localization to mid-cell during cytokinesis, and that DmxA is likely activated before the cytoplasm of the two daughters is separated and remains active until cytokinesis is complete.

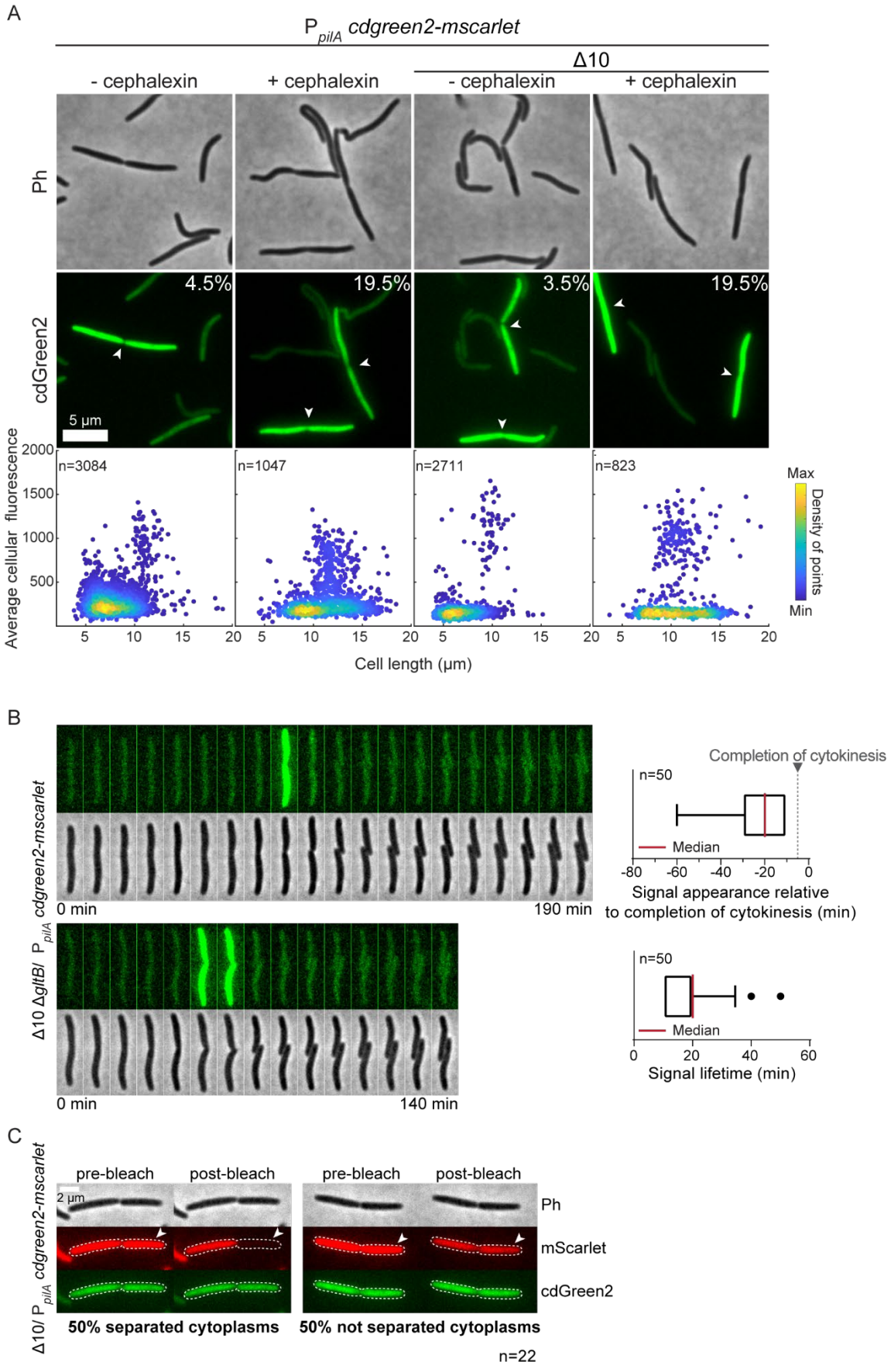

Figure 5. DmxA DGC activity is stimulated during cytokinesis. (A) Analysis of the cdGreen2 fluorescence in WT and Δ10 in the presence or absence of cephalexin. Upper panel, phase contrast and epifluorescence images of cells expressing cdGreen2 in the presence or absence of cephalexin.

The percentage of cells with a high cdGreen2 fluorescence is indicated. White arrowheads indicate cells with high fluorescence. Bottom panel, scatter plots for which the average cellular fluorescence of each cell was plotted relative to its cell length. (B) cdGreen2 fluorescence in Δ10 cells during the cell cycle. Left panels, epifluorescence and phase-contrast images from time-lapse microscopy of cells expressing cdGreen2. cdGreen2 fluorescence is visible shortly before completion of cytokinesis. Right panels, analysis of the appearance and lifetime of the high cdGreen2 fluorescence relative to completion of cytokinesis. The first time point after completion of cytokinesis is defined as t=0 and indicated by the grey vertical bar. In the box plot, boxes enclose the 25th and 75th percentile with the red line representing the median; whiskers represent the 1.5 times the interquartile range. *n* = 50. To follow cells on hard agar by time-lapse microscopy for extended periods of time and to avoid that they move out of the field of view, the strain contains a Δ*gltB* mutation. (C) Fluorescence recovery after photobleaching of diving cells expressing cdGreen2 and mScarlet, where the mScarlet signal of one half of the cell was bleached. Post-bleached image was recorded after 2 s recovery. All dividing cells analyzed here showed a high cdGreen2 fluorescent signal.

Lack of DmxA affects the recruitment of the T4aPM to the nascent and new cell poles

We have recently shown that the bipolarly-localized T4PM is incorporated at the nascent and new poles during and immediately after cytokinesis. This process starts with the assembly of the PilQ secretin in the outer membrane and depends on the Tgl pilotin (Herfurth *et al.*, 2023, Friedrich *et al.*, 2014), and ends with incorporaton of the cytoplasmic ring formed by PilM , as well as the localization of the extension and retraction ATPases, PilB and PilT (Friedrich *et al.*, 2014). To understand if those processes are affected by lack of DmxA, we followed the localization of PilQ-sfGFP, Tgl-sfGFP in Δ*dmxA* cells by fluorescence time-lapse microscopy.

In WT cells, PilQ-sfGFP localization and assembly at the nascent and new poles occurred symmetrically in the two daughter cells (Fig. 6A). By contrast, in the absence of DmxA, PilQ-sfGFP incorporation to the nascent and new poles was not only significantly delayed but also asymmetric in the two daughter cells, resulting in many cells with a unipolar PilQ-sfGFP cluster only at the old pole (Fig. 6A). Moreover, we observed that this defect in polar PilQ-sfGFP incorporation was typically not corrected until the next cell division event occurred (Fig. 6A). Supporting these findings, time-lapse fluorescence microscopy of cells expressing an active Tgl-sfGP fusion, which serves as a proxy to study secretin assembly, showed that, in WT cells, Tgl-sfGFP localized at the constriction site and this cluster was inherited equally by the two daughter cells, whereas in the Δ*dmxA* mutant, the Tgl-cluster was mostly only visible at the new poles late after completion of cell division and at different time points in the two daughter cells (Fig. 6B). In some cells, we even observed the appearance of a Tgl-cluster at the old cell pole (Fig. 6B).

To further analyze and quantify the differences in the localization of Pil proteins in the absence of DmxA, we analyzed the localization of T4PM components in snapshots. In WT cells, and in agreement with previous observations, endogenously expressed PilQ-sfGFP, mCherry-PilM and mCherry-PilT generally localize in a bipolar symmetric pattern, while PilB-mCherry mostly

localized unipolarly (Fig. 6C) (Potapova *et al.*, 2020, Friedrich *et al.*, 2014, Chang *et al.*, 2016). However, in the absence of DmxA, the localization of all fluorescent proteins was shifted toward more asymmetric and unipolar (Fig. 6C). Together, because PilQ is the first component of the T4PM to be incorporated and because all remaining components studied follow the same localization changes, we conclude that lack of DmxA leads to a defect in the localization of the T4PM proteins that originates from a defect in the assembly of the PilQ secretin.

To understand how the localization pattern of the T4PM and T4P extension in Δ*dmxA* cells correlated with the abnormal reversal frequency of the mutant (Fig 1B-C), we performed time-lapse epifluorescence microscopy of moving cells expressing PilB-mCherry. In WT cells, PilB-mCherry dynamically localized at the leading cell pole. PilB-mCherry also generally localized at the leading cell pole of Δ*dmxA* mutant cells. However, 29% of cells failed to dynamically switch polarity of PilB-mCherry, resulting in cells in which either the cluster disappeared and reappeared at the leading cell pole, or switched multiple times between leading and lagging pole to finally relocate at the leading pole (Fig. S5). This defect in the relocation of PilB to the other pole could partially originate from the lack of the T4PM at one of the poles (but also see below).

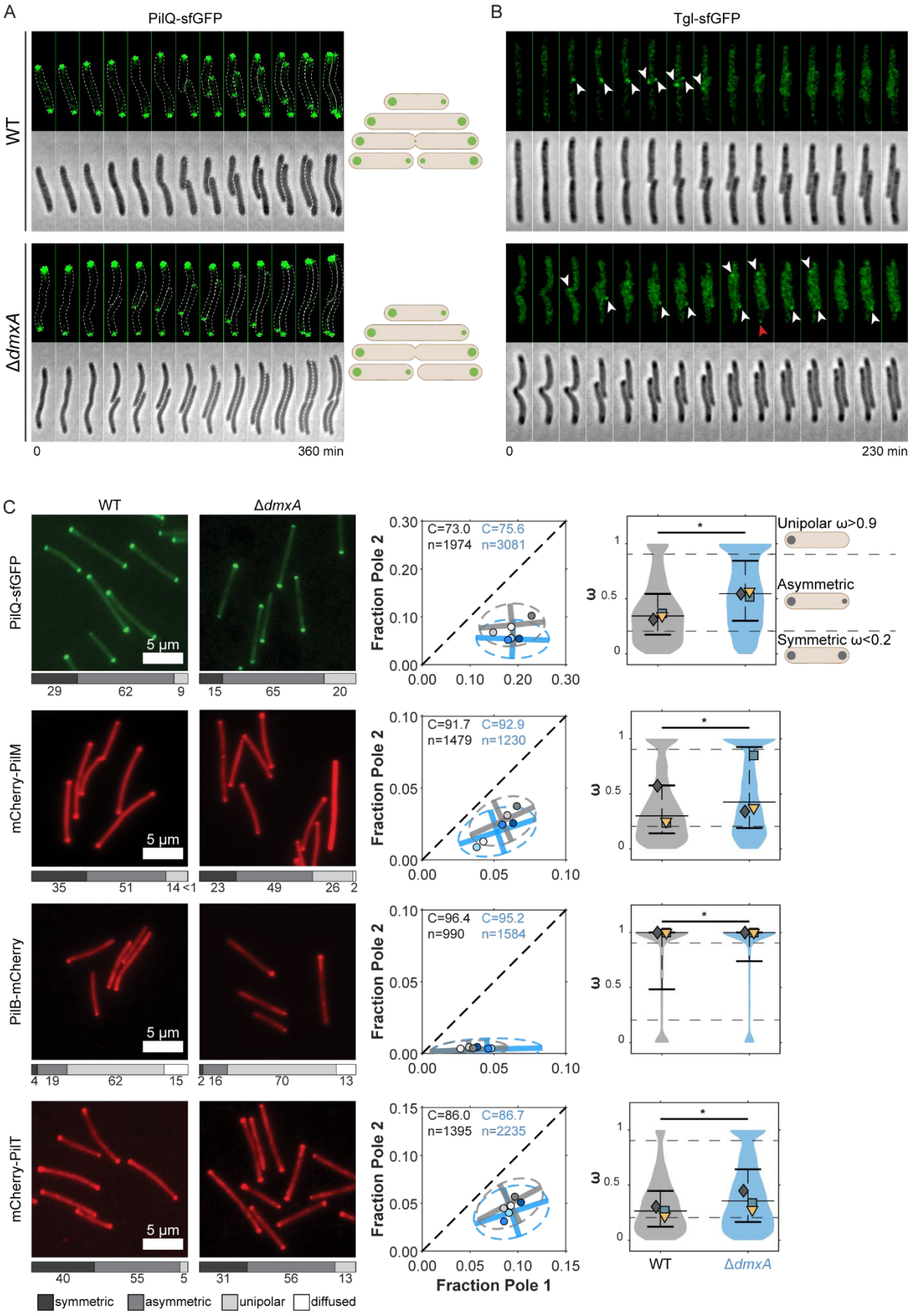

Figure 6. DmxA regulates the equal distribution and incorporation of the polar T4PM proteins in both daughter cells during cytokinesis. (A-B) PilQ-sfGFP and Tgl-sfGFP localization in the absence of DmxA during the cell cycle. Epifluorescence and phase-contrast images from time-lapse microscopy

of cells expressing (A) PilQ-sfGFP or (B) Tgl-sfGFPin the indicated strains. To follow cells on hard agar by time-lapse microscopy for extended periods of time and to avoid that they move out of the field of view, the strains contains a Δ*gltB* mutation. Schematics indicate dominant localization patterns of PilQ-sfGFP in WT and Δ*dmxA* cells during the cell cycle.In (B), white arrows indicate Tgl-sfGFP clusters. (C) Snapshots of WT and Δ*dmxA* cells expressing PilQ-sfGFP, mCherry-PilM, PilB-mCherry and mCherry-PilT. Cells were incubated in chitosan-coated µ-Dishes to enhance single-cell motility by both motility systems (Ducret *et al.*, 2013, Hu *et al.*, 2011). Left, representative epifluorescence images. The percentage of symmetric, asymmetric, unipolar and diffused cells is indicated below the images. Middle, polar fraction of the fluorescence intensities in single cells. Dispersion of the single-cell measurements in WT (grey) and Δ*dmxA* (blue) is represented by error bars and ellipses. Black dashed lines represent the symmetry line. Average cellular cytoplasmic fluorescence is indicated by a "C" and analyzed number of cells (n) from three biological replicates is indicated. Right, violin plots indicate the distribution of ω. Error bars indicate median and 25th and 75th percentile of the measurements. Large single points represent the median of each replicate.

Lack of DmxA affects the distribution of RomR between the two daughter cells after cytokinesis

Components of the polarity module have also been shown to relocate in response to cell division (Harvey *et al.*, 2014). To assess how the proteins of the polarity module localized during division in the presence or absence of DmxA, we analyzed the localization of RomR-mCherry, which is at the base of the localization of all the other proteins of the polarity module (Carreira *et al.*, 2020). In WT, we observed that most of RomR-mCherry is recruited to mid-cell before completion of cytokinesis and that this cluster is equally distributed to the two daughter cells (Fig. 7). In the absence of DmxA, however, RomR-mCherry was inherited in different amounts by the two daughter cells either because it did not significantly relocate to mid-cell during division or because the cluster was asymmetrically distributed between the two daughters (Fig. 7). This generally resulted in one daughter cell with a low amount of RomR-mCherry and a more symmetric distribution than WT cells and a second daughter with a high amount of RomR-mCherry and a more asymmetric distribution (see below). Also, despite RomR-mCherry accumulation in the cells with lower amounts increased over time, this defect was typically not corrected before the next cell division. This results in a heterogeneous population with different amounts of polar RomR. In conclusion, at the single-cell level, DmxA is important for the symmetric distribution of RomR to the daughter cells. Of note, a population-based measurement showed that, in the Δ*dmxA* mutant, RomR and the other polarity proteins, accumulated at WT-levels (Fig. S6).

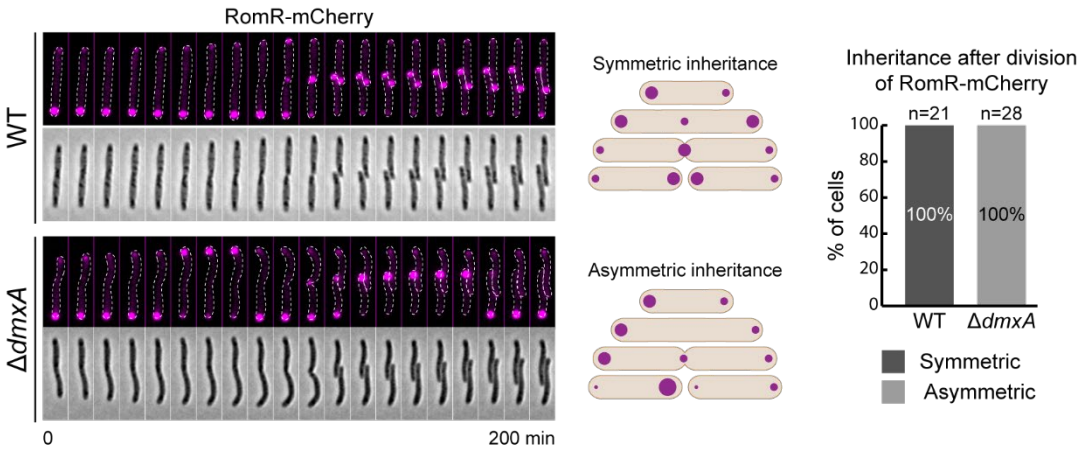

Figure 7. DmxA regulates the equal distribution of RomR in both daughter cells. Left, RomR-mCherry localization in the absence of DmxA during the cell cycle. Epifluorescence and phase-contrast images from time-lapse microscopy of cells expressing RomR-mCherry in the indicated strains. To follow cells on hard agar by time-lapse microscopy for extended periods of time and to avoid that they move out of the field of view, the strains contains a Δ*gltB* mutation. Middle, Schematics indicate dominant localization patterns of RomR-mCherry in WT and Δ*dmxA* cells during the cell cycle. Right, frequency of symmetric and asymmetric inheritance of RomR-mCherry in WT and Δ*dmxA.*

Discussion

C-di-GMP is a bacterial second messenger that regulates a variety of processes in response to cellular or environmental signals. In *M. xanthus*, motility is regulated by c-di-GMP and previous studies have shown that DmxA is the only DGC that is implicated in the regulation of T4P-dependent motility. DmxA is an integral membrane protein with two regulatory GAF domains and a GGDEF domain. Here we showed that DmxA, not only regulates T4P-dependent motility, but also gliding motility and that the motility defect arises from an abnormal regulation of the reversal frequency independently of the Frz chemosensory system. Moreover, we show that this defect results from an asymmetric distribution and a delay in the incorporation of polar proteins at the new pole of the daughter cells.

In vitro characterization of DmxA showed that it is a canonical DGC that oligomerizes to generate c-di-GMP. Because tandem GAF domains have been implicated with oligomerization of proteins (Heikaus *et al.*, 2009) and because a variant only containing the GAF domains oligomerized *in vitro*, we propose that the GAF domains are responsible for the oligomerization and activation of DGC activity. In addition to oligomerization, DGCs usually are allosterically regulated through their I-site, which only has moderate c-di-GMP binding affinity in DmxA. This is reflected by its high K_i (~15 µM) and suggests that (i) rather than allosteric control through the I-site, DmxA activity is mainly regulated through its oligomerization state and that (ii) DmxA possesses the capacity to synthesize high amounts of c-di-GMP before it is inactivated through product inhibition.

Other active DGCs, such as DgcA and PleD from *C. crescentus*, have been determined to be regulated by their I-site with a lower K_i of 1 µM and 6 µM, respectively (Christen *et al.*, 2006). Interestingly, PleD acitivity, similarly to DmxA, is additionally regulated through the phosphorylation of an N-terminal receiver domain which subsequently induces its oligomerization (Paul *et al.*, 2008), while DgcA only consists of the catalytic GGDEF domain (Christen *et al.*, 2006).

Additionally, our studies showed that DmxA localizes to mid-cell during cytokinesis in every division event, and its localization is lost when cytokinesis is completed. Using genetic and biochemical analysis, we show that localization to the constriction site depends on the divisome and on the transmembrane domains of DmxA. Specifically, using proximity labeling, we identified FtsK, which is important for recruiting late division proteins FtsQ, -L and -B (Cameron & Margolin, 2023), as a potential interaction candidate of DmxA.

DmxA does not significantly contribute to the global level of c-di-GMP. However, using a c-di-GMP biosensor, we observed that during cytokinesis, the level of c-di-GMP in the Δ10 strain only containing DmxA, significantly increased and then decreased upon completion of

cytokinesis. Because inhibition of DGC activity of DmxA through c-di-GMP *in vitro* was relatively low, this is consistent with the idea that DmxA can produce high levels of c-di-GMP in a short time. Additionally, the DmxA cluster appears ~30 min before completion of cytokinesis, whereas c-di-GMP increases only ~20 min before. Because dimerization is required to activate DGC activity and the DmxA$^{\Delta TMH}$ variant that did not localize to mid-cell did not support DmxA function, we suggest that DmxA has to localize at high concentrations at the nascent poles at the constriction site during cytokinesis to trigger dimerization by the GAF domains and activation of DGC activity. Upon completion of cytokinesis, the DmxA cluster disintegrates, likely by following the disintegration of the divisome, and, therefore, the c-di-GMP level stops increasing and eventually rapidly decreases. We suggest that upon completion of cytokinesis, one or more PDEs may cause a drop in the c-di-GMP level in the daughter cells immediately after cell division. Because no PDE was implicated with the regulation of motility (Skotnicka *et al.*, 2015), it would be interesting to study if one of the PDEs encoded by the *M. xanthus* genome is specifically involved in this step or if one or more of these PDEs acts redundantly.

The investigation of the role of c-di-GMP and DmxA in motility showed that, despite DmxA only being active during a short period of the cell cycle, DmxA DGC activity is essential for the regulation of motility. Specifically, we show that late during cytokinesis, DmxA is important for the symmetric distribution and incorporation of proteins at the new poles of the two daughter cells. Here we show that the Δ*dmxA* mutant has a delay in the incorporation of the PilQ secretin at the new pole causing a more asymmetric distribution of proteins of the T4PM. Additionally, we observed that in WT cells, RomR is evenly distributed between the two daughter cells upon division. In contrast, in the Δ*dmxA* mutant, RomR is asymmetrically distributed in the two daughter cells resulting in a heterogeneous population. Because RomR is important for the correct polar localization of the other components of the polarity module (Carreira *et al.*, 2020, Zhang *et al.*, 2012b, Szadkowski *et al.*, 2019, Keilberg *et al.*, 2012, Leonardy *et al.*, 2007), we suggest that in the absence of DmxA all the proteins of the polarity module are mislocalized. The exact localization of the polarity module in the absence of DmxA has to be studied in the future.

Several lines of evidence support that DmxA regulates synthesis of the cell envelope late during cytokinesis. Specifically, our results suggest that DmxA could regulate the synthesis and/or modifications of septal PG late during cytokinesis and this could affect the equal distribution and incorporation of polar landmarks in the two daughter cells. First, in the Δ*dmxA* mutant, PilQ incorporation to the nascent and new poles is delayed. The PilQ secretin is the first component of the T4PM to be assembled (Friedrich *et al.*, 2014), and its incorporation at the nascent and new poles depends on binding to peptidoglycan (PG) via its PG-binding AMIN

domains (Herfurth *et al.*, 2022, Carter *et al.*, 2017). Second, RomR is a dynamic cytoplasmic protein with an intrinsic affinity to the poles (Carreira *et al.*, 2020, Zhang *et al.*, 2012b), and its localization to the new pole is affected in the absence of DmxA. Moreover, the RomR polarity defect resulting from the Δ*dmxA* mutation cannot be dynamically and rapidly recovered upon completion of cytokinesis, suggesting that the properties of the new poles are affected. Third, in ~30% of the Δ*dmxA* population, PilB cannot successfully switch polarity.

In conclusion, a defect in the generation of the new poles of the daughter cells in the Δ*dmxA* mutant could result in the delayed incorporation of the T4PM and mislocalization of the polarity module that together could lead to a defect in the establishment of leading/lagging cell polarity and a defect in the regulation of the reversal frequency.

Interestingly, many bacteria, such as *C. crescentus*, *P. aeruginosa* and *Shewanella,* are inherently asymmetrically polarized (e.g. possess a unipolar flagellum or T4P). These bacteria utilize polar landmarks such as HubP in *Shewanella* (FimV in *P. aeruginosa*) or chemotaxis proteins in *P. aeruginosa* (i.e. CheA) to recruit DGCs and PDEs to the cell poles (Rick *et al.*, 2022, Rossmann *et al.*, 2019) . These unipolar localized enzymes generate a gradient of c-di-GMP within the cell. During cytokinesis, this c-di-GMP gradient, together with other polar landmarks such as TipN in *C. crescentus* (Davis *et al.*, 2013), is important for localization and/or activity of c-di-GMP effectors. This, in turn, results in the generation of phenotypically distinct daughter cells. The daughter cell with a low level of c-di-GMP will be equipped with motility machineries that allow spreading of the colony (e.g. the flagellum), and the other daughter cell, with a high c-di-GMP level, will be non-motile (Laventie *et al.*, 2019a, Rick *et al.*, 2022, Abel *et al.*, 2013). Remarkably, *M. xanthus* cells are generally set-up symmetrically, and instead of localizing DGCs and PDEs to the cell poles during cytokinesis to generate different offspring, an increase in c-di-GMP at the division site during cytokinesis, leads to identical offspring.

Altogether, we suggest a model, in which DmxA is recruited by the divisome late during cytokinesis through protein-protein interactions via its transmembrane domains. High levels of DmxA at mid-cell cause dimerization mediated by the GAF domains. In response to its activation, DmxA drastically increases the cellular c-di-GMP level to regulate the distribution and incorporation of polar integrated or associated proteins (e.g. PilQ and RomR) at both daughter cells through the correct assembly of new PG at the cells pole and the positioning of a polar landmark(s).

Acknowledgement

The authors thank Andrea Harms for help with operon mapping experiments, Memduha Muratoglu for generating strains SA9307, SA9300, SA9342, Dorota Skotnicka for generating SA5666, Anke Treuner-Lange for the strain SA6755. This work was supported by Deutsche Forschungsgemeinschaft (DFG, German Research Council) within the framework of the SFB987 “Microbial Diversity in Environmental Signal Response” as well as by the Max Planck Society.

Conflict of Interest

The authors declare no conflict of interest.

Availability of data and materials

The authors declare that all data supporting this study are available within ^ the article and its Supplementary Information files.

Experimental procedures

Bacterial strains and growth media. *M. xanthus* cells were grown at 32°C in 1% CTT (1% (w/v) Bacto Casitone in TPM buffer (10 mM Tris-HCl pH 8.0, 1 mM K_2HPO_4/KH_2PO_4 pH 7.6, and 8 mM $MgSO_4$)) liquid medium or on 1.5% agar supplemented with 1% CTT (Hodgkin & Kaiser, 1977). Oxytetracyline and kanamycin at a concentration of 10 μg ml^{-1} and 50 μg ml^{-1} respectively, were used when needed. Cephalexin at a concentration of 35 μg ml^{-1} was used during one generation time (~4-5 h). All *M. xanthus* strains are derivatives of the WT strain DK1622 (Kaiser, 1979). The *M. xanthus* strains and plasmids used in this work are listed in Tables 1 and 2, respectively. In-frame deletions or gene replacements were generated as described previously (Shi *et al.*, 2008), and plasmids for complementation experiments were integrated in a single copy by site specific recombination into the Mx8 *attB* site, the *MXAN_18-19* site or by homologous recombination at the endogenous locus. All in-frame deletions and plasmid integrations were verified by PCR. Plasmids were propagated in *E. coli* Mach1, which was grown at 37°C in lysogeny broth (LB) medium (10 mg tryptone ml^{-1}, 5 mg yeast extract ml^{-1} and 10 mg NaCl ml^{-1}) supplemented when required with kanamycin (50 μg ml^{-1}) or tetracycline (25 μg ml^{-1}).

Operon mapping. Mapping of the *ftsB-dmxA* operon was performed by reverse-transcriptase analysis of the intergenic region indicated in Fig. S3E as described previously (Herfurth *et al.*, 2022). Briefly, 1 × 10^9 WT cells from an exponentially growing suspension culture were harvested (3 min, 8,000 × *g,* room temperature (RT)) and resuspended in 200 μl lysis-buffer (100 mM Tris-HCl pH 7.6, 1 mg ml^{-1} lysozyme). After incubation at 25°C for 5 min, cells were lysed and RNA was purified according to manufacturer's instructions with the exception that the on-column DNase treatment was omitted. RNA was eluted in RNase-free water, subsequently treated with Turbo DNase and purified using the Monarch RNA Cleanup Kit (50 μg) (NEB) and eluted in RNase-free water. 1 μg of RNA was used for cDNA synthesis using the LunaScript RT SuperMix Kit (NEB) with and without reverse-transcriptase. cDNA, the mock reaction without reverse-transcriptase, or genomic DNA were used as template for PCR using the primer combinations 3702_map_fwd2 /3703_map_rev2; 3703_map_fwd2 /3704_map_rev; 3704_map_fwd2 /3705_map_rev and 3705_map_fwd2 /3706_map_rev (Table 3).

Cell length determination. 5-μl aliquots of exponentially growing cultures were spotted on 1% agarose supplemented with 0.2% CTT. Cells were immediately covered with a cover slide, and imaged using a DMi8 Inverted microscope and DFC9000 GT camera (Leica). To assess cell length, cells were segmented using Omnipose (Cutler *et al.*, 2022), segmentation was manually curated using Oufti (Paintdakhi *et al.*, 2016) and analyzed using Matlab R2020a (The MathWorks).

Detection of EPS accumulation. Colony-based EPS assays were performed as described previously (Pérez-Burgos *et al.*, 2020). Briefly, exponentially growing cells were harvested (3 min, 6,000 × *g,* RT) and resuspended in 1% CTT to a calculated density of 7 × 10^9 cells ml^{-1}. 20-µl aliquots were placed on 0.5% agar plates supplemented with 0.5% CTT and 10 or 20 µg ml^{-1} of Trypan blue or Congo red, respectively. Plates were incubated at 32°C and imaged at 24 h.

Motility assays. Population-based motility assays were performed as previously (Shi & Zusman, 1993). Briefly, exponentially growing cells were harvested (3 min, 8,000 *g*, RT) and resuspended in 1% CTT to a calculated density of 7 × 10^9 cells ml^{-1}. 5-µl aliquots of cell suspensions were spotted on 0.5% and 1.5% agar (Invitrogen) supplemented with 0.5% CTT and incubated at 32°C. Cells were imaged after 24 h using a M205FA Stereomicroscope (Leica) and a DMi8 inverted microscope (Leica) equipped with a Hamamatsu ORCA-Flash V2 digital CMOS camera (Hamamatsu Photonics) and DFC9000 GT camera (Leica), respectively. To analyze the movement of single cells, strains were imaged using a DMi8 Inverted microscope and DFC9000 GT camera (Leica). For the visualization of single cells moving by T4P-dependent motility, 5 µl exponentially growing cell suspensions were placed in a 24-well polystyrene plate (Falcon). After 10 min incubation in the dark at RT, 200 µl of 1% methylcellulose in MMC buffer (10 mM MOPS, 4 mM $MgSO_4$, 2 mM $CaCl_2$, pH 7.6) were added and cells were incubated for additional 30 min in the dark at RT. Cells were imaged for 15 min with 30 s intervals. To visualize individual cells moving by gliding motility, exponentially growing cultures were diluted to 3 × 10^8 and 5 µl were spotted on 1.5% agar plates supplemented with 0.5% CTT and immediately covered with a cover slide. Cells were incubated 4 h at 32°C and then visualized for 15 min with 30 s intervals at RT. Pictures were analyzed using ImageJ (Schindelin et al., 2012).

Epifluorescence microscopy. Unless otherwise indicated, for epifluorescence microscopy, cells were visualized following a slightly modified protocol (Schumacher & Søgaard-Andersen, 2018). Briefly, 5 µl exponentially growing cells were placed on a glass coverslip attached to a plastic frame. Cells were covered with a thick 1% agarose pad supplemented with 0.2% CTT. For long time-lapse microscopy, the pad was additionally sealed with parafilm to reduce evaporation. Alternatively, when indicated, epifluorescence microscopy studies of moving cells were performed in the presence of chitosan. Chitosan-coated µ-Dish (ibidi) were prepared as described in (Ducret *et al.*, 2013), 1 ml of exponentially growing cells were diluted in 1 ml MC7 buffer (10 mM MOPS pH 7.0, 1 mM $CaCl_2$), spotted on the chitosan-coated µ-Dish, and imaged after 30 min incubation. Cells were imaged using a DMi8 inverted microscope and a Hamamatsu ORCA-Flash4.0 V2 Digital CMOS C11440 or a DFC9000 GT (Leica) camera.

Data was analyzed using Oufti (Paintdakhi *et al.*, 2016), Metamorph® v 7.5 (Molecular Devices), Matlab R2020A and ImageJ (Schindelin *et al.*, 2012). To identify and analyze polar fluorescence signals in the cells, we used a custom-made Matlab script (Szadkowski *et al.*, 2019). Briefly, cells were segmented and polar clusters having an average fluorescence signal of 1.5 standard deviation (SD) (i.e. MglA) or 2 SD (i.e. MglB, RomR, SgmX, PilQ, PilM, PilB and PilT) above the average cytoplasmic fluorescence and a size of three or more pixels, were identified. For each cell with polar clusters, an asymmetry index (ω) was calculated as:

$$\omega = \frac{\text{total fluorescence at pole 1} - \text{ total fluorescence at pole 2}}{\text{total fluorescence at pole 1} + \text{ total fluorescence at pole 2}}$$

Pole 1 was assigned to the pole with the highest fluorescence. The localization patterns were binned from the ω values as follows: unipolar (ω > 0.9), bipolar asymmetric (0.9 > ω > 0.2) and bipolar symmetric (0.2 > ω > 0). Diffuse localization was determined when no polar signal was detected (ω=0). To plot the dispersion of the single-cell measurements, violin plots were prepared using Matlab R2020a and a modified version of the script violin.m (Hoffmann, 2015). Additionally, ellipses in which the direction and length of error bars are defined by the eigenvectors and square root of the corresponding eigenvalues of the polar fraction covariance matrix for each strain were prepared as in (Carreira *et al.*, 2020). For calculating the average cytoplasmic fluorescence, cells with and without clusters were included.

Negative stain transmission electron microscopy. 10 µl of *M. xanthus* cells exponentially grown in liquid were placed on one side of the electron microscopy grid (Plano) and incubated at RT for 40 min. To avoid evaporation during this step, the grid was incubated in humid air conditions. The liquid was blotted through the grid by capillarity by applying the side of the grid on Whatman paper. Cells were washed three times with 10 µl of double distilled water and stained with a staining solution (0.25% (v/v) UA-zero EM Stain (Plano) in double distilled water). After 1 min incubation, the liquid was blotted and cells were washed once with double distilled water to remove the excess of staining. Transmission electron microscopy was done with a JEOL JEM-1400 electron microscope at 100 kV.

Immunoblot analysis. Immunoblots were carried out as described (Sambrook & Russell, 2001). Rabbit polyclonal α-PilA (dilution: 1:2,000) (Treuner-Lange *et al.*, 2020), α-LonD (dilution: 1:5000) (Treuner-Lange *et al.*, 2020), α-PilB (dilution: 1:2,000) (Jakovljevic *et al.*, 2008), α-PilT (dilution: 1:3,000) (Jakovljevic *et al.*, 2008), α-PilC (dilution: 1:2,000) (Bulyha *et al.*, 2009), α-FtsZ (dilution: 1:25,000) (Treuner-Lange *et al.*, 2013), and α-mCherry (dilution: 1:1000) (BioVision), were used together with and horseradish peroxidase-conjugated goat α-rabbit immunoglobulin G (dilution: 1:15,000) (Sigma) as secondary antibody respectively. Mouse α-GFP antibodies (dilution: 1:2,000) (Roche) were used together with horseradish peroxidase-

conjugated sheep α-mouse immunoglobulin G (dilution: 1:2000) (GE Healthcare) as a secondary antibody. Blots were developed using Luminata Forte Western HRP Substrate (Millipore) on a LAS-4000 imager (Fujifilm).

T4P shear off assay. T4P were sheared from *M. xanthus* cells following a slightly modified protocol (Treuner-Lange *et al.*, 2020). Briefly, cells grown for three days on 1% CTT 1.5% agar plates at 32°C were scraped off the agar and resuspended in pili resuspension buffer (100 mM Tris-HCl pH 7.6, 150 mM NaCl) (1 ml per 60 mg cells). Cell suspensions were vortexed for 10 min at maximum speed. For determining the cellular PilA level, a 100 µl aliquot was harvested (10 min, 21,100 *g*, 4°C) and the pellet was resuspended in 200 µl 1×sodium dodecyl sulfate (SDS) buffer (60 mM Tris-HCl pH 6.8, 2% (w/v) SDS, 10% (v/v) glycerol, 0.1 M dithiothreitol, 5 mM EDTA, 0.005% Bromophenol Blue), and denatured at 95°C for 10 min. The remaining cell suspension was centrifuged three times (20 min, 21,000 *g,* 4 °C) to remove cell debris. Pili in the cell-free supernatant were precipitated by adding 10×pili precipitation buffer (final concentrations: 100 mM $MgCl_2$, 2% (w/v) PEG 6000, 100 mM Tris-HCl pH 7.6, 150 mM NaCl) for at least 2 h at 4°C and were harvested (21,000 *g*, 30 min, 4°C). The pellet was resuspended in 1×SDS buffer (2 µl per mg vortexed cells) and boiled for 10 min at 95°C. Samples were separated by SDS-PAGE and analyzed for PilA accumulation by immunoblot using PilA antibodies. Blots were developed as previously indicated.

C-di-GMP quantifications. The c-di-GMP level of *M. xanthus* cells was determined as in (Spangler *et al.*, 2010). Briefly, 4 ml of exponentially growing cells were harvested by centrifugation (20 min, 2,500 *g*, 4°C). Cells were mixed with 300 µl ice cold extraction buffer (high-pressure liquid chromatography [HPLC]-grade acetonitrile-methanol-water [2:2:1, v:v:v]), and incubated 15 min at 4°C to quench metabolism. Extraction was performed at 95°C for 10 min, samples were centrifuged (10 min, 21,130 *g*, 4°C) and supernatant containing extracted metabolites was transferred into a new Eppendorf tube. The pellet was washed with 200 µl extraction buffer and centrifuged (10 min, 21,130 *g*, 4°C). This step was repeated once more. The residual pellet containing proteins was reserved and the three supernatants containing c-di-GMP were pooled and evaporated to dryness in a vacuum centrifuge. Subsequently, the samples with c-di-GMP were dissolved in HPLC-grade water for analysis by liquid chromatography-coupled tandem mass spectrometry (LC-MS/MS). In parallel, to determine protein concentration for each sample, the residual pellets were resuspended in 800 µl of 0.1 M NaOH, and heated for 15 min at 95°C until dissolution. Protein level was determined using a 660 nm Protein Assay (Pierce) following manufacturer's instructions.

Protein purification. For expression and purification of $_{MalE}$DmxA and variants, proteins were expressed in *E. coli* Rosetta DE3 growing in 5052-Terrific-Broth (Studier, 2014) (0.5% (v/v) glycerol, 0.05% (w/v) glucose, 0.2% (w/v) lactose, 2.4% (w/v) yeast extract, 2% (w/v) tryptone,

25 mM Na_2HPO_4, 25 mM KH_2PO_4, 50 mM NH_4Cl, 5 mM Na_2SO_4, 2 mM $MgSO_4$) auto-induction medium supplemented with 25 µg ml^{-1} chloramphenicol and 100 µg ml^{-1} carbenicillin. Cells were grown at 37°C until OD_{600}=1, shifted to 18°C and further incubated overnight. Cells were harvested and resuspended in MalE-lysis buffer (100 mM Tris-HCl pH7.2, 500 mM NaCl, 10 mM $MgCl_2$, 5 mM DTT) supplemented with EDTA-free protease inhibitor cocktail (Roche) and lysed by sonication for ten cycles of 30 pulses of sonication and 30 s breaks using a Hielscher UP200st set to pulse=70%, amplitude=70%. The lysate was cleared by centrifugation at 16,000 *g,* 4°C for 30 min and loaded onto a 5 ml HighTrap MBP column (Cytiva) with amylose resin using an Äkta-Pure system (GE Healthcare). The column was washed with 10 column volumes of lysis buffer and the protein was eluted with MalE-elution buffer (100 mM Tris-HCl pH7.2, 500 mM NaCl, 10 mM $MgCl_2$, 5 mM DTT, 10 mM Maltose). The elution fractions containing $_{MalE}$DmxA were pooled and loaded on a HiLoad 16/600 Superdex 200pg (GE Healthcare) size exclusion chromatography column, which was pre-equilibrated with SEC-buffer (50 mM Tris-HCl pH7.2, 250 mM NaCl, 10 mM $MgCl_2$, 5 mM DTT, 5% glycerol (v/v)) and protein was eluted using SEC-buffer. Subsequently, protein was either used fresh or snap-frozen in SEC-buffer.

In vitro nucleotide binding assay. C-di-GMP binding was determined by Bio-Layer Interferometry using the BLItz system (ForteBio) (Sultana & Lee, 2015) equipped with Streptavidin SA biosensor (ForteBio). Briefly, 500 nM biotinylated c-di-GMP in SEC-buffer supplemented with 0.1% (v/v) Tween-20 was immobilized onto the biosensors for 120 s, and unbound molecules were washed off for 30 s. Association and dissociation of the protein was carried out during 120 and 120 s respectively.

DGC activity assay. DGC activity assays were performed, using the EnzCheck® Pyrophosphate Assay Kit (Thermo) as described (Severin & Waters, 2017). Reactions contained 1 µM protein, and, if not indicated otherwise, 50 µM GTP. In Fig. S2E GMP, GDP, cGMP and cAMP were added to a final concentration of 100 µM per reaction.

Proximity labeling. For proximity labeling, 50 ml of exponentially growing cell suspension were incubated with 100 µM biotin, and cephalexin. After 4 h incubation, cells were harvested by centrifugation (8,000 *g,* 10 min, 4°C), resuspended in 600 µl RIPA buffer (50 mM Tris-HCl pH 7.0, 150 mM NaCl, 0.5% (w/v) sodium deoxycholate, 0.2% (w/v) SDS, 1% (v/v) Triton-X100) supplemented with protease inhibitor cocktail (Roche) and lysed by 30 pulses of sonication using a Hielscher UP200st set to pulse 50%, amplitude 50%. The lysate was cleared by centrifugation (10 min, 8,000 *g*, at 4°C) and the pellet was discarded. To remove the excess of biotin in the supernatant, SpinTrap G-25 columns (Cytiva), pre-equilibrated with RIPA buffer, were used following manufacturer's instructions. To enrich biotinylated targets, 500 µl of each sample was incubated for 1 h at 4°C with 50 µl streptavidin magnetic beads (Pierce), previously

equilibrated two times with 1 ml RIPA buffer. To remove unspecific proteins, the beads were washed three times with 1 ml RIPA buffer, two times with 1 ml 1 M KCl, and three times with 1 ml 50 mM Tris-HCl pH 7.6. Finally, proteins were eluted using on-bead digest as described previously (Treuner-Lange *et al.*, 2020). Briefly, 100 µl elution buffer 1 (100 mM ammonium bicarbonate, 1 µg trypsin (Promega)) were added to each sample. After 30 min incubation at 30°C, the supernatant containing the digested proteins was collected. Beads were washed twice with elution buffer 2 (10 mM ammonium bicarbonate, 5 mM Tris(2-carboxyethyl)phosphine hydrochloride (TCEP)) and added to the first elution fraction. Digestion continued overnight at 30°C. Next, the peptides were incubated with 10 mM iodoacetamide for 30 min at 25°C in the dark. Prior to LC-MS analysis, peptides samples were desalted using C18 solid phase extraction spin columns (Macherey-Nagel). Peptide mixtures were then analyzed using liquid chromatography-mass spectrometry (LC-MS) carried out on an Exploris 480 instrument connected to an Ultimate 3000 RSLC nano and a nanospray flex ion source (all Thermo Scientific). Peptide separation was performed on a reverse phase HPLC column (75 µm x 42 cm) packed in-house with C18 resin (2.4 µm; Dr. Maisch). The following separating gradient was used: 98% solvent A (0.15% formic acid) and 2% solvent B (99.85% acetonitrile, 0.15% formic acid) to 30% solvent B over 40 min at a flow rate of 300 nl/min. Peptides were ionized at a spray voltage of 2.3 kV, ion transfer tube temperature set at 275°C, 445.12003 m/z was used as internal calibrant. The data acquisition mode was set to obtain one high resolution MS scan at a resolution of 60,000 full width at half maximum (at m/z 200) followed by MS/MS scans of the most intense ions within 1 s (cycle 1s). To increase the efficiency of MS/MS attempts, the charged state screening modus was enabled to exclude unassigned and singly charged ions. The dynamic exclusion duration was set to 14 sec. The ion accumulation time was set to 50 ms (MS) and 50 ms at 17,500 resolution (MS/MS). The automatic gain control (AGC) was set to $3x10^6$ for MS survey scan and $2x10^5$ for MS/MS scans. The quadrupole isolation was 1.5 m/z, collision was induced with an HCD collision energy of 27 %. MS raw data was then analyzed with MaxQuant (Branon *et al.*, 2018), and an *M. xanthus* UniProt database (The-UniProt-Consortium, 2019). MaxQuant was executed in standard settings without “match between runs” option. The search criteria were set as follows: full tryptic specificity was required (cleavage after lysine or arginine residues); two missed cleavages were allowed; carbamidomethylation (C) was set as fixed modification; oxidation (M) and deamidation (N,Q) as variable modifications. The MaxQuant proteinGroups.txt file were further processed by the SafeQuant R package for statistical analysis (Glatter *et al.*, 2012).

Total proteome analysis. The total proteome of *M. xanthus* cells grown in suspension culture was determined following a slightly modified protocol (Treuner-Lange *et al.*, 2020). Briefly, 2 ml of exponentially growing suspension cultures were harvested (8,000 *g,* 3 min, RT). The cells were resuspended in 1 ml PBS and again pelleted. Subsequently, the supernatant was

discarded and the pellet snap-frozen in liquid nitrogen. The pellet was suspended in 150 µl 2% SLS and proteins were precipitated using acetone and subsequently digested in 0.5% SLS with 1 µg trypsin and incubation for 30 min at 30˚C, and further incubated overnight in the presence of 5 mM TCEP. Following, acetylation using 10 mM iodoacetamide for 30 min at 25˚C in the dark, the peptides were desalted using C18 solid phase extraction. For label-free protein quantification, peptide mixtures were analyzed using liquid chromatography-mass spectrometry (LC-MS). The data was acquired in data independent acquisition mode and the MS raw data was then analyzed by DIA-NN as described (Schwabe *et al.*, 2022). Data were further analyzed and plotted using Python (3.7).

Bioinformatics. The KEGG databases (Kanehisa & Goto, 2000) was used to assign functions to proteins and to identify homologs of *M. xanthus* proteins in other bacteria using a reciprocal best BlastP hit method. Protein domains were identified using InterPro (Blum *et al.*, 2021),SMART (Letunic *et al.*, 2015), and the predicted AlphaFold structures. The DmxA protein sequence without the N-terminal transmembrane helices (amino acid 1-209) was used for AlphaFold and AlphaFold-Multimer modeling via ColabFold (1.5.0) (Jumper *et al.*, 2021, Evans *et al.*, 2022, Mirdita *et al.*, 2022). The predicted Local Distance Difference Test (pLDDT) and predicted Alignment Error (pAE) graphs of the five models generated were made using a custom Matlab R2020a (The MathWorks) script. Models were ranked based on combined pLDDT and pAE values, with the best-ranked models used for further analysis and presentation. Per residue model accuracy was estimated based on pLDDT values (>90, high accuracy; 70-90, generally good accuracy; 50-70, low accuracy; <50, should not be interpreted) (Jumper *et al.*, 2021). Relative domain positions were validated by pAE. The pAE graphs indicate the expected position error at residue X if the predicted and true structures were aligned on residue Y; the lower the pAE value, the higher the accuracy of the relative position of residue pairs and, consequently, the relative position of domains/subunits/proteins (Jumper *et al.*, 2021). PyMOL version 2.4.1 (http://www.pymol.org/pymol) was used to analyze and visualize the models. The phylogenetic tree was prepared in MEGA7 (Kumar *et al.*, 2016) using the Neighbor-Joining method (Saitou & Nei, 1987). Bootstrap values (500 replicates) are shown next to the branches (Felsenstein, 1985). RNA-seq. data were plotted using the BioMap function in Matlab. The base-by-base alignment coverage of RNA-sequencing and Cappable-sequencing reads of (Kuzmich *et al.*, 2021) were plotted for each position.

Statistics. Statistical comparisons of the distribution of ω values were performed in Matlab using the ranksum function (Mann-Whitney test). Statistical analysis of the colony expansion, the metabolomic measurements and the single cell motility assays were performed using GraphPad Prism (GraphPad Software, LLC) using the One-Way ANOVA function. The cell

length distribution was statistically analyzed using the Mann-Whitney test function in GraphPad Prism. PilA immunoblots were analyzed using a student's t-test in GraphPad Prism.

Literature

Abel, S., Bucher, T., Nicollier, M., Hug, I., Kaever, V., Abel Zur Wiesch, P., and Jenal, U. (2013) Bi-modal distribution of the second messenger c-di-GMP controls cell fate and asymmetry during the *Caulobacter* cell cycle. *PLoS Genet* **9**: e1003744.

Blackhart, B.D., and Zusman, D.R. (1985) "Frizzy" genes of *Myxococcus xanthus* are involved in control of frequency of reversal of gliding motility. *Proc Natl Acad Sci U S A* **82**: 8767-70.

Blum, M., Chang, H.Y., Chuguransky, S., Grego, T., Kandasaamy, S., Mitchell, A., Nuka, G., Paysan-Lafosse, T., Qureshi, M., Raj, S., Richardson, L., Salazar, G.A., Williams, L., Bork, P., Bridge, A., Gough, J., Haft, D.H., Letunic, I., Marchler-Bauer, A., Mi, H., Natale, D.A., Necci, M., Orengo, C.A., Pandurangan, A.P., Rivoire, C., Sigrist, C.J.A., Sillitoe, I., Thanki, N., Thomas, P.D., Tosatto, S.C.E., Wu, C.H., Bateman, A., and Finn, R.D. (2021) The InterPro protein families and domains database: 20 years on. *Nucleic Acids Res* **49**: D344-D354.

Branon, T.C., Bosch, J.A., Sanchez, A.D., Udeshi, N.D., Svinkina, T., Carr, S.A., Feldman, J.L., Perrimon, N., and Ting, A.Y. (2018) Efficient proximity labeling in living cells and organisms with TurboID. *Nat Biotechnol* **36**: 880-87.

Buddelmeijer, N., Judson, N., Boyd, D., Mekalanos, J.J., and Beckwith, J. (2002) YgbQ, a cell division protein in *Escherichia coli* and *Vibrio cholerae*, localizes in codependent fashion with FtsL to the division site. *Proc Natl Acad Sci U S A* **99**: 6316-21.

Bulyha, I., Schmidt, C., Lenz, P., Jakovljevic, V., Hone, A., Maier, B., Hoppert, M., and Søgaard-Andersen, L. (2009) Regulation of the type IV pili molecular machine by dynamic localization of two motor proteins. *Mol Microbiol* **74**: 691-706.

Bustamante, V.H., Martinez-Flores, I., Vlamakis, H.C., and Zusman, D.R. (2004) Analysis of the Frz signal transduction system of *Myxococcus xanthus* shows the importance of the conserved C-terminal region of the cytoplasmic chemoreceptor FrzCD in sensing signals. *Mol Microbiol* **53**: 1501-13.

Cameron, T.A., and Margolin, W. (2023) Insights into the assembly and regulation of the bacterial divisome. *Nat Rev Microbiol*.

Carreira, L.A.M., Szadkowski, D., Lometto, S., Hochberg, G.K.A., and Søgaard-Andersen, L. (2023) Molecular basis and design principles of switchable front-rear polarity and directional migration in Myxococcus xanthus. *Nat Commun* **14**: 4056.

Carreira, L.A.M., Szadkowski, D., Müller, F., and Søgaard-Andersen, L. (2022) Spatiotemporal regulation of switching front-rear cell polarity. *Curr Opin Cell Biol* **76**: 102076.

Carreira, L.A.M., Tostevin, F., Gerland, U., and Søgaard-Andersen, L. (2020) Protein-protein interaction network controlling establishment and maintenance of switchable cell polarity. *PLoS Genet* **16**: e1008877.

Carter, T., Buensuceso, R.N., Tammam, S., Lamers, R.P., Harvey, H., Howell, P.L., and Burrows, L.L. (2017) The type IVa pilus machinery is recruited to sites of future cell division. *mBio* **8**: e02103-16.

Chang, Y.W., Rettberg, L.A., Treuner-Lange, A., Iwasa, J., Søgaard-Andersen, L., and Jensen, G.J. (2016) Architecture of the type IVa pilus machine. *Science* **351**: aad2001.

Christen, B., Christen, M., Paul, R., Schmid, F., Folcher, M., Jenoe, P., Meuwly, M., and Jenal, U. (2006) Allosteric control of cyclic di-GMP signaling. *J Biol Chem* **281**: 32015-24.

Christen, M., Kulasekara, H.D., Christen, B., Kulasekara, B.R., Hoffman, L.R., and Miller, S.I. (2010) Asymmetrical distribution of the second messenger c-di-GMP upon bacterial cell division. *Science* **328**: 1295-7.

Cutler, K.J., Stringer, C., Lo, T.W., Rappez, L., Stroustrup, N., Brook Peterson, S., Wiggins, P.A., and Mougous, J.D. (2022) Omnipose: a high-precision morphology-independent solution for bacterial cell segmentation. *Nat Methods* **19**: 1438-48.

Davis, N.J., Cohen, Y., Sanselicio, S., Fumeaux, C., Ozaki, S., Luciano, J., Guerrero-Ferreira, R.C., Wright, E.R., Jenal, U., and Viollier, P.H. (2013) De- and repolarization mechanism of flagellar morphogenesis during a bacterial cell cycle. *Genes Dev* **27**: 2049-62.

Dinet, C., and Mignot, T. (2023) Unorthodox regulation of the MglA Ras-like GTPase controlling polarity in *Myxococcus xanthus*. *FEBS Lett* **597**: 850-64.

Ducret, A., Theodoly, O., and Mignot, T. (2013) Single cell microfluidic studies of bacterial motility. *Methods Mol Biol* **966**: 97-107.

Eberhardt, C., Kuerschner, L., and Weiss, D.S. (2003) Probing the catalytic activity of a cell division-specific transpeptidase in vivo with beta-lactams. *J Bacteriol* **185**: 3726-34.

Evans, R., O'Neill, M., Pritzel, A., Antropova, N., Senior, A., Green, T., Žídek, A., Bates, R., Blackwell, S., Yim, J., Ronneberger, O., Bodenstein, S., Zielinski, M., Bridgland, A., Potapenko, A., Cowie, A., Tunyasuvunakool, K., Jain, R., Clancy, E., Kohli, P., Jumper, J., and Hassabis, D. (2022) Protein complex prediction with AlphaFold-Multimer. *bioRxiv*: 2021.10.04.463034.

Felsenstein, J. (1985) Confidence-limits on phylogenies - an approach using the bootstrap. *Evolution* **39**: 783-91.

Friedrich, C., Bulyha, I., and Søgaard-Andersen, L. (2014) Outside-in assembly pathway of the type IV pilus system in *Myxococcus xanthus*. *J Bacteriol* **196**: 378-90.

Glatter, T., Ludwig, C., Ahrné, E., Aebersold, R., Heck, A.J., and Schmidt, A. (2012) Large-scale quantitative assessment of different in-solution protein digestion protocols reveals superior cleavage efficiency of tandem Lys-C/trypsin proteolysis over trypsin digestion. *J Proteome Res* **11**: 5145-56.

Goley, E.D., Yeh, Y.C., Hong, S.H., Fero, M.J., Abeliuk, E., McAdams, H.H., and Shapiro, L. (2011) Assembly of the *Caulobacter* cell division machine. *Mol Microbiol* **80**: 1680-98.

Hartzell, P., and Kaiser, D. (1991) Function of MglA, a 22-kilodalton protein essential for gliding in *Myxococcus xanthus*. *J Bacteriol* **173**: 7615-24.
Harvey, C.W., Madukoma, C.S., Mahserejian, S., Alber, M.S., and Shrout, J.D. (2014) Cell division resets polarity and motility for the bacterium *Myxococcus xanthus*. *J Bacteriol* **196**: 3853-61.
Heikaus, C.C., Pandit, J., and Klevit, R.E. (2009) Cyclic nucleotide binding GAF domains from phosphodiesterases: structural and mechanistic insights. *Structure* **17**: 1551-57.
Herfurth, M., Pérez-Burgos, M., and Søgaard-Andersen, L. (2023) The mechanism for polar localization of the type IVa pilus machine in *Myxococcus xanthus*. *mBio*: in press.
Herfurth, M., Treuner-Lange, A., Glatter, T., Wittmaack, N., Hoiczyk, E., Pierik, A.J., and Søgaard-Andersen, L. (2022) A noncanonical cytochrome c stimulates calcium binding by PilY1 for type IVa pili formation. *Proc Natl Acad Sci U S A* **119**: e2115061119.
Hodgkin, J., and Kaiser, D. (1977) Cell-to-cell stimulation of movement in nonmotile mutants of *Myxococcus*. *Proc Natl Acad Sci U S A* **74**: 2938-42.
Hodgkin, J., and Kaiser, D. (1979) Genetics of gliding motility in *Myxococcus xanthus* (Myxobacterales) - Two gene systems control movement. *Mol Gen Genet* **171**: 177-91.
Hu, W., Hossain, M., Lux, R., Wang, J., Yang, Z., Li, Y., and Shi, W. (2011) Exopolysaccharide-independent social motility of *Myxococcus xanthus*. *PLoS ONE* **6**: e16102.
Iniesta, A.A., Garcia-Heras, F., Abellon-Ruiz, J., Gallego-Garcia, A., and Elias-Arnanz, M. (2012) Two systems for conditional gene expression in *Myxococcus xanthus* inducible by isopropyl-beta-D-thiogalactopyranoside or vanillate. *J Bacteriol* **194**: 5875-85.
Jakobczak, B., Keilberg, D., Wuichet, K., and Søgaard-Andersen, L. (2015) Contact- and protein transfer-dependent stimulation of assembly of the gliding motility machinery in *Myxococcus xanthus*. *PLoS Genet* **11**: e1005341.
Jakovljevic, V., Leonardy, S., Hoppert, M., and Søgaard-Andersen, L. (2008) PilB and PilT are ATPases acting antagonistically in type IV pilus function in *Myxococcus xanthus*. *J Bacteriol* **190**: 2411-21.
Jenal, U., Reinders, A., and Lori, C. (2017) Cyclic di-GMP: second messenger extraordinaire. *Nat Rev Microbiol* **15**: 271-84.
Julien, B., Kaiser, A.D., and Garza, A. (2000) Spatial control of cell differentiation in *Myxococcus xanthus*. *Proc Natl Acad Sci U S A* **97**: 9098-103.
Jumper, J., Evans, R., Pritzel, A., Green, T., Figurnov, M., Ronneberger, O., Tunyasuvunakool, K., Bates, R., Zidek, A., Potapenko, A., Bridgland, A., Meyer, C., Kohl, S.A.A., Ballard, A.J., Cowie, A., Romera-Paredes, B., Nikolov, S., Jain, R., Adler, J., Back, T., Petersen, S., Reiman, D., Clancy, E., Zielinski, M., Steinegger, M., Pacholska, M., Berghammer, T., Bodenstein, S., Silver, D., Vinyals, O., Senior, A.W., Kavukcuoglu, K., Kohli, P., and Hassabis, D. (2021) Highly accurate protein structure prediction with AlphaFold. *Nature* **596**: 583-89.
Kaczmarczyk, A., Hempel, A.M., von Arx, C., Bohm, R., Dubey, B.N., Nesper, J., Schirmer, T., Hiller, S., and Jenal, U. (2020) Precise timing of transcription by c-di-GMP coordinates cell cycle and morphogenesis in *Caulobacter*. *Nat Commun* **11**: 816.
Kaczmarczyk, A., Vliet, S.v., Jakob, R.P., Reinders, A., Klotz, A., Maier, T., and Jenal, U. (2022) A novel biosensor reveals dynamic changes of c-di-GMP in differentiating cells with ultra-high temporal resolution. *bioRxiv*: 2022.10.18.512705.
Kaiser, D. (1979) Social gliding is correlated with the presence of pili in *Myxococcus xanthus*. *Proc Natl Acad Sci U S A* **76**: 5952-956.
Kanehisa, M., and Goto, S. (2000) KEGG: kyoto encyclopedia of genes and genomes. *Nucleic Acids Res* **28**: 27-30.
Katis, V.L., Harry, E.J., and Wake, R.G. (1997) The *Bacillus subtilis* division protein DivIC is a highly abundant membrane-bound protein that localizes to the division site. *Mol Microbiol* **26**: 1047-55.
Keilberg, D., Wuichet, K., Drescher, F., and Søgaard-Andersen, L. (2012) A response regulator interfaces between the Frz chemosensory system and the MglA/MglB GTPase/GAP module to regulate polarity in *Myxococcus xanthus*. *PLoS Genet* **8**: e1002951.
Konovalova, A., Petters, T., and Søgaard-Andersen, L. (2010) Extracellular biology of *Myxococcus xanthus*. *FEMS Microbiol Rev* **34**: 89-106.
Kreiling, V., and Thormann, K.M. (2023) Polarity of c-di-GMP synthesis and degradation. *Microlife* **4**: uqad014.
Kumar, S., Stecher, G., and Tamura, K. (2016) MEGA7: Molecular Evolutionary Genetics Analysis Version 7.0 for Bigger Datasets. *Mol Biol Evol* **33**: 1870-4.
Kuzmich, S., Blumenkamp, P., Meier, D., Szadkowski, D., Goesmann, A., Becker, A., and Søgaard-Andersen, L. (2021) CRP-Like transcriptional regulator MrpC curbs c-di-GMP and 3',3'-cGAMP nucleotide levels during development in *Myxococcus xanthus*. *mBio* **13**: e0004422.
Laventie, B.J., Sangermani, M., Estermann, F., Manfredi, P., Planes, R., Hug, I., Jaeger, T., Meunier, E., Broz, P., and Jenal, U. (2019a) A surface-induced asymmetric program promotes tissue colonization by *Pseudomonas aeruginosa*. *Cell Host Microbe* **25**: 140-152 e6.
Laventie, B.J., Sangermani, M., Estermann, F., Manfredi, P., Planes, R., Hug, I., Jaeger, T., Meunier, E., Broz, P., and Jenal, U. (2019b) A surface-induced asymmetric program promotes tissue colonization by *Pseudomonas aeruginosa*. *Cell Host Microbe* **25**: 140-152.e6.
Leonardy, S., Freymark, G., Hebener, S., Ellehauge, E., and Søgaard-Andersen, L. (2007) Coupling of protein localization and cell movements by a dynamically localized response regulator in *Myxococcus xanthus*. *EMBO J* **26**: 4433-44.

Leonardy, S., Miertzschke, M., Bulyha, I., Sperling, E., Wittinghofer, A., and Søgaard-Andersen, L. (2010) Regulation of dynamic polarity switching in bacteria by a Ras-like G-protein and its cognate GAP. *EMBO J* **29**: 2276-89.

Letunic, I., Doerks, T., and Bork, P. (2015) SMART: recent updates, new developments and status in 2015. *Nucleic Acids Res* **43**: D257-60.

Lori, C., Ozaki, S., Steiner, S., Bohm, R., Abel, S., Dubey, B.N., Schirmer, T., Hiller, S., and Jenal, U. (2015) Cyclic di-GMP acts as a cell cycle oscillator to drive chromosome replication. *Nature* **523**: 236-9.

Luciano, J., Agrebi, R., Le Gall, A.V., Wartel, M., Fiegna, F., Ducret, A., Brochier-Armanet, C., and Mignot, T. (2011) Emergence and modular evolution of a novel motility machinery in bacteria. *PLoS Genet* **7**: e1002268.

Mauriello, E.M., Mouhamar, F., Nan, B., Ducret, A., Dai, D., Zusman, D.R., and Mignot, T. (2010) Bacterial motility complexes require the actin-like protein, MreB and the Ras homologue, MglA. *EMBO J* **29**: 315-26.

Mercier, R., Bautista, S., Delannoy, M., Gibert, M., Guiseppi, A., Herrou, J., Mauriello, E.M.F., and Mignot, T. (2020) The polar Ras-like GTPase MglA activates type IV pilus via SgmX to enable twitching motility in *Myxococcus xanthus*. *Proc Natl Acad Sci U S A* **117**: 28366-28373.

Mignot, T., Shaevitz, J.W., Hartzell, P.L., and Zusman, D.R. (2007) Evidence that focal adhesion complexes power bacterial gliding motility. *Science* **315**: 853-6.

Mirdita, M., Schutze, K., Moriwaki, Y., Heo, L., Ovchinnikov, S., and Steinegger, M. (2022) ColabFold: making protein folding accessible to all. *Nat Methods* **19**: 679-682.

Muñoz-Dorado, J., Marcos-Torres, F.J., Garcia-Bravo, E., Moraleda-Munoz, A., and Perez, J. (2016) Myxobacteria: moving, killing, feeding, and surviving together. *Front Microbiol* **7**: 781.

Nan, B., Bandaria, J.N., Moghtaderi, A., Sun, I.-H., Yildiz, A., and Zusman, D.R. (2013) Flagella stator homologs function as motors for myxobacterial gliding motility by moving in helical trajectories. *Proc Natl Acad Sci U S A* **110**: E1508-13.

Nan, B., Chen, J., Neu, J.C., Berry, R.M., Oster, G., and Zusman, D.R. (2011) Myxobacteria gliding motility requires cytoskeleton rotation powered by proton motive force. *Proc Natl Acad Sci U S A* **108**: 2498-503.

Nan, B., Mauriello, E.M., Sun, I.H., Wong, A., and Zusman, D.R. (2010) A multi-protein complex from *Myxococcus xanthus* required for bacterial gliding motility. *Mol Microbiol* **76**: 1539-54.

Nudleman, E., Wall, D., and Kaiser, D. (2006) Polar assembly of the type IV pilus secretin in *Myxococcus xanthus*. *Mol Microbiol* **60**: 16-29.

Paintdakhi, A., Parry, B., Campos, M., Irnov, I., Elf, J., Surovtsev, I., and Jacobs-Wagner, C. (2016) Oufti: an integrated software package for high-accuracy, high-throughput quantitative microscopy analysis. *Mol Microbiol* **99**: 767-77.

Pandit, J., Forman, M.D., Fennell, K.F., Dillman, K.S., and Menniti, F.S. (2009) Mechanism for the allosteric regulation of phosphodiesterase 2A deduced from the X-ray structure of a near full-length construct. *Proc Natl Acad Sci U S A* **106**: 18225-30.

Paul, R., Jaeger, T., Abel, S., Wiederkehr, I., Folcher, M., Biondi, E.G., Laub, M.T., and Jenal, U. (2008) Allosteric regulation of histidine kinases by their cognate response regulator determines cell fate. *Cell* **133**: 452-61.

Paul, R., Weiser, S., Amiot, N.C., Chan, C., Schirmer, T., Giese, B., and Jenal, U. (2004) Cell cycle-dependent dynamic localization of a bacterial response regulator with a novel di-guanylate cyclase output domain. *Genes Dev* **18**: 715-27.

Pérez-Burgos, M., García-Romero, I., Jung, J., Schander, E., Valvano, M.A., and Søgaard-Andersen, L. (2020) Characterization of the exopolysaccharide biosynthesis pathway in *Myxococcus xanthus*. *J Bacteriol* **202**: e00335-20.

Potapova, A., Carreira, L.A.M., and Søgaard-Andersen, L. (2020) The small GTPase MglA together with the TPR domain protein SgmX stimulates type IV pili formation in *M. xanthus*. *Proc Natl Acad Sci U S A* **117**: 23859-68.

Rick, T., Kreiling, V., Hoing, A., Fiedler, S., Glatter, T., Steinchen, W., Hochberg, G., Bahre, H., Seifert, R., Bange, G., Knauer, S.K., Graumann, P.L., and Thormann, K.M. (2022) GGDEF domain as spatial on-switch for a phosphodiesterase by interaction with landmark protein HubP. *NPJ Biofilms Microbiomes* **8**: 35.

Römling, U., Galperin, M.Y., and Gomelsky, M. (2013) Cyclic di-GMP: the first 25 years of a universal bacterial second messenger. *Microbiol Mol Biol Rev* **77**: 1-52.

Rossmann, F.M., Rick, T., Mrusek, D., Sprankel, L., Dorrich, A.K., Leonhard, T., Bubendorfer, S., Kaever, V., Bange, G., and Thormann, K.M. (2019) The GGDEF Domain of the Phosphodiesterase PdeB in Shewanella putrefaciens Mediates Recruitment by the Polar Landmark Protein HubP. *J Bacteriol* **201**: e00534-18.

Saitou, N., and Nei, M. (1987) The Neighbor-Joining Method - a New Method for Reconstructing Phylogenetic Trees. *Mol Biol Evol* **4**: 406-25.

Sambrook, J., and Russell, D.W., (2001) *Molecular cloning: a laboratory manual*. Cold Spring Harbor Laboratory Press, Cold Spring Harbor, N.Y.

Schindelin, J., Arganda-Carreras, I., Frise, E., Kaynig, V., Longair, M., Pietzsch, T., Preibisch, S., Rueden, C., Saalfeld, S., Schmid, B., Tinevez, J.Y., White, D.J., Hartenstein, V., Eliceiri, K., Tomancak, P., and Cardona, A. (2012) Fiji: an open-source platform for biological-image analysis. *Nat Methods* **9**: 676-82.

Schumacher, D., Bergeler, S., Harms, A., Vonck, J., Huneke-Vogt, S., Frey, E., and Søgaard-Andersen, L. (2017) The PomXYZ proteins self-organize on the bacterial nucleoid to stimulate cell division. *Dev Cell* **41**: 299-314.e13.

Schumacher, D., and Søgaard-Andersen, L. (2017) Regulation of cell polarity in motility and cell division in *Myxococcus xanthus*. *Annu Rev Microbiol* **71**: 61-78.

Schumacher, D., and Søgaard-Andersen, L. (2018) Fluorescence live-cell imaging of the complete vegetative cell cycle of the slow-growing social bacterium *Myxococcus xanthus*. *J Vis Exp*.
Schwabe, J., Pérez-Burgos, M., Herfurth, M., Glatter, T., and Søgaard-Andersen, L. (2022) Evidence for a widespread third system for bacterial polysaccharide export across the outer membrane comprising a composite OPX/beta-barrel rranslocon. *mBio* **13**: e0203222.
Severin, G.B., and Waters, C.M. (2017) Spectrophotometric and mass spectroscopic methods for the quantification and kinetic evaluation of in vitro c-di-GMP synthesis. *Methods Mol Biol* **1657**: 71-84.
Shi, W., and Zusman, D.R. (1993) The two motility systems of *Myxococcus xanthus* show different selective advantages on various surfaces. *Proc Natl Acad Sci U S A* **90**: 3378-82.
Shi, X., Wegener-Feldbrugge, S., Huntley, S., Hamann, N., Hedderich, R., and Søgaard-Andersen, L. (2008) Bioinformatics and experimental analysis of proteins of two-component systems in *Myxococcus xanthus*. *J Bacteriol* **190**: 613-24.
Siewering, K., Jain, S., Friedrich, C., Webber-Birungi, M.T., Semchonok, D.A., Binzen, I., Wagner, A., Huntley, S., Kahnt, J., Klingl, A., Boekema, E.J., Søgaard-Andersen, L., and van der Does, C. (2014) Peptidoglycan-binding protein TsaP functions in surface assembly of type IV pili. *Proc Natl Acad Sci U S A* **111**: E953-61.
Skotnicka, D., Petters, T., Heering, J., Hoppert, M., Kaever, V., and Søgaard-Andersen, L. (2015) c-di-GMP regulates type IV pili-dependent-motility in *Myxococcus xanthus*. *J Bacteriol* **198**: 77-90.
Skotnicka, D., Steinchen, W., Szadkowski, D., Cadby, I.T., Lovering, A.L., Bange, G., and Søgaard-Andersen, L. (2020) CdbA is a DNA-binding protein and c-di-GMP receptor important for nucleoid organization and segregation in *Myxococcus xanthus*. *Nat Commun* **11**: 1791.
Spangler, C., Bohm, A., Jenal, U., Seifert, R., and Kaever, V. (2010) A liquid chromatography-coupled tandem mass spectrometry method for quantitation of cyclic di-guanosine monophosphate. *J Microbiol Methods* **81**: 226-31.
Studier, F.W. (2014) Stable expression clones and auto-induction for protein production in *E. coli*. *Methods Mol Biol* **1091**: 17-32.
Sultana, A., and Lee, J.E. (2015) Measuring protein-protein and protein-nucleic acid interactions by biolayer interferometry. *Curr Protoc Protein Sci* **79**: 19.25.1-19.25.26.
Sun, H., Zusman, D.R., and Shi, W. (2000) Type IV pilus of *Myxococcus xanthus* is a motility apparatus controlled by the *frz* chemosensory system. *Curr Biol* **10**: 1143-46.
Sun, M., Wartel, M., Cascales, E., Shaevitz, J.W., and Mignot, T. (2011) Motor-driven intracellular transport powers bacterial gliding motility. *Proc Natl Acad Sci U S A* **108**: 7559-64.
Szadkowski, D., Carreira, L.A.M., and Søgaard-Andersen, L. (2022) A bipartite, low-affinity roadblock domain-containing GAP complex regulates bacterial front-rear polarity. *PLoS Genet* **18**: e1010384.
Szadkowski, D., Harms, A., Carreira, L.A.M., Wigbers, M., Potapova, A., Wuichet, K., Keilberg, D., Gerland, U., and Søgaard-Andersen, L. (2019) Spatial control of the GTPase MglA by localized RomR-RomX GEF and MglB GAP activities enables *Myxococcus xanthus* motility. *Nat Microbiol* **4**: 1344-55.
The-UniProt-Consortium (2019) UniProt: a worldwide hub of protein knowledge. *Nucleic Acids Res* **47**: D506-515.
Treuner-Lange, A., Aguiluz, K., van der Does, C., Gomez-Santos, N., Harms, A., Schumacher, D., Lenz, P., Hoppert, M., Kahnt, J., Munoz-Dorado, J., and Søgaard-Andersen, L. (2013) PomZ, a ParA-like protein, regulates Z-ring formation and cell division in *Myxococcus xanthus*. *Mol Microbiol* **87**: 235-53.
Treuner-Lange, A., Chang, Y.W., Glatter, T., Herfurth, M., Lindow, S., Chreifi, G., Jensen, G.J., and Søgaard-Andersen, L. (2020) PilY1 and minor pilins form a complex priming the type IVa pilus in *Myxococcus xanthus*. *Nat Commun* **11**: 5054.
Treuner-Lange, A., Macia, E., Guzzo, M., Hot, E., Faure, L.M., Jakobczak, B., Espinosa, L., Alcor, D., Ducret, A., Keilberg, D., Castaing, J.P., Lacas Gervais, S., Franco, M., Søgaard-Andersen, L., and Mignot, T. (2015) The small G-protein MglA connects to the MreB actin cytoskeleton at bacterial focal adhesions. *J Cell Biol* **210**: 243-56.
Wartel, M., Ducret, A., Thutupalli, S., Czerwinski, F., Le Gall, A.V., Mauriello, E.M., Bergam, P., Brun, Y.V., Shaevitz, J., and Mignot, T. (2013) A versatile class of cell surface directional motors gives rise to gliding motility and sporulation in Myxococcus xanthus. *PLoS Biol* **11**: e1001728.
Wu, S.S., and Kaiser, D. (1995) Genetic and functional evidence that type IV pili are required for social gliding motility in *Myxococcus xanthus*. *Mol Microbiol* **18**: 547-58.
Wu, S.S., and Kaiser, D. (1997) Regulation of expression of the *pilA* gene in *Myxococcus xanthus*. *J Bacteriol* **179**: 7748-58.
Wu, S.S., Wu, J., and Kaiser, D. (1997) The *Myxococcus xanthus pilT* locus is required for social gliding motility although pili are still produced. *Mol Microbiol* **23**: 109-21.
Zhang, Y., Ducret, A., Shaevitz, J., and Mignot, T. (2012a) From individual cell motility to collective behaviors: insights from a prokaryote, *Myxococcus xanthus*. *FEMS Microbiol Rev* **36**: 149-64.
Zhang, Y., Franco, M., Ducret, A., and Mignot, T. (2010) A bacterial Ras-like small GTP-binding protein and its cognate GAP establish a dynamic spatial polarity axis to control directed motility. *PLoS Biol* **8**: e1000430.
Zhang, Y., Guzzo, M., Ducret, A., Li, Y.Z., and Mignot, T. (2012b) A dynamic response regulator protein modulates G-protein-dependent polarity in the bacterium *Myxococcus xanthus*. *PLoS Genet* **8**: e1002872.

Table 1. Strains used in this work.

Strain	Genotype	Reference
M. xanthus		
DK1622	Wildtype	(Kaiser, 1979)
DK10410	Δ*pilA*	(Wu *et al.*, 1997)
SA3387	Δ*mglB*	(Leonardy *et al.*, 2010)
SA3922	Δ*gltB*	(Jakobczak *et al.*, 2015)
SA7192	*pilQ-sfGFP*	(Potapova *et al.*, 2020)
SA7507	***romR-mCherry***	(Szadkowski *et al.*, 2019)
SA7896	*mCherry-pilM*	(Treuner-Lange *et al.*, 2020)
SA8802	Δ*frzE*	**(Szadkowski *et al.*, 2019)**
SA12017	*pilQ-sfGFP* Δ*gltB*	(Herfurth *et al.*, 2023)
SA12021	*tgl-sfGFP* Δ*gltB*	(Herfurth *et al.*, 2023)
SA12027	WT *MXAN_18-19::*pMH97 (P_{van} *sfGFP-miniTurboID-FLAG*)	This study
SA5666	Δ10 (Δ*MXAN_1525*, Δ*MXAN_4029*, Δ*MXAN_5199*, Δ*MXAN_7362,* Δ*gacB*, Δ*gacA*, Δ*MXAN_2997*, Δ*MXAN_5366*, Δ*dmxB*, Δ*MXAN_5791*)	This study
SA6755	Δ*ftsZ MXAN_18-19::*pMAT86 (P_{van} *ftsZ*)	This study
SA9307	*mCherry-pilT*	This study
SA9300	*pilB-mCherry*	This study
SA7442	Δ*dmxA*	This study
SA7447	Δ*dmxA attB::*pTP140 (P_{nat} *dmxA*)	This study
SA7459	Δ*dmxA romR mCherry*	This study
SA7466	Δ*dmxA* Δ*pilA*	This study
SA7479	Δ*dmxA* Δ*frzE*	This study
SA7485	*dmxA-mVenus*	This study
SA7488	$dmxA^{R615A}$*-mVenus*	This study
SA8505	Δ*dmxA pilQ-sfGFP*	This study
SA8511	Δ*ftsZ MXAN_18-19::*pMAT86 (P_{van} *ftsZ*) *dmxA-mVenus*	This study
SA8572	Δ*dmxA pilB-mCherry*	This study
SA8575	Δ*dmxA mCherry-pilT*	This study
SA8576	Δ*dmxA mCherry-pilM*	This study
SA8580	$dmxA^{E626A}$*-mVenus*	This study
SA8589	*dmxA mVenus* Δ*gltB*	This study
SA8596	Δ*dmxA attB::*pMP172 (P_{pilA} *dmxA-miniTurboID-FLAG*)	This study
SA9082	*attB::*pMH123 (P_{pilA} *cdGreen2 mScarlet*)	This study
SA9083	Δ10* *attB::*pMH123 (P_{pilA} *cdGreen2 mScarlet*)	This study
SA9084	Δ10* Δ*gltB attB::*pMH123 (P_{pilA} *cdGreen2 mScarlet*)	This study
SA12010	Δ*dmxA* Δ*gltB*	This study
SA12013	Δ*dmxA tgl-sfGFP*	This study
SA12015	$dmxA^{\Delta GAF\times2\ (\Delta223\text{-}532)}$*-mVenus*	This study
SA12019	Δ*dmxA pilQ-sfGFP* Δ*gltB*	This study
SA12022	Δ*dmxA tgl-sfGFP* Δ*gltB*	This study
SA12034	$dmxA^{\Delta TMH\ (\Delta3\text{-}222)}$*-mVenus*	This study
SA12038	WT *attB::*pMH110 (P_{pilA} *ftsK-miniTurboID-FLAG*)	This study
SA12056	*romR-mCherry* Δ*gltB*	This study
SA12063	Δ10* Δ*gltB*	This study
SA12064	Δ*dmxA romR-mCherry* Δ*gltB*	This study
SA12065	$dmxA^{TMH\ (1\text{-}167)}$*-mVenus*	This study
E. coli		
Mach1	Δ*recA*1398 *endA*1 *tonA* Φ80Δ*lacM*15 Δ*lacX*74 *hsdR*(r_{K^-} m_{K^+})	Invitrogen
Rosetta2(DE3)	F^- *ompT hsdS*$_B$(r_B- m_B-) *gal dcm* (DE3) pRARE2	Novagen/Merck

* Δ10 mutations are described in detail in strain SA5666.

Table 2. Plasmids used in this work.

Plasmid	Description	Reference
pBJ114	*galK,* Km^r	(Julien *et al.*, 2000)
pSWU30	*attP,* Tet^r	(Wu & Kaiser, 1997)
pSW105	*attP,* P_{pilA} Km^r	(Jakovljevic *et al.*, 2008)
pMR3690	*MXAN_18-19, vanR* P_{van}, Km^r	(Iniesta *et al.*, 2012)
pMR3691	*MXAN_18-19, vanR* P_{van}, Tet^r	(Iniesta *et al.*, 2012)
pMAL-c6t	Overexpression vector, His_6-MalE	NEB
pAP19	pBJ114, in-frame deletion construct for *frzE,* Km^r	(Potapova *et al.*, 2020)
pAP37	pBJ114, *pilQ* replacement by *pilQ-sfGFP,* Km^r	(Potapova *et al.*, 2020)
pDJS01	pBJ114, in-frame deletion construct for *dmxB,* Km^r	(Skotnicka *et al.*, 2015)
pDJS02	pBJ114, in-frame deletion construct for *MXAN_ 5366,* Km^r	(Skotnicka *et al.*, 2015)
pDJS03	pBJ114, in-frame deletion construct for *MXAN_ 7362,* Km^r	(Skotnicka *et al.*, 2015)
pDK25	pBJ114, in-frame deletion construct for *gltB,* Km^r	(Jakobczak *et al.*, 2015)
pIH01	pBJ114, in-frame deletion construct for *gacA,* Km^r	(Skotnicka *et al.*, 2015)
pIH03	pBJ114, in-frame deletion construct for *MXAN_ 5791,* Km^r	(Skotnicka *et al.*, 2015)
pLC220	pBJ114, *tgl* replacement by *tgl-sfGFP,* Km^r	(Herfurth *et al.*, 2023)
pMAT162	pBJ114, in-frame deletion construct for *pilA,* Km^r	(Szadkowski *et al.*, 2019)
pMAT336	pBJ114, *pilM* replacement by *mCherry-pilM,* Km^r	(Treuner-Lange *et al.*, 2020)
pNGS010	pBJ114, in-frame deletion construct for *MXAN_ 2997,* Km^r	(Skotnicka *et al.*, 2015)
pTP120	pBJ114, in-frame deletion construct for *MXAN_1525,* Km^r	(Skotnicka *et al.*, 2015)
pTP121	pBJ114, in-frame deletion construct for *MXAN_ 5199,* Km^r	(Skotnicka *et al.*, 2015)
pTP125	pBJ114, in-frame deletion construct for *gacB,* Km^r	(Skotnicka *et al.*, 2015)
pTP127	pBJ114, in-frame deletion construct for *MXAN_ 4029,* Km^r	(Skotnicka *et al.*, 2015)
pTP140	pSWU30, P_{nat}-*dmxA,* Tet^r	(Skotnicka *et al.*, 2015)
pMAT74	pBJ114, in-frame deletion construct for *ftsZ*	This work
pMAT86	pMR3691, P_{van} *ftsZ*, Tet^r	This work
pMEM23	pBJ114, *pilB* replacement by *pilB-mCherry,* Km^r	This work
pMEM33	pBJ114, *pilT* replacement by *mCherry-pilT,* Km^r	This work
pMH52	p-EX-k168, *miniTurboID-FLAG*, Km^r	This work
pMH97	pMR3690, P_{van} *sfGFP-miniTurboID-FLAG*, Km^r	This work
pMH110	pSW105, *ftsK-miniTurboID-FLAG*, Km^r	This work
pMH113	pMAL-c6t, $dmxA^{223\text{-}722}$	This work
pMH114	pMAL-c6t, $dmxA^{223\text{-}547}$	This work
pMH115	pMAL-c6t, $dmxA^{546\text{-}722}$	This work
pMH116	pMAL-c6t, $dmxA^{223\text{-}722,\ R615A}$	This work
pMH117	pMAL-c6t, $dmxA^{223\text{-}722,\ E626A}$	This work
pMH123	pSW105, *cdGreen2 mScarlet*, Km^r	This work
pMP072	pBJ114, in-frame deletion construct for *dmxA,* Km^r	This work
pMP093	pBJ114, *dmxA* replacement by *dmxA-mVenus*, Km^r	This work
pMP095	pBJ114, *dmxA* replacement by $dmxA^{R615A}$*-mVenus,* Km^r	This work

pMP165	pBJ114, for complementation of Δ*dmxA* with *dmxA*^{E626A}-mVenus in the native site, Km^{r}	This work
pMP172	P_{pilA} *dmxA-miniTurboID-FLAG* in pSW105, Km^{R}	This work
pMP175	pBJ114, *dmxA* replacement by *dmxA*$^{\Delta GAF\times2\ (\Delta223\text{-}532)}$-*mVenus,* Km^{r}	This work
pMP179	pBJ114, *dmxA* replacement by *dmxA*$^{\Delta TMH\ (\Delta3\text{-}222)}$-*mVenus,* Km^{r}	This work
pMP182	pBJ114, for complementation of Δ*dmxA* with *dmxA*$^{TMH\ (1\text{-}167)}$-*mVenus* in the native site, Km^{r}	This work

Supplementary Information for

A burst of c-di-GMP during cytokinesis ensures the generation of phenotypically identical and symmetrical daughter cells

María Pérez-Burgos, Marco Herfurth, Andreas Kaczmarczyk, Katrin Huber, Timo Glatter, Urs Jenal, Roland Seifert, and Lotte Søgaard-Andersen

This file contains:

- Supplementary Figures 1-6
- Supplementary Experimental Procedures
- Table S1-S3
- Supplementary References

Supplemental Figures and Legends

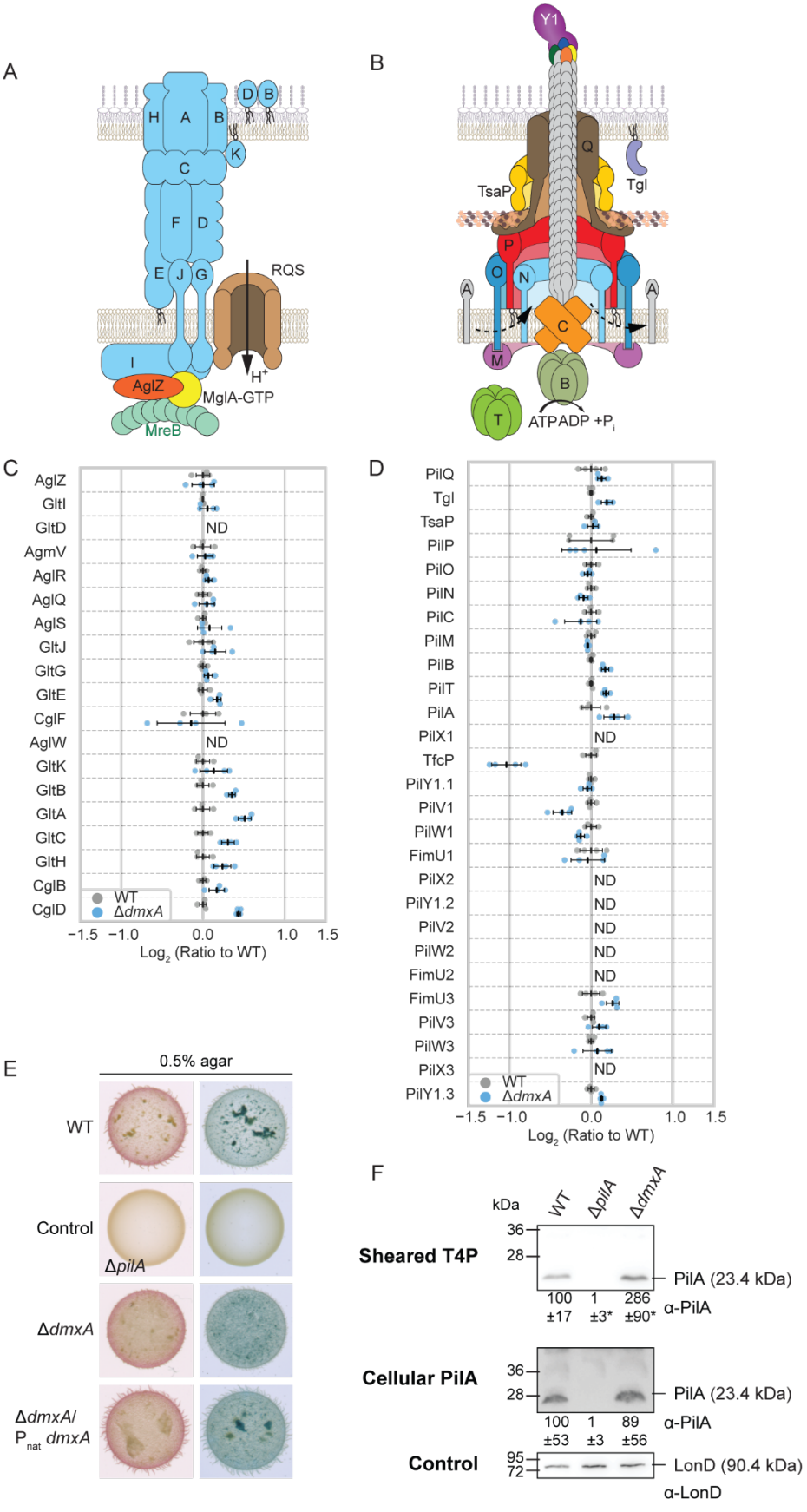

Figure S1. Proteome and phenotypic characterization of the Δ*dmxA* mutant. (A) Architectural model of the gliding motility machine of *M. xanthus.* Proteins labeled with single letters in blue or brown have the Glt or Agl prefix, respectively (Jakobczak *et al.*, 2015, Luciano *et al.*, 2011, Mignot *et al.*, 2007, Nan *et al.*, 2013, Nan *et al.*, 2010, Wartel *et al.*, 2013, Treuner-Lange *et al.*, 2015, Islam *et al.*, 2023). The AglR/-Q/-S complex harnesses proton-motive force to power gliding motility (Nan *et al.*, 2011, Sun *et al.*, 2011). (B) Architectural model of the T4aPM of *M. xanthus* (Chang *et al.*, 2016). Proteins labeled with single letters have the Pil prefix. The pilus fiber is formed by PilA subunits and a priming complex, composed of PilY1 and four minor pilins (blue: PilX, orange: PilV, green: PilW, yellow: FimU) that remains at the tip of the extended T4aP (Chang *et al.*, 2016, Treuner-Lange *et al.*, 2020). Tgl is an OM lipoprotein that is required for PilQ secretin assembly (Nudleman *et al.*, 2006, Friedrich *et al.*, 2014, Herfurth *et al.*, 2023). The ATPases PilB/-T interact with the base of the T4aPM in a mutually exclusive manner to stimulate extension or retraction of the pilus, respectively (Bischof *et al.*, 2016, Chang *et al.*, 2016, Takhar *et al.*, 2013). Bent arrows indicate incorporation of and removal of PilA subunits from the pilus base during extension and retraction, respectively. In A and B, lipoproteins are indicated by wavy black lines. (C-D) Log_2 fold-change of the accumulation of proteins of the (C) Glt/Agl complex for gliding or (D) T4PM in the Δ*dmxA* strain and WT cells compared to the mean of WT is shown. ND, not detected. Data points represent data from four biological replicates. Error bars, mean ± standard deviation (SD) based on these four replicates. (E) Determination of EPS synthesis. Cell suspensions of strains of the indicated genotypes were spotted on 0.5% agar supplemented with 0.5% CTT and Congo red or Trypan blue and incubated for 24 h. Δ*pilA* does not accumulate EPS (Black *et al.*, 2006) and was used as negative control. (F) T4P shear-off assay. Immunoblot detection of PilA in sheared T4P (top) and in total cell extract (bottom). Protein was isolated from the same number of cells from the indicated strains grown on 1% CTT 1.5% agar plates. Protein from the same number of cells was loaded per lane. The blot for cellular PilA was stripped and then probed with α-LonD as a loading control. Calculated molecular weights of proteins are indicated. Numbers indicate the average level of PilA from three biological replicates normalized to the loading control and relative to WT (100%). * $p<0.05$, student's t-test compared to WT.

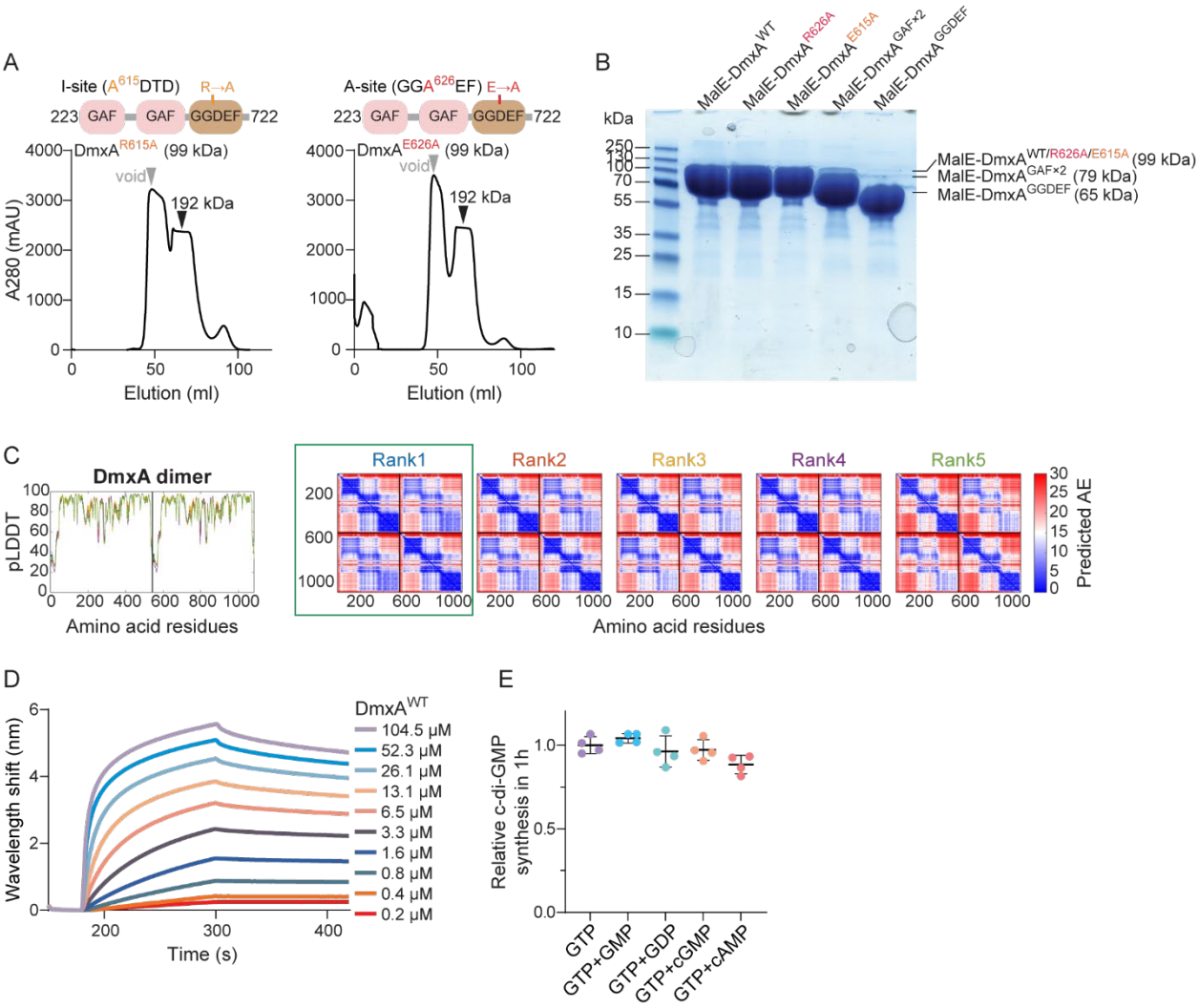

Figure S2. *In silico* and *in vitro* analysis of the DmxA variants. (A) SEC of DmxA^{WT} variants. Domain architectures of truncated DmxA variants are shown above chromatograms. Gray arrows indicate the void volume and black arrows the elution volume with the corresponding calculated molecular weight. (B) Purification of DmxA^{WT} variants. Purified MalE-tagged DmxA variants were separated by SDS-PAGE and stained with Coomassie blue. Calculated molecular weights of proteins are indicated. Molecular size markers are indicated on the left. (C) pLDDT and pAE plots for five models of the DmxA dimer structure in Fig. 2C predicted by AlphaFold. The model marked by a green box was used for further analysis. (D) Bio-Layer Interferometric analysis of the binding kinetics of DmxA^{WT} to c-di-GMP. Streptavidin-coated sensors were loaded with 500 nM biotinylated c-di-GMP and probed with different concentrations of DmxA^{WT}. The interaction kinetics were followed by monitoring the wavelength shifts resulting from changes in the optical thickness of the sensor surface during association or dissociation of the analyte. (E) *In vitro* DGC assay of DmxA^{WT} in the presence of different nucleotides. The relative amount of c-di-GMP synthesized after 1 h was determined as in Fig. 2D. Measurements of four technical replicates are plotted relative to the corresponding mean. Error bars indicate mean ± SD.

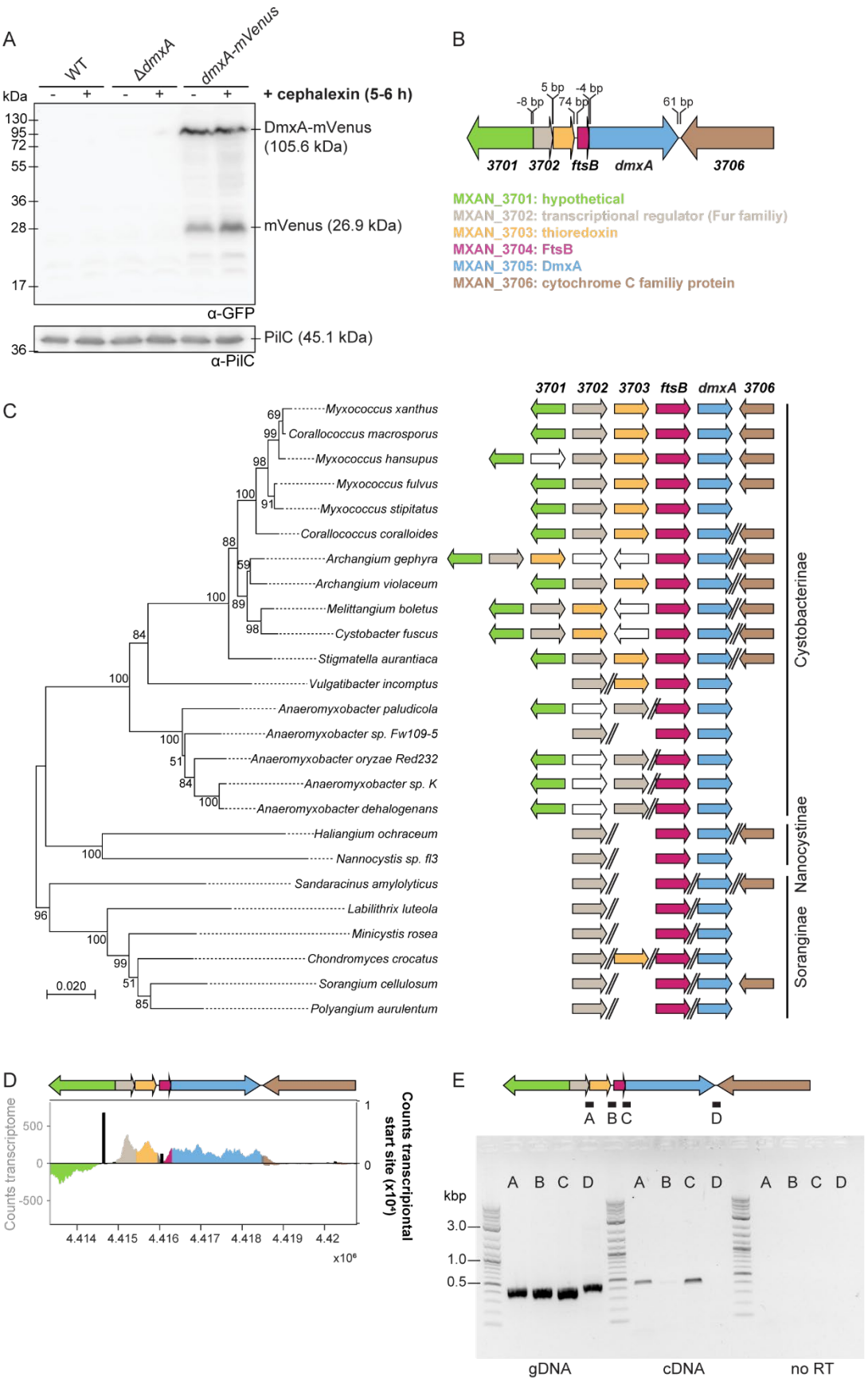

Figure S3. Analysis of the *dmxA* locus. (A) Immunoblot detection of DmxA-mVenus. Protein from the same number of cells from exponentially growing suspension cultures treated with or without cephalexin for 5 h was loaded per lane. The same blot was stripped before applying a new antibody. PilC served as a loading control. Calculated molecular weights of proteins are indicated. (B) Genetic neighborhood

of *dmxA*. Genes are drawn to scale and *MXAN* numbers or gene names are indicated. Putative protein function is indicated. (C) Conservation of *dmxA* and its genetic neighborhood in other Myxococcales (Table S1). Double slashes indicate no close proximity between the genes. (D) RNA-seq and Cappable-seq as base-by-base alignment coverage for total RNA isolated from cells growing in 1% CTT broth (Kuzmich *et al.*, 2021). Positive and negative values indicate reads mapped to the forward and reverse strand, respectively. Reads assigned to a gene are colored according to the gene color code in A; intergenic regions are in gray. Cappable-seq coverage is shown as black bars. (E) Operon mapping of the *ftsB-dmxA* locus. Upper panel, genetic organization of *ftsB-dmxA* locus as in B. Letters and black lines below the genes indicate the fragments amplified by PCR (~400-500 bp). Bottom panel, the PCR products amplified using genomic DNA, cDNA, and an enzyme-free reverse transcription reaction (no RT) as templates were separated on a 1% agarose gel. Letters above the individual lanes correspond to the letters of the primer combinations depicted above. Molecular size markers in kilo base-pairs are shown on the left.

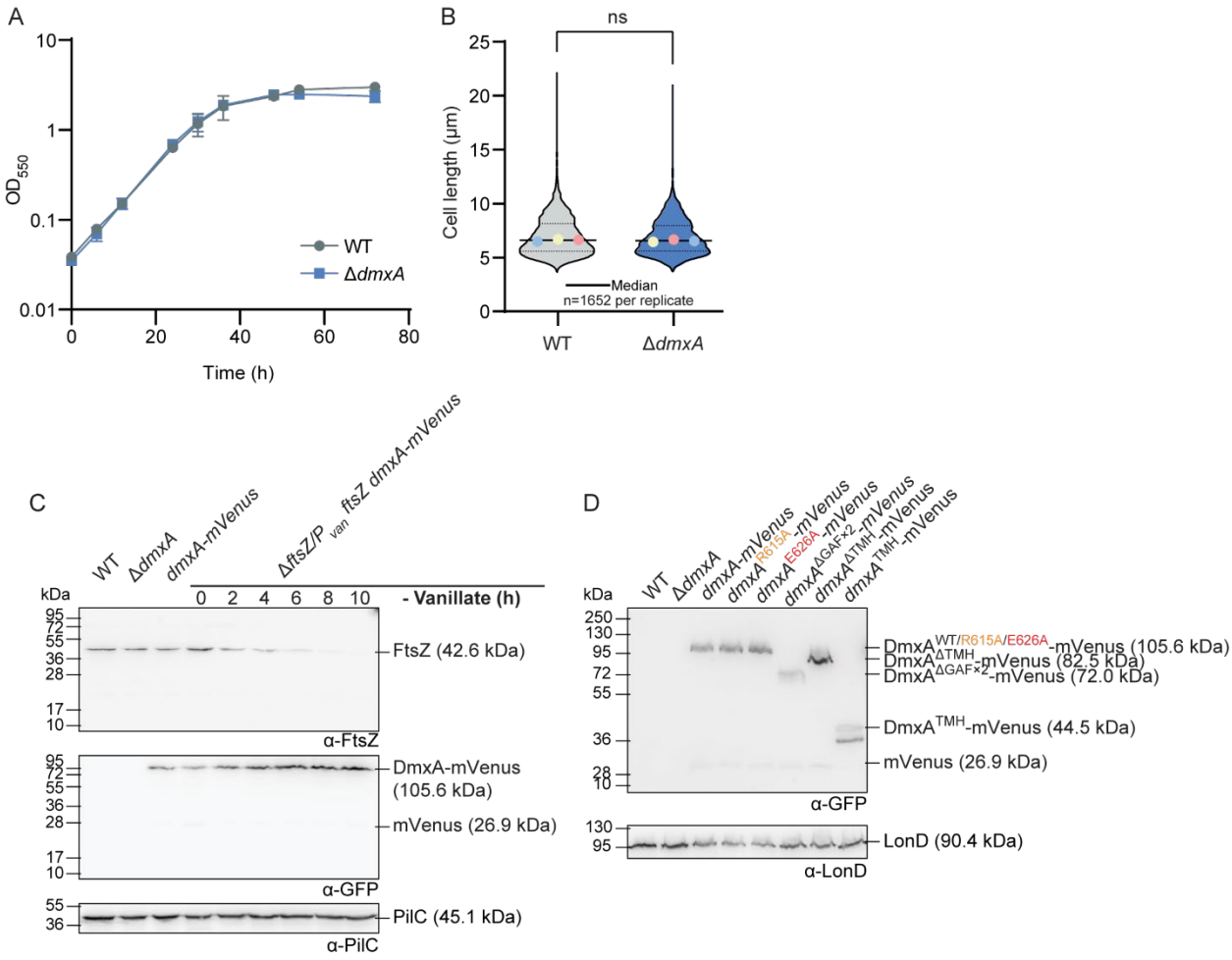

Figure S4. DmxA-mVenus localization but not accumulation depends on the divisome. (A) Growth curve. Exponentially growing cells were diluted to an optical density (OD) at 550 nm (OD_{550}) of 0.04 and growth was followed over time. Growth curves were generated from three biological replicates. (B) Cell length determination. The cell length distribution of three biological replicates is shown in a violin plot. Each violin indicates the probability density of the data at different cell length values. Single points represent the median of the three replicates. Median values is represented by a continuous black line. Dashed lines indicate 25th and 75th percentiles. Samples were compared using a Mann-Whitney test; ns, not significant. (C) Immunoblot detection of FtsZ and DmxA-mVenus. Protein from the same number of cells from exponentially growing suspension cultures was loaded per lane. For the depletion of FtsZ, cells were exponentially grown in suspension culture in the presence of 10 µM vanillate for ~8 generations before the start of the experiment. Then, cells were washed and subsequently incubated for 10 h in 1% CTT broth without vanillate. The same blot was stripped before applying a new antibody. LonD served as a loading control. Calculated molecular weights of proteins are indicated. (D) Immunoblot detection of DmxA-mVenus variants. Protein from the same number of cells from

exponentially growing suspension cultures was loaded per lane. The same blot was stripped before applying a new antibody. LonD served as a loading control. Calculated molecular weights of proteins are indicated.

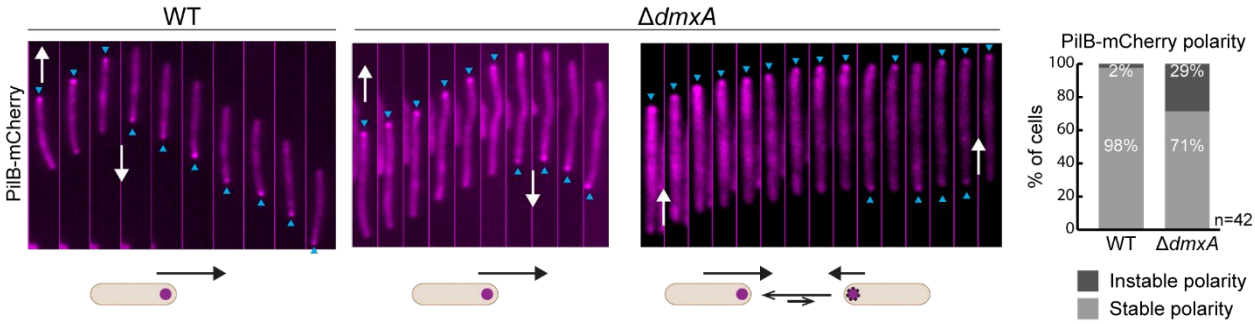

Figure S5. DmxA is important for the correct polar and dynamic localization of PilB. Left, Localization of PilB-mCherry in WT and Δ*dmxA.* Cells were imaged by time-lapse epifluorescence microscopy every 30 s. Right, frequency of stable and instable PilB-mCherry polarity in WT and ΔdmxA.

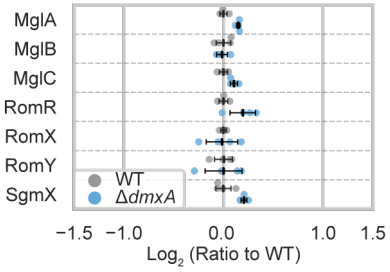

Figure S6. The Δ*dmxA* mutant accumulates WT-levels of proteins of the polarity module. Log_2 fold-change of the accumulation of proteins of the polarity module in the Δ*dmxA* strain and WT cells compared to the mean of WT is shown. Data points represent four biological replicates. Error bars, mean ± standard deviation (SD) in these replicates.

Supplementary Experimental Procedures

Plasmid construction. All oligonucleotides used are listed in Table S3. All constructed plasmids were verified by DNA sequencing.

pMAT74 (for in-frame deletion of *ftsZ*): up- and downstream fragments were amplified using genomic DNA from *M. xanthus* DK1622 as DNA template and the primer pairs ftsZ-up EcoRI/ftsZ-overlapping reverse and ftsZ-overlapping forward/ftsZ-down HindIII, respectively. Subsequently, the up- and downstream fragments were used as a template for an overlapping PCR with the primer pair ftsZ-up EcoRI/ftsZ-down HindIII to generate the AD fragment. The AD fragment was digested with EcoRI and HindIII, cloned in pBJ114 and sequenced.

pMAT86 (plasmid for expression of *ftsZ* from the *18::19* site under the control of the vanillate promoter): the *ftsZ* fragment was amplified using genomic DNA from *M. xanthus* DK1622 as DNA template and the primer pair ftsZ-start NdeI/ftsZ-stop KpnI. The fragment was digested with NdeI and KpnI, cloned into pMR3691 and sequenced.

pMEM23 (plasmid for replacement of *pilB* with *pilB-mCherry* in the native site): the *pilB-mCherry* fragment was amplified using pAP12 (Potapova *et al.*, 2020) as a DNA template and the primer primer pairs pilB-mCA-EcoRI/pilB-mc-B-overlay. The downstream fragment of *pilB* was amplified using genomic DNA from *M. xanthus* DK1622 and the primer pair pilB-C-overlay/pilB-D-HindIII. To generate the full length insert, an overlapping PCR using the two fragments as DNA templates and the primer pair pilB-mCA-EcoRI/pilB-D-HindIII was performed. The fragment was digested with EcoRI and HindIII, cloned into pBJ114 and sequenced.

pMEM33 (plasmid for replacement of *pilT* with *mCherry-pilT* in the native site): the fragment was amplified using pAP87 (Potapova *et al.*, 2020) as a DNA template and the primer primer pair PilT fw EcoRI/PilT rev HindIII. The fragment was digested with EcoRI and HindIII, cloned into pBJ114 and sequenced.

pMH52 (plasmid containing a *M. xanthus* codon optimized *miniTurboID-FLAG*) The miniTurboID sequence (Branon *et al.*, 2018) was codon optimized for *M. xanthus*, synthesized with a N-terminal GGGS-linker and an C-terminal FLAG-tag and cloned into the pEX-k168.

pMH97 (plasmid for expression of *sfGFP-miniTurboID-FLAG* from the *18::19* site under the control of the vanillate promoter): the *sfGFP* and *miniTurboID-FLAG* fragments were amplified with the primer pairs sfGFP_fwd_NdeI/sfGFP_rev_OV from pMAT321 (Treuner-Lange *et al.*, 2020) and TurboID_fwd_OV/TurboID_rev_EcoRI from pMH52. Next, and overlapping PCR was performed using the previous PCR products and the primer pair sfGFP_fwd_NdeI/TurboID_rev_EcoRI. The product was digested with NdeI and EcoRI, cloned into pMR3690 and sequenced.

pMH098 (plasmid for replacement of *ftsK* with *ftsK-miniTurboID-FLAG* in the native site): up- and downstream fragments were amplified using genomic DNA from *M. xanthus* DK1622 as DNA template and the primers FtsK_A_BamHI/FtsK_B_TID_OV and FtsK_C_TID_OV/FtsK_D_HindIII, respectively. The *miniTurboID-FLAG* fragment was amplified using pMH52 and the primer pair TID_fwd_FtsK_OV/TID_rev_FtsK_OV. To generate the full length insert, an overlapping PCR using the three fragments as DNA templates and the primer pair FtsK_A_BamHI/FtsK_D_HindIII was performed. The fragment was digested with BamHI and HindIII, cloned into pBJ114 and sequenced.

pMH110 (plasmid for expression of *ftsK-miniTurboID-FLAG* from the *attB* site under the control of the *pilA* promoter): *ftsK* was amplified using genomic DNA from *M. xanthus* DK1622 as DNA template and the primer pair FtsK_fwd_XbaI_2/FtsK_B_TID_OV 2. The *miniTurboID-FLAG* insert was amplified from pMH98 using the primer pair TID_fwd_FtsK_OV/Flag_rev HindIII. To

generate the full length insert, an overlapping PCR using the two fragments as DNA templates and the primer pair FtsK_fwd_XbaI_2/Flag_rev HindIII was performed. The fragment was digested with XbaI and HindIII, cloned into pSW105 and sequenced.

pMH113 (plasmid for expression of *malE-dmxA*$^{223\text{-}722}$): the *dmxA*$^{223\text{-}722}$ insert was amplified using genomic DNA from *M. xanthus* DK1622 as DNA template and the primer pair MalE-fwd_NotI/DmxA_Rev_HindIII. The fragment was digested with HindIII and NotI, cloned into pMAL-c6t and sequenced.

pMH114 (plasmid for expression of *malE-dmxA*$^{223\text{-}547}$): the *dmxA*$^{223\text{-}547}$ insert was amplified using genomic DNA from *M. xanthus* DK1622 as DNA template and the primer pair MalE-fwd_NotI/DmxA_GAF2_rev_HindIII. The fragment was digested with HindIII and NotI, cloned into pMAL-c6t and sequenced.

pMH115 (plasmid for expression of *malE-dmxA*$^{546\text{-}722}$): the *dmxA*$^{546\text{-}722}$ insert was amplified using genomic DNA from *M. xanthus* DK1622 as DNA template and the primer pair MalE-fwd_NotI/ DmxA_GGDEFonly_Fwd_NotI. The fragment was digested with HindIII and NotI, cloned into pMAL-c6t and sequenced.

pMH116 (plasmid for expression of *malE-dmxA*$^{223\text{-}722,\ R615A}$): the *dmxA*$^{223\text{-}722,\ R615A}$ insert was amplified using pMP082 as DNA template and the primer pair MalE-fwd_NotI/DmxA_Rev_HindIII. The fragment was digested with HindIII and NotI, cloned into pMAL-c6t and sequenced.

pMH117 (plasmid for expression of *malE-dmxA*$^{223\text{-}722,\ E626A}$): the *dmxA*$^{223\text{-}722,\ E626A}$ insert was amplified using pTP139 as DNA template and the primer pair MalE-fwd_NotI/DmxA_Rev_HindIII. The fragment was digested with HindIII and NotI, cloned into pMAL-c6t and sequenced.

pMH123 (plasmid for expression of codon optimized cdGreen2 biosensor and mScarlet from the *attB* site under the control of the *pilA* promoter): the codon optimized cdGreen2 biosensor and mScarlet full-length insert was amplified using pAKS1160 (Kaczmarczyk *et al.*, 2022) as DNA template and the primer pair cdG-Sensor_fwd_XbaI/cdG-Sensor_rev_HindIII. The fragment was digested with XbaI and HindIII, cloned into pSW105 and sequenced.

pTP139 (plasmid for expression of His_6-*dmxA*$^{223\text{-}722,\ E626A}$): the *dmxA*$^{223\text{-}722,\ E626A}$ insert was amplified using pTP137 (Skotnicka *et al.*, 2015) as DNA template and the primer pairs 3705 GAF1 forw NdeI/3705 E626A (-) and 3705 E626A (+)/3705 rev BamHI. To generate the full length insert, an overlapping PCR using the two fragments as DNA templates and the primer pair 3705 GAF1 forw NdeI/3705 rev BamHI was performed. The fragment was digested with NdeI and BamHI, cloned into pET28a(+) (Novagen) and sequenced.

pMP072 (for in-frame deletion of *dmxA*): up- and downstream fragments were amplified from genomic DNA using the primer pairs 3705_A/3705_B and 3705_C/3705_D, respectively. Subsequently, the up- and downstream fragments were used as a template for an overlapping PCR with the primer pair 3705_A/3705_D to generate the AD fragment. The AD fragment was digested with XbaI and KpnI, cloned in pBJ114 and sequenced.

pMP082 (plasmid for expression of His_6-*dmxA*$^{223\text{-}722,\ R615A}$): the *dmxA*$^{223\text{-}722,\ R615A}$ insert was amplified using pTP137 (Skotnicka *et al.*, 2015) as DNA template and the primer pairs 3705 GAF1 forw NdeI/3705 R615A (-) and 3705 R615A (+)/3705 rev BamHI. To generate the full length insert, an overlapping PCR using the two fragments as DNA templates and the primer pair 3705 GAF1 forw NdeI/3705 rev BamHI was performed. The fragment was digested with NdeI and BamHI, cloned into pET28a(+) (Novagen) and sequenced.

pMP092 (plasmid for expression of *dmxA-mVenus* under control of P_{nat} from the *attB* site): the P_{nat} *dmxA* fragment was amplified from gDNA using the primer pair 3704 prmt forw +XbaI/3705_rev no stop 1. The mVenus fragment was amplified using pLC20 (Szadkowski *et*

al., 2019) as DNA template and the primer pair 3705_mVenus fw/mVenus_Kpn rev. To generate the full length insert, an overlapping PCR using the two fragments as DNA templates and the primer pair 3704 prmt forw +XbaI/mVenus_Kpn rev was performed. The fragment was digested with KpnI and XbaI, cloned into pSWU30 and sequenced.

pMP093 (plasmid for replacement of *dmxA* with *dmxA-mVenus* in the native site): up- and downstream fragments were amplified using genomic DNA from *M. xanthus* DK1622 as DNA template and the primer pairs 3705_native forw/3705_rev no stop 1 and 3705_native middle fw/3705_native rev, respectively. The mVenus fragment was amplified using pMP092 as DNA template and the primer pair 3705_mVenus fw/3705_native middle rev. To generate the full length insert, an overlapping PCR using the three fragments as DNA templates and the primer pair 3705_native forw/3705_native rev was performed. The fragment was digested with KpnI and XbaI, cloned into pBJ114 and sequenced.

pMP095 (plasmid for replacement of *dmxA* with *dmxA*^{R615A}*-mVenus* in the native site): up- and downstream fragments were amplified using pMP093 as DNA template and the primer pairs 3705_native forw/3705 R615A (-) and 3705 R615A (+)/3705_native rev, respectively. To generate the full length insert, an overlapping PCR using the two fragments as DNA templates and the primer pair 3705_native forw/3705_native rev was performed. The fragment was digested with KpnI and XbaI, cloned into pBJ114 and sequenced.

pMP164 (plasmid for expression of *dmxA-mVenus* from the native site in a Δ*dmxA* strain): up- and downstream fragments were amplified using genomic DNA from *M. xanthus* DK1622 as a template and the primers 3705_A/3705_rev no stop 1 and 3705_native middle fw/3705_D respectively. mVenus was amplified from pMP093 as a template and the primers 3705_mVenus fw/3705_native middle rev. To generate the AD insert, an overlapping PCR using the three fragments as a DNA template and the primer pair 3705_A/3705_D was performed. The AD fragment was digested with KpnI and XbaI, cloned into pBJ114 and sequenced.

pMP165 (plasmid for expression of *dmxA*^{E626A}*-mVenus* from the native site in a Δ*dmxA* strain): the mutation E626A was introduced into the plasmid pMP164 by using the primer pairs 3705_A/3705 E626A (-) and 3705 E626A (+)/3705_D and pMP164 as a DNA template for the PCR. To generate the AD insert, an overlapping PCR using both fragments as a DNA template and the primer pair 3705_A/3705_D was performed. The AD fragment was digested with KpnI and XbaI, cloned into pBJ114 and sequenced.

pMP172 (plasmid for expression of P_{pilA} *dmxA-miniTurboID-FLAG* from the *attB* site): the *dmxA* fragment was amplified with the primer pair 3705_PpilA forw/3705_rev no stop 1 from pMP092, and the *miniTurboID-FLAG* fragment was amplified with the primer pair 3705_miniTurboID fw/Flag_rev HindIII from pMH52. Next, and overlapping PCR was performed using the previous PCR products and the primer pair 3705_PpilA forw/Flag_rev HindIII. The product was digested with XbaI and HindIII, cloned into pSW105 and sequenced.

pMP175 (for generation of an in-frame deletion of the GAF domains of native *dmxA*): up- and downstream fragments were amplified from pMP164 using the primer pairs 3705_PpilA forw/3705_B (GAFx1) and 3705_C (GAFx2)/3705_D (GAFx2), respectively. Subsequently, the up- and downstream fragments were used as a template for an overlapping PCR with the primer pair 3705_PpilA forw/3705_D (GAFx2) to generate the AD fragment. The AD fragment was digested with XbaI and KpnI, cloned in pBJ114 and sequenced.

pMP179 (for generation of an in-frame deletion of the TMH domains of native *dmxA*): up- and downstream fragments were amplified from pMP164 using the primer pairs 3705_A/3705_B3 (TMD) and 3705_C3 (TMD)/3705_D (TMD)2, respectively. Subsequently, the up- and downstream fragments were used as a template for an overlapping PCR with the primer pair 3705_A/3705_D (TMD)2 to generate the AD fragment. The AD fragment was digested with KpnI and XbaI, cloned in pBJ114 and sequenced.

pMP182 (plasmid for expression of *dmxA*$^{TMH\ (1\text{-}167)}$*-mVenus* from the native site in a Δ*dmxA* strain): up- and downstream fragments were amplified using pMP164 as a DNA template and the primers 3705_A/3705_TMH rev and 3705_mVenus fw2/3705_D respectively. To generate the AD insert, an overlapping PCR using the two fragments as a DNA template and the primer pair 3705_A/3705_D was performed. The AD fragment was digested with KpnI and XbaI, cloned into pBJ114 and sequenced.

Table S1. Fully sequenced myxobacterial genomes used for the 16S rRNA tree

Species and strain name
Anaeromyxobacter dehalogenans 2CP-C
Anaeromyxobacter sp. Fw109-5
Anaeromyxobacter sp. K
Anaeromyxobacter oryzae Red232
Anaeromyxobacter paludicola Red630
Archangium gephyra DSM 2261
Archangium violaceum SDU34
Chondromyces crocatus Cm c5
Corallococcus macrosporus DSM 14697
Corallococcus coralloides DSM 2259
Cystobacter fuscus DSM 52655
Haliangium ochraceum DSM 14365
Labilithrix luteola DSM 27648
Melittangium boletus DSM 14713
Minicystis rosea DSM 24000
Myxococcus fulvus 124B02
Myxococcus hansupus (*Myxococcus* sp. mixupus)
Myxococcus stipitatus DSM 14675
Myxococcus xanthus DK1622
Nannocystis sp. fl3
Polyangium aurulentum SDU3-1
Sandaracinus amylolyticus DSM 53668
Sorangium cellulosum So ce 56
Stigmatella aurantiaca DW4/3-1
Vulgatibacter incomptus DSM 27710

Table S2. Proteins that are significantly enriched in DmxA-miniTurboID and FtsK-miniTurboID proximity labeling

Locus	Annotation	Description
MXAN_0755	Pkn9	Serine/threonine protein kinase
MXAN_1350	-	Histidine kinase
MXAN_1460	FtsK	FtsK/SpoIIIE family protein
MXAN_2680	PktA12	Serine/threonine protein kinase
MXAN_2710	-	Putative lipoprotein
MXAN_3106	KilC	Secretin-family (Tad pilus)
MXAN_3108	KilD	FHA domain/TPR protein (Tad pilus)
MXAN_3550	-	Chromosome segregation protein SMC
MXAN_3705	DmxA	GAF domain/GGDEF domain protein
MXAN_4024	-	Uncharacterized protein
MXAN_4591	Pkn1	Serine/threonine-protein kinase Pkn1
MXAN_4700	PskA7	Serine/threonine protein kinase
MXAN_4735	-	Putative membrane protein
MXAN_5591	-	FHA domain/tetratricopeptide repeat protein
MXAN_5723	-	MJ0042 family finger-like domain protein
MXAN_6183	PktB5	Serine/threonine protein kinase
MXAN_6420	Pkn2	Serine/threonine protein kinase Pkn2
MXAN_6605	CsdK2	PilZ-DnaK family protein

Table S3. Oligonucleotides used in this work[1]

Primer name	Sequence 5‘-3‘	Brief description
3702_map_fwd2	TGACCACCTGGTCTGTACGC	Primers used for operon mapping.
3703_map_rev2	GGGGGCCATAGTCCTTCTGG	
3704_map_rev2	TCATTGCGCAGGGCCTCATT	
3703_map_fwd2	CGCGAACCAGGCGATGATTG	
3704_map_fwd2	AGGCCCTGCGCAATGAGATT	
3705_map_rev2	AATGGCCACCACGACGAAGG	
3705_map_fwd2	GCCGCTGAGGATCACCATGT	
3706_map_rev2	CTCTGGGGCATCGGCCTG	
ftsZ-up EcoRI	GCGCGAATTCGGTGGACACGGATGGCGACG	For deletion of *ftsZ*
ftsZ-overlapping reverse	CGTCTGGCCCTTGTTCTGATCGAACTGGTC	
ftsZ-overlapping forward	CAGAACAAGGGCCAGACGGAACTGCCGTAA	
ftsZ-down HindIII	GCGCAAGCTTTTGCGCAGCTGCCAGCCGATG	
ftsZ-start NdeI	GGAATTCCATATGGACCAGTTCGATCAGAAC	For expression of *ftsZ* under the P_{van} promoter
ftsZ-stop KpnI	GCGCGGTACCTTACGGCAGTTCCGTCTGGC	
sfGFP_fwd_NdeI	GCGCCATATGAGCAAAGGAGAAGAACT	For expression of *sfGFP-miniTurboID-FLAG* under the P_{van} promoter
sfGFP_rev_OV	CGCCCCCGCCTTTGTAGAGCTCATCCATGC	
TurboID_fwd_OV	GCTCTACAAAGGCGGGGGCGGGAGCATGAT	
TurboID_rev_EcoRI	GCGCGAATTCTCACTTGTCGTCGTCGTC	
FtsK_A_BamHI	GCGCGGATCCACGAGGACGACATGCTCGACGC	For replacement of *ftsK* with *ftsK-miniTurboID-FLAG*
FtsK_B_TID_OV	CGCCCCCGCCCATGGCCCCGGCGCCGGGCA	
TID_fwd_FtsK_OV	CGGGGCCATGGGCGGGGGCGGGAGCATGAT	
TID_rev_FtsK_OV	CACGTGGGCCTCACTTGTCGTCGTCGTCCT	
FtsK_C_TID_OV	CGACAAGTGAGGCCCACGTGGCCGCCGTCT	
FtsK_D_HindIII	GCGCAAGCTTCACCTTGAGGGCCACGAAGCCGG	
FtsK_fwd_XbaI_2	GCGCTCTAGACAGCCGAAATGTAGGTTCCCCGTCCTGAGC	For expression of *ftsK-miniTurboID-FLAG* from the *attB* site and the P_{pilA}
FtsK_B_TID_OV 2	CGCCCCCGCCCATGGCCCCGGCGCCGGGCATGTCG	
TID_fwd_FtsK_OV	CGGGGCCATGGGCGGGGGCGGGAGCATGAT	
Flag_rev HindIII	GCGCAAGCTTTCACTTGTCGTCGTCGTC	
MalE-fwd_NotI	GCGCGCGGCCGCGAGATCGAAGGCGCCGTGC	For expression and purification of MalE-tagged DmxA protein variants
DmxA_Rev_HindIII	GCGCAAGCTTTCAGGACGCGTTCGCCGCCT	
DmxA_GAF2_rev_HindIII	CTGAGGATCCTCACGTGGTGGCCATGCGCTCCA	
DmxA_GGDEFonly_Fwd_NotI	CTGAGGATCCTCACGTGGTGGCCATGCGCTCCA	
3705 GAF1 forw NdeI	ATCGCATATGGAGATCGAAGGCGCCGTGC	For expression and purification of His-tagged DmxA protein variants
3705 E626A (-)	GACGAACTCCGCGCCGCCGTA	
3705 E626A (+)	TACGGCGGCGCGGAGTTCGTC	
3705 R615A (-)	GTCCGTATCGGCCGCCATCGTC	
3705 R615A (+)	GACGATGGCGGCCGATACGGAC	
3705 rev BamHI	ATCGGGATCCTCAGGACGCGTTCGCCGC	
cdG-Sensor_fwd_XbaI	ATGCTCTAGAATGAATTCGGAACCGCCGCC	For expression of cdGreen and mScarlet from the *attB* site and the P_{pilA}
cdG-Sensor_rev_HindIII	ATTCAAGCTTTCACTTGTACAGTTCATCCATACCACCG	
3705_A	ATCGGGTACCAAGGTGACGTCGCACAAGAT	

3705_B	CTTCAGCTGAGACGGAAACTCGGGAAG	For deletion of *dmxA*
3705_C	TTTCCGTCTCAGCTGAAGGCGGCGAAC	
3705_D	ATCGTCTAGACATCACCGGGTGGACCGTCA	
3704 prmt forw +XbaI	ATCGTCTAGATTCCTCAACGCGCTGGCGCTG	For P_{nat} *dmxA-mVenus*
3705_rev no stop 1	GCCGCCGCCGGACGCGTTCGCCGCCTTCAG	
3705_mVenus fw	AACGCGTCCGGCGGCGGCGGCTCCATGGTGAGCAAGGG	
mVenus_Kpn rev	CGCGCCGGGTACCTTACTTGTACAGCTCGTCCA	
3705_native forw	ATATGGTACCTCCGCTACGGGGCGCCGCTG	For replacement of *dmxA* with *dmxA-mVenus*
3705_native middle rev	CCCGGCTGCATCAAGGACTTACTTGTACAGCTCGTC	
3705_native middle fw	GACGAGCTGTACAAGTAAGTCCTTGATGCAGCCGGG	
3705_native rev	CGCGTCTAGACATCCCCGAGTCGGCCATCG	
3705_PpilA forw	CGCGTCTAGAATGACGTCGCTTCCCGAGTT	For P_{pilA} *dmxA-miniTurboID-FLAG*
3705_miniTurboID fw	AACGCGTCCGGCGGCGGCGGCTCCATGATCCCGCTCCTGA	
3705_B (GAFx1)	CGCGCGCAGCTTCACCGAGGCCACCAG	For in-frame deletion of the GAF domains of native *dmxA*
3705_C (GAFx2)	TCGGTGAAGCTGCGCGCGCAGCTCTAC	
3705_D (GAFx2)	ATCGGGTACCGGACGCGTTCGCCGCCTTCA	
3705_B3 (TMD)	TTCGATCTCCGTCATGGGGACTCCAGG	For native site complementation of Δ*dmxA* with $dmxA^{\Delta TMH}$-*mVenus*
3705_C3 (TMD)	CCCATGACGGAGATCGAAGGCGCCGTG	
3705_D (TMD)2	ATCGTCTAGACAGCGGCGCCCCGTAGCGGA	
3705_TMH rev	GGAGCCGCCGCCGCCCAGCACCAGGTGGTAGAGGC	For native site complementation of Δ*dmxA* with $dmxA^{TMH\ (1\text{-}167)}$-*mVenus*
3705_mVenus fw2	CTGGTGCTGGGCGGCGGCGGCTCCATGGTGAGCAAGGG	
pilB-mCA-EcoRI	GCGCGAATTCGATCACCTCGCGTTTGAAG	For replacement of *pilB* with *pilB-mCherry*
pilB-mCB-overlay	GAGGAAGGTTGACTACTTGTACAGCTCGTCCATG	
pilB-mCC+ overlay	GACGAGCTGTACAAGTAGTCAACCTTCCTCCCAC	
pilB-D-HindIII	GCGCAAGCTTGGTCTGCATGCCGAACTTCG	
PilT fw EcoRI	CGCGAATTCGCTCCTTCCTCC	For replacement of *pilT* with *mCherry-pilT*
PilT rev HindIII	GCGCAAGCTTCTAACGACCAC	

[1] Underlined sequences indicate restriction sites.

Supplementary References

Bischof, L.F., Friedrich, C., Harms, A., Søgaard-Andersen, L., and van der Does, C. (2016) The type IV pilus assembly ATPase PilB of *Myxococcus xanthus* interacts with the inner membrane platform protein PilC and the nucleotide-binding protein PilM. *J Biol Chem* **291**: 6946-57.

Black, W.P., Xu, Q., and Yang, Z. (2006) Type IV pili function upstream of the Dif chemotaxis pathway in *Myxococcus xanthus* EPS regulation. *Mol Microbiol* **61**: 447-56.

Branon, T.C., Bosch, J.A., Sanchez, A.D., Udeshi, N.D., Svinkina, T., Carr, S.A., Feldman, J.L., Perrimon, N., and Ting, A.Y. (2018) Efficient proximity labeling in living cells and organisms with TurboID. *Nat Biotechnol* **36**: 880-87.

Chang, Y.W., Rettberg, L.A., Treuner-Lange, A., Iwasa, J., Søgaard-Andersen, L., and Jensen, G.J. (2016) Architecture of the type IVa pilus machine. *Science* **351**: aad2001.

Friedrich, C., Bulyha, I., and Søgaard-Andersen, L. (2014) Outside-in assembly pathway of the type IV pilus system in *Myxococcus xanthus*. *J Bacteriol* **196**: 378-90.

Herfurth, M., Pérez-Burgos, M., and Søgaard-Andersen, L. (2023) The mechanism for polar localization of the type IVa pilus machine in *Myxococcus xanthus*. *mBio*: in press.

Islam, S.T., Jolivet, N.Y., Cuzin, C., Belgrave, A.M., My, L., Fleuchot, B., Faure, L.M., Mahanta, U., Kezzo, A.A., Saidi, F., Sharma, G., Fiche, J.B., Bratton, B.P., Herrou, J., Nollmann, M., Shaevitz, J.W., Durand, E., and Mignot, T. (2023) Unmasking of the von Willebrand A-domain surface adhesin CglB at bacterial focal adhesions mediates myxobacterial gliding motility. *Sci Adv* **9**: eabq0619.

Jakobczak, B., Keilberg, D., Wuichet, K., and Søgaard-Andersen, L. (2015) Contact- and protein transfer-dependent stimulation of assembly of the gliding motility machinery in *Myxococcus xanthus*. *PLoS Genet* **11**: e1005341.

Kaczmarczyk, A., Vliet, S.v., Jakob, R.P., Reinders, A., Klotz, A., Maier, T., and Jenal, U. (2022) A novel biosensor reveals dynamic changes of c-di-GMP in differentiating cells with ultra-high temporal resolution. *bioRxiv*: 2022.10.18.512705.

Kuzmich, S., Blumenkamp, P., Meier, D., Szadkowski, D., Goesmann, A., Becker, A., and Søgaard-Andersen, L. (2021) CRP-like transcriptional regulator MrpC curbs c-di-GMP and 3',3'-cGAMP nucleotide levels during development in *Myxococcus xanthus*. *mBio* **13**: e0004422.

Luciano, J., Agrebi, R., Le Gall, A.V., Wartel, M., Fiegna, F., Ducret, A., Brochier-Armanet, C., and Mignot, T. (2011) Emergence and modular evolution of a novel motility machinery in bacteria. *PLoS Genet* **7**: e1002268.

Mignot, T., Shaevitz, J.W., Hartzell, P.L., and Zusman, D.R. (2007) Evidence that focal adhesion complexes power bacterial gliding motility. *Science* **315**: 853-6.

Nan, B., Bandaria, J.N., Moghtaderi, A., Sun, I.-H., Yildiz, A., and Zusman, D.R. (2013) Flagella stator homologs function as motors for myxobacterial gliding motility by moving in helical trajectories. *Proc Natl Acad Sci U S A* **110**: E1508-13.

Nan, B., Chen, J., Neu, J.C., Berry, R.M., Oster, G., and Zusman, D.R. (2011) Myxobacteria gliding motility requires cytoskeleton rotation powered by proton motive force. *Proc Natl Acad Sci U S A* **108**: 2498-503.

Nan, B., Mauriello, E.M., Sun, I.H., Wong, A., and Zusman, D.R. (2010) A multi-protein complex from *Myxococcus xanthus* required for bacterial gliding motility. *Mol Microbiol* **76**: 1539-54.

Nudleman, E., Wall, D., and Kaiser, D. (2006) Polar assembly of the type IV pilus secretin in *Myxococcus xanthus*. *Mol Microbiol* **60**: 16-29.

Potapova, A., Carreira, L.A.M., and Søgaard-Andersen, L. (2020) The small GTPase MglA together with the TPR domain protein SgmX stimulates type IV pili formation in *M. xanthus*. *Proc Natl Acad Sci U S A* **117**: 23859-68.

Skotnicka, D., Petters, T., Heering, J., Hoppert, M., Kaever, V., and Søgaard-Andersen, L. (2015) c-di-GMP regulates type IV pili-dependent-motility in *Myxococcus xanthus*. *J Bacteriol* **198**: 77-90.

Sun, M., Wartel, M., Cascales, E., Shaevitz, J.W., and Mignot, T. (2011) Motor-driven intracellular transport powers bacterial gliding motility. *Proc Natl Acad Sci U S A* **108**: 7559-64.

Szadkowski, D., Harms, A., Carreira, L.A.M., Wigbers, M., Potapova, A., Wuichet, K., Keilberg, D., Gerland, U., and Søgaard-Andersen, L. (2019) Spatial control of the GTPase MglA by localized RomR-RomX GEF and MglB GAP activities enables *Myxococcus xanthus* motility. *Nat Microbiol* **4**: 1344-55.

Takhar, H.K., Kemp, K., Kim, M., Howell, P.L., and Burrows, L.L. (2013) The platform protein is essential for type IV pilus biogenesis. *J Biol Chem* **288**: 9721-9728.

Treuner-Lange, A., Chang, Y.W., Glatter, T., Herfurth, M., Lindow, S., Chreifi, G., Jensen, G.J., and Søgaard-Andersen, L. (2020) PilY1 and minor pilins form a complex priming the type IVa pilus in *Myxococcus xanthus*. *Nat Commun* **11**: 5054.

Treuner-Lange, A., Macia, E., Guzzo, M., Hot, E., Faure, L.M., Jakobczak, B., Espinosa, L., Alcor, D., Ducret, A., Keilberg, D., Castaing, J.P., Lacas Gervais, S., Franco, M., Søgaard-Andersen, L., and Mignot, T. (2015) The small G-protein MglA connects to the MreB actin cytoskeleton at bacterial focal adhesions. *J Cell Biol* **210**: 243-56.

Wartel, M., Ducret, A., Thutupalli, S., Czerwinski, F., Le Gall, A.V., Mauriello, E.M., Bergam, P., Brun, Y.V., Shaevitz, J., and Mignot, T. (2013) A versatile class of cell surface directional motors gives rise to gliding motility and sporulation in *Myxococcus xanthus*. *PLoS Biol* **11**: e1001728.

8.4 A miniTurboID-based proximity labeling protocol to identify conditional protein interactomes in vivo in *Myxococcus xanthus*

This chapter contains a detailed description of proximity labeling in *M. xanthus.* This part of the thesis is written in a manuscript style and was submitted for publication at the time of submission of this thesis. I contributed to this work by designing, performing and analyzing experiments, preparing the figures and the manuscript.

I performed experiments and analysis in Fig. 1A-C, 2A.

A miniTurboID-based proximity labeling protocol to identify conditional protein interactomes *in vivo* in *Myxococcus xanthus*

Marco Herfurth[1,3,4,*], Franziska Müller[1,3,4,], Lotte Søgaard-Andersen[1] and Timo Glatter[2,3,5,***]**
[1]Department for Ecophysiology, Max-Planck Institute for Terrestrial Microbiology, Marburg, Germany
[2]Facility for Proteomics and Mass Spectrometry, Max-Planck Institute for Terrestrial Microbiology, Marburg, Germany
[3]These authors contributed equally.
[4]Technical contact
[5]Lead contact
*marco.herfurth@mpi-marburg.mpg.de (M.H.)
**franziska.müller@mpi-marburg.mpg.de (F.M.)
***timo.glatter@mpi-marburg.mpg.de (T.G.)

Summary

Protein-protein interactions is foundational for many cellular processes. Such interactions are especially challenging to identify if they are transient or depend on environmental conditions. This protocol details steps to identify stable and transient protein interactomes in the bacterium *Myxococcus xanthus* using biotin ligase mini-TurboID-based proximity labeling. We include instructions for optimizing the expression of control proteins, *in vivo* biotin labeling of bacteria grown on a surface or in suspension culture, enrichment of biotinylated proteins, and sample processing for proteomic analysis.

Highlights

- Optimization of mini-TurboID-based biotin proximity labeling *in vivo*
- Step-by-step protocol from protein design to identification of conditional interactomes
- *In vivo* biotinylation and LC-MS workflow for quantitative identification of biotinylated proteins
- Protocol identifies known and new potentional interaction partners of the small GTPase MglA

Graphical abstract

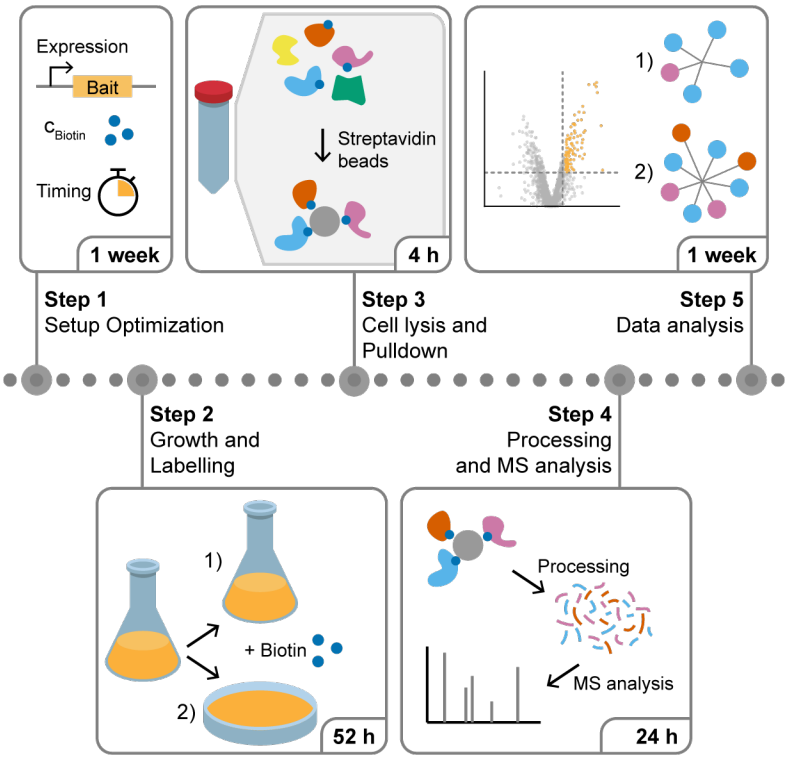

Before you begin

This protocol describes the steps for conducting biotin ligase-based proximity labeling in live *Myxococcus xanthus* cells using mini-TurboID (mTurboID)[1], followed by shotgun proteomics mass spectrometry to identify protein interactomes. In this method, the protein of interest, or bait, is fused to mTurboID, which catalyzes the formation of a highly reactive but short-lived biotinoyl-5'-AMP intermediate from biotin and ATP. This intermediate then diffuses out of the active site of the enzyme and covalently couples biotin to amine groups in Lys residues within a distance of a few nm[2]. Therefore, only proteins that are in close proximity to the tagged bait protein are biotinylated[2]. Subsequently, biotinylated proteins are purified using magnetic Streptavidin affinity beads (Strep beads) and identified using mass spectrometry. A distinct advantage of mTurboID-based proximity labeling is that the highly reactive biotinoyl-5'-AMP intermediate covalently couples biotin to proteins in proximity of the bait, and, therefore, not only allows to identify stable interaction partners but also low-affinity, transiently interacting protein partners.

We describe the general steps for applying mTurboID-based proximity labeling in bacteria by identifying the proximity interaction network of the Ras-like GTPase MglA, which controls the cell polarity of *M. xanthus* cells[3-5]. The rod-shaped *M. xanthus* cells translocates on surfaces with defined leading and lagging cell poles[5]. MglA is the key regulator of motility and localizes to and defines the leading cell pole in its active GTP-bound state[3,5,6]. At this pole, MglA interacts with downstream effector proteins to activate two different motility systems[7-11]. Occasionally, the localization of MglA switches to the opposite pole resulting in an inversion of the direction of cell motility[3-5]. The mechanisms underlying the dynamic polar localization of MglA as well as the downstream effectors of MglA are well-studied and offer a good foundation to establish and benchmark mTurboID-based proximity labeling in *M. xanthus*[3,6,8,11-16]. We recommend to establish, adapt and optimize this protocol to different bacterial systems by using a bait protein with established and verified protein interaction partners, ideally including direct and/or indirect

as well as conditional interactions. Also, using MglA as a test bait allows studying conditional interactomes. Specifically, the two motility systems of *M. xanthus*, type IVa pili (T4aP)-dependent motility and gliding motility rely on surface contact to translocate cells[4]. Furthermore, surface contact was reported to activate proteins that regulate *M. xanthus* polarity[17], suggesting that surface contact is important for the activation and/or regulation of the two motility systems, and that MglA might potentially have different interactomes depending on whether *M. xanthus* cells are grown on a surface or in suspension culture.

To obtain optimal results and reduce the non-specific background, it is important to consider that the mTurboID bait protein (in our case MglA-mTurboID-FLAG) is active and expressed at or close to native levels. Moreover, it is important to include a control protein (here a sfGFP-mTurboID-FLAG fusion) that localizes to the same subcellular compartment as the bait to reduce the non-specific background and increase specificity in the proteomics data. Additionally, the bait and control protein should be tagged with a tag (i.e. FLAG-tag, Myc-Tag, etc.) to be able to assess the expression and stability of the bait and control protein fusions using western blotting.

In *M. xanthus,* the gene encoding the MglA-mTurboID-FLAG is integrated by double homologous recombination at the native site to replace the wild-type allele, offering high strain stability and native expression levels of the bait protein. The control protein is expressed from a plasmid integrated in a single copy by site specific recombination into the genome and under the control of an inducible promotor, allowing the adjustment of the expression level to that of the bait protein.

Preparing strains containing mTurboID fusions

Timing: 2-3 weeks

The main preparation to start proximity labeling is the design and generation of bacterial strains expressing the bait protein fused to mTurboID (MglA-mTurboID-FLAG), as well as a matching control protein fusion (sfGFP-mTurboID-FLAG).

1. Generate appropriate plasmids.
   Note: Standard cloning methods were used to generate plasmids expressing the bait protein fusion and the control protein under control of an inducible promoter. Cloning methods, plasmid backbones and inducible promoters vary strongly between bacteria and have to be chosen accordingly.
2. Transform and verify strains.
   Note: Transformation and verification of strains depend on the organism and the used backbones. We routinely use electroporation as a method for transformation and double homologous recombination to integrate the construct encoding the bait-mTurboID fusion and site specific recombination to integrate the plasmid encoding the control protein.

Key resources table

REAGENT or RESOURCE	SOURCE	IDENTIFIER
Antibodies		
α-FLAG	Rockland	600-401-383
α-LonD	Treuner-Lange *et al.*[18]	N/A
Goat α-rabbit immunoglobulin G peroxidase conjugate	Sigma	A0545-1ML
Bacterial and virus strains		

Myxococcus xanthus DK1622	Kaiser *et al.*[19]	DK1622
M. xanthus mglA::*mglA-mTurboID*-Flag	This study	SA12042
M. xanthus 18-19::Pvan *sfGFP-mTurboID-Flag*	This study	SA12027
Chemicals, peptides, and recombinant proteins		
Biotin	ThermoFisher Scientific	29129
Streptavidin-HRP	Bio-Rad	STAR5B
Vanillate	Sigma Aldrich	H36001
Gentamycinsulfate	Carl Roth	0233.4
Kanamycinsulfate	Carl Roth	T832.4
Ammonium bicarbonate	Sigma-Aldrich	A6141
Sodium dodecyl sulfate	Carl Roth	CN30.3
Sodium deoxycholate	Sigma-Aldrich	D6750
Triton X-100	Carl Roth	3051.2
Tris-(2-carboxyethyl)-phosphine hydrochloride (TCEP)	Sigma-Aldrich	75259
Iodoacetamide	Sigma-Aldrich	I1149
Trypsin - Sequencing Grade Modified	Promega	V5111
Acetonitrile, LC-MS grade	Thermo Fisher Scientific	51101
Trifluoroacetic acid	Thermo Fisher Scientific	85183
Water, LC-MS grade	Thermo Fisher Scientific	51140
Formic acid, LC-MS grade	Thermo Fisher Scientific	85178
Chromabond C18 Spin columns	Macherey-Nagel	730522.25
Acclaim PepMap100 trap column C18 5 µm, 0.5 x 5 mm	Thermo Fisher Scientific	160454
ReproSil-Pur 120 C18-AQ, 2.4 µm	Dr. Maisch	r124.aq.0001
Critical commercial assays		
660nm protein assay	Pierce	22662
G25 desalting columns	Cytiva	28918007
Streptavidin magnetic beads	Pierce	88817
cOmplete™ Protease Inhibitor Cocktail	Roche	11836145001
4–20% Mini-PROTEAN TGX PAGE gel	Bio-Rad	4561093
Restore™ PLUS erstern Blot Stripping Buffer	Thermo scientific	46430
Recombinant DNA		
Mini-TurboID	Brandon *et al.*[1]	N/A
Software and algorithms		
MaxQuant	https://www.maxquant.org/	Version 2.0.3.0 and higher
Perseus	https://maxquant.net/perseus/	Version 1.6.10.43 and higher

Materials and equipment

TPM-buffer

Reagent	Final concentration
Tris-HCl pH 7.6	10 mM
Potassium phosphate pH 7.6	1 mM
$MgSO_4$	8 mM
ddH_2O	

Stable for several months at room temperature (RT).

Alternatives: Other buffers such as PBS are also appropriate for washing cells and can be adjusted to the organism used.

RIPA lysis buffer

Reagent	Final concentration
Tris-HCl pH 7.0	50 mM
NaCl	150 mM
Triton X-100	1% (vol/vol)
Sodium deoxycholate (SDC)	0.5% (wt/vol)
Sodium dodecyl sulfate (SDS)	0.2% (wt/vol)
ddH_2O	

Store at 4°C for up to a year.

CRITICAL: Contact with Triton X-100, SDS and SDC cause skin and eye irradiation. Wear protective gloves/ protective clothing/eye protection/face protection. Do not inhale SDS.
Alternatives: Different lysis buffer formulations may be adjusted to your organism. Adjusting NaCl or detergent concentrations may impact the stringency of the streptavidin enrichment.

4×Laemmli-buffer

Reagent	Final concentration
Tris-HCl pH 6.8	200 mM
Ethylenediaminetetraacetic acid (EDTA)	150 mM
Dithiothreitol (DTT)	400 mM
SDS	8% (wt/vol)
Glycerol	40% (vol/vol)
ddH_2O	

Prepare freshly.DTT degrades over time.

CRITICAL: Contact with SDS and DTT cause skin and eye irradiation. Wear protective gloves/ protective clothing/eye protection/face protection. Do not inhale SDS.

10×TBS

Reagent	Final concentration
Tris-HCl pH 7.6	500 mM
NaCl	1.5 mM
ddH_2O	

As required, dilute 1:10 to make 1×TBS. Store at 4°C–25°C for up to a year.

CTT growth medium

Reagent	Final concentration
Casitone	1% (wt/vol)
Tris-HCl pH 7.6	10 mM
MgSO4	8 mM
Potassium phosphate pH 7.6	1 mM
ddH_2O	

Autoclave immediately. Stable for several months at RT.
Alternatives: Growth media have to be adjusted to the individual organism.

2.5 mM TCEP reduction buffer

Reagent	Final concentration
Tris-(2-carboxyethyl)-phosphine hydrochloride (TCEP)	2.5 mM
Ammonium bicarbonate	100 mM

Can be aliquoted and stored at -20°C for several weeks. Avoid thaw-freeze cycles of aliquots.

5mM Iodoacetamide alkylation buffer

Reagent	Final concentration
Iodoacetamide	5 mM
ddH_2O, MilliQ	

Can be aliquoted and stored at -20°C for several weeks. Avoid thaw-freeze cycles of aliquots.

SPE Buffer 1

Reagent	Final concentration
Trifluoroacetic acid	0.1 % (vol/vol)
ddH_2O, HPLC grade	

SPE Buffer 2

Reagent	Final concentration
Acetonitrile	50 % (vol/vol)
Trifluoroacetic acid	0.1 % (vol/vol)
ddH_2O, HPLC grade	

LC buffer A

Reagent	Final concentration
Formic acid, LC-MS grade	0.15 % (vol/vol)
ddH_2O, LC-MS grade	

LC buffer B

Reagent	Final concentration
Acetonitrile, LC-MS grade	50 % (vol/vol)
Formic acid, LC-MS grade	0.15 % (vol/vol)
ddH_2O, LC-MS grade	

- 100 mM biotin stock solution: add 122 mg biotin in a total of 5 ml 1M Tris pH 7.6 and titrate with KOH until biotin is fully dissolved.

Store in aliquots at -20°C for up to a year.

- 500 mM vanillate stock solution: add 840.7 mg vanillate to a total of 10 ml ddH_2O and titrate with KOH until vanillate is fully dissolved.
  Store at 4°C for up to a year.
- Transfer-buffer: Add 36.3 g Tris and 22.5 g glycine, fill to 1 l with ddH_2O. Do not adjust the pH.
  Stable for several months at RT.
- TBST-buffer: Add 0.5 ml Tween20 to 1 l of TBS.
  Stable for several months at RT.
- 5% (wt/vol) non-fat milk in TBST: Dissolve 25 g of milkpowder in 500 ml of 1×TBST.
  Stable for several days at 4°C.
  Alternatives: Concentration of milk powder may be adjusted to avoid background in western blots.
- 3% (wt/vol) Bovine serum albumin (BSA) in TBST: Dissolve 15 g of BSA in 500 ml of TBST.
  Stable for several days at 4°C.
  Alternatives: Concentration of BSA may be adjusted to avoid background in western blots.
- Kanamycin stock solution: add 500 mg kanamycinsulfate in 10 ml ddH_2O.
  Store in aliquots at -20°C.

CRITICAL: Kanamycin is harmful. Wear protective gloves/ protective clothing/eye protection/face protection.

- Gentamycin stock solution: add 100 mg gentamycinsulfate in 10 ml ddH_2O.
  Store in aliquots at -20°C.

CRITICAL: Gentamycin is harmful. Wear protective gloves/ protective clothing/eye protection/face protection.

- CTT supplemented with kanamycin and/or gentamycin: Add 1 µl per ml of the gentamycin or kanamycin stock solution to the CTT medium.
  Prepare freshly.

Step-by-step method details

Determine the concentrations of vanillate, biotin and labeling time for proximity labeling experiments using western blot

Timing: 1-2 weeks

In this step, the amount of inducer used to express the control protein (sfGFP-mTurboID-FLAG) is titrated to reach a level similar to that of the bait protein. Additionally, the amount of biotin and the labeling time is adjusted.

1. To adjust the accumulation of bait and control protein to similar levels, whole cell lysates of cells, grown in the presence of different concentrations of inducer (in our case vanillate), are prepared and analysed by western blot.
   a. Prepare culture of strains synthesizing the bait protein or the control protein.
      i. Resuspend a single colony per strain in 5 ml CTT liquid medium and incubate cultures with shaking for 8 h at 32°C in the dark.
      Note: Incubation times should be adjusted to the doubling time of the bacterium used. *M. xanthus* cells growing in suspension culture have a doubling time of 5 to 6 h. Also *M. xanthus* cells are light-sensitive and therefore incubated in the dark. These parameters can be adjusted to suit other bacteria.

ii. Dilute the cultures to an OD_{550nm}=0.1 in 10 ml CTT. For the strain expressing the control protein, inoculate 5 cultures with an OD_{550nm}=0.1.

b. To induce synthesis of the control protein from the vanillate inducible promoter, add vanillate to the five cultures to final concentrations of 0, 5, 10, 50, and 100 µM, and incubate the cultures with shaking for maximal 3 generations (≈18 h) at 32°C in the dark to make sure that cells remain in the exponential growth phase.

c. Take samples for SDS-PAGE by normalizing cultures to an OD_{550nm}=14.
   i. Harvest cells by centrifugation at 4,500 g for 10 min at RT and resuspend to an OD_{550nm}=14 in 1×Laemmli buffer.
   ii. Boil samples at 95°C for 10 min with shaking at 1,000 rpm.
   iii. Briefly centrifuge the samples to sediment condensation in the lid.

Pause point: Samples can be stored at -20°C for weeks.

d. Load 15 µl of each sample on an Any kD™ Mini-PROTEAN® TGX™ Precast Protein Gel and run the gels at 150 V for 45 min in an electrophoresis cell.
e. Transfer the gel to 0.2 µm nitrocellulose membrane using the 7 min TurboTransfer program using the TransBlot® Turbo™Transfer System.
f. Block the membrane with 5 % milk for 1 h at RT.
g. Incubate the membrane with α-FLAG primary antibody (1:2,000 in 1% milk TBS) over night at -4°C.
h. Wash the membrane three times with 1×TBST for 5 min each.
i. Incubate the membrane with α-rabbit secondary antibody (1:15,000 in 1% milk TBS) for 1 h at -4°C.
j. Wash the membrane three times with 1×TBST for 5 min each.
k. Develop the blot using the luminescent image analyzer LAS-4000 after applying the Luminata Western HRP Substrate.
l. Strip the membrane by incubating it in 15 ml stripping-buffer for 15 min at RT.
m. Wash the membrane three times with 1×TBST for 5 min each.
n. Block the membrane with 5% milk for 1 h at RT.
o. Wash the membrane three times with 1×TBST for 5 min each.
p. Incubate the membrane with Streptavidin-HRP (1:4,000 in 3% BSA-TBS) over night at 4°C.
q. Wash the membrane three times with 1×TBST for 5 min each.
r. Develop the blot using a luminescent image analyzer after applying the Luminata Western HRP Substrate.

Note: Using western blot, we determined that 5-10 µM vanillate are sufficient to reach the same level of accumulation of the bait and control proteins (Fig. 1A). Additionally, we observed that the sfGFP-mTurboID-FLAG fusion is degraded when increasing the expression (50 and 100 µM vanillate).

2. To optimize the amount of biotin added to the cells for the labeling reaction, whole cell lysates of cells grown with different biotin concentrations for 4 h are prepared and analysed by western blot.
   a. Prepare culture of strains synthesizing the bait protein or the control protein.
      i. Resuspend a single colony per strain in 5 ml CTT liquid medium and incubate cultures with shaking for 8 h at 32°C in the dark.
      ii. Dilute cultures to an OD_{550nm}=0.1 in 10 ml CTT. For the strain expressing the control protein, inoculate 5 cultures with an OD_{550nm}=0.1.

b. Induce synthesis of the control protein using the experimentally determined vanillate concentration and incubate culture with shaking for 18 h at 32°C (see comment in Step 1b about incubation).
c. Induce labelling by adding biotin to 0, 5, 25, 50, 100, 200, and 500 µM final concentration to the cultures. Incubate with shaking for 4 h at 32°C in the dark.
d. Take samples for SDS-PAGE by normalizing cultures to an OD_{550nm}=14.
   i. Harvest cells by centrifugation at 4,500 g for 10 min at RT and resuspend to an OD_{550nm} =14 in 1×Laemmli buffer.
   ii. Boil samples at 95°C for 10 min with shaking at 1,000 rpm.
   iii. Briefly centrifuge the samples to sediment condensation in the lid.
e. Load 15 µl of each sample on an Any kD™ Mini-PROTEAN® TGX™ Precast Protein Gel and run the gels at 150 V for 45 min in an electrophoresis cell.
f. Transfer the gel to 0.2 µm nitrocellulose membrane using the 7 min TurboTransfer program using the TransBlot® Turbo™Transfer System.
g. Block the membrane with 5% milk for 1 h at RT.
h. Wash the membrane three times with 1×TBST for 5 min each.
i. Incubate the membrane with Streptavidin-HRP (1:4,000 in 3% BSA-TBS) over night at 4°C.
j. Wash the membrane three times with 1×TBST for 5 min each.
k. Develop the blot using a luminescent image analyzer after applying the Luminata Western HRP Substrate.

Note: Generally, concentrations between 50 µM and 100 µM are already saturating the labeling reaction (Fig. 1B). Ideally, the concentration is chosen as low as possible to reduce the amount of free biotin in the lysate.

3. The labelling time after addition of biotin should be optimized to ensure labeling level and specificity. To optimize the labeling time, whole cell lysates at different timepoints after addition of biotin to a fixed concentration are prepared and analysed by western blot. For the test experiments we used 50 µM biotin to induce the labeling reaction because this concentration yielded robust and strong labeling as determined in step 2.
   a. Prepare culture of strains accumulating the bait protein and the control. Because samples will be taken from the same culture at different time points the culture is started with a larger volume.
      i. Resuspend a single colony per strain in 5 ml CTT liquid medium and incubate cultures with shaking for 18 h at 32°C in the dark (see comment in Step 1b about incubation).
      ii. Dilute cultures to an OD_{550nm}=0.3 in 10 ml CTT and incubate cultures with shaking for 8 h at 32°C in the dark.
      iii. Dilute cultures to an OD_{550nm}=0.1 in 50 ml CTT.
      iv. Add vanillate to a final concentration as determined in step 1 to induce synthesis of the control (sfGFP-mTurboID-FLAG) and incubate culture with shaking for 18 h at 32°C in the dark (see comment in Step 1b about incubation).
   b. Induce labelling by adding 50 µM biotin to the cultures.
   c. Incubate the cultures with shaking for 0 min, 10 min, 30 min, 1 h, 2 h, 4 h, 6 h, 24 h at 32°C in the dark.
   d. Take samples for SDS-PAGE by normalizing cultures to an OD_{550nm}=14.
      i. Harvest cells by centrifugation at 4,500 *g* for 10 min at RT and resuspend to an OD_{550nm} =14 in 1×Laemmli buffer.
      ii. Boil samples at 95°C for 10 min with shaking at 1,000 rpm.

iii. Briefly centrifuge the samples to sediment condensation in the lid.

e. Load 15 µl of each sample on an Any kD™ Mini-PROTEAN® TGX™ Precast Protein Gel and run the gels at 150 V for 45 min in an electrophoresis cell.
f. Transfer the gel to 0.2 µm nitrocellulose membrane using the 7 min TurboTransfer program using the TransBlot® Turbo™Transfer System.
g. Block the membrane with 5% milk for 1 h at RT.
h. Wash the membrane three times with 1×TBST for 5 min each.
i. Incubate the membrane with Streptavidin-HRP (1:4,000 in 3% BSA-TBS) over night at 4°C.
j. Wash the membrane three times with 1×TBST for 5 min each.
k. Develop the blot using a luminescent image analyzer after applying the Luminata Western HRP Substrate.

Note: Labeling times likely depend on the organism and protein used and should be optimized accordingly. We determined the optimal labeling time to be 4 h, based on the observation that labeling with proteins saturated between 2 h and 8 h (Fig. 1C).

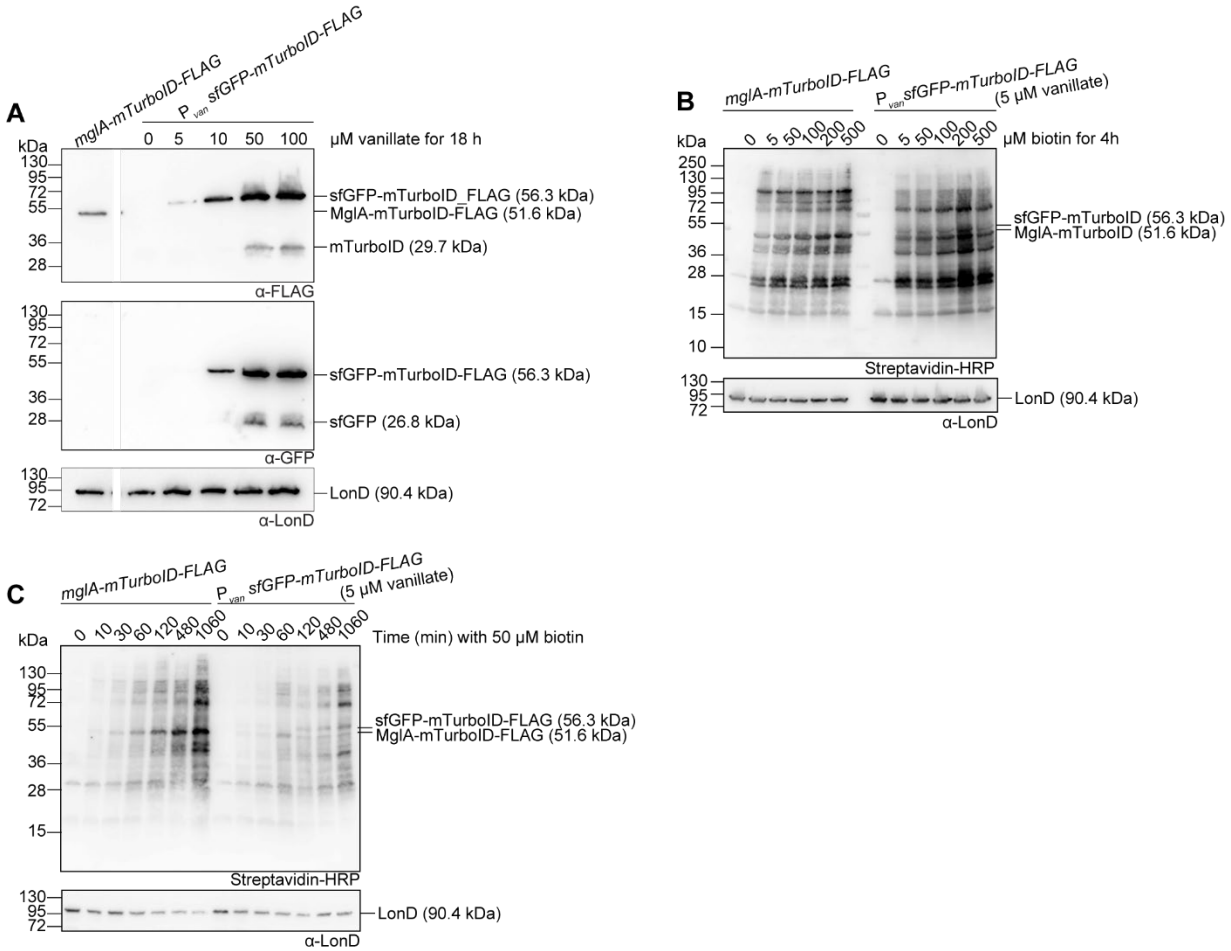

Figure 1 Optimization of vanillate concentration, biotin concentration and labeling time. (A-C) Protein from the same amount of cells was loaded in each lane and separated by SDS-PAGE. Blots were probed with the indicated antibodies or Streptavidin-HRP. Before probing with a different antibody, blots were treated with stripping-buffer. LonD was used as a loading control. In (A), gap indicates lanes removed for presentation purposes.

Preparation and labeling of cells grown on a surface or in suspension culture

Timing: 52 h

After optimizing the vanillate and biotin concentration, as well as the labeling time, biotinylated proteins are enriched using Strep beads. To compare cells grown on a surface with cells grown in suspension culture, vanillate was added to the control cells in suspension culture and in 150 mm petri dishes. Each strain was analyzed in biological triplicates to verify reproducibility.

4. Induction of labeling in cells in suspension culture.
    a. Resuspend single colonies in 10 ml CTT liquid medium and incubate cultures with shaking for 8 h at 32°C in the dark.
    b. Dilute cultures to an OD_{550nm}=0.1 in 50 ml CTT, induce synthesis of the control protein by adding vanillate and incubate cultures with shaking for 18 h at 32°C in the dark (see comment in Step 1b about incubation).
    Note: Adjust vanillate concentration to the concentration determined in step 1. For the presented experiment we used 5 µM.
    c. Add biotin to each suspension culture and incubate the cells for 4 h.
    Note: Use the biotin concentration determined in step 2 and adjust the time determined in step 3, for these experiments we used 50 µM biotin.

5. Labeling in cells grown on a surface.
    a. Prepare suspension cultures of strains accumulating the bait protein and the control in biological triplicates.
        i. Resuspend a single colony per replicate in 5 ml CTT liquid medium and incubate cultures with shaking for 8 h at 32°C in the dark.
        ii. Dilute cultures to an OD_{550nm} =0.1 in 20 ml CTT and incubate cultures with shaking for 18 h at 32°C in the dark (see comment in Step 1b about incubation).
    b. Dilute each culture in 40 ml CTT to OD_{550nm}=0.05 in 40 ml, transfer the cell suspension to a Petri dish (Ø=150 mm) and incubate for 8 h at 32°C in the dark.
    c. To induce synthesis of the control protein from the vanillate inducible promoter, add vanillate to the Petri dishes with the corresponding strains and continue for 18 h at 32°C in the dark (see comment in Step 1b about incubation).
    Note: Adjust the vanillate concentration to the concentration determined in step 1. For the presented experiment we used 5 µM.
    d. To induce the labeling reaction, add biotin to the cells for 4 h at 32°C in the dark.
    Note: Adjust the biotin concentration to the concentration determined in step 2 and adjust the time determined in step 3, for the presented experiment we used 50 µM biotin.
    CRITICAL: Do not agitate Petri dishes as agitation will lead to detachment of cells from the bottom of the petri dish.
    e. After labelling, scrape cells off the surface using a cell scraper and combine cells of the 3 Petri dishes of one replicate.

Enrichment of biotinylated proteins and on-bead digest

Timing: 20 h

After *in vivo* labeling cells are lysed and biotinylated proteins enriched using Strep beads. Subsequently, biotinylated proteins are eluted and digested using an on-bead digest procedure.

6. Enrichment of biotinylated proteins using Strep beads
    a. Harvest cells by centrifugation at 8,000 *g* for 10 min at RT.
    b. Wash the cell pellet by resuspending in 10 ml TPM buffer
    c. Harvest cells at 8,000 *g* for 10 min at 4°C and discard the supernatant.
    d. Repeat steps b and c three times.
    Note: Extensive washing ensures that free biotin, which could interfere with the enrichment of biotinylated proteins, is removed efficiently.
    e. Resuspend the cell pellet in 600 µl RIPA buffer.
    f. Sonicate for 30 s with a Hielscher UP200st set to amplitude=50% and pulse=50%.
    g. Pellet cell debris at 8,000 *g* for 10 min 4°C. In the meantime, start equilibrating the desalting columns.
    h. Equilibrate G25-Desalting columns
        Note: Desalting columns are used to remove any free biotin left in the lysate. Instead of a spin protocol, desalting columns can also be used with a gravity protocol for more efficient removal of free biotin.
        i. Remove the top and bottom seal of the column and remove the filter with forceps.
        ii. Load the desalting column onto a 15 ml Falcon tube using an appropriate adapter.
        iii. Load 2-3 ml of RIPA buffer on the desalting column and let the buffer drain by gravity. Repeat this step.
        iv. Load 2-3 ml of RIPA buffer on the desalting column and empty the desalting column by centrifugation at 1,000 *g* for 2 min.
    i. Transfer 500 µl of the cleared lysate on a desalting column and let the lysate enter the column bed.
    j. Transfer the desalting column into a new falcon tube and collect the cleared lysate by centrifugation at 1,000 *g* for 2 min.
    k. Measure the protein concentration in all samples.
        a. Dilute 10 µl of the desalted lysate in 90 µl ddH2O.
        b. In a 96-well plate: Mix 10 µl ddH2O, and 10 µl of BSA standards with 190 µl 660nm Protein Assay. In triplicates: Mix 10 µl of the diluted lysates with 190 µl 660nm Protein Assay.
        c. Mix all wells by shaking and measure the absorbance at 660 nm in an appropriate plate reader (i.e. Tecan M200).

    Note: Dilute samples and use BSA standards according to the linear range of the assay used to measure the protein concentration.
    l. Dilute all lysates to the same protein concentration
    Note: We use 2,000 µg/ml in our experiments.
    m. Equilibrate Strep beads.
        i. Resuspend 40 µl of Strep beads per sample in 1 ml RIPA buffer.
        ii. Separate beads using a magnetic rack.
        iii. Repeat wash.
        iv. Resupend beads in 500 µl RIPA.
    n. Mix 500 µl desalted lysate and 500 µl equilibrated beads in a 2 ml Eppendorf tube and incubate for 1 h on a rotary shaker at 4°C.

    Note: In our hands, 2 ml tubes allow easier separation of magnetic beads.
    o. Separate the Strep beads from the lysate using a magnetic rack.
    p. Wash the beads twice with 1 ml RIPA buffer.

q. Wash the beads twice with 1 ml 1 M KCl.
r. Wash the beads three times with 1 ml 50 mM Tris-HCl pH 7.6.
s. Wash the beads with 1 ml Ammonium bicarbonate (ABC).
t. Resuspend beads in 100 µl ABC.

Pause point: Remove ABC and snap-freeze the dry beads in liquid nitrogen. Beads can be stored at -80°C until proceeding with the on-bead digest.

CRITICAL: Liquid nitrogen can cause severe burns when in contact with the skin/ eye. Wear appropriate protection.

7. Perform on-bead digest of enriched proteins.

   Note: As on-bead digest is performed by directly adding the endopeptidase trypsin to proteins enriched on Strep beads, all detergents and protease inhibitors have to be removed prior to adding the protease.

   a. Add 200 µl on-bead digestion buffer (1µg trypsin in 100 mM ABC) to the beads, vortex and incubate for 30 min on a thermomixer at 30°C at 1,200 rpm. Make sure the beads are always fully resuspended.
   b. Separate, collect supernatant and transfer into new eppendorf tube.
   c. Add 100 µl TCEP reduction buffer to the beads, vortex and separate beads.
   d. Collect supernatant and add to trypsin containing sample.
   e. Let reaction proceed at 30°C overnight.
   f. After tryptic digest, add 5 µl alkylation buffer, vortex and incubate for 30 min in the dark

   Pause point: Proceed with solid phase extraction or freeze samples at -20°C.

Solid phase extraction of tryptic peptides

Timing: 3 h

In this step the peptide sample are desalted and prepared for LC-MS injection

8. Acidify samples by adding 50 µl of 5% Trifluoroacetic acid (TFA).
9. Condition C18-columns with 200 ul Acetonitrile and spin at 8 *g* on a table top centrifuge for 30 s.
10. Equilibrate columns with 400 µl SPE Buffer 1, centrifuge at 15 *g* for 30 s at RT.
11. Load sample and spin at 8 *g* for 1 min at RT.

Note: Depending on sample and cartridge dimensions, the centrifugation time, speed and buffer volumes may be adopted. The SPE columns should never run completely dry. Repeatedly discard the centrifugation flowthough.

12. Wash loaded peptide sample by adding 400 µl Buffer 1, centrifuge at 15 *g* for 30 s at RT.
13. Transfer the SPE column with bound peptides to a new eppi. Add 400 µl SPE Buffer 2 and centrifuge 15 *g* for 30 s at RT.
14. Concentrate eluted peptide mixture under vacuum to dryness. Drying process in a SpeedVac takes around 2 h.
15. Reconstitute peptides in 50 µl Buffer 1, vortex and transfer sample into LC vial and proceed with LC-MS analysis. Otherwise, peptides can be stored dry for several month.

Pause point: Peptide sample can be stored dry for several month.

LC-MS analysis

Timing: 75 min per sample

Here we describe an example for an LC-MS acquisition method suited for mTurboID affinity purification experiments. This individually established routine includes an Ultimate 3000 RSLC system connected to an Exploris 480 Orbitrap mass spectrometer using a data dependent acquisition (DDA) MS strategy for label-free protein quantification.

Note: With the variety of possible LC-MS/MS analytical set ups including column origin, important parameters can vary substantially, depending on the installed HPLC and MS system.

16. Load 5 µl peptide material onto the Pre-column with 10 µl/min flow LC-Buffer A (0.15% Formic acid).
17. For peptide separation use a self-packed C18 column with 42 cm length and 75 µm ID x 360 µm OD column heated at 60°C using an in-house designed column heater.
18. Perform peptide separation at constant flow rate of 300 nl/min using a 40 min gradient from 6-35% LC buffer B (99.85% Acetonitrile/0.15 % Formic acid) on a 42 cm self-packed analytical.

Note: The implementation of a column heater will reduce back pressure and allow the use of longer column for better peptide separation. If no column heater is used shorter columns are used to prevent LC overpressure.

19. Eluting peptides are ionized with a spray voltage of 2.3 kV in positive mode.
20. Set the capillary temperature to 300°C.
21. Acquire MS1 survey scan (scan range m/z 350-1,650) in profile mode with following parameters:
    a. Set Orbitrap resolution to 60,000
    b. AGC target setting to 300% ($3e^6$) and max fill time to 25 ms
    c. RF lens 40%
22. Acquire MS/MS fragment spectra in data dependent acquisition (DDA) mode with following parameters:
    a. Quadrupole isolation window m/z 1.5
    b. For fragmentation include ions with charge states 2-6
    c. Set Orbitrap resolution to 15,000
    d. AGC target setting to 200% ($2e^5$) and max fill time set to “Auto”
    e. HCD normalized collision energy 27
    f. Dynamic exclusion 20 s
    g. Set cycle time for MS/MS sequencing attempts to 1 s

Optional: Next to DDA other MS acquisition strategies like data independent acquisition (DIA) are possible options for protein label-free quantification. The choice of the MS acquisition strategy is based on several factors including sample complexity and observed data robustness.

Protein label-free quantification using MaxQuant

Timing: 4 h

The MS raw data is analyzed with MaxQuant for protein label-free quantification (LFQ). MaxQuant is a widely used, freely available analysis software with several implemented strategies including label-free, isotopic and isobaric protein quantification.

23. Download MaxQuant (https://www.maxquant.org/) and install software on an appropriate PC.
24. Download *Myxococcus xanthus* protein sequence database in fasta format via uniprot (https://www.uniprot.org/)
25. Load raw files and "set experiment" according to experimental set up.
26. Process MaxQuant with "Label-free quantification" and "min. ratio count" set to "1". For modifications set Carbamidomethyl on (C) as fixed; oxidation on (M) and deamidation on (DQ) as variable. Activate "Require MS/MS for LFQ comparisons" to include only peptides identified by defined identification FDRs.
27. With few excaptions MaxQuant is best performed in standard settings.
28. Locate the MaxQuant output ".txt" folder and use the "LFQ intensities" in the "proteinGroups.txt" output for further analysis.

Note: The MaxQuant output tables offer detailed information on identified peptides and proteins helpful for further monitoring and troubleshooting. In order to evaluate comparability across samples and to avoid label-free quantification biases make sure homogenous distribution of number unique peptides and intensites found in the "proteinGroups.txt" table.

Expected outcomes

The presented protocol allows the identification of the protein interactome of the key motility regulator MglA in live *M. xanthus* cells under two different conditions using mTurboID-based proximity labeling. First, the expression level of the ectopically expressed control protein (sfGFP-mTurboID-FLAG) was adjusted to match the level of MglA-mTurboID-FLAG expressed from the native site. Second, biotin-labeling efficiency was verified using western blot and optimized by adjusting the biotin concentration and labeling time. The optimized procedure was then applied to study the protein interactome of MglA in two different cell states – cells grown on a surface and cells grown in suspension culture.
After conducting the proximity labeling, LC-MS/MS analysis and label-free protein quantification, the significance and degree of protein enrichment versus control strains are calculated using Perseus[20] and visualized in volcano plots. Using defined enrichment criteria (log2ratio≥2; *p*-value≤0.03), several proteins were identified that are indicative of the general success of the proximity labeling experiment:
First, the MglA-mTurboID-FLAG bait was enriched, representing an important experimental quality control. It is noteworthy that MglA did not show strong enrichment. This is likely caused by the general high MglA background abundance, the small size of MglA (22 kDa) and potentially reduced tryptic cleavage sites due to biotinylation (see Limitations). Second, inspection of the data revealed the enrichment of proteins that have previously been shown to interact with MglA and include direct protein interactors and/or proteins functionally linked to motility. These proteins are highlighted in Figure 2. Specifically, among proteins known to interact with MglA, we identified the GAP proteins MglB and RomY[13,14,16], the gliding motility protein AglZ[8,11] and GltJ[21] and the regulators of T4aP-dependent motility FrzS and SgmX[7,9,10], demonstrating the feasibility of the mTurboID proximity labeling protocol. Of note,

while most of these interactions were verified using *in vitro* methods and purified proteins, proximity labeling was able verify these interactions *in vivo.* Third, we identified RomR, which is part of the MglA GEF but likely does not interact directly with MglA(Szadkowski 2019). Fourth, we identified other proteins with a verified function in motility including PilM, which is essential for T4aP-dependent motility[22]. Fifth, we identified FrgA[23], SgnC[24], NmpS[25] and PglH[26], all of which have been implicated in motility or its regulation. Because PilM, GltJ, SgnC and PglH were identified as potential interaction partners of MglA, they are interesting candidates to further extend our understanding of of how MglA stimulates the two motility systems.

Because external conditions, such as surface contact, can influence the subcellular localization of proteins in bacteria on short time scales, e.g. in *Pseudomonas aeruginosa* proteins that promote surface colonization localize within seconds after surface contact[27], we conducted proximity labeling under two different conditions (growth on surface and suspension culture). Although many of the potential interactions were detected independently of the two conditions), we identified distinct candidates for the two conditions. For example, PglH and the DnaJ/TPR domain protein MXAN_2049, which is encoded directly next to *pglH*, and the PilT5 protein, which is a paralog of the T4aP retraction ATPase PilT, were only enriched when cells were grown on a surface, while PilM was only enriched in cells grown in suspension culture. These observations suggest that the interaction network of MglA changes upon surface contact. Thus, conducting the proximity labelling under different environmental conditions can help to identify conditional interactions and generate snapshots of condition-dependent protein interactions.

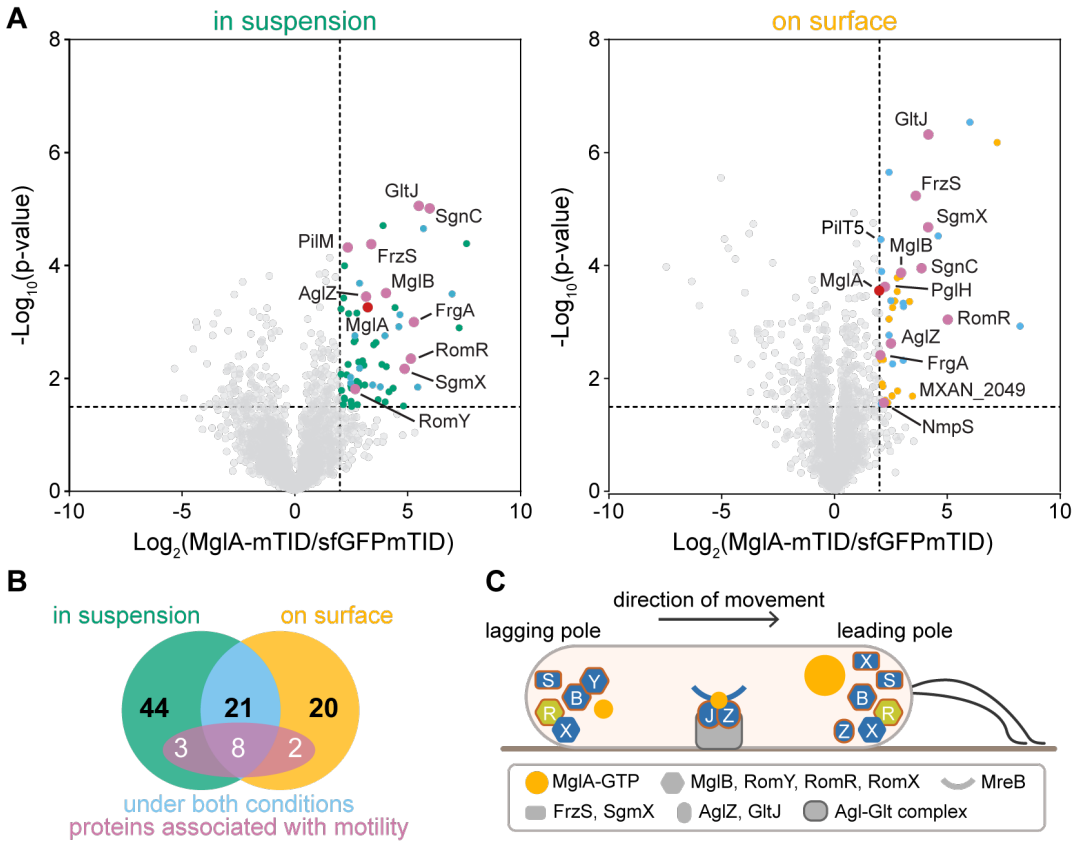

Figure 2

(A) Volcanoplots representing the results from proximity labeling experiments with cells expressing MglA-mTurboID-FLAG during surface growth and growth in suspension culture. Plots show the comparison of MglA-mTurboID-FLAG and sfGFP-

mTurboID-FLAG from suspension cultures (left) and during surface growth (right). The X-axis represents the log2ratio of group mean intensities from three experiments. The Y-axis represents the statistical significance of the corresponding targets. Dashed lines represent the threshold (log2ratio>2; *p*-value<0.03). Points represent identified proteins, MglA is shown in red, remaining proteins are indicated using the same colour code as in (B). Known motility proteins or regulatory proteins are labeled with their names. (B) Venn diagram showing the number of proteins enriched exclusively in suspension cultures (green), exclusively during surface growth (yellow) and under both conditions (blue). Known motility proteins or regulatory proteins in these three categories are shown (pink). Colours correspond to coloured points in the volcano plots in (A). (C) Schematic cell with the localization of known interaction partners of MglA. Proteins corresponding to their shapes described in the legend below. Letter within shape represents the last letter of a protein. Blue indicates known direct interaction partners of MglA. Green indicates protein that has not been shown to directly interact with MglA. Orange line mark proteins identified in the proximity labeling experiments.

Limitations

Despite the potential of proximity labeling to uncover protein interactomes, some limitations are associated with this approach. Inheritently, the method does not allow to distinguish whether a significantly enriched protein directly interacts with the bait, or if the interaction is indirect. Alternative methods (i.e. pull-down assay, FRET-microscopy and co-immunoprecipitation) have to be used to further distinguish between direct and indirect interaction.

Enrichment and identification of small proteins or membrane proteins can be challenging due to a lack of (surface exposed) Lys residues. Furthermore, biotinylated Lys residues provide a poor substrate for tryptic digestion and, consequently, are more difficult to identify due to a higher degree of miscleaved products. For transmembrane proteins the topology should be considered, since the periplasm lacks ATP, the biotinylation reaction does not work in that compartment. This additionally limits TurboID based proximity labeling to the cytoplasm or to cytoplasmic parts of IM proteins. As an alternative, APEX2-based proximity labeling has been reported for periplasmic proteins[28].

In addition, the proximity labeling reaction is mainly regulated by the availability of biotin and temperature and therefore is difficult to control on short timescales. UV light inducible systems like the recently introduced LOV-TurboID[29] may provide improved temporal control of the labeling reaction.

Troubleshooting

Problem 1:

The mTurboID-bait protein does not bind to the Strep beads/ proportionally high amount of bait-protein remains in the flow through.

Potential solution:

This could be due to an excess of free biotin in the lysate.

- Increase the amount of washing steps (Step 6.a) or the washing volume of the culture.
- Switch from spin protocol to gravity protocol for the desalting column.
- Check and possibly increase the volume of beads used for affinity purification.

Problem 2:

The mTurboID-fusion is degraded .

Potential solution:

Changing the sequence or length of the linker between protein of interest and mTurboID may increase fusion stability. Also fusing mTurboID to a different terminus of the bait protein may increase stability. Alternatively, other proximity labeling tags, such as TurboID[1] or UltraID[30] could be tested for enhanced stability.

Problem 3:
The mTurboID-fusion is not stable or not synthesized.
Potential solution:
Change the promoter used for the expression of the fusion protein or codon optimization also can enhance the efficiency of protein expression.

Problem 4:
Varying protein recovery across samples after LC-MS analysis.
Potential solution:
Optimize the lysis condition including choice of detergent, heat exposure, disruption method (e.g. sonication, bead disruption, etc.) and enzymatic support (e.g. lysozyme).

Problem 5:
Contaminated chromatograms and/or poor protein recovery after LC-MS analysis despite enrichment confirmed by western blot.
Potential solution:
Include more bead washing steps before on-bead digest or adopt optimize protein elution/digest strategy (e.g. detergent and heat elution with subsequent acetone precipitation and in-solution digest).

Resource availability
Lead contact
Timo Glatter (timo.glatter@mpi-marburg.mpg.de)

Materials availability
Plasmids and strains are available upon request.

Data and code availability
The dataset generated during this study are available upon request.

Acknowledgments
The authors thank María Pérez Burgos for construction of plasmids and strains. This work was generously funded by the Max Planck Society.

Author contributions
M.H., F.M. and T.G. performed experiments and analysed data. T.G. performed MS analysis. M.H., F.M., L.S-A. and T.G. wrote the manuscript. L.S.-A. acquired funding. L.S.-A. and T.G. provided supervision.

Declaration of interests
The authors declare no competing interests.

References

1. Branon, T.C., Bosch, J.A., Sanchez, A.D., Udeshi, N.D., Svinkina, T., Carr, S.A., Feldman, J.L., Perrimon, N., and Ting, A.Y. (2018). Efficient proximity labeling in living cells and organisms with TurboID. Nat Biotechnol *36*, 880-887. 10.1038/nbt.4201.
2. Qin, W., Cho, K.F., Cavanagh, P.E., and Ting, A.Y. (2021). Deciphering molecular interactions by proximity labeling. Nat Methods *18*, 133-143. 10.1038/s41592-020-01010-5.
3. Carreira, L.A.M., Szadkowski, D., Müller, F., and Søgaard-Andersen, L. (2022). Spatiotemporal regulation of switching front-rear cell polarity. Curr Opin Cell Biol *76*, 102076. 10.1016/j.ceb.2022.102076.
4. Zhang, Y., Ducret, A., Shaevitz, J., and Mignot, T. (2012). From individual cell motility to collective behaviors: insights from a prokaryote, *Myxococcus xanthus*. FEMS Microbiol Rev *36*, 149-164. 10.1111/j.1574-6976.2011.00307.x.
5. Schumacher, D., and Søgaard-Andersen, L. (2017). Regulation of cell polarity in motility and cell division in *Myxococcus xanthus*. Annu Rev Microbiol *71*, 61-78. 10.1146/annurev-micro-102215-095415.
6. Dinet, C., and Mignot, T. (2023). Unorthodox regulation of the MglA Ras-like GTPase controlling polarity in *Myxococcus xanthus*. FEBS Lett *597*, 850-864. 10.1002/1873-3468.14565.
7. Bautista, S., Schmidt, V., Guiseppi, A., Mauriello, E.M.F., Attia, B., Elantak, L., Mignot, T., and Mercier, R. (2023). FrzS acts as a polar beacon to recruit SgmX, a central activator of type IV pili during *Myxococcus xanthus* motility. EMBO J *42*, e111661. 10.15252/embj.2022111661.
8. Mauriello, E.M., Mouhamar, F., Nan, B., Ducret, A., Dai, D., Zusman, D.R., and Mignot, T. (2010). Bacterial motility complexes require the actin-like protein, MreB and the Ras homologue, MglA. EMBO J *29*, 315-326. 10.1038/emboj.2009.356.
9. Mercier, R., Bautista, S., Delannoy, M., Gibert, M., Guiseppi, A., Herrou, J., Mauriello, E.M.F., and Mignot, T. (2020). The polar Ras-like GTPase MglA activates type IV pilus via SgmX to enable twitching motility in *Myxococcus xanthus*. Proc Natl Acad Sci U S A *117*, 28366-28373. 10.1073/pnas.2002783117.
10. Potapova, A., Carreira, L.A.M., and Søgaard-Andersen, L. (2020). The small GTPase MglA together with the TPR domain protein SgmX stimulates type IV pili formation in *M. xanthus*. Proc Natl Acad Sci U S A *117*, 23859-23868. 10.1073/pnas.2004722117.
11. Treuner-Lange, A., Macia, E., Guzzo, M., Hot, E., Faure, L.M., Jakobczak, B., Espinosa, L., Alcor, D., Ducret, A., Keilberg, D., et al. (2015). The small G-protein MglA connects to the MreB actin cytoskeleton at bacterial focal adhesions. J Cell Biol *210*, 243-256. 10.1083/jcb.201412047.
12. Carreira, L.A.M., Tostevin, F., Gerland, U., and Søgaard-Andersen, L. (2020). Protein-protein interaction network controlling establishment and maintenance of switchable cell polarity. PLoS Genet *16*, e1008877. 10.1371/journal.pgen.1008877.
13. Leonardy, S., Miertzschke, M., Bulyha, I., Sperling, E., Wittinghofer, A., and Søgaard-Andersen, L. (2010). Regulation of dynamic polarity switching in bacteria by a Ras-like G-protein and its cognate GAP. EMBO J *29*, 2276-2289. 10.1038/emboj.2010.114.
14. Szadkowski, D., Carreira, L.A.M., and Søgaard-Andersen, L. (2022). A bipartite, low-affinity roadblock domain-containing GAP complex regulates bacterial front-rear polarity. PLoS Genet *18*, e1010384. 10.1371/journal.pgen.1010384.
15. Szadkowski, D., Harms, A., Carreira, L.A.M., Wigbers, M., Potapova, A., Wuichet, K., Keilberg, D., Gerland, U., and Søgaard-Andersen, L. (2019). Spatial control of the GTPase MglA by localized RomR-RomX GEF and MglB GAP activities enables *Myxococcus xanthus* motility. Nat Microbiol *4*, 1344-1355. 10.1038/s41564-019-0451-4.
16. Zhang, Y., Franco, M., Ducret, A., and Mignot, T. (2010). A bacterial Ras-like small GTP-binding protein and its cognate GAP establish a dynamic spatial polarity axis to control directed motility. PLoS Biol *8*, e1000430. 10.1371/journal.pbio.1000430.
17. Kaimer, C., and Zusman, D.R. (2013). Phosphorylation-dependent localization of the response regulator FrzZ signals cell reversals in *Myxococcus xanthus*. Mol Microbiol *88*, 740-753. 10.1111/mmi.12219.

18. Treuner-Lange, A., Chang, Y.W., Glatter, T., Herfurth, M., Lindow, S., Chreifi, G., Jensen, G.J., and Søgaard-Andersen, L. (2020). PilY1 and minor pilins form a complex priming the type IVa pilus in *Myxococcus xanthus*. Nat Commun *11*, 5054. 10.1038/s41467-020-18803-z.
19. Kaiser, D. (1979). Social gliding is correlated with the presence of pili in *Myxococcus xanthus*. Proc Natl Acad Sci U S A *76*, 5952-5956. 10.1073/pnas.76.11.5952.
20. Tyanova, S., Temu, T., Sinitcyn, P., Carlson, A., Hein, M.Y., Geiger, T., Mann, M., and Cox, J. (2016). The Perseus computational platform for comprehensive analysis of (prote)omics data. Nat Methods *13*, 731-740. 10.1038/nmeth.3901.
21. Mignot, T., Attia, B., My, L., Castaing, J.P., Dinet, C., Le Guenno, H., Schmidt, V., Espinosa, L., Anantharaman, V., and Aravind, L. (2023). A novel molecular switch controls assembly of bacterial focal adhesions. Researchsquare. doi.org/10.21203/rs.3.rs-2617569/v1.
22. Friedrich, C., Bulyha, I., and Søgaard-Andersen, L. (2014). Outside-in assembly pathway of the type IV pilus system in *Myxococcus xanthus*. J Bacteriol *196*, 378-390. 10.1128/JB.01094-13.
23. Cho, K., Treuner-Lange, A., O'Connor, K.A., and Zusman, D.R. (2000). Developmental aggregation of *Myxococcus xanthus* requires *frgA*, an *frz*-related gene. J Bacteriol *182*, 6614-6621. 10.1128/JB.182.23.6614-6621.2000.
24. Youderian, P., and Hartzell, P.L. (2006). Transposon insertions of magellan-4 that impair social gliding motility in *Myxococcus xanthus*. Genetics *172*, 1397-1410. 10.1534/genetics.105.050542.
25. Bretl, D.J., Ladd, K.M., Atkinson, S.N., Muller, S., and Kirby, J.R. (2018). Suppressor mutations reveal an NtrC-like response regulator, NmpR, for modulation of type-IV pili-dependent motility in *Myxococcus xanthus*. PLoS Genet *14*, e1007714. 10.1371/journal.pgen.1007714.
26. Yu, R., and Kaiser, D. (2007). Gliding motility and polarized slime secretion. Mol Microbiol *63*, 454-467. 10.1111/j.1365-2958.2006.05536.x.
27. Laventie, B.J., Sangermani, M., Estermann, F., Manfredi, P., Planes, R., Hug, I., Jaeger, T., Meunier, E., Broz, P., and Jenal, U. (2019). A surface-induced asymmetric program promotes tissue colonization by *Pseudomonas aeruginosa*. Cell Host Microbe *25*, 140-152 e146. 10.1016/j.chom.2018.11.008.
28. Ganapathy, U.S., Bai, L., Wei, L., Eckartt, K.A., Lett, C.M., Previti, M.L., Carrico, I.S., and Seeliger, J.C. (2018). Compartment-specific labeling of bacterial periplasmic proteins by peroxidase-mediated biotinylation. ACS Infect Dis *4*, 918-925. 10.1021/acsinfecdis.8b00044.
29. Lee, S.Y., Cheah, J.S., Zhao, B., Xu, C., Roh, H., Kim, C.K., Cho, K.F., Udeshi, N.D., Carr, S.A., and Ting, A.Y. (2023). Engineered allostery in light-regulated LOV-Turbo enables precise spatiotemporal control of proximity labeling in living cells. Nat Methods *20*, 908-917. 10.1038/s41592-023-01880-5.
30. Kubitz, L., Bitsch, S., Zhao, X., Schmitt, K., Deweid, L., Roehrig, A., Barazzone, E.C., Valerius, O., Kolmar, H., and Bethune, J. (2022). Engineering of ultraID, a compact and hyperactive enzyme for proximity-dependent biotinylation in living cells. Commun Biol *5*, 657. 10.1038/s42003-022-03604-5.

9. Discussion and outlook of the study

Aim of this study was to investigate different aspects of the assembly of the T4aP machine in *M. xanthus*. Using cell biology, biochemistry and bioinformatics we could elucidate that the assembly of the T4aP machine is affected by the environmental conditions (i.e. the calcium concentration) and that assembly is coupled to the cell cycle of *M. xanthus.* Furthermore, we have shown that c-di-GMP, synthesized by the DGC DmxA, plays an important role in ensuring the symmetrical assembly of the T4aP machines at the new poles of the daughter cells.

We determined an important function of calcium in the assembly of the T4aP machine by promoting the stability of PilY1.1. In addition, we observed that calcium affects the efficiency at which cells move by means of T4aP-dependent motility, suggesting that it has a broader effect on T4aP function. The pseudopilus of the T2SS has been demonstrated to be stabilized by binding calcium and a similar mechanism could promote the assembly of T4aP in the presence of calcium. Therefore, it will be interesting to study the general effect on calcium in T4aP formation of *M. xanthus*. Furthermore, we identified a noncanonical cytochrome *c* as accessory protein for the formation of T4aP. This illustrates that T4aP accessory proteins can belong to diverse and unexpected protein families.

Second we analyzed the coordination between the assembly of the T4aP machine and cytokinesis. We propose that AMIN domain containing secretins are recruited to the pole by binding to a specific type of PG. In the future, it will be interesting to determine the exact properties of this PG. Furthermore, we find that DmxA and c-di-GMP have an impact on the recruitment of PilQ to the new poles. This suggests a connection between PG composition and c-di-GMP synthesis during cytokinesis, which could be an interesting topic for further investigations. Additionally, we observed that cells lacking DmxA hyper-reverse and have a defect in the distribution of RomR between the two daughter cells. This implies a more general role of c-di-GMP in the coordination of the formation of the new cell pole and the establishment of polar landmarks. Therefore, it will be important to precisely define, which processes c-di-GMP regulates during cytokinesis. Specifically, the identification of the c-di-GMP effectors and the polar landmarks will be of great interest to understand the function of c-di-GMP in *M. xanthus*.

By establishing the miniTurboID based proximity labeling in *M. xanthus* we could link the localization of DmxA to the divisome and find new potential interactors for MglA. This underlines that proximity labeling is a powerfull tool that will be of great use for the elucidation of other interaction networks in *M. xanthus*.

Acknowledgments

First, I want to thank Prof. Dr. Lotte Søgaard-Andersen for providing me with guidance and many opportunities to freely explore microbiology and develop as a scientist. Second, I want to thank Prof. Dr. Martin Thanbichler, Prof. Dr. Gert Bange and Prof. Dr. Lennart Randau for helpful discussions and for being in my thesis committee.

Special thanks go to, Dr. Anke Treuner-Lange for the supervision and discussions in the beginning of my journey through the world of T4P and for encouraging me to be curious; Dr. María Pérez Burgos for great teamwork, fun and fruitful exchange of theories, support, believing in my ideas (and many plasmids and strains to test those), and for helping me to focus and finish things; Dr. Timo Glatter for saving me from many western blots by opening the world of proteomics to me and for many chats in the hallway; Yvonne Ried, Steffi Lindow, Andrea Harms and Susanne Kneip for fun conversations during morning coffees and lunch breaks and for keeping the lab running.

I also want to thank Cisco, Luis, Dobro, Anna, Memduha and Ozan for the time in lab 2, and Franzi, Michael, Johannes, Michel, Philip, Jana and Dominik for help and discussions throughout the last few years.

Last, I want to thank my family that allowed me to pursue my ideas by mentally and financially supporting me along this long way, and everyone else that supported me throughout the years.